Spatio-temporal patterns of forest disturbance in western North America: implications for forest resilience

Michele Susan Buonanduci

A dissertation

submitted in partial fulfillment of the

requirements for the degree of

Doctor of Philosophy

University of Washington

2023

Reading Committee:

Brian J. Harvey, Chair

Maureen C. Kennedy

Patrick C. Tobin

Program Authorized to Offer Degree:

Quantitative Ecology and Resource Management

University of Washington

Abstract

Spatio-temporal patterns of forest disturbance in western North America: implications for forest resilience

Michele Susan Buonanduci

Chair of the Supervisory Committee:
Brian J. Harvey
School of Environmental and Forest Sciences

Globally, forest disturbance activity is changing in response to changing climate. As disturbance regimes change, concerns have been raised that the mechanisms of forest resilience (i.e., the capacity of forests to tolerate disturbance) may begin to break down. To successfully monitor, forecast, and manage for forest resilience in the context of changing disturbance regimes, quantifying indicators of forest resilience across spatial and temporal scales is critical. In this dissertation, I quantified facets of forest resilience to biotic disturbance (i.e., insects and plant pathogens) and wildfire in western North America. First, I evaluated compensatory responses of forests following severe bark beetle outbreak. I found that compensatory growth responses are strongly shaped by both the characteristics and spatial arrangement of surviving trees, and that increased post-disturbance growth acts as a key mechanism of forest resilience by providing continuity in forest function. Next, I characterized the patterns and drivers of biotic disturbance hotspots, an emerging phenomenon in the western United States (US) in which two or more distinct biotic disturbance agents co-occur in space and time. I found that while biotic disturbance hotspots are driven by forest composition and regionally important bioclimatic factors, they are also stochastic processes that cannot be predicted solely from deterministic landscape characteristics or other known drivers. Interactions among multiple disturbances such as these are important to understand, as they have the potential to erode compensatory responses and therefore mechanisms of forest resilience. Finally, I quantified the range of variation in burn severity patch structure characterizing Northwest US fire regimes. Despite changes in climate and fire activity in recent decades, I found that the range of variation in high-severity burn patches, conditional on fire size, has remained remarkably stationary in recent decades. Stationarity in the relationship between burn severity patterns and fire size offers a simple yet powerful means to anticipate the range of ecological effects of future fire activity at regional scales. Building on this finding, I conducted a simulation study demonstrating that shifts in fire size distributions towards larger fire events will lead to increasingly large high-severity burn patches with interior areas that are increasingly far from unburned seed sources following fire. Large high-severity patches directly affect rates of tree regeneration and forest recovery following fire, along with the potential for forests to transition to non-forest ecosystems. Collectively, this work provides insights into a range of mechanisms of forest resilience in western North America and has important implications for managing forests in the face of continued climate change and increasing disturbance activity.

TABLE OF CONTENTS

LIST OF FIGURES

LIST OF TABLES

ACKNOWLEDGEMENTS

This dissertation would not have been possible without the support, guidance, and friendship of so many people.

First, I'd like to acknowledge my advisor, Brian Harvey. Thank you for the countless opportunities and endless encouragement. You have a passion for science that kept me curious and energized even when grad school had me feeling worn down. Through the emphasis you place on building community, you've brought together a lab group that feels like family, and I feel so lucky to be a part of it. You have helped me grow as a scientist while supporting me as a whole person, and for that I am not sure I can fully express the extent of my gratitude.

Thank you to my committee members for making each degree milestone a valuable and enjoyable learning experience. Maureen Kennedy, thank you for going above and beyond as both a committee member and collaborator. I have learned so much through working with you these past few years. Patrick Tobin, thank you for the complementary perspective you have brought to my research and for your thoughtful questions. Ashley Steel, thank you for joining so many meetings from afar and late at night in your time zone. Beyond that, thank you for pushing my statistical thinking in ways that I will carry with me in my career. Abby Swann, thank you for your commitment to ensuring this whole process was reasonable and fair, and for always reminding me to broaden my perspective. In our conversations over the years, you each offered insights and asked questions that stretched my thinking. In doing so, you each made me a better scientist.

Thank you to my collaborators for contributing to this research and strengthening its relevance outside of academia. Josh Halofsky and Dan Donato, thank you for bringing a critical management perspective to my research here on the west side. Further, thank you for being the dynamic duo that you are; collaborating with you has been such a fun and rewarding experience. Mike Battaglia, thank you for sharing so many insights regarding Fraser Experimental Forest, the Colorado Rockies, and forest management more broadly.

An enormous thank you to the Fraser Experimental Forest field crew: Felicity Carroll, Nicole Lau, Arielle Link, Aileen Liu, Sahale Riedel, and Thadeus Sternberg. Without your tireless efforts, my Master's research and the first chapter of this dissertation would not have been possible. Thank you for working through heat, wind, and lightning to collect thousands of trees' worth of data. Your curiosity and questions pushed me to think more deeply about my study system, and your energy and good spirits carried me through a long field season away from home. I learned so much through working with and getting to know each of you.

My research was made possible by support of numerous funding agencies. The first two chapters of my dissertation were supported by the McIntire-Stennis Cooperative Forestry Research Program (grant no. NI17MSCFRXXXG003/project accession no. 1012773) from the USDA National Institute of Food and Agriculture and by the National Science Foundation (DEB 1853520). The second two chapters were supported by a U.S. Geological Survey Northwest Climate Adaptation Science Center award (G17AC000218) and a Graduate Research Innovation award (#21-1-01-26) from the Joint Fire Science Program. Additional funding was provided by the School of Environmental and Forest Sciences, the Quantitative Ecology and Resource Management Program, and the Student Technology Fee.

Thank you to the members of the Harvey Lab, past and present. First, Michelle Agne and Saba Saberi, thank you for enthusiastically welcoming me into your small but mighty group in those early days. Michelle, you have cheered me on and commiserated with me throughout this journey. Thank you for your friendship and for keeping me grounded when I have needed it most. Saba, thank you for the energy and humor you bring to every situation, and for folding me into your circle of friends when I was new to Seattle and to UW. I feel so lucky to know you. Jenna Morris, I am so glad we joined the lab at the same time and embarked on largely parallel journeys together. You are one of the most thoughtful people I know, and I can't imagine this journey without your friendship, kindness, and understated humor. Don Radcliffe, thank you for your commitment to building community both within our lab and within SEFS more broadly. Your 'dad jokes' have kept us laughing (and groaning) together, even in challenging times. Madison Laughlin, I have so enjoyed getting to know you over the years and seeing you progress from field technician to research assistant to MS and PhD student in the lab! You never cease to impress me, both in your scientific endeavors and in your ability to exude a level of chill even in stressful times. Liliana Rangel-Parra, I'm so glad (and frankly amazed) that you braved moving across the country at the start of a global pandemic to join our lab. Thank you for deepening my appreciation of the understory and commiserating with me when new technologies threw our teaching for a loop. Sofia Kruszka, thank you for the thousands of ways, both seen and unseen, that you have kept our lab running smoothly these past few years. I am so glad you are sticking around to pursue a graduate degree, and I can't wait to see all of the incredible things you will no doubt accomplish! Angie Gonzalez, you have become such an integral part of our lab group in such a short amount of time. Thank you for jumping right in with so much energy; I am so grateful you chose us.

To the QERM community, thank you for inspiring me with your quantitative prowess. And to my cohort, Anne Polyakov and Connie Okasaki, I'm not sure I would have survived that very first year without you. I am so grateful we started this journey together. To the SEFS community, thank you for including me as one of your own. I feel so fortunate to have met, befriended, and learned so much from so many of you.

Finally, thank you to my friends and family for all of your support, care, and encouragement; you are the reason I am where I am today. Mom and Dad, thank you for supporting me through life's ups and downs, and never once doubting me when I decided to stay in school for what seemed like forever. Justine, thank you for always picking up the phone when I need advice or just want to vent, and for always validating my feelings. I couldn't have asked for a better sister. Megan, thank you for being such a fierce and loving friend. You are like family to me, and I am so lucky to have you. Lila and Olivia, I can't imagine this chapter of my life without you in it. Thank you for your friendship, for the many shared dishes of pasta and glasses of wine, and for helping make Seattle feel like home. Vy, you inspired me to take the leap and head back to grad school. Thank you for always pushing me to be a better person, and for always being down for an adventure.

To my partner Paul, I am immensely grateful for your love and support through this experience. And to our cat Maple, thank you for being a comforting and playful presence in these final few months of writing.

PUBLISHED MATERIALS

A portion of the materials presented in this dissertation have been published through the peer-review process. This article is reproduced in full here as Chapter 1 and is reprinted with permission from Springer Nature.

Buonanduci, M.S., Morris, J.E., Agne, M.C., Battaglia, M.A., & Harvey, B.J. (2023). Fine-scale spatial heterogeneity shapes compensatory responses of a subalpine forest to severe bark beetle outbreak. *Landsc Ecol*, 38, 253–270. doi: 10.1007/s10980-022-01553-2

INTRODUCTION

Natural disturbances have widespread and important effects on the structure and function of ecosystems (Pickett & White 1985; Franklin *et al.* 2002). By altering the composition and configuration of vegetation and organic materials on the landscape, disturbances shape ecological patterns and processes (Franklin *et al.* 2000; Turner 2010). Those patterns and processes, in turn, shape subsequent disturbances. Globally, disturbance activity (including disturbance frequency, severity, and extent) is changing in response to changing climate (Turner 2010). As disturbance regimes change, concerns have been raised that the mechanisms of ecosystem resilience (i.e., the capacity of ecosystems to tolerate disturbance) may begin to break down (Millar & Stephenson 2015; Trumbore *et al.* 2015).

The field of landscape ecology seeks to understand the feedbacks between pattern, process, and disturbance activity across multiple spatial scales (McKenzie *et al.* 2011; Turner & Gardner 2015; Newman *et al.* 2019). In a landscape ecology context, a key facet of ecosystem resilience is spatial resilience, defined here as "the measure of how spatial attributes, processes, and feedbacks vary over space and time in response to disturbances and affect the resilience of ecosystems" (Allen *et al.* 2016; Chambers *et al.* 2019). Spatial resilience is an emergent property resulting from landscape composition (e.g., richness, diversity) and configuration (e.g., patch structure, proximity, connectivity) that can shape forest resilience (Chambers *et al.* 2019). Because ecological landscapes, and the disturbance regimes operating within those landscapes, are inherently complex and hierarchical systems (Newman *et al.* 2019), understanding and managing for ecological resilience in these systems requires multi-scale approaches (Chambers *et al.* 2019).

In forest ecosystems, maintaining or promoting forest resilience has become a primary goal of management (Seidl *et al.* 2016; Albrich *et al.* 2020). Forest disturbance regimes are highly sensitive to climate (Seidl *et al.* 2016), and changing disturbance regimes are expected to have substantial impacts in forest systems (Johnstone *et al.* 2016). While resilient forests are a frequently cited management priority, important facets of resilience remain ambiguously defined or difficult to quantify (Seidl *et al.* 2016; Albrich *et al.* 2020). Quantifiable indicators of forest resilience include the natural range of variation for disturbance regimes (i.e., the expected range of ecosystem conditions, including disturbed area, vegetation cover, or patch size distribution) and mechanisms of post-disturbance forest recovery (i.e., growth and recolonization) (Johnstone *et al.* 2016; Seidl *et al.* 2016; Chambers *et al.* 2019). Changes in disturbance regimes and compound effects of interacting disturbance agents can produce ecosystem conditions that depart from the natural range of variation to which forests are adapted; this departure can cause forest systems to shift to alternative (i.e., non-forested) states (Seidl & Turner 2022). To successfully monitor, forecast, and manage for forest resilience in the context of changing disturbance regimes, quantifying indicators of forest resilience across spatial and temporal scales is critical (Seidl *et al.* 2016; Albrich *et al.* 2020).

Taking a landscape ecology and spatial resilience lens, each chapter of this dissertation asks how information about the spatial configuration of a landscape or disturbance can be used to better understand an ecological process that impacts forest resilience. Harnessing geospatial datasets at scales ranging from individual trees to subcontinents, my work builds insights regarding biotic (i.e., bark beetles, plant pathogens) and abiotic (i.e., wildfire) disturbances in temperate forests of western North America. In Chapters 1 and 2, I use spatial and spatio-temporal statistical models to elucidate mechanisms driving patterns of biotic disturbance activity and compensatory forest growth responses. In Chapters 3 and 4, I develop an approach to quantify and simulate spatial metrics of wildfire burn severity that are directly linked to post-fire forest recovery.

The compensatory responses of trees following disturbance are strongly influenced by their spatial configuration and serve as key mechanisms of forest resilience (Romme *et al.* 1986). In Chapter 1, I use individual tree-level long-term monitoring data to evaluate how the fine-scale spatial configuration and composition of trees within a stand shape growth and recruitment following severe bark beetle outbreak. Following biotic disturbances caused by a single agent (e.g., a single species of bark beetle), these compensatory responses provide continuity and rapid recovery of forest function. Conversely, when disturbance agents interact and co-occur, their combined effects can erode these mechanisms and reduce the capacity of forest systems to recover (Buma, 2015; Paine et al., 1998). In Chapter 2, I use aerial detection survey data to evaluate spatio-temporal patterns of biotic disturbance interactions, describing where and when biotic disturbance 'hotspots' (areas where two or more distinct biotic disturbances overlap in space and time) tend to occur on a regional scale. Together, these chapters provide a deeper understanding of the resilience of forests to biotic disturbance activity.

In fire-prone forest ecosystems, the size and structure of high-severity burn patches are key components determining wildfire impact and setting the template for post-fire recovery (Harvey *et* *al.* 2016b; Gill *et al.* 2022). Anticipating the ecological effects of future fire therefore requires understanding the potential range of resulting burn severity patterns. In Chapter 3, I use satellite-derived burn severity data to quantify the range of wildfire patch structure occurring across a gradient of fire regimes and forest ecosystems in the Northwest US. Further, I evaluate whether the relationships between spatial patterns of burn severity and overall fire size are stationary in space and time (i.e., whether these relationships vary by geographic region or time period). In Chapter 4, I build on the approach and findings from Chapter 3 and conduct a simulation study quantifying potential future burn severity patterns in Northwestern Cascadia, a fire-prone region in the Pacific Northwest US where empirical information about fire activity is currently lacking. By quantifying the range of burn severity patterns and therefore ecological effects that may occur with future fire activity, the findings from these chapters can inform both pre- and post-fire management strategies.

The chapters of this dissertation are connected conceptually through the frameworks of landscape ecology, disturbance ecology, and spatial resilience. Understanding the nature of past disturbances, interactions between multiple disturbances, and feedbacks between disturbance and landscape configuration continue to be important frontiers in ecology. Furthermore, deepening our understanding of these processes is key to managing for forest resilience as disturbance activity continues to change.

Chapter 1. FINE-SCALE SPATIAL HETEROGENEITY SHAPES COMPENSATORY RESPONSES OF A SUBALPINE FOREST TO SEVERE BARK BEETLE OUTBREAK

1.1 Abstract

Context: Growth releases of individuals that survive disturbances are important compensatory response mechanisms that contribute to ecological resilience. However, the role of fine-scale spatial heterogeneity in shaping compensatory growth responses is poorly understood for many broad-scale disturbances.

Objectives: We quantified how fine-scale spatial structure affects individual and aggregate tree growth leading up to and following a severe mountain pine beetle (MPB; *Dendroctonus ponderosae*) outbreak. We asked: (1) How does individual tree growth vary with tree- and neighborhood-scale characteristics? (2) How do within-stand aggregate growth and overstory recruitment vary with neighborhood-scale characteristics?

Methods: We used a spatially explicit long-term monitoring dataset of a subalpine lodgepole pine (*Pinus contorta* var. *latifolia*) forest (in Colorado, USA) in which every tree ≥ 5 cm diameter was measured and mapped prior to (1989, 2004) and following (2018) a severe MPB outbreak (2003–2011). We used spatial regression to characterize drivers of growth.

Results: Overall, we found strong evidence for post-outbreak compensatory responses across spatial scales. Neighborhood characteristics shaped both individual and aggregate growth, with the magnitude of growth strongly mediated by pre-outbreak neighborhood structure and neighborhood mortality. Variation in tree-scale growth, combined with the spatial arrangement of surviving trees, resulted in highly variable emergent patterns of aggregate growth and recruitment.

Conclusions: Our findings highlight the importance of fine-scale landscape configuration in shaping forest resilience. Quantifying compensatory responses in a spatially explicit framework at different scales is critical for modeling post-disturbance forest dynamics, which is increasingly important as climate warms and forest disturbance regimes change.

1.2 INTRODUCTION

Disturbances play an integral role in shaping the structure, function, composition, and development pathways of forests worldwide (Pickett & White 1985; Franklin *et al.* 2002). In North America, biotic disturbance agents (i.e., insects and pathogens) affect more forested area than wildfire annually (Dale *et al.* 2001; van Lierop *et al.* 2015). Eruptive species of native bark beetles (Curculionidae: Scolytinae) are among the most impactful disturbance agents; subcontinental-scale outbreaks can affect millions of hectares (ha) of forests over the course of several years to a decade, often resulting in >80% mortality of host tree basal area (BA) within affected stands (Romme *et al.* 1986; Meddens *et al.* 2012; Simard *et al.* 2012; Jarvis & Kulakowski 2015).

Forests adapted to periodic disturbance exhibit some level of resilience, the capacity to tolerate disturbance without shifting to an alternative (e.g., non-forested) state (Holling 1973). The growth release of forests following bark beetle outbreak, driven by the responses of individual survivors to increased resource availability (e.g., light, water, nutrients), is an important compensatory response mechanism (Romme *et al.* 1986; Veblen *et al.* 1991) contributing to forest resilience. While seedling establishment is often the primary mechanism of resilience following stand-replacing disturbances such as wildfire, the growth release of previously established trees is a more important mechanism of resilience following stand-releasing disturbances such as bark beetle outbreaks (Hawkes *et al.* 2003; Astrup *et al.* 2008; Axelson *et al.* 2009; DeRose & Long 2010). Strong growth responses often occur for trees that were suppressed pre-outbreak, typically small-diameter trees and non-host or shade-tolerant species (Cole & Amman 1980; Hawkins *et al.* 2013). Growth releases are well documented as stand-level means, with dendroecological reconstructions of periods of growth release commonly used to detect the occurrence of past outbreaks (Alfaro *et al.* 2003; Jarvis & Kulakowski 2015). However, post-outbreak increases in resource availability and corresponding growth releases are unlikely to be uniform within a stand, highlighting the importance of within-stand spatial structure in shaping forest capacity for resilience (Cumming 2011).

Understanding mechanisms of forest resilience to disturbances is increasingly important as climate warms and disturbance activity accelerates worldwide (Turner 2010). The abundance, species composition, and spatial distribution of surviving trees are all biological legacies (Franklin *et al.* 2000) that persist through bark beetle outbreaks and shape forest recovery (Nigh *et al.* 2008; Dhar & Hawkins 2011). Within-stand landscape pattern is itself an important biological legacy influencing the growth release of survivors (Wild *et al.* 2014), yet the role of fine-scale spatial pattern in shaping both individual and stand-level compensatory responses remains largely unexplored (Wild *et al.* 2014; Bače *et al.* 2015). Building an understanding of how spatial heterogeneity affects disturbance and resilience dynamics requires repeated, spatially explicit measurements (Lutz *et al.* 2014; Bače *et al.* 2015); thus, opportunities to build this understanding at the scale of individual trees are relatively rare. However, such insight is critical for characterizing how forest structure, demography, and function respond to disturbances such as bark beetle outbreaks (Dhar & Hawkins 2011; Pfeifer *et al.* 2011; Turner *et al.* 2013).

Here, we used a spatially explicit long-term monitoring dataset of a lodgepole pine (*Pinus contorta* var. *latifolia*) forest to characterize within-stand landscape drivers of individual and aggregate tree growth, both leading up to and following a severe mountain pine beetle (MPB; *Dendroctonus ponderosae*) outbreak. We studied three 2-ha plots in Fraser Experimental Forest (Colorado, USA) in which every tree ≥ 5 centimeters (cm) in diameter was censused, measured, and mapped leading up to (1989, 2004) and following (2018) a severe MPB outbreak (2003–2011) to address the following questions: *(Q1) How do individual diameter growth rates of live trees vary with tree- and neighborhood-scale characteristics? (Q2) How do within-stand aggregate BA growth and overstory recruitment vary with neighborhood-scale characteristics?* For each question, we identified tree- and neighborhood-scale characteristics expected to affect growth responses and tested hypothesized relationships (Table 1.1).

Table 1.1. Hypothesized relationships of individual and aggregate growth responses with tree- and neighborhood-scale characteristics.

Scale	Characteristic	Hypothesized relationship	
		Direction	Justification
Question 1: Individual diameter growth			
Tree	Size	-	Growth rates decline as trees age and increase in size (Weiner & Thomas 2001), and growth release is expected to be greatest for small trees that were resource limited prior to the outbreak (Hawkins *et al.* 2013).
	Species	+/-	Late-seral, shade-tolerant species (subalpine fir and Engelmann spruce) expected to exhibit the greatest growth release relative to lodgepole pine (Hawkins *et al.* 2013); growth rates for Engelmann spruce expected to be greater than those for subalpine fir (Andrus *et al.* 2018).
Neighborhood	Density	-	Neighborhood density relates to increased resource competition (Contreras *et al.* 2011).
	Conspecifics	-	Conspecific neighboring trees expected to relate to increased resource competition (Chesson 2000; Getzin *et al.* 2006).
	Mortality	+	Neighborhood mortality relates to increased resource availability for survivors (Nigh *et al.* 2008; Hawkins *et al.* 2013).
	Topography	-	Convex microsites and steep slopes expected to relate to lower moisture availability.
Question 2: Within-stand aggregate basal area growth and overstory recruitment			
Neighborhood	Stem density	+	A greater number of trees corresponds to a greater potential for aggregate BA growth (Long & Vacchiano 2014) and overstory recruitment (Pukkala *et al.* 2009).
	Basal area	-	Aggregate BA growth expected to decrease with BA, following a size-related decline in stand growth (i.e., as individual tree growth rates decline with size) (Weiner & Thomas 2001). Recruitment also expected to decline with BA (Porté & Bartelink 2002; Pukkala *et al.* 2009).
	Late-seral proportion	+	Higher growth and establishment rates expected for late-seral, shade-tolerant species.
	Mortality	+	Neighborhood mortality expected to relate to increased growth responses of individual surviving trees.
	Topography	-	Convex microsites and steep slopes expected to relate to lower moisture availability.

1.3 METHODS

1.3.1 *Study area*

Fraser Experimental Forest (FEF) is located within the Arapaho-Roosevelt National Forest (Colorado, USA) in the Southern Rockies Ecoregion (Appendix A, Figure 1.6). The study stands are in subalpine forest composed of lodgepole pine seral to subalpine fir (*Abies lasiocarpa*) and Engelmann spruce (*Picea engelmannii*), with small quantities of quaking aspen (*Populus tremuloides*), gray alder (*Alnus incana*), Scouler's willow (*Salix scouleriana*), and Douglas-fir (*Pseudotsuga menziesii*) (Appendix A, Figure 1.7). Elevation ranges from 2790 to 2970 m. Stands are >300 years old, established following a stand-replacing fire in 1685 (Bradford *et al.* 2008). Climate is temperate and continental (Huckaby & Moir 1998) with mean monthly temperatures ranging from -8 degrees Celsius (°C) in January to 14°C in July, a mean annual temperature of 3°C, and a mean annual precipitation of 505 millimeters (30-year normals, 1991-2020) (PRISM Climate Group 2021).

Between 2003 and 2010, a widespread, synchronous MPB outbreak occurred throughout the Southern Rockies, triggered by a severe drought in 2001–2002 (Chapman *et al.* 2012) (Chapman et al. 2012). Increasing MPB activity was noted in FEF in 2003 (Tishmack *et al.* 2005), reaching epidemic levels by 2006 (Hubbard *et al.* 2013) and subsiding by 2011 (Vorster *et al.* 2017). High rates of lodgepole pine mortality were documented in FEF over the course of the outbreak, with MPB killing 90% of lodgepole pine trees over 30 cm in diameter at breast height (DBH) (Rhoades *et al.* 2017; Buonanduci *et al.* 2020).

1.3.2 *Sampling design*

Three 2-ha long-term monitoring plots were established in 1938 (Wilm & Dunford 1948) and surveyed periodically leading up to (1938, 1940, 1946, 1960, 1989, 2004) and following (2018) the MPB outbreak (Buonanduci *et al.* 2020). Prior to 2004, each survey consisted of a complete census of every living tree measuring at least 9 cm in DBH (measured 140 cm above the ground). In 2004 and 2018, the minimum DBH threshold was lowered to 5 cm. During each survey, DBH was recorded for each living tree and mortality cause was determined for all dead trees that were alive in the previous survey. In July and August 2018, we mapped all live and dead surveyed trees (n = 9357) within each plot to their horizontal coordinates and local elevation using Field-Map technology (Hédl *et al.* 2009).

1.3.3 *Growth metrics*

The MPB outbreak in FEF occurred between approximately 2003 and 2011. While some mortality from MPB occurred prior to 2004 and was noted in the 2004 survey, 90% of MPB-caused tree mortality in the plots occurred after the 2004 survey (Buonanduci *et al.* 2020). Therefore, we used the 1989–2004 inter-survey period to quantify pre-outbreak growth and the 2004–2018 inter-survey period to quantify post-outbreak growth.

At the individual tree scale, we quantified the growth rate of trees between successive surveys as annualized diameter increment, calculated from successive DBH measurements (Table 1.2, Figure 1.1a). We quantified growth release of individual trees as the difference in annualized diameter growth rate between the two growth periods (i.e., post-outbreak minus pre-outbreak growth rate) (Table 1.2, Figure 1.1a). Rather than evaluating standardized diameter growth (i.e., growth relative to tree size), we accounted for potential growth-size relationships by including tree size as a covariate in our statistical modeling. Our individual tree scale analysis focused on lodgepole pine, Engelmann spruce, and subalpine fir, which accounted for >99% of pre-outbreak live BA in the study plots. Growth rate estimates are below zero in some cases (6% and 2% of trees in pre- and post-outbreak periods, respectively; Table 1.2, Figure 1.1a), which we attribute to measurement error from slight differences in positioning of diameter tapes among surveys.

Table 1.2. Descriptive statistics for individual and aggregate growth responses used in modeling.

Metric[a]	Growth period	n	Min	Max	Mean	Median
Individual diameter growth						
Lodgepole pine growth (cm/yr)	Pre-outbreak	2995	-0.11	0.68	0.06	0.05
	Post-outbreak	1401	-0.18	0.68	0.16	0.14
	Release	832	-0.59	0.48	0.09	0.08
Engelmann spruce growth (cm/yr)	Pre-outbreak	96	0.01	0.47	0.21	0.21
	Post-outbreak	177	-0.09	0.94	0.33	0.29
	Release	84	-0.48	0.50	0.10	0.07
Subalpine fir growth (cm/yr)	Pre-outbreak	160	0.01	0.65	0.21	0.20
	Post-outbreak	466	-0.17	0.96	0.28	0.26
	Release	146	-0.30	0.46	0.10	0.09
Within-stand aggregate growth						
Basal area growth of live trees ($m^2ha^{-1}yr^{-1}$)	Pre-outbreak[b]	505	-0.01	0.65	0.18	0.17
	Post-outbreak[b]	459	-0.01	0.75	0.22	0.20
	Release[b]	459	-0.36	0.58	0.03	0.02
Overstory recruitment (stems/ha)[c]	Pre-outbreak	506	0	500	55	0
	Post-outbreak[d]	505	0	1100	144	100
	Release[d]	505	-300	1100	90	100

[a] Response variables are included here; see Appendix B, Table 1.3 – Table 1.5 for predictor variables.

[b] Datasets exclude raster cells with surviving basal area equal to zero, for which late-seral proportion could not be calculated.

[c] Values presented here are scaled up to a per-ha basis. Unscaled 10 m raster cell counts were used for modeling.

[d] Datasets exclude raster cells with initial basal area equal to zero, for which late-seral and mortality proportions could not be calculated.

(a) *Individual diameter growth*

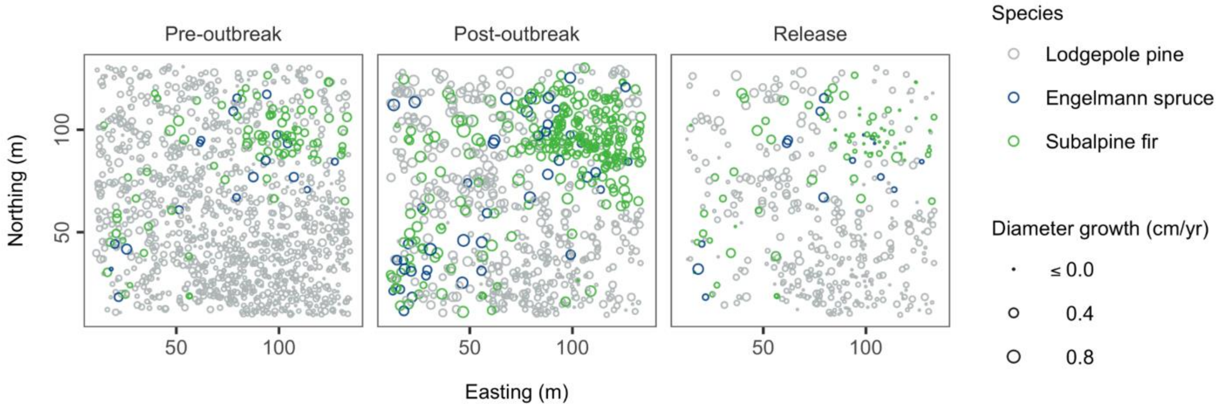

(b) *Aggregate basal area growth*

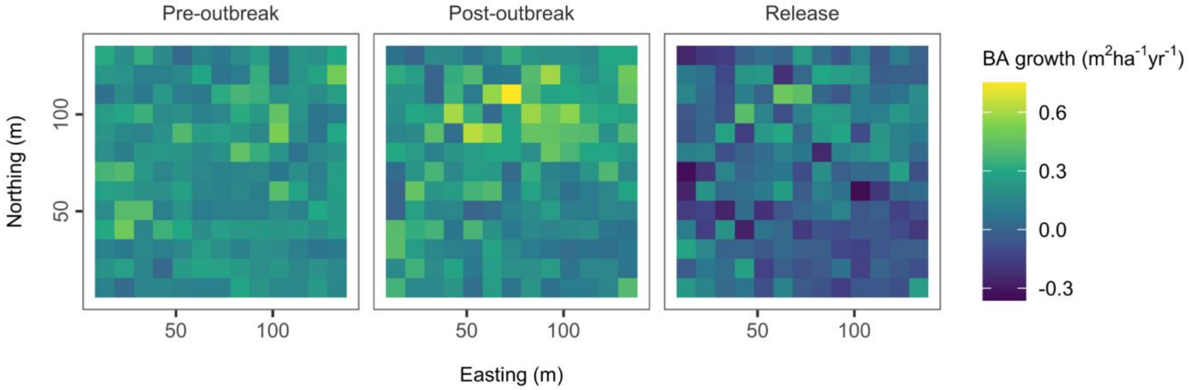

(c) *Aggregate overstory recruitment*

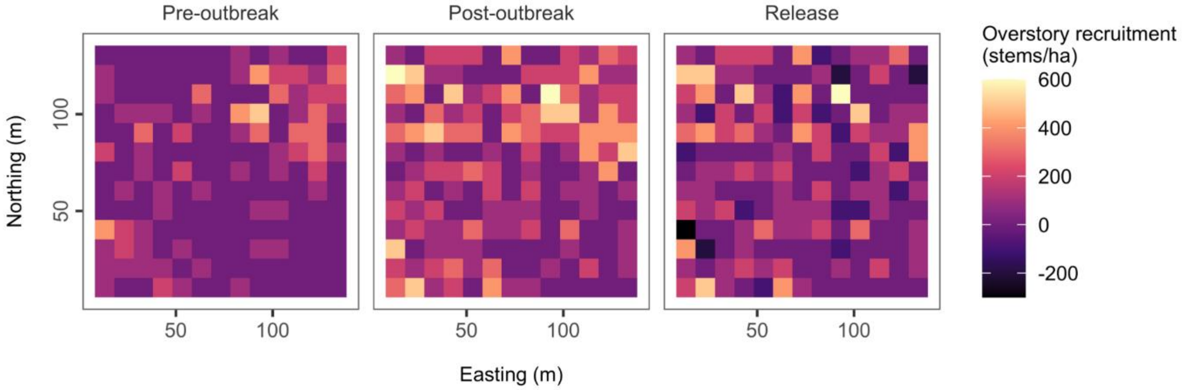

Figure 1.1. Individual and aggregate tree growth responses in one plot. (a) Individual diameter growth of live trees. (b) Aggregate basal area (BA) growth of live trees. (c) Aggregate overstory recruitment (ingrowth into $\geq$ 9 cm DBH size class). Cell size is 10 m and coordinates are relative to southwest corner of plot. To avoid boundary effects, trees located <10 m from the edge of each plot were excluded from individual tree growth analyses, and raster cell centroids were positioned $\geq$10 m from the edge of each plot for aggregate tree growth analyses. Plot C3 is shown here; growth responses within all three plots included in Appendix A.

At the within-stand scale, we quantified aggregate BA growth of live trees, a proxy for biomass accumulation, by rasterizing the point pattern of individual trees within each plot at a spatial resolution of 10 m. Within each 10 m raster cell and using only those trees that were alive and surveyed at both the beginning and end of each inter-survey period, we quantified BA growth as the total annualized change in live BA between successive surveys, calculated using successive DBH measurements (Table 1.2, Figure 1.1b). This metric does not account for net decreases in total live BA due to mortality, which we incorporated as a covariate in this analysis. BA growth estimates are below zero in some cases due to measurement error in the field (1% and 0.2% of raster cells in pre- and post-outbreak periods, respectively; Table 1.2, Figure 1.1b). We quantified aggregate BA growth release for each raster cell as the difference in BA growth between the two growth periods (i.e., post-outbreak minus pre-outbreak growth rate). Because the minimum survey diameter was lowered from 9 cm DBH in 1989 to 5 cm DBH in 2004, we only included trees ≥ 9 cm DBH when quantifying aggregate BA growth to allow for comparability of metrics between periods. For illustrative purposes, we also quantified net change in total live BA (i.e., BA growth minus BA mortality) (Figure 1.2) but did not evaluate net change as a response variable in our modeling.

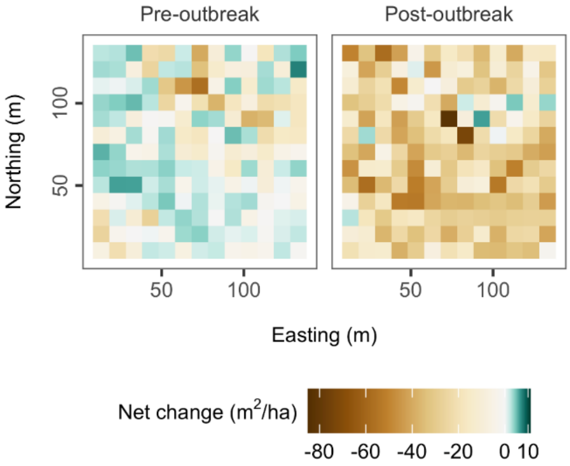

Figure 1.2. Net change in total live basal area within one plot. Cell size is 10 m and coordinates are relative to southwest corner of plot. Plot C3 is shown here; net changes in live basal area within all three plots included in Appendix A.

Finally, also at the within-stand scale, we quantified aggregate overstory recruitment, a measure of advance regeneration. We quantified overstory recruitment by counting the number of trees within each 10 m raster cell that grew to exceed the minimum survey diameter during the inter-survey period and were thus surveyed for the first time at the end of the inter-survey period (i.e., ingrowth density; Table 1.2, Figure 1.1c). We quantified overstory recruitment release for each raster cell as the difference in ingrowth density between the two growth periods (i.e., post-outbreak minus pre-outbreak). As with aggregate BA growth, we only included trees > 9 cm DBH when quantifying overstory recruitment.

1.3.4 *Potential predictors of individual tree growth*

Tree size was quantified using DBH recorded at the start of each growth period (i.e., DBH recorded in 1989 was used as a predictor for pre-outbreak growth and DBH recorded in 2004 was used as a predictor for post-outbreak growth and growth release). Neighborhood density was quantified using a distance-dependent tree competition index, calculated as the sum of horizontal angles originating from each focal tree and spanning the DBH of each neighbor tree (Rouvinen & Kuuluvainen 1997; Contreras *et al.* 2011). We calculated neighborhood density within a 10 m radius as follows:

$$\text{Neighborhood density} = \sum_{i=1}^{n} \arctan\left(\frac{\text{DBH}_i}{\text{distance}_i}\right) \tag{1.1}$$

where neighboring trees are indexed i = 1, …, n; DBH_i is the DBH of neighboring tree i; and distance_i is the distance between the center of the focal tree and the center of neighboring tree i. This index accounts for the number of neighboring trees, their proximity to the focal tree, and their size. We calculated neighborhood density using all neighboring trees, regardless of species. To quantify the relative density of conspecific trees, we calculated the proportion of the neighborhood density index contributed by the same species as the focal tree. To quantify neighborhood mortality, we calculated the proportion of the neighborhood density index that was killed (due to MPB or any other cause) during the growth period.

Fine-scale topography (i.e., elevation and slope) was quantified using a 1 m resolution digital elevation model developed from the local elevation of each individual tree measured in the field. We quantified local topographic position (i.e., topographic convexity versus concavity) using a topographic position index (Weiss 2001) calculated within a 10 m radius as follows:

$$\text{Topographic position} = z_0 - \bar{z} \tag{1.2}$$

where z_0 is the elevation of the cell containing the focal tree, and $\bar{z}$ is the average elevation around the focal cell within a predetermined radius. This index is positive when the focal tree is in a position higher than its neighbors on average (convex local topography) and negative when the focal tree is in a position lower than its neighbors on average (concave local topography).

Calculating neighborhood density and topographic position required specifying the neighborhood radius a priori. We chose a neighborhood radius of 10 m, comparable to radii used in tree competition studies conducted in lodgepole pine stands in British Columbia, Canada (Thorpe *et al.* 2010) and ponderosa pine (*Pinus ponderosa*) stands in Montana, USA (Woodall *et al.* 2003; Contreras *et al.* 2011). To avoid boundary effects, trees located <10 m from the edge of each plot were excluded from analysis.

1.3.5 *Potential predictors of within-stand aggregate growth and recruitment*

Stem density and BA were quantified within each 10 m raster cell using live trees surveyed at the beginning of each growth period (i.e., live trees surveyed in 1989 were used for pre-outbreak growth metrics and live trees surveyed in 2004 were used for post-outbreak growth metrics and their release). Because only live trees that survived to the end of each growth period were used to calculate aggregate BA growth, only those same surviving trees were used to calculate stem density and BA for use as predictors of aggregate BA growth. Conversely, all live trees surveyed at the beginning of each growth period (regardless of survival) were used to calculate stem density and BA for use as predictors of overstory recruitment; this is because all initial live trees would potentially play a role, both leading up to and during the growth period, in the establishment of understory trees and their growth into the overstory (e.g., through seed production and competition).

We calculated late-seral proportion within each 10 m raster cell as the proportion of BA (i.e., surviving BA for growth and initial live BA for recruitment) composed of Engelmann spruce, subalpine fir, or any other late-seral species (i.e., those species present in the plots in smaller quantities). We calculated the mortality proportion within each 10 m raster cell as the proportion of initial live BA that was killed (due to MPB or any other causes) during the growth period. Topographic position and slope were calculated using the centroid of each raster cell as the focal location, using methods described above. To avoid boundary effects, raster cell centroids were positioned ≥10 m from the edge of each plot (i.e., a 5 m interior plot buffer was excluded from analysis).

1.3.6 *Statistical analyses*

We used Bayesian spatial regression models to make inference regarding the potential influence of covariates on each individual tree and aggregate growth metric. Growth responses for tree or raster cell i (i = 1, …, n) were modeled as random variables Y_i with mean μ_i measured at locations s_i. Models take the following form:

$$g(\mu_i) = \beta_0 + \sum_{k=1}^{K} \beta_k x_{ik} + a_i + \gamma_i \tag{1.3}$$

Here, g() is a link function, x_{ik} (k = 1, …, K) are covariates, a_i is a random effect of plot, and γ_i is a spatial random effect modeled as a continuous Gaussian random field (GRF) measured at location s_i,

$$\gamma_i(s_i) \sim \mathrm{GRF}(0, \Sigma) \tag{1.4}$$

We modeled the covariance matrix Σ using a Matérn covariance function parameterized by marginal standard deviation σ_γ and practical range r (distance at which correlation drops to approximately 0.1) (Lindgren *et al.* 2011).

Across growth periods, we found evidence for non-linear changes in aggregate BA growth with surviving stem density, which we modeled using a quadratic term for surviving stem density as a covariate. In the post-outbreak period (2004–2018), we found evidence for non-linear changes in individual tree growth rates with DBH for all three species, which we modeled using a smooth term on the DBH covariate. Thus, individual tree models in the post-outbreak period include a term u_l, which takes the form of a random walk of order one modeled at indices l of the binned DBH covariate:

$$u_l \sim \mathrm{Normal}(u_{l-1}, \sigma_u^2) \tag{1.5}$$

Continuous growth responses (individual tree growth and aggregate BA growth), and the difference in aggregate overstory recruitment between time periods (which takes both positive and negative values), were modeled as Normal random variables with an identity link. Discrete pre- and post-outbreak overstory recruitment count responses were modeled as Poisson random variables with a log link.

Following methods described in Buonanduci *et al.* (2020), we used the Integrated Nested Laplace Approximation (INLA) and Stochastic Partial Differential Equation (SPDE) approaches to implement spatial models in a Bayesian framework (Lindgren *et al.* 2011; Blangiardo & Cameletti 2015) (Appendix B, Figure 1.12). To avoid spatial overfitting, we used penalized complexity priors for the marginal standard deviation and practical range of the GRF (Fuglstad *et al.* 2019). We used uninformative priors for all other parameters (Krainski *et al.* 2019). Both the INLA and SPDE approaches were implemented in R (R Core Team 2022) using the *R-INLA* package (www.r-inla.org).

We evaluated model fit via the conditional predictive ordinate (CPO; Pettit 1990), which is a leave one out cross-validation score. The sum of log CPO values is a useful summary of model fit, with larger sums indicating a better-fitting model (Blangiardo & Cameletti 2015). To enable comparison of the magnitude of coefficients within each model, we standardized all covariates within each dataset by subtracting their means and dividing by two times their standard deviations. A covariate or interaction term was considered an important predictor if the 95% credible interval for the coefficient did not include zero. We validated each model using standard regression diagnostics and tested for residual spatial autocorrelation using Moran's I (Cliff & Ord 1981). We conducted sensitivity analyses to confirm that varying the spatial resolution of individual tree growth covariates (i.e., using 5, 10, or 15 m radii to quantify neighborhood characteristics) or aggregate growth response variables (i.e., using 5, 10, or 15 m raster cells to quantify aggregate metrics) would not qualitatively change the results and conclusions (Appendix B, Figure 1.13 – Figure 1.15).

When modeling individual tree growth responses, we first fit a single model for each growth period with species included as the only fixed effect to test for overall differences in species-specific magnitudes of growth. We then fit species-specific models for each growth response, including all potential covariates. Because we expected some covariate effects might vary with tree size, we considered interaction terms between DBH and all other covariates. To limit the overall number of statistical tests, we added interaction terms to each model only if they were important predictors (i.e., 95% credible interval for the interaction term did not include zero) and they increased model fit (i.e., increased the sum of log CPO values).

1.4 RESULTS

1.4.1 *Heterogeneity in tree- and neighborhood-scale characteristics*

Within stands and across growth periods, tree- and neighborhood-scale characteristics varied widely (Appendix B, Table 1.3 – Table 1.5). Neighborhood density and composition, for example, were highly variable within stands both pre- and post-outbreak, with live BA ranging from 0.6 – 115.9 m^2/ha and late-seral proportion ranging from 0.0 – 1.0 (Appendix B, Table 1.4 and Table 1.5). Neighborhood mortality proportion was relatively low on average in the pre-outbreak period (mean ranging from 0.1 to 0.2 across datasets) compared to the post-outbreak period (mean ranging from 0.5 to 0.8 across datasets); however, a wide range in neighborhood mortality proportion was observed within plots across both periods (minimum ranging from 0.0 – 0.07 and maximum ranging from 0.6 – 1.0 across datasets; Appendix B, Table 1.3 – Table 1.5).

1.4.2 *Individual tree diameter growth*

Within each growth period (i.e., pre-outbreak, post-outbreak, and release), diameter growth responses of late-seral, shade-tolerant species (i.e., Engelmann spruce and subalpine fir) were greater than those of lodgepole pine (Table 1.2, Figure 1.1a), with estimated mean growth responses being greatest for Engelmann spruce, followed by subalpine fir and then lodgepole pine (based on regression models with species as the only fixed effect; Appendix B, Table 1.6). Estimated mean growth releases for each species were greater than zero (based on intercept-only regression models; Appendix B, Table 1.7). The direction and magnitude of effects of covariates varied by growth period and species (Figure 1.3, Appendix B, Table 1.8).

1.4.2.1 Pre-outbreak growth (1989–2004)

In the pre-outbreak period, neighborhood density had a strong effect on growth rates across species, with lodgepole pine, Engelmann spruce, and subalpine fir growth rates all decreasing with neighborhood density (Figure 1.3). For lodgepole pine, the negative effect of neighborhood density lessened with increasing DBH (Figure 1.3), suggesting that growth rates of small lodgepole pine decreased more sharply with neighborhood density than growth rates of large lodgepole pine. Interaction terms of DBH and neighborhood mortality suggest growth rates varied marginally with neighborhood mortality, though the direction of effects differed both with tree size and by species (Figure 1.3). Additional marginal effects of neighborhood conspecifics and slope steepness were observed for Engelmann spruce, and additional marginal effects of DBH and slope steepness were observed for subalpine fir (Figure 1.3).

1.4.2.1 Post-outbreak growth (2004–2018)

In the post-outbreak period, neighborhood density, neighborhood mortality, and DBH had strong effects on growth rates across species, with lodgepole pine, Engelmann spruce, and subalpine fir growth rates all decreasing with neighborhood density and increasing with neighborhood mortality (Figure 1.3). Growth rates of all species increased with DBH up to ~10–20 cm DBH, beyond which growth rates decreased with further increases in DBH (Appendix B, Figure 1.16). Furthermore, effects of neighborhood-scale characteristics varied with tree size and among species. For lodgepole pine, growth rates of small trees decreased more sharply with neighborhood density than growth rates of large trees; conversely, for subalpine fir, growth rates of large trees decreased more sharply with neighborhood density than growth rates of small trees (Figure 1.3). For both lodgepole pine and Engelmann spruce, the positive effect of neighborhood mortality lessened with greater DBH (Figure 1.3). Additional marginal effects of neighborhood conspecifics were observed for all species, and additional marginal effects of slope steepness were observed for Engelmann spruce and subalpine fir, though the direction of effects varied (Figure 1.3).

1.4.2.1 Growth release

For all three tree species, growth releases were strongly related to DBH and neighborhood mortality, with growth releases being greatest for small trees and decreasing with greater DBH (Figure 1.3, Figure 1.4). Growth releases of all species increased with neighborhood mortality, and for lodgepole pine and Engelmann spruce, growth releases of small trees increased more sharply with neighborhood mortality than growth releases of large trees (Figure 1.3, Figure 1.4). Growth releases of lodgepole pine and subalpine fir decreased with neighborhood density, though the effect of neighborhood density lessened with greater DBH for lodgepole pine (Figure 1.3, Figure 1.4). An additional marginal effect of slope steepness was observed for Engelmann spruce. While we could not evaluate the effect of neighborhood conspecifics for subalpine fir growth releases due to issues of collinearity, we did not detect an effect of neighborhood conspecifics on growth releases of the other species.

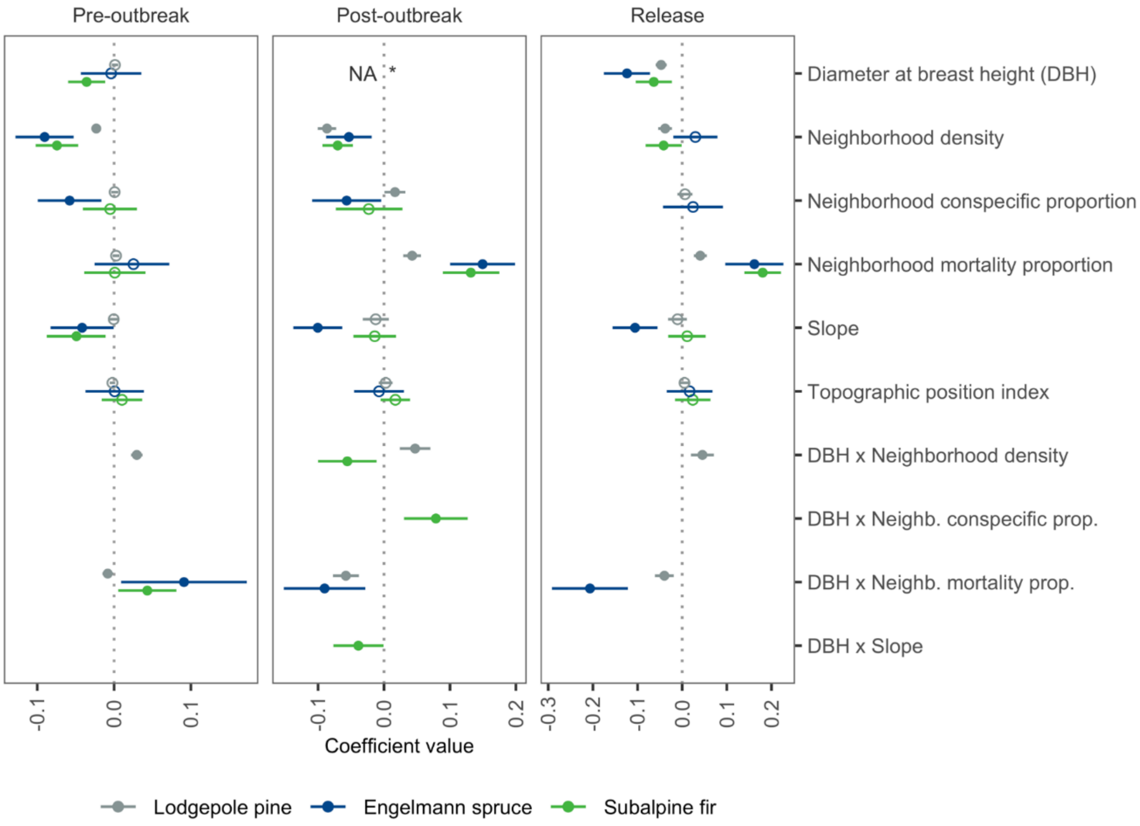

Figure 1.3. Effect of covariates on individual tree diameter growth responses. Here and in Figure 1.5, dots represent the medians of the posteriors and horizontal lines represent 95% credible intervals. Closed circles represent statistically important predictors, and open circles represent predictors that are not statistically important. The effects for each predictor are per 2 SD within each growth period- and species-specific dataset. Blank spaces indicate covariates not evaluated in a particular model. *See Appendix B, Figure 1.16 for non-linear effect of DBH in the post-outbreak period.

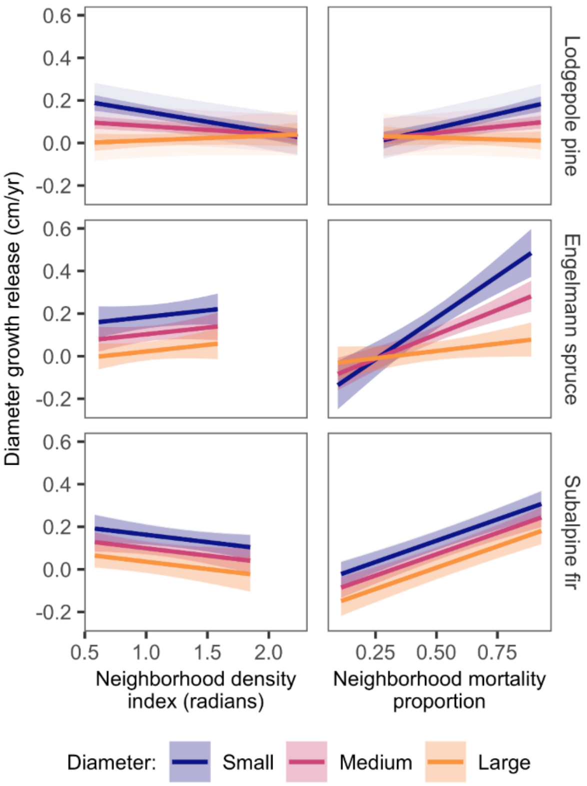

Figure 1.4. Change in relationship between covariates (x-axis) and predicted individual diameter growth release (y-axis) across gradients of tree diameter. Small, medium, and large diameters specified as 10, 20, and 30 cm respectively for lodgepole pine and 10, 25, and 40 cm respectively for Engelmann spruce and subalpine fir. Solid lines represent posterior medians, dark shading represents 95% credible intervals for predictions at one location, and light shading represents variability in 95% credible intervals for predictions across locations (i.e., variability modeled by the spatial GRF; not visible for Engelmann spruce or subalpine fir due to low level of variation attributed to spatial GRF in these models). Predictions consider each combination of covariates in isolation, holding all other covariates at zero (i.e., their average values).

1.4.3 *Within-stand net change in live basal area*

Net changes in total live BA (i.e., BA growth minus mortality) were largely negative in the post-outbreak period (Figure 1.2). Within plots, net changes in live BA over the pre-outbreak period ranged from -57.3 to 9.8 m^2/ha (mean = -3.8 m^2/ha, median = 0.2 m^2/ha). Over the post-outbreak period, net changes in live BA ranged from -86.0 to 7.1 m^2/ha (mean = -26.5 m^2/ha, median = -27.0 m^2/ha; Figure 1.2).

1.4.4 *Within-stand aggregate basal area growth*

Aggregate BA growth varied widely across the within-stand landscape and between growth periods (Table 1.2, Figure 1.1b). BA growth releases also varied widely across the within-stand landscape (Table 1.2, Figure 1.1b), though the mean was not statistically different from zero (based on an intercept-only regression model; Appendix B, Table 1.9).

The direction and magnitude of factors associated with within-stand aggregate BA growth varied by growth period (Figure 1.5a, Appendix B, Table 1.10). Pre-outbreak, BA growth rates were unrelated to mortality proportion (Figure 1.5a). Pre-outbreak BA growth rates increased with surviving BA (i.e., BA of live trees that survived the growth period), increased then plateaued with surviving stem density (positive main effect and negative quadratic term), and increased with the proportion of surviving BA composed of late-seral species (Figure 1.5a). Post-outbreak, BA growth rates decreased with mortality proportion and were unrelated to surviving BA (Figure 1.5a). Post-outbreak BA growth rates increased then plateaued with surviving stem density (positive main effect and negative quadratic term) and increased with the proportion of surviving BA composed of late-seral species (Figure 1.5a). BA growth releases decreased with mortality proportion and surviving BA, increased then plateaued with surviving stem density, and increased with the proportion of surviving BA composed of late-seral species (Figure 1.5a).

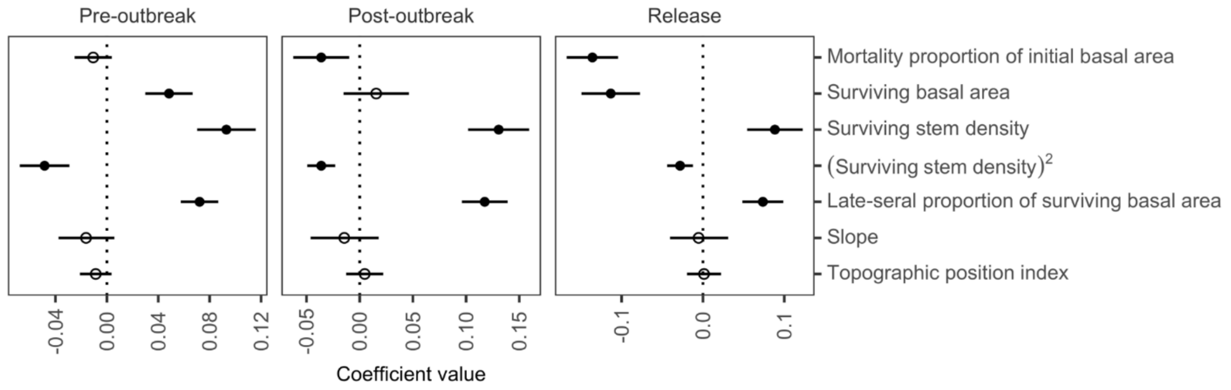

(a) *Basal area growth*

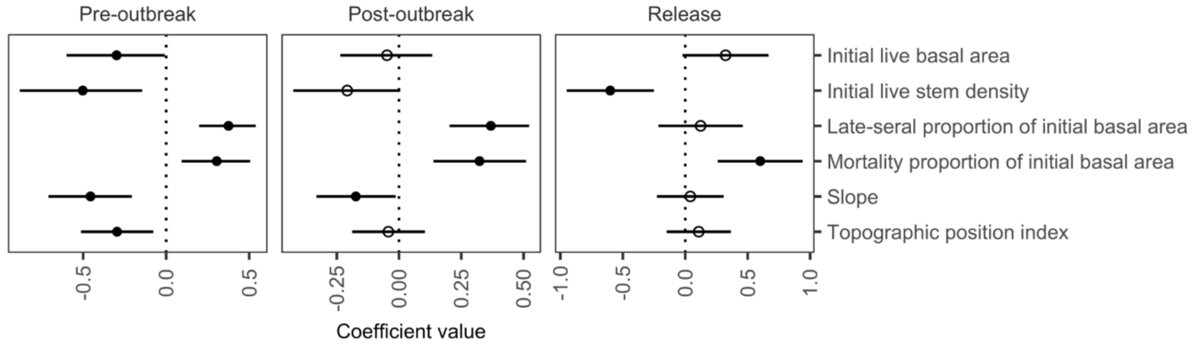

(b) *Overstory recruitment*

Figure 1.5. Effect of covariates on aggregate growth responses. (a) Aggregate basal area growth of live trees. (b) Aggregate overstory recruitment. Symbols are described in Figure 1.3.

1.4.5 *Within-stand aggregate overstory recruitment*

Overstory recruitment density varied widely across the within-stand landscape and between growth periods (Table 1.2, Figure 1.1c). On average, recruitment release was statistically greater than zero (based on an intercept-only regression model; Appendix B, Table 1.11). Pre- and post-outbreak, overstory recruitment was predominantly lodgepole pine (49% and 56% of stems), followed by subalpine fir (34% and 33% of stems) and Engelmann spruce (13% and 9% of stems), with species-specific spatial patterns generally following patterns of the pre-outbreak canopy (Appendix A, Figure 1.11).

The factors associated with within-stand aggregate overstory recruitment remained relatively consistent across time periods, though the relative magnitude of effects changed (Figure 1.5b, Appendix B, Table 1.12). Pre-outbreak, overstory recruitment decreased with initial live BA (i.e., BA of trees alive at the beginning of the growth period), initial live stem density, slope, and topographic position (i.e., convexity) (Figure 1.5b). Pre-outbreak overstory recruitment increased with both the proportion of BA composed of late-seral species as well as with mortality proportion (Figure 1.5b). Post-outbreak, overstory recruitment also decreased with slope and increased with both the proportion of BA composed of late-seral species and with mortality proportion (Figure 1.5b). Overstory recruitment releases decreased with initial live stem density and increased with mortality proportion (Figure 1.5b).

1.5 DISCUSSION

Using a unique spatially explicit long-term monitoring dataset, our study highlights mechanisms of forest recovery following bark beetle outbreak and demonstrates the importance of spatial heterogeneity in directing ecosystem response to disturbance. Overall, we found strong evidence for compensatory responses of forests at multiple scales following the outbreak, with increases in individual tree diameter growth and overstory recruitment density, as well as stability in aggregate BA growth of live trees despite outbreak-induced decreases in live BA. Neighborhood characteristics shaped both individual and aggregate growth responses following severe MPB outbreak, with the magnitude of responses strongly mediated by pre-outbreak neighborhood structure and neighborhood mortality. Individual tree growth responses varied widely with tree- and neighborhood-scale characteristics; this tree-scale variation, combined with the spatial arrangement of survivors, resulted in highly variable emergent patterns of within-stand aggregate BA growth and overstory recruitment. Our findings have important implications for understanding the role of spatial heterogeneity in shaping post-disturbance forest dynamics and associated ecosystem services (Turner *et al.* 2013).

1.5.1 *Strong post-outbreak compensatory responses occurred across spatial scales*

Following the severe mortality caused by the MPB outbreak, we found strong compensatory responses in both individual and aggregate within-stand growth, demonstrating an important mechanism of forest resilience at multiple spatial scales. As expected, diameter growth rates of individual surviving trees increased on average for all species, and overstory recruitment density increased as growth releases of small-diameter trees enabled a greater number of understory trees to grow into the overstory. Rates of recovery can be variable following bark beetle outbreak; some stands recover relatively quickly (e.g., within several decades), while others are much slower to return to pre-outbreak BA and density (Griesbauer & Green 2006). Further research would be needed to determine the rate of recovery in our study stands, particularly in the context of a warming and drying climate. However, our finding of accelerated recruitment of overstory trees suggests that responses of growth to resource release will eventually compensate for the reduction in overstory BA and stem density resulting from the outbreak.

Compensatory responses of surviving trees were sufficient to maintain continuity in rates of biomass accumulation across stands, which has important implications for carbon sequestration both leading up to and following bark beetle outbreaks. Aggregate BA growth varied widely with both stand structure and growth responses of individual trees, implying similarly wide spatial variation in carbon fluxes at the within-stand scale (Pfeifer *et al.* 2011). Despite net changes in live BA being largely negative in the post-outbreak period (i.e., fewer live trees contributing to aggregate BA growth), aggregate BA growth did not change on average from pre- to post-outbreak, suggesting that though spatially variable within stands, there was overall stability in rates of biomass accumulation when scaled up to the stand. Our results are consistent with findings elsewhere in the Southern Rockies, where stability in biomass accumulation has been found despite increases in mortality at aggregate stand scales (Chai *et al.* 2019), and compensatory responses following beetle outbreaks is strong among stands across the region (Rodman *et al.* 2022). Our results are also consistent with findings that net uptake of atmospheric carbon within stands can recover within just a few years of MPB outbreak (Brown *et al.* 2012). This stability in within-stand productivity and carbon uptake despite substantial losses of live biomass is an important dimension of forest resilience (Turner *et al.* 2013; Davis *et al.* 2022), one that is facilitated by rapid redistribution of productivity within a stand following stand-releasing disturbance (Romme *et al.* 1986).

1.5.2 *Pre-outbreak neighborhood structure and neighborhood mortality drive compensatory growth responses*

Consistent and strong effects of neighborhood structure on tree growth in our study highlight the importance of resource competition, an inherently spatial process, in driving compensatory responses to disturbance across scales. Prior to and following the outbreak, individual tree diameter growth rates and aggregate overstory recruitment density decreased with neighborhood density (i.e., neighborhood competition). Conversely, aggregate BA growth increased with surviving neighborhood density (since a higher number of surviving trees translates to a higher potential for aggregate growth). However, this positive relationship plateaued in high-density neighborhoods as competition imposed limits on further increases in aggregate growth. The differing forms of these relationships reflect the similar role yet differing signature of neighborhood density in shaping individual- versus aggregate-level growth rates (Long & Vacchiano 2014). Our results illustrate the inherent tradeoff between individual and aggregate growth within a stand (Long *et al.* 2004) and demonstrate the importance of competition for resources (i.e., light, water, nutrients) as a mechanism limiting tree growth (Craine & Dybzinski 2013) across spatial scales.

Following the outbreak, neighborhood mortality strongly drove compensatory growth responses, particularly for small-diameter trees. Small-diameter trees responded more strongly to resources released by overstory mortality compared to large-diameter trees, supporting similar tree-scale findings elsewhere (Cole & Amman 1980; Veblen *et al.* 1991; Hawkins *et al.* 2013). While small-diameter trees generally have a greater capacity for diameter growth compared to large-diameter trees, their growth is also more likely to be suppressed via competition for light and belowground resources when growing in the mid- to lower-canopy of uneven-aged stands (Oliver & Larson 1996; Caspersen *et al.* 2011). When mortality occurs nearby, particularly severe overstory mortality that increases light availability, small-diameter trees therefore demonstrate the greatest growth release (Romme *et al.* 1986). At the within-stand scale, our finding that overstory recruitment density increased with neighborhood mortality follows from the strong growth responses of small-diameter trees, which effectively accelerated the growth of understory trees into the overstory. Our findings highlight how the interaction of tree- and neighborhood-scale characteristics can result in strong compensatory growth responses following stand-releasing disturbances.

While neighborhood mortality strongly shaped growth responses following the outbreak, growth responses prior to the outbreak were less consistently affected by nearby mortality. Pre-outbreak growth rates of some trees increased with neighborhood mortality while others decreased; aggregate BA growth was unrelated to mortality, whereas aggregate overstory recruitment density increased with mortality. Following low-level disturbance or mortality resulting from gradual decline, growth releases of nearby trees may be mixed or modest (Thompson *et al.* 2007). Mortality levels were relatively low during the pre-outbreak period, which likely explains why growth responses to neighborhood mortality were mixed. In the absence of severe and punctuated disturbance (i.e., in the context of background mortality), our results suggest compensatory responses to neighborhood mortality may be inconsistent or difficult to detect.

Across a range of mortality levels, our findings suggest a persistent legacy of pre-outbreak neighborhood structure on post-outbreak growth responses. After accounting for neighborhood mortality, growth releases of individual lodgepole pine and subalpine fir, as well as releases of aggregate overstory recruitment, decreased with initial neighborhood density (i.e., density of neighboring live trees at the start of the outbreak). Our results suggest a tradeoff in the role of pre-disturbance suppression on post-disturbance compensatory response. While small-diameter trees, those most likely to be suppressed, demonstrated the strongest responses to neighborhood mortality, trees experiencing high levels of pre-outbreak suppression may have had a reduced capacity for recovery once resource availability increased. This is potentially due to physiological effects of suppression (Wright *et al.* 2000) or persistent impacts of standing dead trees, which can impede growth by continuing to shade surviving trees or inflicting injury via falling branches (Dhar & Hawkins 2011). Interestingly, we found no evidence that growth releases of Engelmann spruce decreased with initial neighborhood density, suggesting this species may be more capable of persisting through and recovering from suppression once resources are released (Andrus *et al.* 2018). Our results for lodgepole pine (a shade-intolerant species) and Engelmann spruce (a shade-tolerant species) support the idea that growth releases of shade-intolerant species are more negatively impacted by the level of suppression prior to resource release than shade-tolerant species (Wright *et al.* 2000). These size- and species-specific differences in how individual trees responded to neighborhood structure and mortality have important implications for dendroecological reconstructions of historical bark beetle outbreaks (e.g., Negrón & Huckaby 2020), as both the size of the tree at the time of an outbreak as well as its location relative to other trees in a stand will impact the ability to detect a historical outbreak (Thompson *et al.* 2007).

While our study focused on growth responses, our findings also demonstrate the role of pre-outbreak stand structure and outbreak severity in dictating post-outbreak successional dynamics (Diskin *et al.* 2011; Morris *et al.* 2022). When combined, selective mortality of the overstory and growth release of the understory often accelerate the succession of stands towards late-seral, shade-tolerant species (Cole & Amman 1980; Heath & Alfaro 1990). Our finding that late-seral species (i.e., Engelmann spruce and subalpine fir) had the highest growth responses, and that aggregate BA growth and overstory recruitment were highest in areas dominated by late-seral species, suggests our study plots will trend toward dominance by late-seral species following the outbreak, as found elsewhere within our study region (Collins *et al.* 2011, 2012). Lodgepole pine will remain an important component of our study stands, however, as it continued to dominate post-outbreak overstory recruitment (i.e., total number of stems). These findings highlight how pre-outbreak spatial pattern acts as a persistent biological legacy shaping post-outbreak stand development dynamics (Bače *et al.* 2015), which in turn will shape how these stands respond to future disturbance (Turner *et al.* 2013).

1.5.3 *Spatial patterns of aggregate growth emerge from the growth and spatial arrangement of individual trees*

Across the within-stand landscape, aggregate growth responses were driven and constrained by spatial legacies of the outbreak: the growth responses and spatial arrangement of individual survivors. Fine-scale heterogeneity in neighborhood density and mortality led to a wide range of individual tree growth responses. Emergent patterns of aggregate BA growth and overstory recruitment, which also varied widely within stands, follow from this variation in growth responses of individual trees. For example, our finding that aggregate BA growth and overstory recruitment were highest in neighborhoods dominated by late-seral species follows from the greater growth responses of late-seral species relative to lodgepole pine. Similarly, our finding that aggregate overstory recruitment density increased with neighborhood mortality follows from the strong compensatory responses of small-diameter trees. However, while resources released by mortality may increase growth at the tree level for individual survivors, aggregate within-stand growth is strongly determined by the number and size of trees that survive. Post-outbreak aggregate BA growth rates and releases decreased with neighborhood mortality, likely because overstory mortality reduces surviving BA and stem density, thereby reducing the aggregate potential for BA growth (Long & Vacchiano 2014). These results illustrate the limits on aggregate population-level compensatory responses imposed by the number, size, and spatial arrangement of survivors. These results also illustrate the role of within-stand spatial heterogeneity in shaping compensatory growth responses across scales.

Drivers and spatial patterns of aggregate growth shifted from pre- to post-outbreak as overstory mortality altered the growth responses of individual survivors. Prior to the outbreak, for example, aggregate BA growth rates were highest in neighborhoods with larger trees (i.e., after accounting for stem density, aggregate BA growth increased with BA). Following the outbreak, however, neighborhoods composed of small trees yielded levels of aggregate BA growth comparable to neighborhoods composed of the same number of large trees. From pre- to post-outbreak, the relative magnitude of drivers of overstory recruitment also shifted, with fine-scale topography playing a stronger role in the pre-outbreak period compared to the post-outbreak period, when overstory recruitment was related primarily to late-seral proportion and neighborhood mortality. These shifts in drivers of aggregate growth metrics contributed to qualitative shifts in the spatial patterns of BA growth and overstory recruitment from pre- to post-outbreak. Thus, not only did the outbreak alter stand structure directly, redistributing biomass within the stand (Donato *et al.* 2013; Morris *et al.* 2022); it also redistributed within-stand patterns of productivity (Romme *et al.* 1986).

1.6 CONCLUSION

Compensatory responses of forests, wherein the loss of one forest component is compensated for by the growth of another following disturbance, are key mechanisms of resilience with strong stabilizing effects within forest communities (Gonzalez & Loreau 2009). Overall, we found strong evidence for compensatory responses across spatial scales. Overstory recruitment density increased as growth releases of small-diameter trees accelerated growth of understory trees into the overstory. Despite net decreases in live BA caused by the outbreak, increases in growth rates of surviving trees were sufficient to maintain stability in rates of biomass accumulation within our study stands. Our findings illustrate how compensatory responses of individual trees vary widely with size, species, and spatial position within a stand, demonstrating the importance of spatially explicit, individual-based modeling approaches for reconstructing spatial patterns of historical disturbance (Vašíčková *et al.* 2019) and predicting post-disturbance forest dynamics (Seidl *et al.* 2012). Post-outbreak growth rates and growth releases were greatest for small-diameter trees located in neighborhoods with high levels of overstory mortality, with late-seral, shade-tolerant species exhibiting the greatest growth responses both prior to and following the outbreak. This variation in individual tree responses, combined with the spatial pattern of surviving trees, resulted in highly variable emergent patterns of aggregate BA growth and overstory recruitment. Quantifying the ways in which forests compensate for stand-releasing disturbances such as bark beetle outbreaks is critical for modeling post-disturbance stand development and forest carbon dynamics (Dhar & Hawkins 2011; Pfeifer *et al.* 2011). By evaluating forest compensatory responses in a spatially explicit framework, our findings highlight the role of landscape composition and configuration in shaping forest resilience (Chambers *et al.* 2019).

1.7 APPENDIX A: EXTENDED STUDY LOCATION AND PLOT INFORMATION

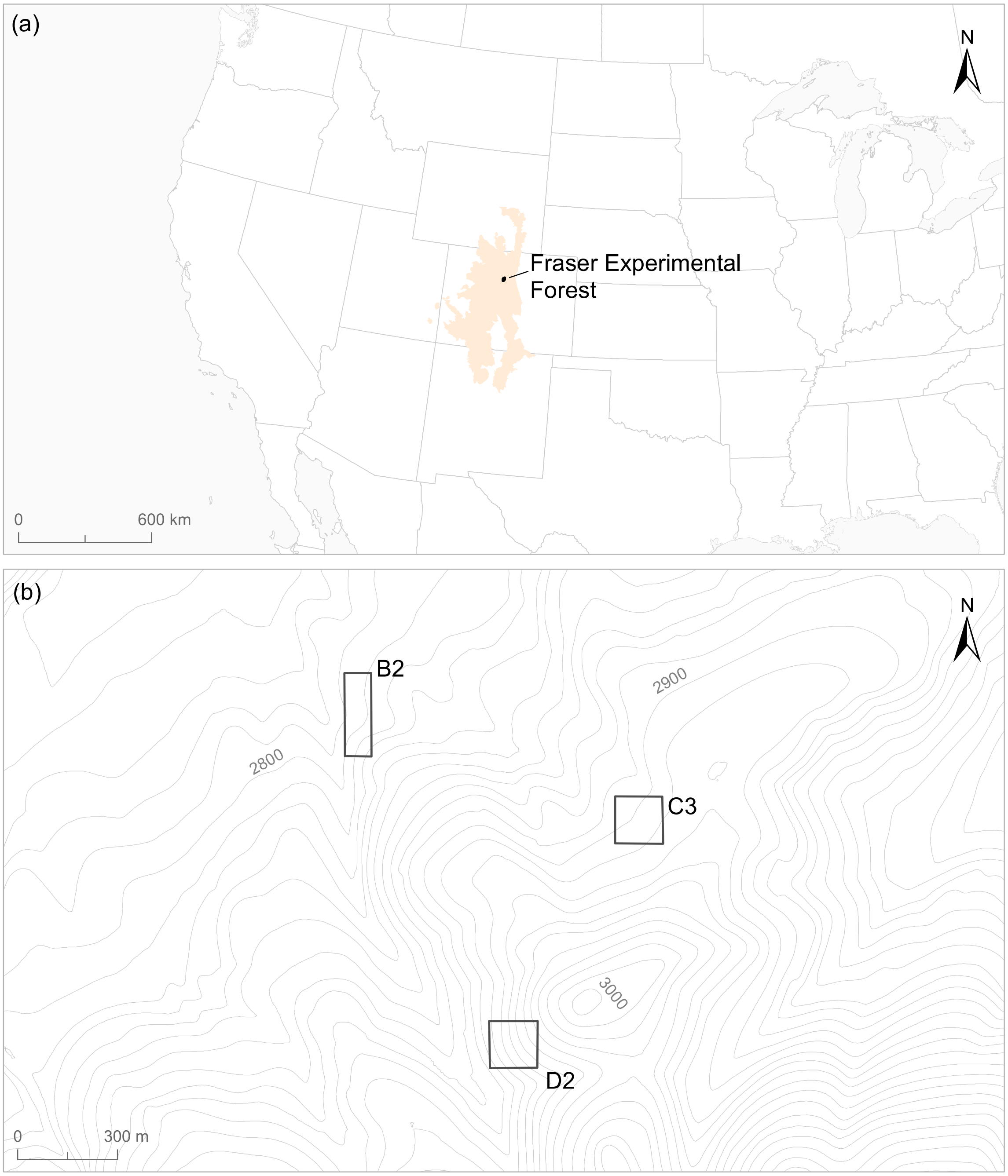

Figure 1.6. Study location map. (a) The Fraser Experimental Forest is located within the Southern Rockies Ecoregion (orange shading) in Colorado, USA. (b) Long-term monitoring plots (black outline) are separated by a minimum distance of 580 meters and are each two hectares in size.

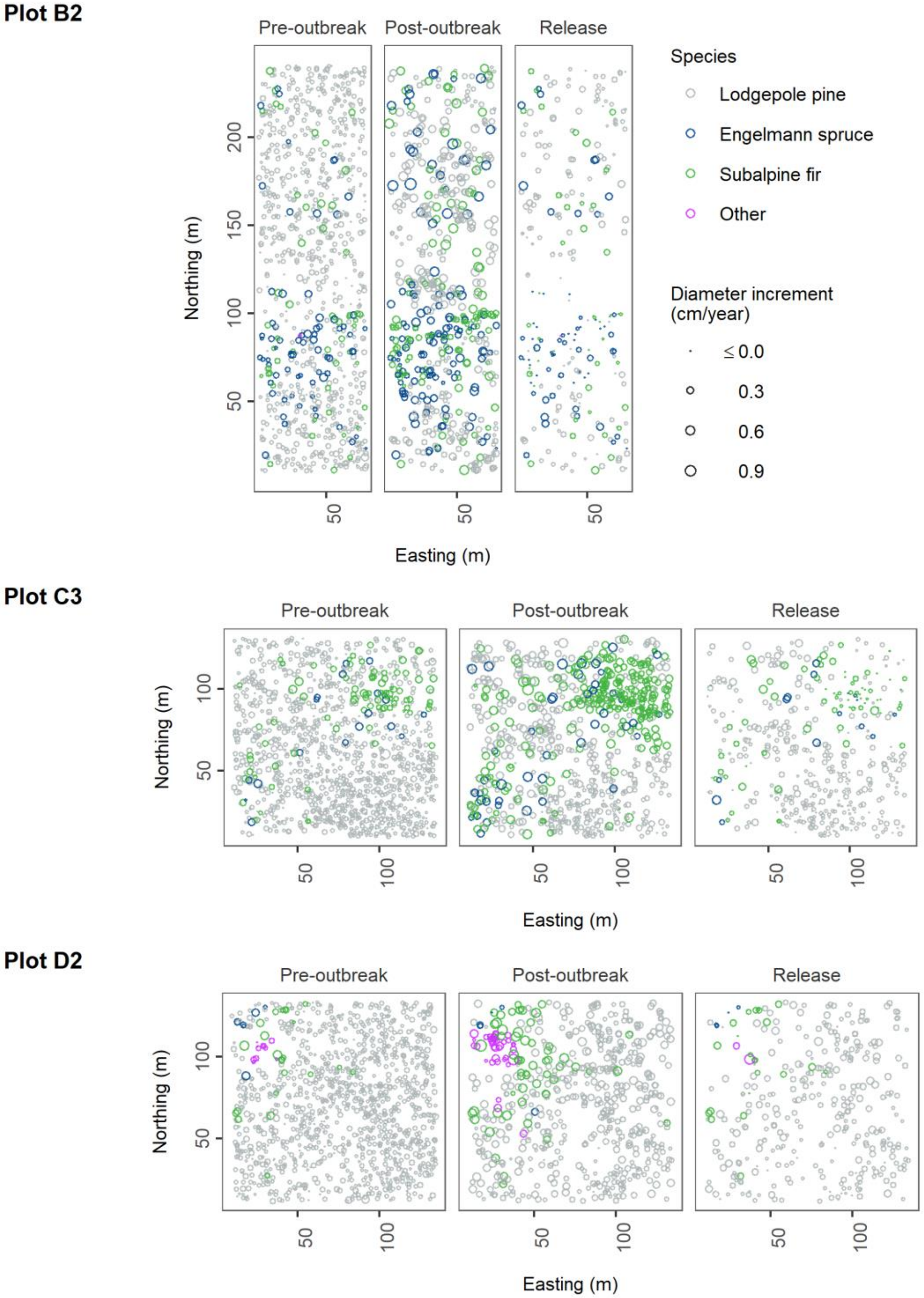

Figure 1.7. Individual tree diameter growth responses. Coordinates are relative to southwest corner of each plot. Species category "Other" includes quaking aspen (*Populus tremuloides*), gray alder (*Alnus incana*), Scouler's willow (*Salix scouleriana*), and Douglas-fir (*Pseudotsuga menziesii*).

Plot B2

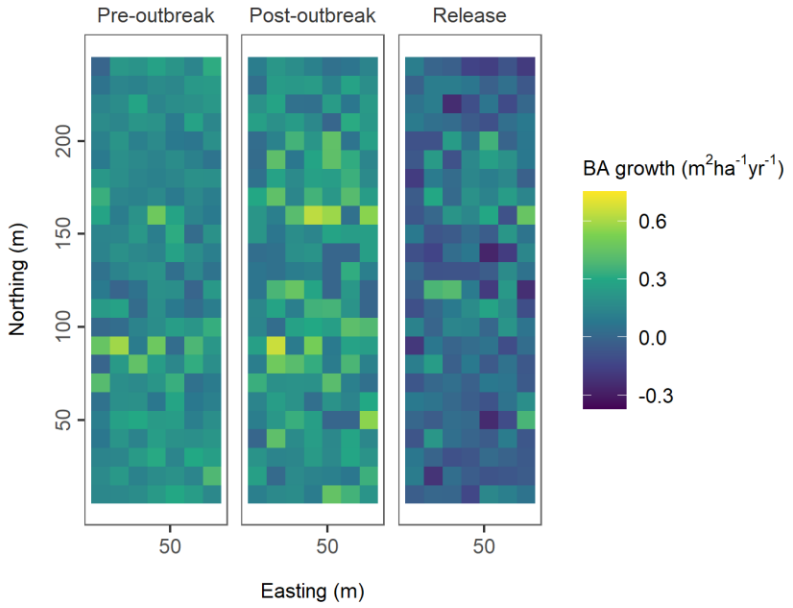

Plot C3

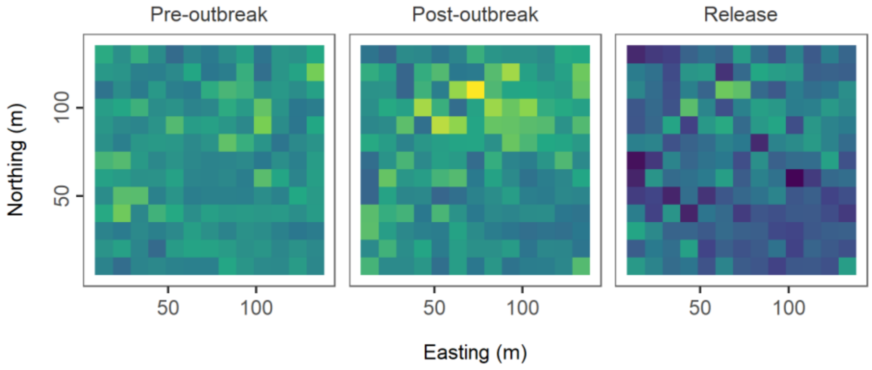

Plot D2

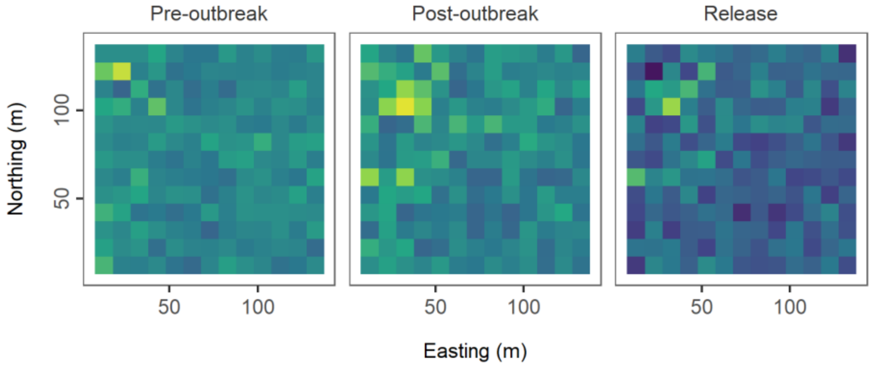

Figure 1.8. Aggregate basal area (BA) growth. Cell size is 10 m and coordinates are relative to southwest corner of each plot.

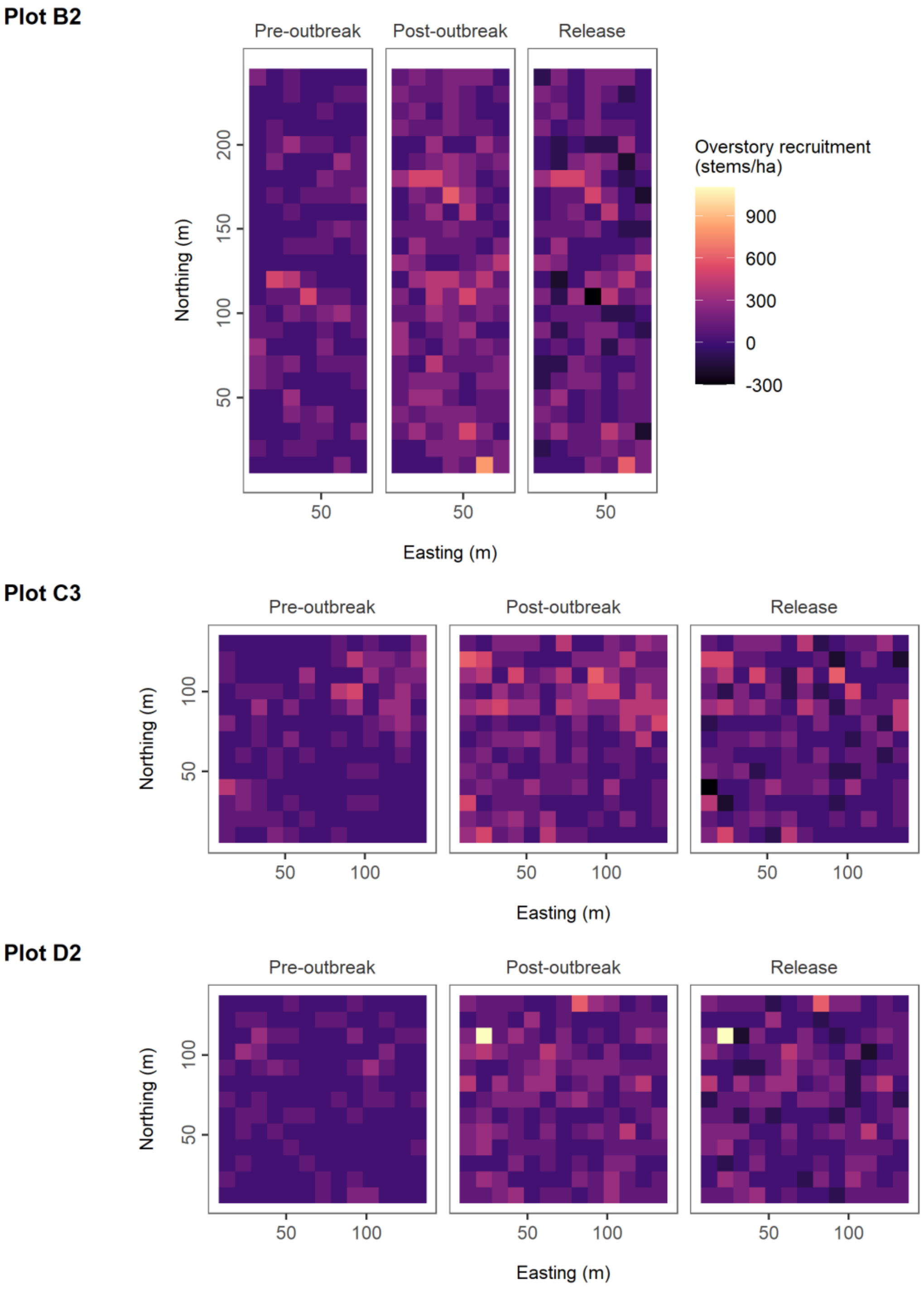

Figure 1.9. Aggregate overstory recruitment. Cell size is 10 m and coordinates are relative to southwest corner of each plot.

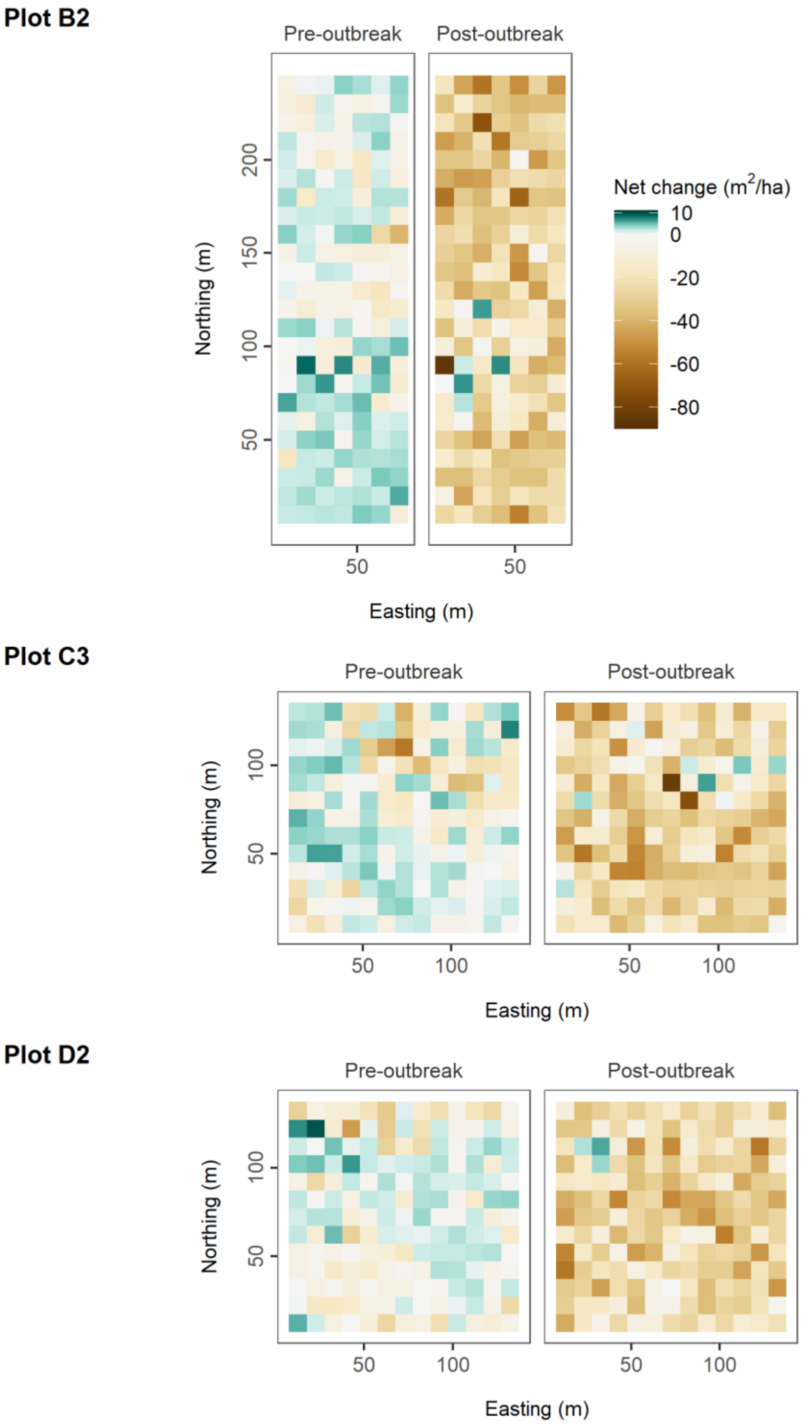

Figure 1.10. Aggregate net live basal area change. Net change is defined as basal area growth minus basal area mortality. Cell size is 10 m and coordinates are relative to southwest corner of each plot.

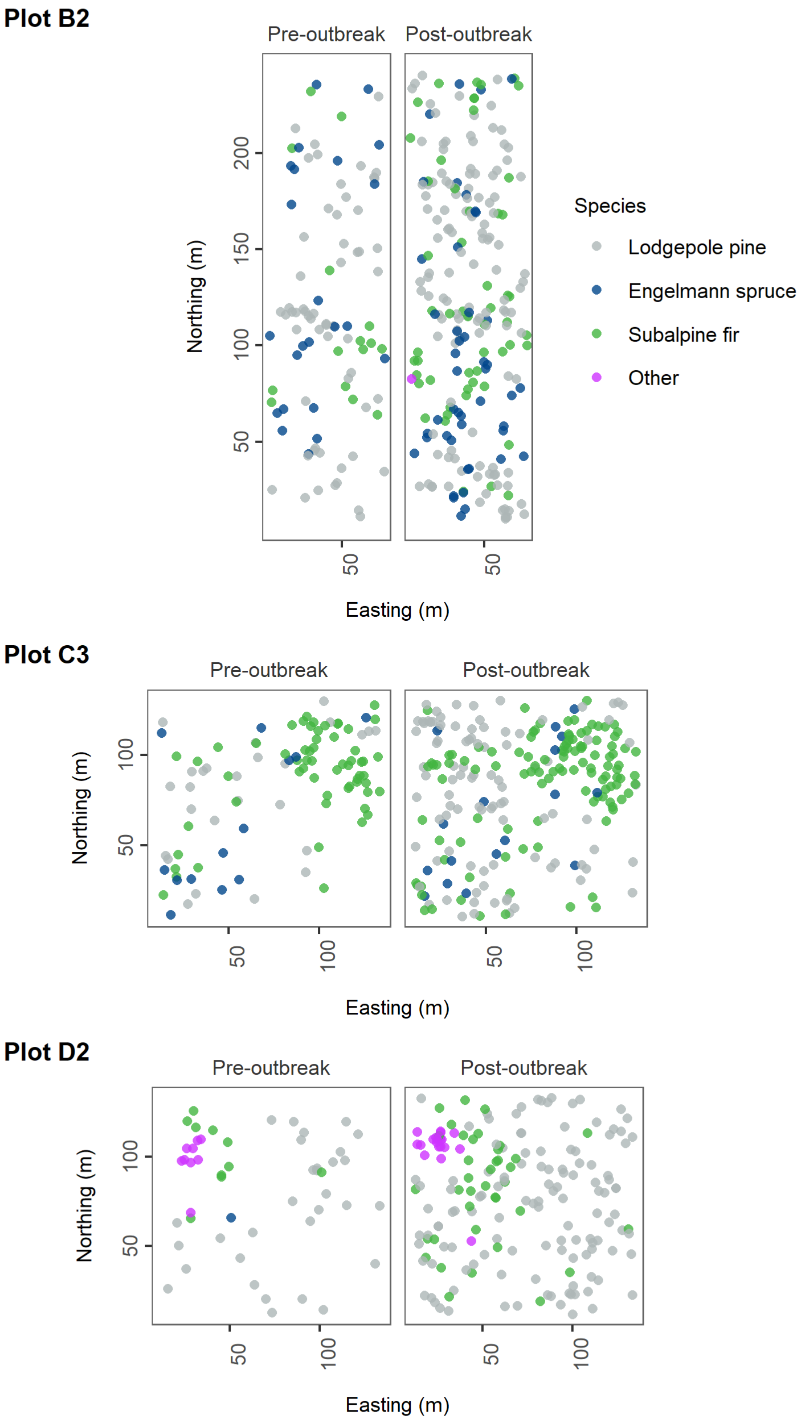

Figure 1.11. Stem maps of overstory recruitment by species. Recruitment is defined as ingrowth into ≥9 cm DBH size class. Coordinates are relative to southwest corner of each plot. Species category "Other" includes quaking aspen (*Populus tremuloides*), gray alder (*Alnus incana*), Scouler's willow (*Salix scouleriana*), and Douglas-fir (*Pseudotsuga menziesii*).

1.8 APPENDIX B: EXTENDED STATISTICAL MODELING INFORMATION

Table 1.3. Descriptive statistics for individual tree diameter growth datasets used in modeling.

Growth period	Metric	Lodgepole pine (n = 2995/1401/832)[a]				Engelmann spruce (n = 96/177/84)[a]				Subalpine fir (n = 160/466/146)[a]			
		Min	Max	Mean	Median	Min	Max	Mean	Median	Min	Max	Mean	Median
Pre-outbreak	Diameter growth (cm/year)	-0.11	0.68	0.06	0.05	0.01	0.47	0.21	0.21	0.01	0.65	0.21	0.20
	Diameter at breast height (cm)	9.0	50.5	22.5	21.7	9.1	63.1	21.9	16.9	9.1	48.1	15.7	12.8
	Neighborhood density index (radians)	0.3	2.5	1.2	1.2	0.3	1.6	1.0	1.0	0.3	1.9	1.1	1.0
	Neighborhood conspecific proportion	0.00	1.00	0.96	1.00	0.00	0.76	0.19	0.10	0.00	0.47	0.13	0.08
	Neighborhood mortality proportion	0.00	0.74	0.12	0.09	0.00	0.62	0.13	0.08	0.00	0.66	0.20	0.15
	Slope (degrees)	0.9	34.0	16.1	15.7	1.9	28.1	14.3	13.7	1.1	31.6	13.1	11.9
	Topographic position index (m)	-1.4	1.0	0.0	0.0	-1.4	0.7	-0.1	0.0	-1.2	0.6	0.0	0.0
Post-outbreak	Diameter growth (cm/year)	-0.18	0.68	0.16	0.14	-0.09	0.94	0.33	0.29	-0.17	0.96	0.28	0.26
	Diameter at breast height (cm)	4.1	35.9	12.6	11.4	5.0	66.7	15.7	11.6	4.8	46.6	11.1	8.6
	Neighborhood density index (radians)	0.3	3.0	1.3	1.2	0.5	1.9	1.1	1.0	0.5	2.7	1.2	1.1
	Neighborhood conspecific proportion	0.00	1.00	0.94	0.97	0.00	0.66	0.18	0.10	0.00	0.76	0.29	0.26
	Neighborhood mortality proportion	0.07	0.98	0.67	0.69	0.04	0.95	0.55	0.59	0.04	0.97	0.51	0.53
	Slope (degrees)	1.6	32.3	16.0	15.5	1.6	28.1	14.0	13.8	1.1	31.6	12.7	11.5
	Topographic position index (m)	-1.3	0.7	0.0	0.0	-1.4	0.7	-0.1	0.0	-1.5	0.7	-0.1	0.0
Release	Diameter growth (cm/year)	-0.59	0.48	0.09	0.08	-0.48	0.50	0.10	0.07	-0.30	0.46	0.10	0.09
	Diameter at breast height (cm)	8.9	35.9	16.1	15.2	10.2	66.7	24.1	19.1	10.4	46.6	18.4	15.8
	Neighborhood density index (radians)	0.3	2.7	1.3	1.3	0.6	1.6	1.1	1.0	0.5	2.3	1.1	1.1
	Neighborhood conspecific proportion	0.00	1.00	0.94	0.98	0.00	0.66	0.22	0.17	0.00	0.73	0.26	0.19
	Neighborhood mortality proportion	0.07	0.98	0.68	0.70	0.04	0.89	0.51	0.52	0.04	0.97	0.55	0.59
	Slope (degrees)	1.6	31.8	16.1	15.3	1.9	28.1	14.4	13.8	1.1	31.6	13.1	11.9
	Topographic position index (m)	-1.3	0.7	0.0	0.0	-1.4	0.4	-0.1	0.0	-1.1	0.6	0.0	0.0

[a] Sample sizes correspond to pre-outbreak/post-outbreak/release datasets for each species.

Table 1.4. Descriptive statistics for aggregate basal area growth datasets used in modeling.

Growth period	Metric	Min	Max	Mean	Median
Pre-outbreak (n = 505)[a]	Basal area growth of live trees ($m^2ha^{-1}yr^{-1}$)	-0.01	0.65	0.18	0.17
	Mortality proportion of initial basal area	0.00	0.87	0.15	0.06
	Surviving basal area (m^2/ha)	0.7	107.2	33.1	33.3
	Surviving stem density (stems/ha)	100	2200	749	700
	Late-seral proportion of surviving basal area	0.00	1.00	0.07	0.00
	Slope (degrees)	1.4	35.7	15.7	15.2
	Topographic position index (m)	-1.0	0.7	0.0	0.0
Post-outbreak (n = 459)[a]	Basal area growth of live trees ($m^2ha^{-1}yr^{-1}$)	-0.01	0.75	0.22	0.20
	Mortality proportion of initial basal area	0.00	0.99	0.78	0.83
	Surviving basal area (m^2/ha)	0.64	63.63	7.48	5.75
	Surviving stem density (stems/ha)	100	2000	318	300
	Late-seral proportion of surviving basal area	0.00	1.00	0.28	0.00
	Slope (degrees)	1.4	35.7	15.7	15.4
	Topographic position index (m)	-1.0	0.7	0.0	0.0
Release (n = 459)[ab]	Basal area growth of live trees ($m^2ha^{-1}yr^{-1}$)	-0.36	0.58	0.03	0.02

[a] Datasets exclude raster cells with surviving basal area equal to zero, for which late-seral proportion could not be calculated.

[b] Covariates are the same as the post-outbreak dataset.

Table 1.5. Descriptive statistics for aggregate overstory recruitment datasets used in modeling.

Growth period	Metric	Min	Max	Mean	Median
Pre-outbreak (n = 506)	Overstory recruitment (stems/ha)[a]	0	500	55	0
	Initial basal area (m^2/ha)	1.3	115.9	39.5	39.4
	Initial stem density (stems/ha)	100	2400	845	800
	Late-seral proportion of initial basal area	0.00	1.00	0.06	0.00
	Mortality proportion of initial basal area	0.00	1.00	0.16	0.06
	Slope (degrees)	1.4	35.7	15.7	15.2
	Topographic position index (m)	-1.0	0.7	0.0	0.0
Post-outbreak (n = 505)[b]	Overstory recruitment (stems/ha)[a]	0	1100	144	100
	Initial basal area (m^2/ha)	1.3	114.0	36.2	36.7
	Initial stem density (stems/ha)	100	2300	798	700
	Late-seral proportion of initial basal area	0.00	1.00	0.09	0.00
	Mortality proportion of initial basal area	0.00	1.00	0.80	0.85
	Slope (degrees)	1.4	35.7	15.7	15.2
	Topographic position index (m)	-1.0	0.7	0.0	0.0
Release (n = 505)[bc]	Overstory recruitment (stems/ha)[a]	-300	1100	90	100

[a] Values presented here are scaled up to a per-ha basis. Original 10 m raster cell counts were used for modeling.

[b] Datasets exclude raster cells with initial basal area equal to zero, for which late-seral and mortality proportions could not be calculated.

[c] Covariates are the same as the post-outbreak dataset.

Table 1.6. Fixed effects and hyperparameters for individual growth models with species as the only fixed effect.

Growth Period	Parameter	mean	sd	0.025quant	0.5quant	0.975quant
Fixed effects						
Pre-outbreak	Intercept	0.1025	0.0043	0.0938	0.1025	0.1112
	Species: Lodgepole pine	-0.1451	0.0048	-0.1544	-0.1451	-0.1357
	Species: Engelmann spruce	0.0148	0.0072	0.0006	0.0148	0.0290
Post-outbreak	Intercept	0.1705	0.0081	0.1546	0.1705	0.1865
	Species: Lodgepole pine	-0.1704	0.0077	-0.1857	-0.1704	-0.1553
	Species: Engelmann spruce	0.0586	0.0105	0.0380	0.0586	0.0791
Release	Intercept	0.0634	0.0086	0.0464	0.0634	0.0803
	Species: Lodgepole pine	-0.0468	0.0103	-0.0670	-0.0468	-0.0265
	Species: Engelmann spruce	0.0358	0.0142	0.0079	0.0358	0.0636
Model hyperparameters for random effects						
Pre-outbreak	Precision for the Gaussian observations	357.5703	9.3141	339.4882	357.4892	376.1657
	Precision for Plot	34280.4574	74349.5198	3941.9346	15298.5136	181585.7362
	Range for Gaussian random field	44.1395	11.4854	26.1563	42.5887	70.9432
	Stdev for Gaussian random field	0.0204	0.0024	0.0161	0.0203	0.0255
Post-outbreak	Precision for the Gaussian observations	89.0667	2.9882	83.2700	89.0407	95.0362
	Precision for Plot	23782.1479	20765.0790	2154.9634	18106.0001	77724.2196
	Range for Gaussian random field	40.7802	5.9002	30.4080	40.3702	53.5597
	Stdev for Gaussian random field	0.0765	0.0061	0.0653	0.0763	0.0892
Release	Precision for the Gaussian observations	118.8108	5.6695	107.8783	118.7440	130.1786
	Precision for Plot	20932.4926	19953.8878	1789.7895	15204.7983	73646.4070
	Range for Gaussian random field	54.1419	11.0206	36.5183	52.7404	79.4675
	Stdev for Gaussian random field	0.0595	0.0060	0.0486	0.0592	0.0720

Table 1.7. Fixed effects and hyperparameters for species-specific individual growth release models with intercept as the only fixed effect.

Species	Parameter	mean	sd	0.025quant	0.5quant	0.975quant
Fixed effects						
Lodgepole pine	Intercept	0.0441	0.0069	0.0304	0.0442	0.0577
Engelmann spruce	Intercept	0.0486	0.0104	0.0283	0.0485	0.0691
Subalpine fir	Intercept	0.0669	0.0114	0.0451	0.0666	0.0901
Model hyperparameters for random effects						
Lodgepole pine	Precision for the Gaussian observations	139.4396	7.2643	125.7371	139.2437	154.2935
	Precision for Plot	6528.6604	8.65E+12	594.7241	5646.0660	19221.8373
	Range for s	67.6541	9.6872	46.4875	68.6314	85.4760
	Stdev for s	0.0353	0.0024	0.0299	0.0356	0.0391
Engelmann spruce	Precision for the Gaussian observations	38.3174	5.8976	27.7233	38.0100	50.8224
	Precision for Plot	16659.6820	17468.6882	822.7788	11270.4939	63537.6609
	Range for s	58.5609	106.1150	4.6767	29.1387	293.4442
	Stdev for s	0.0071	0.0084	0.0007	0.0045	0.0291
Subalpine fir	Precision for the Gaussian observations	78.2523	11.5042	57.6004	77.6463	102.5800
	Precision for Plot	17074.8511	17203.1214	1140.6205	11964.4711	63244.3557
	Range for s	58.2831	17.0592	32.1692	55.8201	98.4628
	Stdev for s	0.0659	0.0113	0.0459	0.0652	0.0901

Table 1.8. Fixed effects and hyperparameters for species-specific individual growth models.

Growth Period	Species	Parameter	mean	sd	0.025quant	0.5quant	0.975quant
Fixed effects							
Pre-outbreak	Lodgepole pine	Intercept	0.0300	0.0026	0.0248	0.0300	0.0352
		DBH	0.0012	0.0021	-0.0029	0.0012	0.0052
		Dens_live	-0.0231	0.0025	-0.0280	-0.0231	-0.0183
		Dens_mort_prop	0.0026	0.0023	-0.0019	0.0026	0.0071
		Dens_consp_prop	0.0007	0.0023	-0.0039	0.0007	0.0053
		Slope	-0.0005	0.0036	-0.0074	-0.0005	0.0066
		TPI	-0.0022	0.0018	-0.0058	-0.0022	0.0014
		DBH:Dens_live	0.0296	0.0038	0.0221	0.0296	0.0370
		DBH:Dens_mort_prop	-0.0082	0.0035	-0.0152	-0.0082	-0.0013
	Engelmann spruce	Intercept	0.1110	0.0080	0.0979	0.1102	0.1296
		Dens_live	-0.0906	0.0193	-0.1286	-0.0906	-0.0527
		DBH	-0.0038	0.0201	-0.0433	-0.0038	0.0356
		Dens_mort_prop	0.0248	0.0244	-0.0243	0.0252	0.0719
		Dens_consp_prop	-0.0576	0.0211	-0.0992	-0.0576	-0.0162
		Slope	-0.0416	0.0209	-0.0827	-0.0416	-0.0004
		TPI	0.0004	0.0193	-0.0375	0.0004	0.0384
		DBH:Dens_mort_prop	0.0911	0.0417	0.0090	0.0910	0.1731
	Subalpine fir	Intercept	0.1077	0.0097	0.0888	0.1076	0.1274
		Dens_live	-0.0744	0.0141	-0.1022	-0.0744	-0.0468
		DBH	-0.0357	0.0123	-0.0598	-0.0358	-0.0115
		Dens_mort_prop	0.0010	0.0203	-0.0387	0.0010	0.0411
		Dens_consp_prop	-0.0052	0.0180	-0.0409	-0.0051	0.0298
		Slope	-0.0492	0.0195	-0.0878	-0.0490	-0.0111
		TPI	0.0103	0.0134	-0.0160	0.0103	0.0367
		DBH:Dens_mort_prop	0.0433	0.0193	0.0053	0.0433	0.0812

Growth Period	Species	Parameter	mean	sd	0.025quant	0.5quant	0.975quant
Post-outbreak	Lodgepole pine	Intercept	0.1441	0.0110	0.1222	0.1441	0.1659
		Dens_live	-0.0865	0.0071	-0.1004	-0.0864	-0.0726
		Dens_mort_prop	0.0426	0.0069	0.0292	0.0426	0.0561
		Dens_consp_prop	0.0168	0.0081	0.0009	0.0168	0.0327
		Slope	-0.0125	0.0100	-0.0321	-0.0126	0.0072
		TPI	0.0026	0.0053	-0.0079	0.0026	0.0130
		DBH:Dens_live	0.0476	0.0118	0.0246	0.0476	0.0707
		DBH:Dens_mort_prop	-0.0578	0.0100	-0.0775	-0.0578	-0.0382
	Engelmann spruce	Intercept	0.3249	0.0129	0.2988	0.3250	0.3503
		Dens_live	-0.0533	0.0175	-0.0878	-0.0533	-0.0189
		Dens_mort_prop	0.1498	0.0249	0.1007	0.1498	0.1987
		Dens_consp_prop	-0.0551	0.0271	-0.1079	-0.0552	-0.0016
		Slope	-0.0994	0.0193	-0.1369	-0.0995	-0.0612
		TPI	-0.0076	0.0191	-0.0452	-0.0076	0.0300
		DBH:Dens_mort_prop	-0.0904	0.0313	-0.1520	-0.0904	-0.0290
	Subalpine fir	Intercept	0.3105	0.0215	0.2693	0.3100	0.3542
		Dens_live	-0.0703	0.0118	-0.0935	-0.0703	-0.0472
		Dens_mort_prop	0.1318	0.0218	0.0893	0.1317	0.1748
		Dens_consp_prop	-0.0232	0.0257	-0.0732	-0.0234	0.0276
		Slope	-0.0142	0.0164	-0.0464	-0.0141	0.0180
		TPI	0.0172	0.0113	-0.0050	0.0172	0.0394
		DBH:Dens_live	-0.0567	0.0226	-0.1010	-0.0567	-0.0123
		DBH:Dens_consp_prop	0.0786	0.0246	0.0301	0.0786	0.1269
		DBH:Slope	-0.0389	0.0193	-0.0767	-0.0389	-0.0011

Growth Period	Species	Parameter	mean	sd	0.025quant	0.5quant	0.975quant
Release	Lodgepole pine	Intercept	0.0417	0.0054	0.0306	0.0418	0.0522
		DBH	-0.0470	0.0063	-0.0594	-0.0470	-0.0347
		Dens_live	-0.0381	0.0078	-0.0536	-0.0381	-0.0229
		Dens_mort_prop	0.0403	0.0074	0.0258	0.0403	0.0549
		Dens_consp_prop	0.0062	0.0085	-0.0106	0.0062	0.0227
		Slope	-0.0109	0.0107	-0.0322	-0.0109	0.0099
		TPI	0.0051	0.0059	-0.0065	0.0051	0.0167
		DBH:Dens_live	0.0453	0.0131	0.0197	0.0453	0.0709
		DBH:Dens_mort_prop	-0.0398	0.0107	-0.0607	-0.0398	-0.0188
	Engelmann spruce	Intercept	0.0421	0.0075	0.0273	0.0421	0.0568
		DBH	-0.1237	0.0263	-0.1754	-0.1237	-0.0720
		Dens_live	0.0295	0.0252	-0.0201	0.0295	0.0790
		Dens_mort_prop	0.1620	0.0332	0.0966	0.1620	0.2272
		Dens_consp_prop	0.0246	0.0343	-0.0428	0.0246	0.0921
		Slope	-0.1053	0.0256	-0.1557	-0.1053	-0.0550
		TPI	0.0167	0.0261	-0.0346	0.0167	0.0680
		DBH:Dens_mort_prop	-0.2066	0.0432	-0.2915	-0.2066	-0.1217
	Subalpine fir	Intercept	0.0479	0.0068	0.0346	0.0478	0.0615
		DBH	-0.0636	0.0205	-0.1040	-0.0636	-0.0233
		Dens_live	-0.0417	0.0205	-0.0820	-0.0417	-0.0014
		Dens_mort_prop	0.1803	0.0209	0.1392	0.1803	0.2213
		Slope	0.0110	0.0214	-0.0315	0.0111	0.0528
		TPI	0.0236	0.0202	-0.0161	0.0236	0.0633

Growth Period	Species	Parameter	mean	sd	0.025quant	0.5quant	0.975quant
Model hyperparameters for random effects							
Pre-outbreak	Lodgepole pine	Precision for the Gaussian observations	464.0512	12.4586	439.9938	463.8978	489.0211
		Precision for Plot	26594.8395	20874.6603	3742.6954	21264.2049	80474.2293
		Range for Gaussian random field	38.0150	11.2696	20.3304	36.5491	64.2693
		Stdev for Gaussian random field	0.0125	0.0017	0.0095	0.0124	0.0162
	Engelmann spruce	Precision for the Gaussian observations	128.7167	19.4686	94.0355	127.5284	170.3296
		Precision for Plot	12220.5186	14829.7137	267.7355	7152.1352	52409.1615
		Range for Gaussian random field	59.8494	100.0890	4.9021	31.3021	290.4421
		Stdev for Gaussian random field	0.0050	0.0051	0.0003	0.0034	0.0184
	Subalpine fir	Precision for the Gaussian observations	215.2622	34.3859	154.0842	213.2549	288.5533
		Precision for Plot	15700.8949	16480.0932	745.9290	10591.7745	59226.0678
		Range for Gaussian random field	64.1975	21.6323	32.8715	60.4718	116.5403
		Stdev for Gaussian random field	0.0547	0.0097	0.0378	0.0540	0.0757
Post-outbreak	Lodgepole pine	Precision for the Gaussian observations	120.6527	4.8360	111.3529	120.5804	130.3961
		Precision for DBH random walk	2657.8764	1650.7279	588.1020	2304.7447	6825.7403
		Precision for Plot	22104.7032	19754.9899	2079.1666	16627.8628	74189.6095
		Range for Gaussian random field	60.2498	16.1133	34.9298	58.1254	97.7540
		Stdev for Gaussian random field	0.0348	0.0047	0.0266	0.0344	0.0448
	Engelmann spruce	Precision for the Gaussian observations	77.4799	8.7330	61.4889	77.0873	95.8183
		Precision for DBH random walk	324.7350	229.5273	79.4278	264.1533	926.7185
		Precision for Plot	23084.5316	24935.1920	1914.2814	15645.8892	88668.7016
		Range for Gaussian random field	52.4776	86.6712	4.6431	27.7395	253.3806
		Stdev for Gaussian random field	0.0099	0.0162	0.0006	0.0052	0.0486
	Subalpine fir	Precision for the Gaussian observations	107.8793	8.3295	92.1910	107.6542	124.9561
		Precision for DBH random walk	708.4145	569.4285	171.0600	544.6879	2218.9017
		Precision for Plot	17217.7367	17704.7216	1109.5697	11915.3209	64304.8382
		Range for Gaussian random field	63.4989	18.1001	36.0524	60.7328	106.6115
		Stdev for Gaussian random field	0.0619	0.0089	0.0459	0.0614	0.0809

Growth Period	Species	Parameter	mean	sd	0.025quant	0.5quant	0.975quant
Release	Lodgepole pine	Precision for the Gaussian observations	161.6891	8.5331	145.6675	161.4333	179.1735
		Precision for Plot	22490.4640	20741.8188	1682.3286	16583.1983	76625.2512
		Range for Gaussian random field	70.5945	26.0674	32.2238	66.4382	133.3719
		Stdev for Gaussian random field	0.0297	0.0052	0.0203	0.0295	0.0404
	Engelmann spruce	Precision for the Gaussian observations	83.3966	13.4040	59.6000	82.5915	111.9995
		Precision for Plot	21715.5916	22839.9184	1673.6039	14914.2871	82218.2479
		Range for Gaussian random field	62.5708	107.1446	6.5956	32.5957	306.1356
		Stdev for Gaussian random field	0.0046	0.0048	0.0004	0.0032	0.0173
	Subalpine fir	Precision for the Gaussian observations	76.6681	9.1646	60.0524	76.1950	96.0695
		Precision for Plot	9962.0872	11845.5019	439.3462	6228.3858	42125.0290
		Range for Gaussian random field	46.2565	67.7015	4.2870	26.3339	211.8456
		Stdev for Gaussian random field	0.0080	0.0112	0.0008	0.0047	0.0357

Table 1.9. Fixed effects and hyperparameters for aggregate basal area growth release models with intercept as the only fixed effect.

Parameter	mean	sd	0.025quant	0.5quant	0.975quant
Fixed effects					
Intercept	0.0127	0.0086	-0.0053	0.0130	0.0290
Model hyperparameters for random effects					
Precision for the Gaussian observations	66.4617	4.7613	57.4182	66.3605	76.1157
Precision for Plot	21713.1976	17252.0653	1854.9447	17303.8771	65211.8350
Range for Gaussian random field	77.2514	26.6689	41.5183	71.6083	144.3492
Stdev for Gaussian random field	0.0552	0.0094	0.0384	0.0546	0.0754

Table 1.10. Fixed effects and hyperparameters for aggregate basal area growth models.

Growth Period	Parameter	mean	sd	0.025quant	0.5quant	0.975quant
Fixed effects						
Pre-outbreak	Intercept	0.0986	0.0050	0.0888	0.0986	0.1088
	BA_mort_prop	-0.0104	0.0074	-0.0249	-0.0104	0.0041
	BA_LS_prop_surv	0.0724	0.0075	0.0577	0.0724	0.0871
	BA_surv	0.0481	0.0094	0.0297	0.0481	0.0664
	Stems_surv	0.0940	0.0116	0.0712	0.0940	0.1169
	Stems_surv^2	-0.0490	0.0099	-0.0683	-0.0490	-0.0296
	Slope	-0.0163	0.0109	-0.0375	-0.0164	0.0055
	TPI	-0.0091	0.0062	-0.0213	-0.0091	0.0032
Post-outbreak	Intercept	0.1130	0.0087	0.0952	0.1132	0.1301
	BA_mort_prop	-0.0369	0.0134	-0.0632	-0.0369	-0.0106
	BA_LS_prop_surv	0.1174	0.0109	0.0959	0.1174	0.1389
	BA_surv	0.0152	0.0157	-0.0156	0.0152	0.0460
	Stems_surv	0.1310	0.0146	0.1023	0.1310	0.1598
	Stems_surv^2	-0.0362	0.0067	-0.0495	-0.0362	-0.0230
	Slope	-0.0142	0.0163	-0.0460	-0.0143	0.0179
	TPI	0.0041	0.0089	-0.0133	0.0041	0.0215
Release	Intercept	0.0173	0.0081	0.0004	0.0176	0.0330
	BA_mort_prop	-0.1364	0.0161	-0.1680	-0.1364	-0.1047
	BA_LS_prop_surv	0.0738	0.0128	0.0487	0.0739	0.0989
	BA_surv	-0.1134	0.0183	-0.1494	-0.1134	-0.0775
	Stems_surv	0.0878	0.0174	0.0536	0.0878	0.1219
	Stems_surv^2	-0.0281	0.0081	-0.0439	-0.0281	-0.0122
	Slope	-0.0055	0.0182	-0.0409	-0.0057	0.0308
	TPI	0.0012	0.0107	-0.0198	0.0012	0.0222

Growth Period	Parameter	mean	sd	0.025quant	0.5quant	0.975quant
Model hyperparameters for random effects						
Pre-outbreak	Precision for the Gaussian observations	244.0901	19.7235	206.7803	243.6605	284.1316
	Precision for Plot	20691.7348	18460.4489	1932.2733	15584.4540	69503.1040
	Range for Gaussian random field	50.9951	23.1539	21.3892	45.8653	109.7973
	Stdev for Gaussian random field	0.0353	0.0059	0.0247	0.0351	0.0477
Post-outbreak	Precision for the Gaussian observations	136.1264	10.8598	115.9673	135.7163	158.6877
	Precision for Plot	23554.5158	20743.7813	2297.8921	17863.2411	77943.1784
	Range for Gaussian random field	76.6454	25.7482	39.4583	72.1593	139.4283
	Stdev for Gaussian random field	0.0579	0.0084	0.0425	0.0576	0.0753
Release	Precision for the Gaussian observations	89.8620	6.6466	77.3205	89.6882	103.4711
	Precision for Plot	24206.1889	28312.6284	2207.0866	15711.3309	97840.8798
	Range for Gaussian random field	74.4565	25.9478	37.5388	69.7684	138.0409
	Stdev for Gaussian random field	0.0499	0.0086	0.0345	0.0494	0.0684

Table 1.11. Fixed effects and hyperparameters for aggregate overstory recruitment release models with intercept as the only fixed effect.

Parameter	mean	sd	0.025quant	0.5quant	0.975quant
Fixed effects					
Intercept	0.4475	0.0335	0.3817	0.4475	0.5133
Model hyperparameters for random effects					
Precision for the Gaussian observations	0.4481	0.0279	0.3962	0.4470	0.5060
Precision for Plot	14017.2360	11020.4671	1523.0973	11205.3195	43991.5667
Range for Gaussian random field	64.9030	123.5993	6.1615	31.5770	330.5680
Stdev for Gaussian random field	0.0182	0.0164	0.0046	0.0132	0.0616

Table 1.12. Fixed effects and hyperparameters for aggregate overstory recruitment models.

Growth Period	Parameter	mean	sd	0.025quant	0.5quant	0.975quant
Fixed effects						
Pre-outbreak	Intercept	-0.3828	0.0347	-0.4524	-0.3822	-0.3161
	BA_mort_prop	0.3032	0.1053	0.0927	0.3045	0.5062
	BA_start	-0.2999	0.1506	-0.5997	-0.2985	-0.0081
	Stems_start	-0.5050	0.1878	-0.8818	-0.5022	-0.1441
	BA_LS_prop_start	0.3739	0.0869	0.1982	0.3757	0.5395
	Slope	-0.4561	0.1279	-0.7089	-0.4555	-0.2065
	TPI	-0.2957	0.1109	-0.5130	-0.2959	-0.0777
Post-outbreak	Intercept	0.1657	0.0205	0.1248	0.1659	0.2054
	BA_mort_prop	0.3237	0.0950	0.1382	0.3234	0.5108
	BA_start	-0.0491	0.0941	-0.2362	-0.0483	0.1335
	Stems_start	-0.2083	0.1096	-0.4248	-0.2079	0.0054
	BA_LS_prop_start	0.3673	0.0815	0.2031	0.3689	0.5231
	Slope	-0.1732	0.0809	-0.3313	-0.1735	-0.0133
	TPI	-0.0425	0.0746	-0.1883	-0.0428	0.1042
Release	Intercept	0.4475	0.0325	0.3837	0.4475	0.5113
	BA_mort_prop	0.6004	0.1733	0.2600	0.6004	0.9405
	BA_start	0.3228	0.1759	-0.0227	0.3228	0.6680
	Stems_start	-0.6004	0.1777	-0.9494	-0.6004	-0.2517
	BA_LS_prop_start	0.1231	0.1719	-0.2145	0.1230	0.4603
	Slope	0.0408	0.1359	-0.2261	0.0408	0.3075
	TPI	0.1080	0.1311	-0.1495	0.1080	0.3653

Growth Period	Parameter	mean	sd	0.025quant	0.5quant	0.975quant
Model hyperparameters for random effects						
Pre-outbreak	Precision for Plot	24391.4525	26131.5239	2128.3920	16624.8252	93851.7216
	Range for Gaussian random field	36.0806	45.9074	3.4372	22.3140	153.7629
	Stdev for Gaussian random field	0.0351	0.0433	0.0029	0.0220	0.1477
Post-outbreak	Precision for Plot	18859.2334	18567.7856	1317.4185	13394.2427	67738.8299
	Range for Gaussian random field	35.9727	39.7759	4.1563	24.1238	140.2797
	Stdev for Gaussian random field	0.0359	0.0394	0.0030	0.0241	0.1391
Release	Precision for the Gaussian observations	0.4778	0.0302	0.4206	0.4770	0.5397
	Precision for Plot	25850.4238	26633.5026	2655.6877	18037.2742	95746.9024
	Range for Gaussian random field	43.6128	61.8289	4.9643	25.3821	194.1286
	Stdev for Gaussian random field	0.0233	0.0229	0.0024	0.0166	0.0839

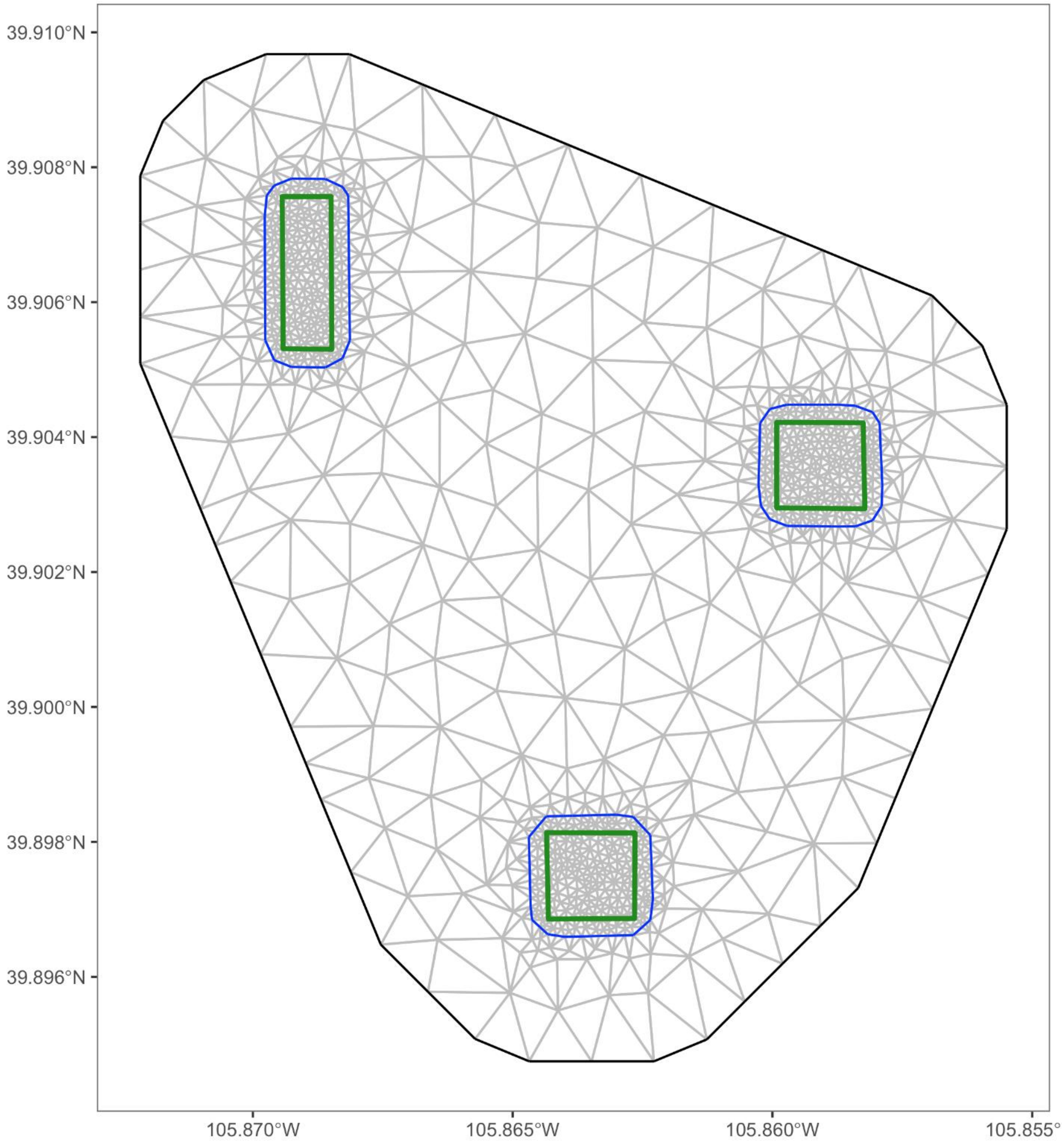

Figure 1.12. Triangulation of the study region, which is used in the Stochastic Partial Differential Equation (SPDE) approach. Green polygons indicate plot boundaries.

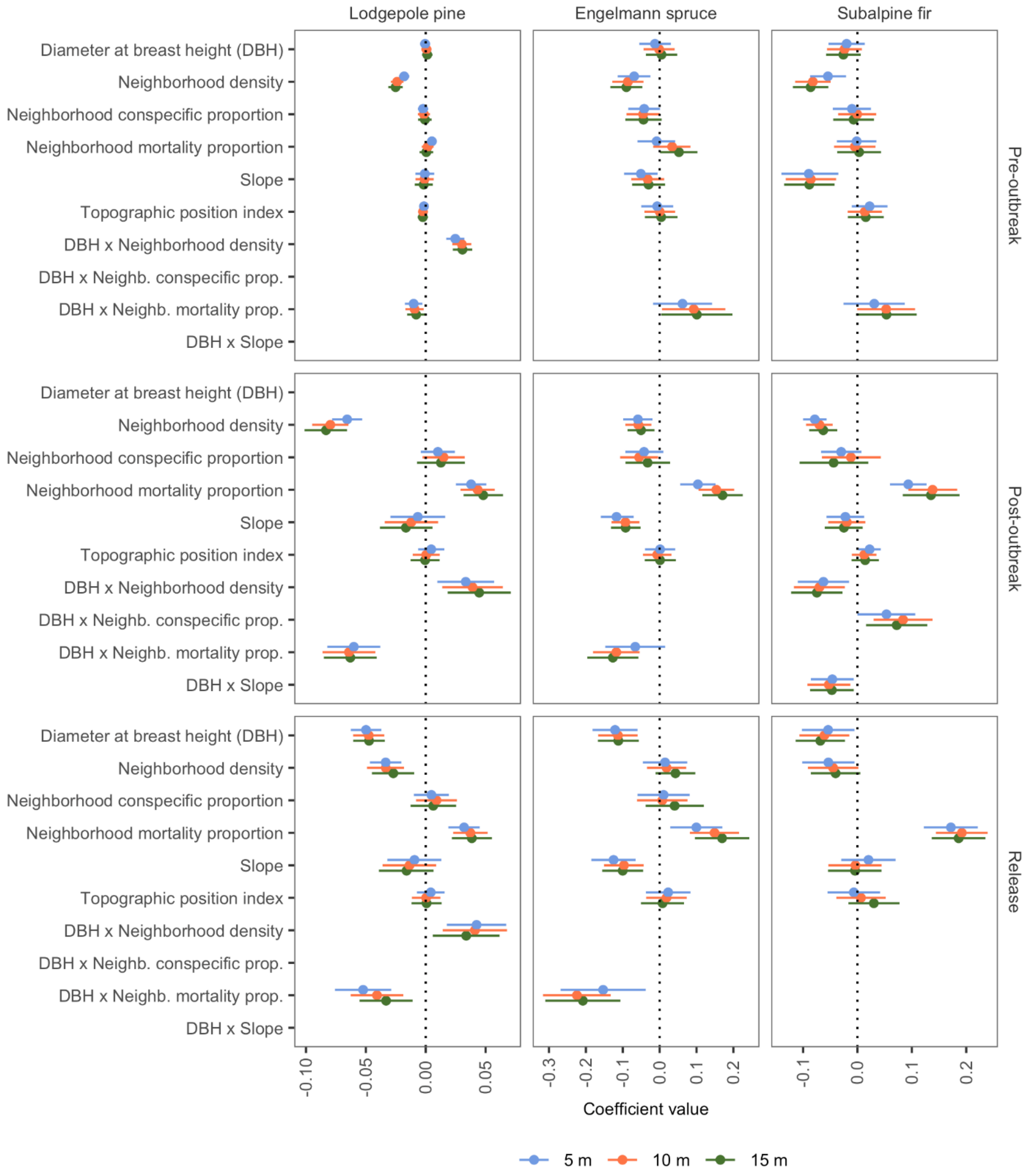

Figure 1.13. Effect of neighborhood radius on individual growth model coefficients. Dots represent the medians of the posteriors and horizontal lines represent 95% credible intervals. The effects for each predictor are per 2 SD within each growth period- and species-specific dataset. To enable comparison, trees <15 m from the edge of each plot were excluded from each of the models.

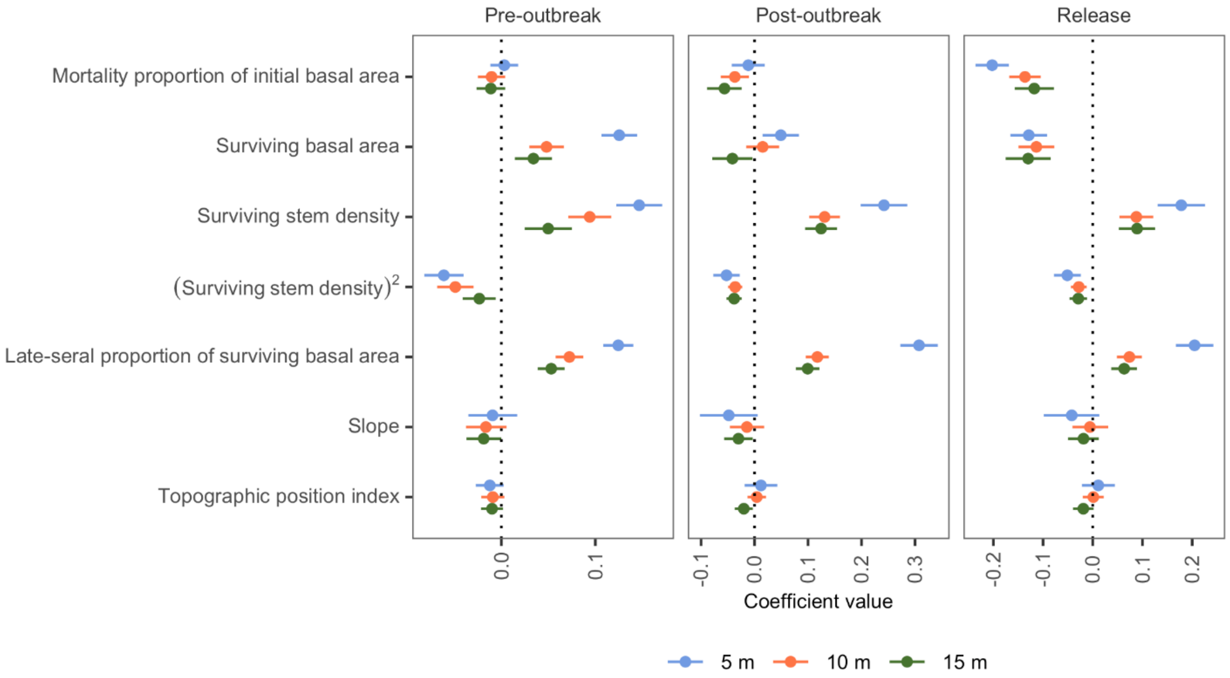

Figure 1.14. Effect of neighborhood radius on aggregate basal area growth model coefficients. Dots represent the medians of the posteriors and horizontal lines represent 95% credible intervals. The effects for each predictor are per 2 SD within each growth period-specific dataset.

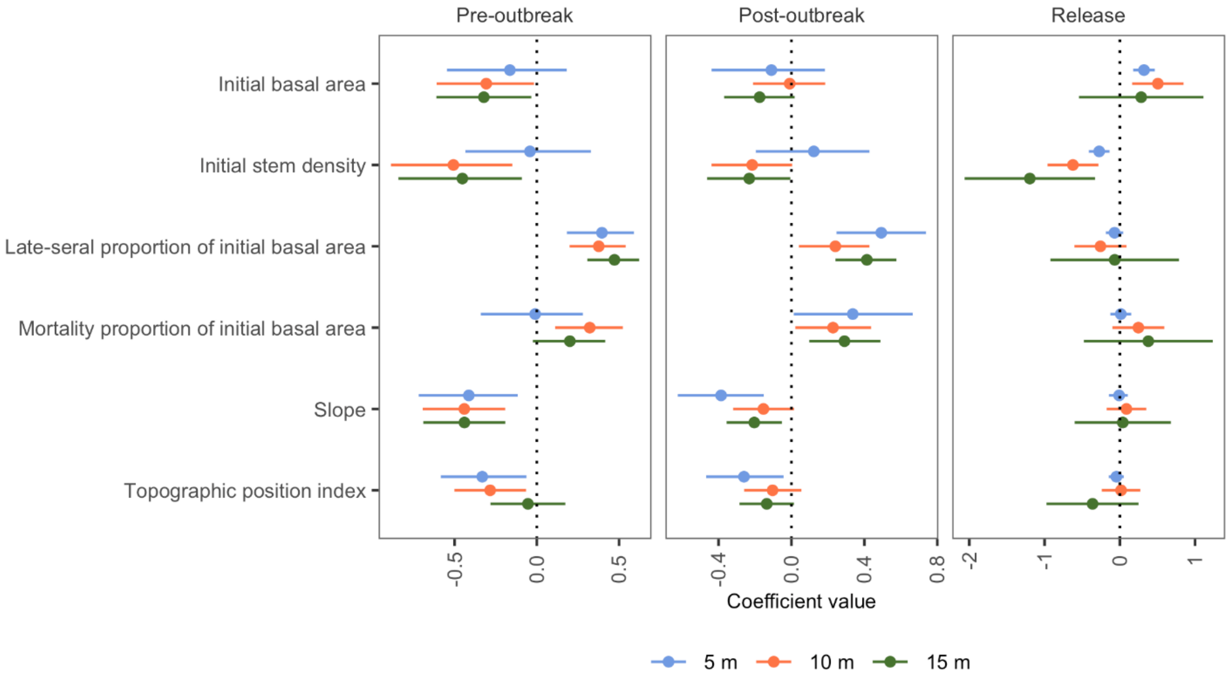

Figure 1.15. Effect of neighborhood radius on aggregate overstory recruitment model coefficients. Dots represent the medians of the posteriors and horizontal lines represent 95% credible intervals. The effects for each predictor are per 2 SD within each growth period-specific dataset.

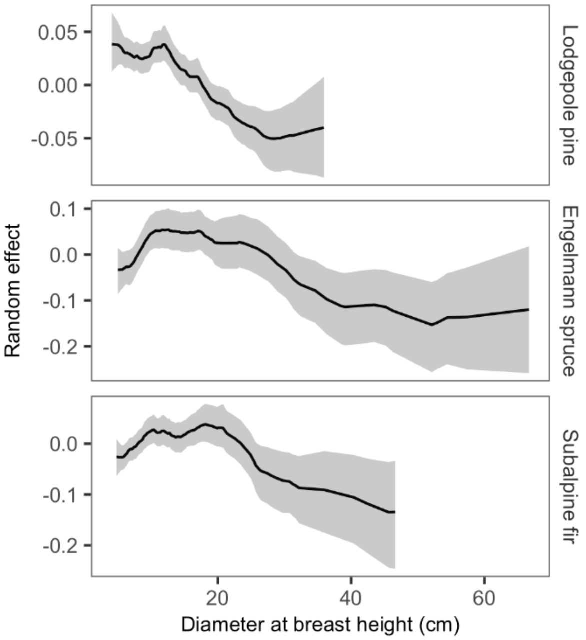

Figure 1.16. Random effect of diameter at breast height (DBH) on post-outbreak individual diameter growth of live trees, modeled as a random walk of order one. Solid line represents posterior median and shading represents 95% credible interval.

Chapter 2. SPATIO-TEMPORAL PATTERNS AND DRIVERS OF BIOTIC DISTURBANCE HOTSPOTS IN WESTERN UNITED STATES CONIFEROUS FORESTS

2.1 Abstract

Globally, forest disturbances caused by herbivorous insects and pathogens have increased, a trend that has been linked to warming and drying climate. With this increase in biotic disturbance activity, an emerging ecological phenomenon has been documented across the western United States (US): biotic disturbance 'hotspots', or areas where two or more biotic disturbance agents co-occur in space and time. Biotic disturbance hotspots may have important implications for the resilience of forests in the face of climate change, particularly if they erode mechanisms of post-disturbance forest recovery. Despite the potential implications of biotic disturbance hotspots for forest resilience, the factors leading to hotspot occurrence remain poorly understood. Here, we characterized the spatio-temporal patterns and drivers of biotic disturbance hotspots occurring from 2000 – 2020 across three broad forested regions in the western US (the Southern Rockies, Middle Rockies, and Cascades). Using spatio-temporal regression models fit to aerial detection survey data, we evaluated whether and to what extent biotic disturbance hotspots can be predicted from predisposing factors (i.e., forest composition, topography, and average climate) expected to increase forest susceptibility to biotic disturbance, as well as inciting factors (i.e., annual weather conditions) known to trigger individual bark beetle and pathogen outbreaks. Our results demonstrate that hotspots have been widespread across the western US in the early part of the 21st century, with each of our study regions experiencing years in which hotspots were detected within $\geq$28% of surveyed areas with the potential for hotspot occurrence. Of the predisposing and inciting factors we evaluated, forest structure and composition were the strongest and most consistent drivers of hotspots. Effects of other factors varied by region, reflecting regional variation in biophysical setting and context. Relative to the predictor variables included in our analysis, spatio-temporal random effects consistently had larger effect sizes and were more closely correlated with model predictions, suggesting that outbreak contagion and other dynamic factors strongly shape patterns of biotic disturbance hotspots. Overall, our findings provide a deeper understanding of interacting biotic

disturbances in western US coniferous forests and have important implications for the resilience of these systems during a period marked by continued increases in biotic disturbance activity.

2.2 INTRODUCTION

Forest disturbances play a critical role in shaping the structure and function of temperate forests worldwide, along with the myriad ecosystem services these forests provide (Thom & Seidl 2016). Globally, biotic disturbance activity (i.e., tree mortality caused by insects and pathogens) has been increasing in recent decades (Kautz *et al.* 2017), linked in large part to the sensitivity of biotic agents to changing climate (Bentz *et al.* 2010; Weed *et al.* 2013; Seidl *et al.* 2017). In the western United States (US), early 21st century biotic disturbance activity has been extensive (Meddens *et al.* 2012; Hicke *et al.* 2020), causing greater amounts of tree mortality between 2003 and 2012 than wildfire (Berner *et al.* 2017). While region- and species-specific trends vary, biotic disturbance activity is expected to continue to increase as climate continues to change (Bentz *et al.* 2010; Kautz *et al.* 2017).

As disturbance regimes change in response to changing climate, interactions among disturbance agents are increasingly important to consider (Turner 2010; Buma 2015; Burton *et al.* 2020). One widespread disturbance interaction emerging in recent decades across the western US is the occurrence of biotic disturbance 'hotspots', areas where two or more distinct biotic disturbances overlap in space and time (Harvey *et al.* In press). Over the period 1997 – 2019, approximately 5 – 18% of the area affected by biotic disturbance each year in western US forests were hotspots (Harvey *et al.* In press). Despite their prevalence, the causes and consequences of biotic disturbance hotspots remain poorly understood.

Biotic disturbance hotspots may have important implications for the resilience of forests in the face of climate change, particularly if disturbance agents have compound or synergistic effects (Paine *et al.* 1998). Many tree-killing bark beetles and plant pathogens are specialists, feeding on or infecting a specific host tree genus or species, and in the case of bark beetles, also preferentially attacking older and larger host trees (Raffa *et al.* 2008). In forests affected by a single biotic disturbance, the selective mortality of specific species and sizes of trees often results in abundant surviving non-host and/or understory trees that facilitate rapid post-disturbance growth responses (Veblen *et al.* 1991) and provide continuity in forest functional attributes such as live carbon stocks (Pfeifer *et al.* 2011). In forests affected by biotic disturbance hotspots, however, the synchronous mortality of multiple host tree species has the potential to dampen compensatory growth responses that might otherwise provide stability in forest function (Harvey *et al.* In press). These effects are likely to be exacerbated in areas subject to increasing climate stress, further decreasing rates of forest recovery and increasing the likelihood that mechanisms of forest resilience could break down.

Biotic disturbance and associated tree mortality is a complex process, with numerous factors shaping both the activity and effects of biotic agents ultimately contributing to tree death. As a conceptual framework, it is useful to consider both 'predisposing' and 'inciting' factors that can drive biotic disturbance activity (Manion 1981). Long-term or persistent factors, including host availability, forest structure, and average climate, can predispose locations to biotic disturbance activity (Raffa *et al.* 2008). Short-term factors, including annual weather conditions, can then incite biotic disturbance activity through various mechanisms. Warm temperatures, for example, directly affect the physiology of insect populations by increasing the potential for insect survival, reproduction, and cohort synchrony, all of which facilitate insect outbreaks (Raffa *et al.* 2008; Bentz *et al.* 2010). Warm and dry conditions also indirectly affect biotic disturbance activity by reducing host tree defenses (Raffa *et al.* 2008; Gaylord *et al.* 2013; Weed *et al.* 2013). Predisposing and inciting factors can shape biotic disturbance activity both individually and in combination, with the relative influence of factors being both variable and context-dependent.

Hotspots of biotic disturbance activity likely arise from a variety of factors, depending on both the identity of individual biotic agents and timing of co-occurrence. Temporally synchronous hotspots may occur when individual biotic agents respond to shared broad-scale drivers, such as multiple bark beetle outbreaks occurring synchronously in response to regional increases in temperature (Bentz *et al.* 2010; Chapman *et al.* 2012; Preisler *et al.* 2012; Hart *et al.* 2017). Temporally lagged hotspots may occur due to mechanistic links between disturbance agents, such as when defoliating insects reduce tree vigor, thereby increasing host tree susceptibility to subsequent bark beetle attack (Hadley & Veblen 1993; Cole *et al.* 2022). Even in the absence of shared or linked mechanisms, some spatio-temporal overlap of biotic disturbance agents is expected to arise randomly due to an overall increase in biotic disturbance activity within a finite forested area, such as the increase observed in western US forests in the early part of the 21st century (Meddens *et al.* 2012). Despite the increasing potential for overlap and interaction of biotic disturbance agents, the broad-scale factors associated with biotic disturbance hotspots (e.g., climate, weather, forest structure, topography) are poorly understood to date.

Here, we address this knowledge gap by characterizing the spatio-temporal patterns and drivers of biotic disturbance hotspots across three broad forested regions in the western US that span differing gradients of forest types and bioclimatic conditions. We focus on temporally synchronous hotspots of common tree-killing biotic agents that are not expected to be mechanistically linked (Table 2.1). We examine predisposing factors (i.e., forest composition, topography, and climate) expected to increase forest susceptibility to biotic disturbance, as well as inciting factors (i.e., annual weather conditions) known to trigger individual bark beetle and pathogen outbreaks (Table 2.2). Using this framework, we ask: *(1). Can the occurrence of biotic disturbance hotspots be predicted from factors known to favor individual biotic disturbance agents? (2). What is the relative importance of predisposing and inciting factors in predicting the occurrence of hotspots?* We expect that predisposing and inciting factors will both drive hotspot occurrence, but that the relative importance of factors will vary by biophysical context and therefore by region.

Table 2.1. Tree-killing biotic agents used to identify biotic disturbance hotspots.

Common name	Scientific name	Host tree species
Bark beetles		
Western pine beetle	*Dendroctonus brevicomis*	Ponderosa pine
Jeffrey pine beetle	*Dendroctonus jeffreyi*	Jeffrey pine
Mountain pine beetle	*Dendroctonus ponderosae*	All pine species; primarily lodgepole, ponderosa, western white, sugar, limber, and whitebark pines
Douglas-fir beetle	*Dendroctonus pseudotsugae*	Douglas-fir
Spruce beetle	*Dendroctonus rufipennis*	Engelmann spruce, Sitka spruce, Brewer spruce
Western balsam bark beetle	*Dryocoetes confusus*	Primarily subalpine fir; occasionally other true firs, Engelmann spruce, and lodgepole pine
Pinyon ips	*Ips confusus*	Pinyon pine
Pine engraver	*Ips pini*	All pine species; primarily ponderosa, lodgepole, and Jeffrey pines
Ips engraver beetles	*Ips spp.*	All pine species
Silver fir beetle	*Pseudohylesinus sericeus*	Primarily Pacific silver fir; occasionally other true firs, Douglas-fir, western hemlock, and Sitka spruce
True fir bark beetles	*Scolytus spp.*	True firs
Douglas-fir engraver	*Scolytus unispinosus*	Douglas-fir
Fir engraver	*Scolytus ventralis*	Primarily grand fir, white fir, red fir, and noble fir; occasionally Douglas-fir, subalpine fir, and western hemlock
Multi-agent mortality "complexes"		
Subalpine fir mortality complex[a]		Subalpine fir
Five-needle pine decline[b]		Five-needle pines; primarily limber, Rocky Mountain bristlecone, and whitebark pines
Pinyon pine mortality		Pinyon pine

[a] Subalpine fir mortality complex includes the effects of western balsam bark beetle activity, *Armillaria* root rot, and other mortality agents (Harvey *et al.* 2021). We treated western balsam bark beetle and subalpine fir mortality complex as separate agents when identifying hotspots; however, because our definition of hotspots required that two or more distinct host tree species be affected, we do not expect that doing so inflated our detection of hotspots.

[b] Five-needle pine decline includes the effects of mountain pine beetle activity and white pine blister rust. We treated mountain pine beetle and five-needle pine decline as separate agents when identifying hotspots; however, as noted above, we do not expect that doing so inflated our detection of hotspots.

Table 2.2. Predictor variables for hotspot occurrence and prevalence.

Category	Predictor variable	Description	Temporally explicit?	Expected direction of effect and justification	
Predisposing factors					
Forest composition	Prevalence of host tree co-occurrence	Number of 510-m subcells containing ≥2 potential host tree species	No	+	Increased potential for hotspot occurrence in areas where host trees tend to co-occur
	Host tree basal area (m^2/ha)	Average total basal area of host species within subcells containing ≥2 potential host tree species	No	+	Increased susceptibility to bark beetle outbreak
	Host tree richness	Average host species richness within subcells containing ≥2 potential host tree species	No	+	Increased susceptibility to co-occurring biotic agents
Topography	Heat load index	Index of potential direct incident radiation	No	+	Increased moisture stress for host trees
	Topographic wetness index	Index of the long-term moisture availability of a given site in the landscape	No	-	Decreased moisture stress for host trees
Average climate	Annual actual evapotranspiration (AET; mm)	Average annual AET, expressed as 30-year normals (1991 – 2020)	No	+	Increased vegetation productivity
	Summer maximum vapor pressure deficit (VPD; hPa)	Average daily maximums for June through August, expressed as 30-year normals (1991 – 2020)	No	+	Increased moisture stress for host trees
	Winter minimum temperature (^{o}C)	Average daily minimums for December through February, expressed as 30-year normals (1991 – 2020)	No	+	Increased overwinter survival for bark beetles
Inciting factors					
Weather	Summer maximum vapor pressure deficit (VPD; hPa)	Average daily maximums for June through August, averaged over the 3-year hotspot detection window and expressed as deviations from 30-year normals	Yes	+	Increased moisture stress for host trees
	Winter minimum temperature (^{o}C)	Average daily minimums for December through February, averaged over the 3-year hotspot detection window and expressed as deviations from 30-year normals	Yes	+	Increased overwinter survival for bark beetles

2.3 METHODS

2.3.1 *Study regions*

We studied three broad forested regions within the western US: the Southern Rockies, the Middle Rockies, and the Cascades (Figure 2.1). These regions are all mountainous, dominated by conifer forests, and comparable in their spatial extents (each 134,000 – 144,000 km^2), but span a range of forest types and bioclimatic conditions (Rollins 2009).

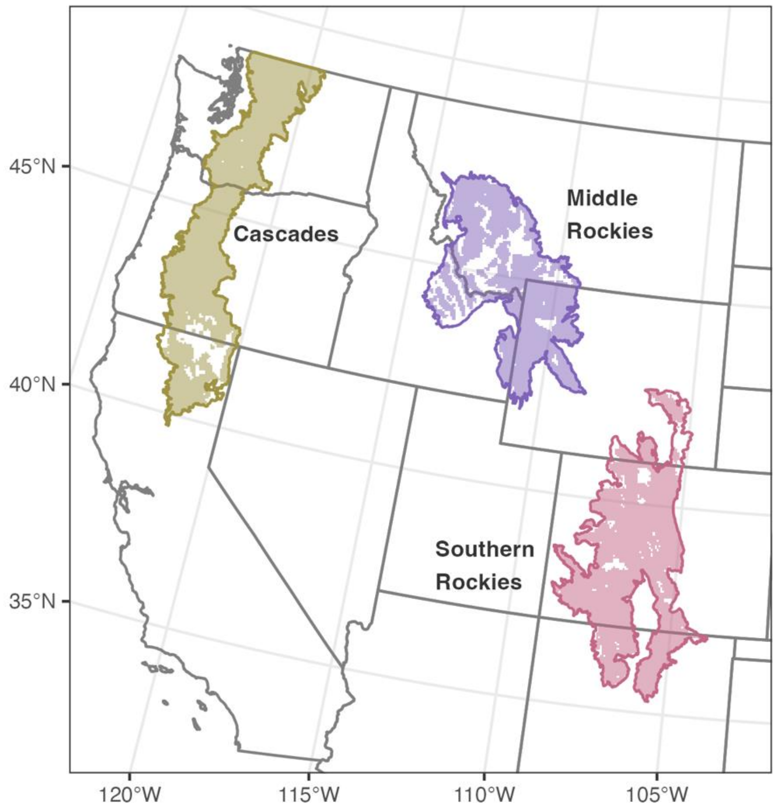

Figure 2.1. Map of study regions. Study regions include the Southern Rockies (red), Middle Rockies (purple), and Cascades (brown). Shading within each region indicates areas for which ADS-derived hotspots data were available. Dark gray lines represent US state boundaries.

The Southern Rockies region (EPA Level III Ecoregion 21; Figure 2.1) extends from 35 – 43° N and 104 – 109° W, with elevations ranging from 1,400 – 4,400 m. The Southern Rockies region has a continental climate with year-round precipitation (Beck *et al.* 2018) and forest types that vary strongly with elevation. Predominant forest types are spruce-fir (*Picea engelmannii* and *Abies lasiocarpa*) and lodgepole pine (*Pinus contorta*) at higher elevations, mixed conifer and aspen (*Populus tremuloides*) at middle elevations, and ponderosa pine (*Pinus ponderosa*) and pinyon-juniper (*Pinus edulis* and *Juniperus* spp.) at lower elevations (Peet 1978; Romme *et al.* 2009).

The Middle Rockies region (EPA Level III Ecoregion 17; Figure 2.1) extends from 42 – 47° N and 109 – 115° W, with elevations ranging from 900 – 4,200 m. The Middle Rockies region comprises the Greater Yellowstone ecosystem to the southeast, with several mountain ranges and intermontane valleys to the northwest. As with the Southern Rockies, the Middle Rockies has a continental climate with year-round precipitation (Beck *et al.* 2018) and forest types that vary along elevational gradients. The predominant forest types in the Middle Rockies are spruce-fir at higher elevations, lodgepole pine at middle elevations, and Douglas-fir (*Pseudotsuga menziesii*) at lower elevations (Marston & Anderson 1991).

The Cascades region (EPA Level III Ecoregions 4, 9, and 77; Figure 2.1) extends from 40 – 49° N and 119 – 123° W, with elevations ranging from 10 – 4,400 m. Climate is temperate west of the Cascade Crest but continental to the east, with dry summers region-wide (Beck *et al.* 2018). Vegetation types vary strongly with elevation as well as geographic position relative to the Cascade Crest, with moist forests occurring west of the Cascade Crest and dry forests to the east (Franklin & Dyrness 1973). In the western Cascades, the most prevalent forest types are mountain hemlock (*Tsuga mertensiana*) at high elevations, transitioning to Douglas-fir and western hemlock (*Tsuga heterophylla*) at lower elevations. In the eastern Cascades, high elevations are dominated by subalpine forests (characterized by spruce, fir, and pine) to the north and white fir/grand fir (*Abies concolor/Abies grandis*) to the south. Lower elevations in the eastern Cascades transition to Douglas-fir and ponderosa pine, with lodgepole pine common in central Oregon (Franklin & Dyrness 1973; Simpson 2013; Reilly *et al.* 2021).

2.3.2 *Biotic disturbance data*

Forest insect and disease impacts are mapped annually via aerial detection surveys (ADS) conducted by the USDA Forest Service, with national records of surveyed and damaged areas dating back to the late 1990s. During ADS, trained observers are flown systematically over forested areas in small aircraft; the observers delineate areas of forest damage on a map while simultaneously characterizing the type of forest damage (i.e., identifying both host tree species and disturbance agent). Studies using ground-truthing methods to quantify the uncertainty in binary (presence/absence) ADS classifications have found that ADS data are approximately 70% accurate when aggregated to 200 –

1,000 m raster cells, which is generally considered sufficient for broad-scale monitoring (Johnson & Ross 2008; Backsen & Howell 2013; Coleman *et al.* 2018).

To quantify biotic disturbance activity, we first downloaded ADS data within each of our study regions for the period 1999 – 2021 from the USDA Forest Health Protection program database (https://www.fs.usda.gov/foresthealth/applied-sciences/mapping-reporting/detection-surveys.shtml). We filtered the ADS data to include only the 16 tree-killing biotic agents that were the focus of our analysis (Table 2.1). Because damage from these agents is typically detected one year following host tree infestation or infection (when foliage of attacked trees begins to fade), we attributed ADS detections of these agents in a given year to the preceding year (i.e., detection data for the period 1999 – 2021 were attributed to the period 1998 – 2020; Meddens et al. 2012, Backsen and Howell 2013). We rasterized the ADS polygon data to 510-m cells containing binary indicators for presence or absence of each biotic disturbance agent within each cell, with zeros assigned only to those cells that were surveyed in a given year but lacked detection. All rasters were generated in the USGS Contiguous USA Albers projection using the *raster* package (Hijmans *et al.* 2022) in R (R Core Team 2022).

To quantify hotspot occurrence and prevalence, we next identified spatio-temporal overlaps in disturbance activity attributed to the 16 biotic agents of interest in our study (Table 2.1). First, we identified hotspot occurrence within 510-m cells. We defined a hotspot as any raster cell in which damage caused by $\geq$ 2 biotic agents and affecting $\geq$ 2 host tree species was detected within a three-year window, including the focal year and previous two years. We further specified that for a hotspot to be attributed to a given cell in a given focal year, at least one of the co-occurring biotic agents must have been detected within the focal year. To increase the computational efficiency of our models, we aggregated this high-resolution (510-m) raster by a factor of 10, with each aggregated 5.1-km cell expressing a binary indicator for hotspot detection in one or more subcells (i.e., hotspot occurrence) as well as a count of subcells in which hotspots were detected (i.e., hotspot prevalence). To accurately express hotspot prevalence at the 5.1-km scale as a proportion, we also quantified the number of subcells with the potential for hotspot detection. Subcells were considered to have the potential for hotspot detection if they were surveyed every year of the three-year hotspot window and were likely to contain $\geq$ 2 co-occurring potential host tree species (based on host tree data described in the following section). After accounting for the three-year hotspot detection window, our final aggregated hotspot dataset included focal years 2000 – 2020.

2.3.3 *Potential predictors of hotspots*

Forest composition was characterized using the USDA Forest Service Individual Tree Species Parameter (ITSP) database (https://www.fs.usda.gov/foresthealth/applied-sciences/mapping-reporting/indiv-tree-parameter-maps.shtml), which provides species-specific basal area rasters modeled from USFS Forest Inventory and Analysis plot data, 30-m Landsat satellite imagery, and local climate, terrain, and soils. The ITSP data are not temporally explicit (i.e., do not account for annual tree growth and mortality) but represent tree species conditions across the US in approximately 2002 (thus corresponding to the beginning of our biotic disturbance dataset) (Krist 2014). First, we downloaded all species-specific basal area rasters available for potential host tree species occurring in our study regions from the ITSP database (Appendix C, Table 2.3) and rescaled them from their native resolution of 240 m to a resolution of 510 m, corresponding to our rasterized hotspots data. We then converted these basal area rasters to presence/absence rasters for each tree species, where we defined presence as >1 m^2/ha host basal area following (Tutland *et al.* 2023). Next, we calculated total host species basal area and richness within each 510-m cell by summing all host species basal area and presence rasters, respectively. Finally, we aggregated host tree presence, basal area, and richness to a 5.1-km scale, where the prevalence of host co-occurrence was calculated as the number of subcells containing two or more host tree species, and basal area and richness were calculated as average values across those subcells containing two or more host tree species (Appendix C, Figure 2.8 – Figure 2.10).

Topographic characteristics were quantified using a 30-m resolution digital elevation model obtained from the USGS LANDFIRE database (https://landfire.gov) (Rollins 2009). Heat load index, an index of potential direct incident radiation ranging from 0 (coolest) to 1 (hottest), was calculated using the *spatialEco* package (Evans 2021) in R following (McCune & Keon 2002; McCune 2007). Topographic wetness index, an index of long-term moisture availability derived from the upslope contributing area and local water accumulation potential of a given site in a landscape, was calculated in ArcMap following (Beven & Kirkby 1979). Higher values of the topographic wetness index indicate topographically wetter areas and lower values indicate topographically drier areas. Both topographic indices were aggregated to a 5.1-km scale, corresponding to our aggregated hotspots data, by averaging all 30-m subcells (Appendix C, Figure 2.11 and Figure 2.12).

Climatic water balance data were obtained from the TerraClimate database (https://www.climatologylab.org/terraclimate.html) (Abatzoglou *et al.* 2018a). We obtained actual evapotranspiration (AET) rasters at a resolution of 1/24 degree (approximately 4 km) on a monthly time step for the period 1991 – 2020. AET represents the amount of water lost from a surface due to evaporation and transpiration and is used as a proxy for plant productivity. We summed monthly actual evapotranspiration by calendar year, averaged the annual rasters to derive 30-year climate normals, and finally rescaled them to 5.1-km cells to correspond with our aggregated hotspots data (Appendix C, Figure 2.13).

Climate and weather data were obtained from the Parameter-elevation Regressions on Independent Slopes Model (PRISM) database (http://prism.oregonstate.edu). We obtained 30-year (1991 – 2020) climate normals and annual weather values at a resolution of 1/24 degree (approximately 4 km), which we rescaled to 5.1-km cells corresponding with our aggregated hotspots data. Summer maximum vapor pressure deficit (VPD) was calculating by averaging values for June through August of a given year, and winter minimum temperature was calculated by averaging values for December of the prior year through February of the focal year. Annual weather values were converted to annual anomalies by subtracting the corresponding 30-year climate normals, and anomalies were averaged across the three-year window corresponding to the temporal window used for hotspot detection (e.g., for focal year 2007, anomalies were averaged for years 2005 – 2007; Appendix C, Figure 2.14 – Figure 2.21).

2.3.4 *Statistical analysis*

We used Bayesian spatio-temporal regression models to evaluate the relative influence of predisposing and inciting factors on hotspot occurrence and prevalence at the 5.1-km scale. The discrete response (count of subcells in which hotspots were detected) for cell location s and time t was modeled as a zero-inflated ("hurdle" model) Binomial random variable Y_{st}. The probability density function takes the following form:

$$P(Y_{st}) = \begin{cases} 1\text{-}p_{st}, & \text{if } Y_{st} = 0 \\ p_{st} \left(\frac{\text{Binomial}(Y_{st} \mid N_{st}, \pi_{st})}{1\text{-Binomial}(0 \mid N_{st}, \pi_{st})} \right), & \text{if } Y_{st} > 0 \end{cases} \tag{2.1}$$

Here, p_{st} is the probability of hotspot occurrence (i.e., hotspot detection in at least one subcell), N_{st} is the number of subcells with the potential for hotspot detection, and π_{st} is the success probability in the Binomial function used for positive counts. The probability of occurrence (Bernoulli) and positive prevalence count (Binomial) were estimated as separate processes, each linked to covariates and random effects as follows:

$$\text{logit}(p_{st}) = \gamma_t + \boldsymbol{\beta}\mathbf{X_{st}} + \epsilon_{st} \tag{2.2}$$

$$\text{logit}(\pi_{st}) = \eta_t + \boldsymbol{\theta}\mathbf{X_{st}} + \omega_{st} \tag{2.3}$$

Here, the linear predictors for occurrence and prevalence are modeled as functions of time-varying intercepts γ_t and η_t respectively, covariates $\mathbf{X_{st}}$, and spatio-temporal random effects ϵ_{st} and ω_{st}, respectively. The time-varying intercepts are modeled as year-specific random walks as follows (for γ_t, with η_t following an analogous form):

$$\gamma_t \sim \text{Normal}(\gamma_{t-1}, \sigma_\gamma) \tag{2.4}$$

The spatio-temporal random effects are modeled as stationary autoregressive Gaussian random fields as follows (for ϵ_{st}, with ω_{st} following an analogous form):

$$\epsilon_{s,t>1} = \phi\epsilon_{s,t-1} + \sqrt{1-\phi^2\delta_{st}} \tag{2.5}$$

$$\epsilon_{s,t=1} \sim \text{MVN}(0, \boldsymbol{\Sigma_\delta}) \tag{2.6}$$

$$\delta_{st} \sim \text{MVN}(0, \boldsymbol{\Sigma_\delta}) \tag{2.7}$$

Here, ϕ ($0 < \phi < 1$) is the temporal autoregression parameter for the Gaussian random field. The spatial covariance matrix $\boldsymbol{\Sigma_\delta}$ is modeled using a Matérn covariance function parameterized by marginal standard deviation σ_δ and practical range r (the distance at which the spatial correlation drops to approximately 0.1) (Lindgren *et al.* 2011).

We fit these spatio-temporal models in a Bayesian framework using the Integrated Nested Laplace Approximation (INLA) and Stochastic Partial Differential Equation (SPDE) approaches (Lindgren *et al.* 2011; Blangiardo & Cameletti 2015) (Appendix D, Figure 2.22 – Figure 2.24). We used penalized complexity priors for the marginal standard deviations and practical ranges of the Gaussian random fields to avoid spatial overfitting (Fuglstad *et al.* 2019). We used uninformative priors for all other parameters (Krainski *et al.* 2019). Both the INLA and SPDE approaches were implemented using the *R-INLA* package (www.r-inla.org) in R.

We fit models using only data from those 5.1-km cells within which $\geq$25% of subcells had the potential for hotspot detection (i.e., $\geq$25% of subcells both [a] contained $\geq$2 host tree species and [b] were surveyed each year of the three-year hotspot detection window). All potential predictor variables (i.e., predisposing and inciting factors), with the exception of the prevalence of host co-occurrence, were included as covariates in both the Bernoulli model of hotspot occurrence and Binomial model of hotspot prevalence. The prevalence of host co-occurrence is in many cases equal to N_{st}, the number of subcells with the potential for hotspot detection (though the two are not always equal, with N_{st} accounting not only for host co-occurrence but also for whether each subcell was surveyed each year). Since N_{st} is explicitly included in our Binomial model of hotspot prevalence, we excluded the prevalence of host co-occurrence as a covariate in that model.

To enable comparison of the magnitude of coefficients within each model, we standardized all covariates within each regional dataset by subtracting their means and dividing by their standard deviations. A covariate was considered a statistically important predictor if the 95% credible interval for the coefficient did not include zero. Because we expected the effects of inciting factors (i.e., annual weather anomalies) might vary with predisposing climate, we considered interaction terms between weather anomalies and their corresponding climate normals. To limit the overall number of statistical tests, we added interaction terms to each model only if they were statistically important predictors (i.e., 95% credible interval for the interaction term did not include zero) and they improved model fit (i.e., decreased model Deviance Information Criterion [DIC] by > 10). We calculated randomized quantile residuals for our zero-inflated Binomial models following (Bai *et al.* 2021) and validated each model using standard regression diagnostics. We evaluated residual spatio-temporal autocorrelation using Moran's I (Cliff & Ord 1981) and empirical variograms calculated using the *gstat* package in R (Pebesma 2004).

2.4 RESULTS

2.4.1 *Observed hotspots*

Hotspot occurrence and prevalence varied both spatially and temporally within each study region (Figure 2.2 – Figure 2.4). Across all 5.1-km cells with the potential for hotspot detection, annual rates of hotspot occurrence ranged from 3 – 38% in the Southern Rockies, from <1 – 49% in the Middle Rockies, and from 10 – 28% in the Cascades (Figure 2.2 – Figure 2.4). Within those 5.1-km cells in which hotspot occurrence was detected, average annual hotspot prevalence ranged from 3 – 14% in the Southern Rockies, from 2 – 15% in the Middle Rockies, and from 5 – 16% in the Cascades (Figure 2.2 – Figure 2.4). In both the Southern Rockies and Middle Rockies, hotspot occurrence and prevalence peaked between the years of 2003 and 2008, whereas occurrence and prevalence in the Cascades peaked around 2009 and again from 2014 – 2017 (Figure 2.2 – Figure 2.4).

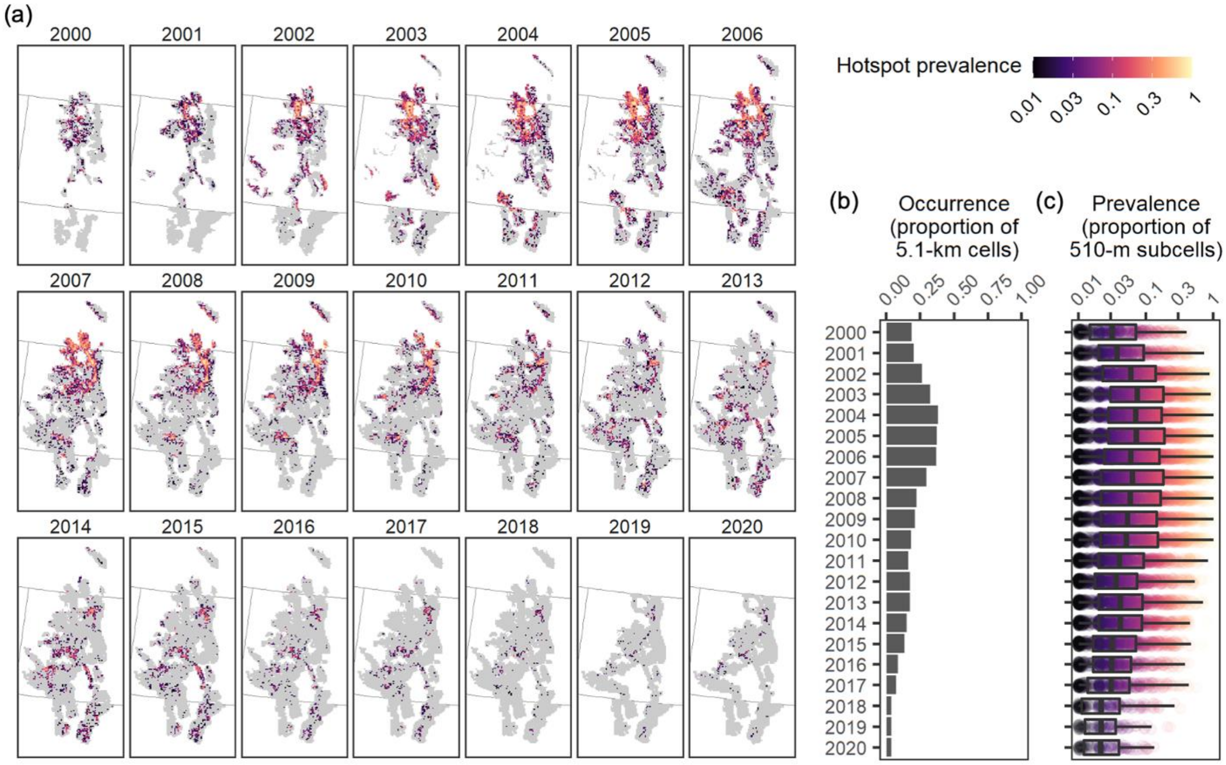

Figure 2.2. Southern Rockies observed hotspots data. (a) Observed spatio-temporal patterns of hotspot occurrence and prevalence within 5.1-km cells with the potential for hotspot detection. Surveyed 5.1-km cells in which zero hotspots were detected are shown in light gray; for those cells where ≥1 hotspots were detected, hotspot prevalence is expressed as a proportion of those 510-m subcells with the potential for hotspot detection. (b) Observed temporal patterns of hotspot occurrence. (c) Observed temporal patterns of hotspot prevalence within those 5.1-km cells where ≥1 hotspots were detected. Note the log-transformed scales in (a) and (c).

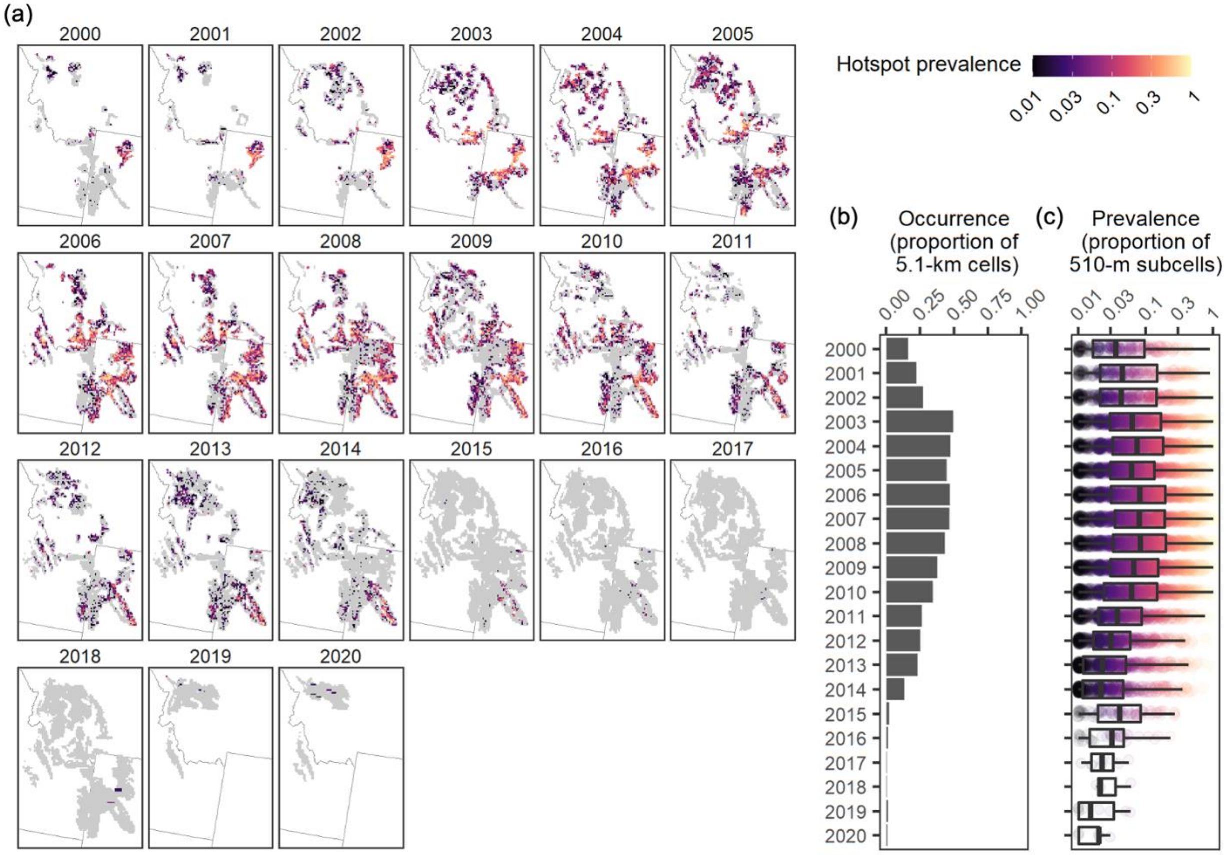

Figure 2.3. Middle Rockies observed hotspots data. Panels are described in Figure 2.2.

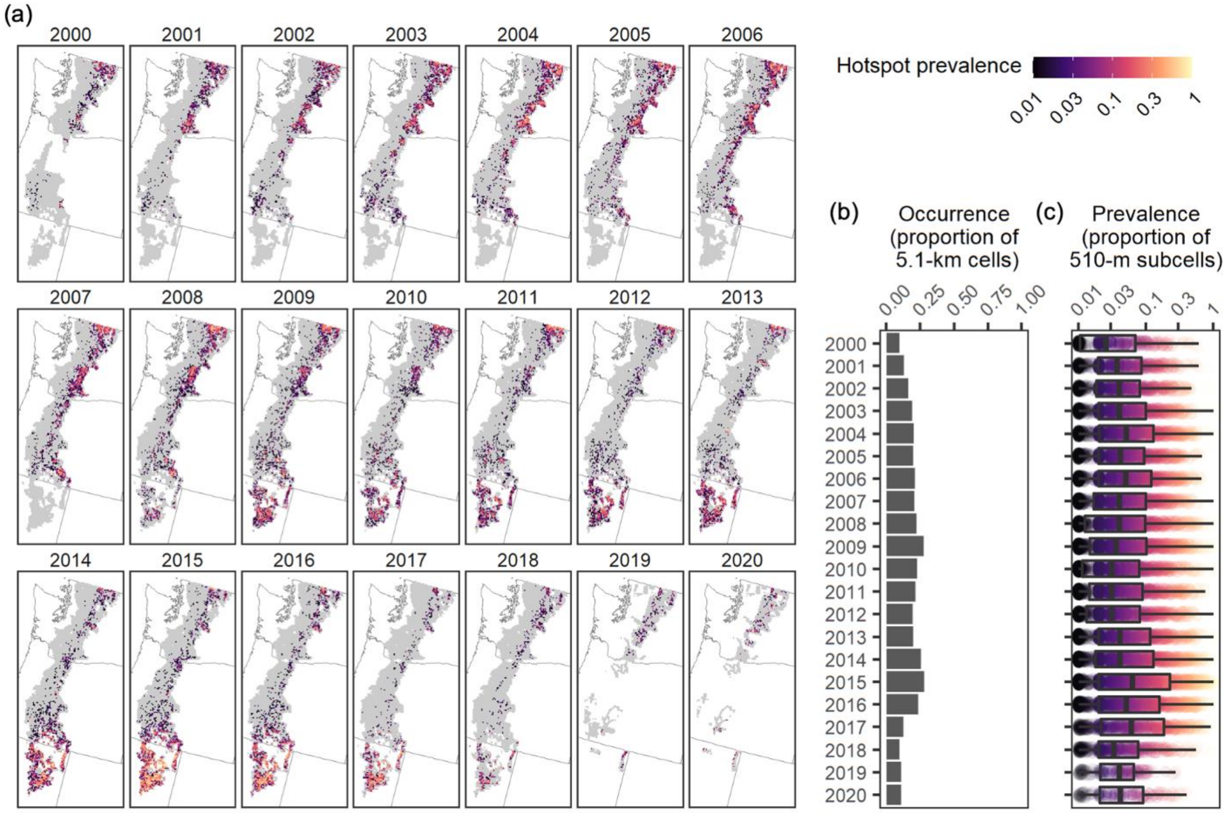

Figure 2.4. Cascades observed hotspots data. Panels are described in Figure 2.2.

The individual biotic agents contributing to hotspot occurrence varied by region. In the Southern Rockies, mountain pine beetle, subalpine fir mortality, and spruce beetle were the most prevalent individual agents contributing to hotspot occurrence; at the 510-m scale, mountain pine beetle was detected in 49% of hotspots, while subalpine fir mortality and spruce beetle were detected in 28% and 27% of hotspots, respectively (Figure 2.5). In the Middle Rockies, mountain pine beetle, five-needle pine decline, and subalpine fir mortality were the most prevalent individual agents, being detected in 67%, 21%, and 19% of hotspots, respectively (Figure 2.5). In the Cascades, fir engraver, mountain pine beetle, and western pine beetle were most prevalent and were detected in 53%, 41%, and 23% of hotspots, respectively (Figure 2.5).

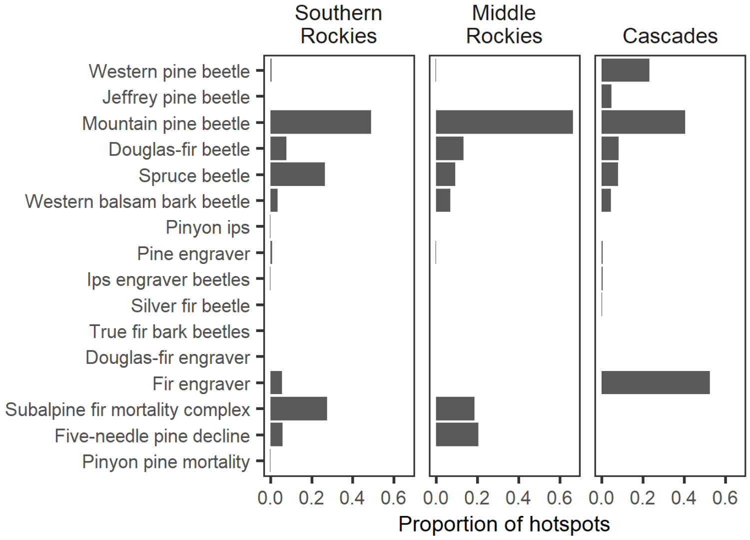

Figure 2.5. Contribution of individual biotic agents to observed hotspots. Contributions are quantified as proportions of observed 510-m hotspots in which each biotic agent was detected.

2.4.2 *Effects of predisposing and inciting factors*

Hotspot occurrence and prevalence were affected by each of the predisposing factors considered in our analysis, with the strength and direction of effects varying by region (Figure 2.6; Appendix D, Table 2.4 – Table 2.6). Forest composition had the strongest and most consistent effects on hotspot occurrence and prevalence; across study regions, hotspot occurrence consistently increased with host co-occurrence, and hotspot occurrence and prevalence both consistently increased with host basal area and richness (Figure 2.6). Hotspot occurrence and prevalence decreased with long-term summer maximum VPD normal as well as topographic heat load index across all regions, though the magnitude of the effect of topographic heat load was small (Figure 2.6).

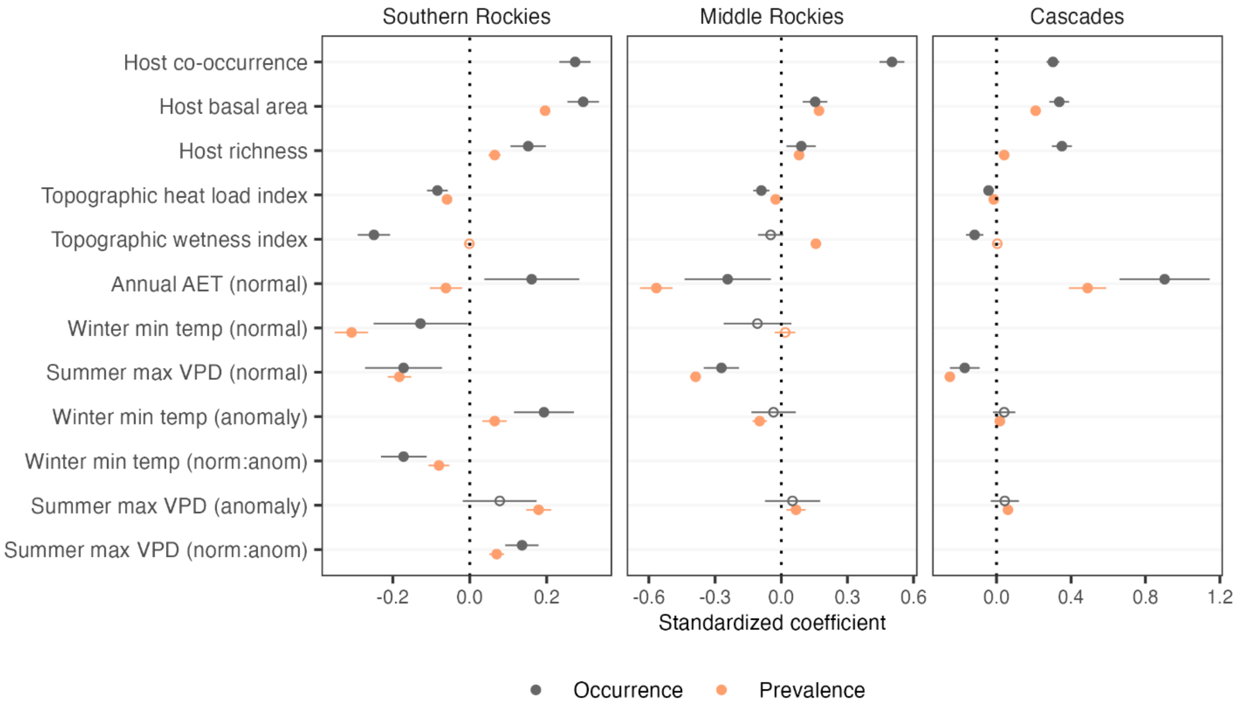

Figure 2.6. Effects of covariates on hotspot occurrence and prevalence. Dots represent posterior means and horizontal lines represent 95% credible intervals. Closed circles represent statistically important predictors and open circles represent predictors that are not statistically important. Blank spaces indicate covariates not evaluated in a particular model. The effects for each predictor are per one standard deviation within each region-specific dataset.

All other predisposing factors considered in our analysis had variable effects across regions. Hotspot occurrence decreased with topographic wetness index in the Southern Rockies and Cascades, whereas hotspot prevalence increased with topographic wetness index in the Middle Rockies. Hotspots decreased with long-term annual AET normals in the Middle Rockies but strongly increased with AET normals in the Cascades; in the Southern Rockies, effects of AET were mixed, with hotspot occurrence increasing but hotspot prevalence decreasing with AET (Figure 2.6). Finally, hotspot occurrence and prevalence decreased with long-term winter minimum temperature normals in the Southern Rockies, whereas winter temperature normals had no detectable effect in the Middle Rockies (Figure 2.6). Winter temperature normals could not be included in the models for the Cascades due to collinearity with AET (Figure 2.6).

Across study regions, inciting factors appeared to have the strongest effects in the Southern Rockies (Figure 2.6). Hotspot occurrence and prevalence increased with winter minimum temperature anomalies in the Southern Rockies, with the positive effect of these anomalies weakening with increasing winter minimum temperature normals (Figure 2.6). Similarly, hotspot prevalence increased with summer maximum VPD anomalies in the Southern Rockies, with the positive effect of these anomalies strengthening with increasing summer maximum VPD normals (Figure 2.6). We detected no effect of inciting factors on hotspot occurrence in either the Middle Rockies or Cascades (Figure 2.6). Hotspot prevalence decreased with winter minimum temperature anomalies in the Middle Rockies, increased with winter minimum temperature anomalies in the Cascades, and increased with summer maximum VPD anomalies in both regions, though the magnitudes of these effects were all modest (Figure 2.6).

2.4.3 *Spatio-temporal random effects*

Compared to the fixed effects estimated in our models, the temporal and spatio-temporal random effects were greater in magnitude and more closely correlated with model-predicted hotspot occurrence and prevalence (Figure 2.7; Appendix D, Figure 2.28 – Figure 2.36). Odds ratios associated with a one standard deviation increase in estimated random effects ranged from 11.3 – 30.1 for hotspot occurrence and from 2.7 – 3.8 for prevalence (Appendix D, Table 2.7). In contrast, odds ratios associated with a one standard deviation increase in estimated fixed effects only ranged from 2.3 – 4.5 for hotspot occurrence and from 1.8 – 2.2 for prevalence (Appendix D, Table 2.7). Overall, odds ratios for random effects were 1.5 – 13.1 times greater than those for corresponding fixed effects (Appendix D, Table 2.7).

The temporal and spatio-temporal random effects estimated in our models reflect the distinct patterns and trends in hotspots across our study regions (Appendix D, Figure 2.25 – Figure 2.33). Peaks in the time-varying random intercepts largely corresponded with peaks in the observed hotspots data (Appendix D, Figure 2.25 – Figure 2.27). The estimated practical range r (distance at which spatial correlation drops close to zero) varied from 55 – 85 km across regions for hotspot occurrence and from 35 – 40 km across regions for hotspot prevalence (Appendix D, Table 2.4 – Table 2.6). Spatial patterns of hotspots were strongly persistent from year to year, with the temporal autoregression parameter ϕ for the spatial random fields varying from 0.88 – 0.93 across all models (Appendix D, Table 2.4 – Table 2.6). Tests of the model residuals confirmed that that the random effects estimated in our models appropriately addressed potential biases associated with spatial and temporal autocorrelation.

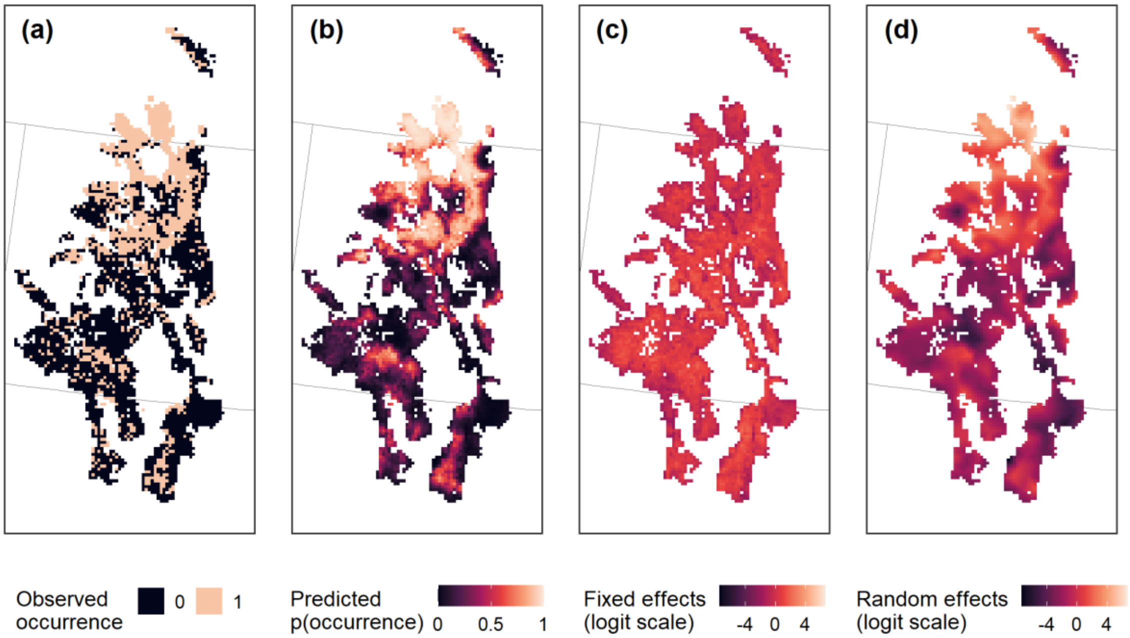

Figure 2.7. Comparison of (a) observed hotspot occurrence, (b) predicted probability of hotspot occurrence, (c) fixed effects of all covariates, and (d) random temporal and spatio-temporal effects. Hotspot occurrence in the Southern Rockies in 2007 is shown here as a representative example.

2.5 DISCUSSION

Using a spatio-temporal modeling approach, our study elucidates the patterns, trends, and drivers of biotic disturbance hotspots across three broad forested regions in the western US. We found that biotic disturbance hotspots occurred widely throughout the western US in the early part of the 21st century (2000 – 2020), with distinct spatio-temporal patterns characterizing each of our study regions. Predisposing and inciting factors both contributed to hotspot occurrence, with forest composition and structure being consistent drivers and other effects varying with the unique biophysical context of each region. Relative to the predictor variables included in our analysis, we found that random spatio-temporal effects estimated in our models were stronger and more closely correlated with hotspot predictions, suggesting that outbreak contagion and other dynamic factors strongly shape patterns of biotic disturbance hotspots. These findings provide a deeper understanding of interacting biotic disturbance agents in the western US during a period when climate and biotic disturbance regimes are both changing.

2.5.1 *Hotspots occur widely and have implications for forest resilience*

Our findings illustrate the widespread extent of biotic disturbance hotspot occurrence across the western US, carrying important implications for forest resilience in a period of increasing biotic disturbance activity. Biotic disturbance hotspots have recently been identified as an emerging ecological phenomenon (Harvey *et al.* In press), and this study provides a foundational understanding of the spatial and temporal patterns of hotspots across the western US in recent decades. While interannual trends varied regionally, each of our study regions experienced years in which hotspots were detected within ≥28% of 5.1-km cells with the potential for hotspot occurrence, with annual occurrence rates as high as 49% observed in the Middle Rockies. Forest disturbances caused by a single host-specific biotic agent are often followed by robust compensatory responses facilitated by increased growth rates of surviving non-host trees (Veblen *et al.* 1991), as shown in Chapter 1. These compensatory responses, which underpin forest recovery and continuity in forest function (Romme *et al.* 1986), serve as important mechanisms of forest resilience. In forests affected by biotic disturbance hotspots, however, these compensatory responses have the potential to be eroded due to the synchronous mortality of multiple host tree species. Compared to forest disturbances caused by single biotic agents, overall tree mortality may not necessarily be more severe in areas affected by hotspots (Tutland *et al.* 2023); however, the mechanisms and rates of forest recovery are likely to be altered (Harvey *et al.* In press). The widespread nature of biotic disturbance hotspots in the western US therefore has important implications for forest resilience as climate continues to change and biotic disturbance activity continues to increase.

2.5.2 *Forest composition and structure are consistent drivers of biotic disturbance hotspots, while other factors vary with biophysical context*

Biotic disturbance hotspots are strongly and consistently driven by the abundance, richness, and spatial distributions of host trees. Even after constraining our analysis to those areas where hotspots could potentially be detected (i.e., surveyed areas where two or more potential host tree species were likely to be present), we found that hotspot occurrence and prevalence increased with host basal area and richness, suggesting forested areas characterized by high tree species diversity and host biomass are most susceptible to biotic disturbance hotspots. Individually, biotic agents are most likely to occur where host tree basal area is high (Shore *et al.* 2000; Fettig *et al.* 2007), and it therefore follows that the likelihood of overlapping biotic agents is greatest where multiple host species co-occur and host basal area is high. Given that forest types vary strongly along elevational gradients in each of our study regions, our finding that hotspots varied with climate normals also likely reflects the climate niches of host tree species and thus the influence of host tree species distributions on hotspot occurrence. For example, the most prevalent biotic agents contributing to hotspot occurrence in our study regions were those known to attack pine, fir, and spruce trees (Table 2.1, Figure 2.5), which largely tend to co-occur at higher elevations in each of our study regions. Because summer maximum VPD and winter minimum temperature both increase with decreasing elevation in our study regions, the negative effects of these two climate normals on hotspots in our study could be attributed to the decreasing likelihood of pine/spruce/fir overlap at lower elevations.

The variable effects of other predisposing and inciting factors considered in our analysis reflect the unique biophysical characteristics of each study region. For example, our finding that annual AET (a proxy for plant productivity) had variable effects on hotspots across study regions likely stem from the differing levels of productivity that characterize each region. The western Cascades are known to be some of the most productive forest ecosystems in the world (Waring & Franklin 1979; Spies *et al.* 2018), and along a gradient of increasing annual AET and host basal area, the Middle Rockies fall at the lower end, with the Southern Rockies being somewhat higher and the Cascades being highest overall (Appendix C, Figure 2.9 and Figure 2.13). Given this range, it is possible that the differing effects of AET observed in our study are related to the complex growth-defense tradeoffs that can occur in host trees (Kane & Kolb 2010; Vázquez-González *et al.* 2020). Since tree-killing bark beetles prefer hosts with thick phloem (Amman 1969), high growth rates may increase infestation probability (Cooper *et al.* 2018; Buonanduci *et al.* 2020) in areas where productivity is generally high. Conversely, in areas where productivity is generally more limited, growth-defense tradeoffs may be amplified (Vázquez-González *et al.* 2020), and host trees may allocate more resources to defense rather than growth. This tradeoff could potentially explain the positive association between annual AET and hotspots that we observed in the Cascades, a highly productive region, versus the negative and mixed associations observed in the Middle and Southern Rockies regions.

Similarly, our finding that inciting factors (i.e., annual weather anomalies) were most important for predicting hotspots in the Southern Rockies likely stems from the unique climate conditions characterizing our study regions. For example, winter minimum temperatures are generally lowest in the Middle Rockies, higher in the Southern Rockies, and highest in the Cascades (Appendix C, Figure 2.15). Concurrently, overwinter survival probability for mountain pine beetle is generally low in the Middle Rockies and high in the Cascades, with the Southern Rockies falling in-between (Bentz *et al.* 2010). Annual weather anomalies are likely to have a greater influence on biotic disturbance activity in areas where climate straddles important temperature thresholds for bark beetle survival and reproduction (Raffa *et al.* 2008; Bentz *et al.* 2010). Thus, it is possible that weather anomalies could be more likely to incite hotspot occurrence in the Southern Rockies where climate conditions suitable to bark beetle outbreak fall within an intermediate range and where proximity to temperature thresholds is therefore important.

2.5.3 *Stochasticity, contagion, and other dynamic factors play an important role in shaping biotic disturbance hotspots*

The temporal and spatio-temporal random effects estimated in our models contributed more strongly to model predictions than fixed effects and closely mirrored observed hotspot patterns and trends, suggesting that stochasticity, contagion, and other dynamic factors play an important role in shaping biotic disturbance hotspots. Biotic disturbances are contagious processes, with local and regional population pressure of biotic agents strongly shaping the dynamics of bark beetle and plant pathogen outbreaks (Raffa *et al.* 2008; Linnakoski *et al.* 2019; Howe *et al.* 2021). The strong spatio-temporal correlation in our dataset and high year-to-year persistence of hotspots suggest that biotic disturbance hotspots can be considered contagious processes as well. We found that temporal and spatio-temporal random effects were more closely correlated with hotspot occurrence and prevalence than the covariates included in our models, suggesting that the strongest predictor of hotspot occurrence at any given location and time is whether other hotspots occurred nearby or in a previous year.

Each of our study regions was affected by large-scale, synchronous bark beetle outbreaks during our study period (2000 – 2020), likely contributing to the patterns and trends in hotspots that we observed. In particular, regional outbreaks of mountain pine beetle have been well-documented across the western US in the early part of the 21st century (Raffa *et al.* 2008; Chapman *et al.* 2012; Preisler *et al.* 2012), and mountain pine beetle was a primary contributor to hotspot occurrence across our study regions. The temporal trends estimated in our models, particularly the peaks in hotspots occurring from 2003 – 2008 in the Southern and Middle Rockies (Appendix D, Figure 2.25 – Figure 2.27), mirror the rapid growth followed by decline in mountain pine beetle populations observed in these regions (Chapman *et al.* 2012; Meddens *et al.* 2012). Rapid depletion of available live host biomass often plays a critical role in ending regional-scale outbreaks (Raffa *et al.* 2008), as sufficient live host trees are necessary to sustain bark beetle and pathogen populations. Because species-specific and temporally explicit tree biomass estimates are not currently available at the spatial extents modeled in our study, we were only able to include one static estimate of host tree basal area in our models. Thus, while we could not explicitly capture the loss in live host biomass caused by regional-scale outbreak activity with our predictor variables, the random effects estimated in our models effectively capture these trends.

2.5.4 *Study limitations and directions for future research*

Despite efforts to standardize data collection across personnel and USDA Forest Service regions (McConnell *et al.* 2000), aerial sketchmapping is inherently subjective in nature (Johnson & Wittwer 2008). Error in ADS data may stem from a number of factors, including (a) measurement accuracy varying with the skill and experience of the observer, (b) surveys varying in the number of observers present and the flight paths flown (e.g., flights following ridge or drainage contours versus flights flown in a grid), and (c) variable survey conditions (e.g., turbulence, weather, ambient lighting) (McConnell *et al.* 2000; Johnson & Ross 2008; Backsen & Howell 2013). Further, data collected during ADS sketchmapping may be biased because surveys are conducted somewhat preferentially, with areas known or suspected to be impacted prioritized for survey. Due to this somewhat preferential sampling, it is possible that our observed rates of hotspot occurrence may be biased high in some years. Semi-automated satellite remote sensing approaches offer an improvement over ADS data in terms of their spatio-temporal coverage and resolution (Rodman *et al.* 2021). However, such approaches are unable to capture the identities of individual biotic agents and are therefore less useful in identifying biotic disturbance hotspots. Despite their limitations, ADS data offer sufficient accuracy at broad scales and remain the best available option for monitoring interactions among biotic disturbance agents across regional extents.

We took a broad approach in our analysis, lumping numerous tree-killing biotic agents and host tree species. By design, our results reflect the patterns and drivers of biotic disturbance hotspots generally, rather than specific combinations of biotic agents. Some biotic disturbance agents may be more likely to co-occur in space and time (e.g., agents targeting commonly co-occurring host trees and responding to similar environmental conditions), while others may be less likely to co-occur (e.g., agents targeting less commonly co-occurring host trees, responding to different environmental conditions, and/or functioning as competitors). Therefore, further research should focus on specific combinations of biotic agents that may be of interest. Additionally, we focused on synchronous co-occurrence of agents that are not expected to be mechanistically linked. Future research should also focus on temporally lagged hotspots that may be occurring due to either expected or novel mechanistic links (Harvey *et al.* In press).

2.6 APPENDIX C: COVARIATES INCLUDED IN MODELING

Table 2.3. Potential host tree species available through the USDA Forest Service Individual Tree Species Parameter (ITSP) database and included in the calculation of host species co-occurrence, basal area, and richness.

Common name	Genus	Species	Present in region		
			Southern Rockies	Middle Rockies	Cascades
Pacific silver fir	*Abies*	*amabilis*			✓
White fir	*Abies*	*concolor*	✓	✓	✓
Grand fir	*Abies*	*grandis*		✓	✓
Subalpine fir	*Abies*	*lasiocarpa*	✓	✓	✓
California red fir	*Abies*	*magnifica*			✓
Fir spp. (other)	*Abies*	spp.			✓
Engelmann spruce	*Picea*	*engelmannii*	✓	✓	✓
Spruce spp. (other)	*Picea*	spp.	✓	✓	✓
Whitebark pine	*Pinus*	*albicaulis*	✓	✓	✓
Rocky Mountain bristlecone pine	*Pinus*	*aristata*	✓		
Lodgepole pine	*Pinus*	*contorta*	✓	✓	✓
Limber pine	*Pinus*	*flexilis*	✓	✓	
Southwestern white pine	*Pinus*	*strobiformis*	✓		
Jeffrey pine	*Pinus*	*jeffreyi*			✓
Sugar pine	*Pinus*	*lambertiana*			✓
Western white pine	*Pinus*	*monticola*		✓	✓
Ponderosa pine	*Pinus*	*ponderosa*	✓	✓	✓
Pinyon spp.	*Pinus*	spp.	✓	✓	✓
Douglas-fir	*Pseudotsuga*	*menziesii*	✓	✓	✓
Western hemlock	*Tsuga*	*heterophylla*		✓	✓
Mountain hemlock	*Tsuga*	*mertensiana*		✓	✓

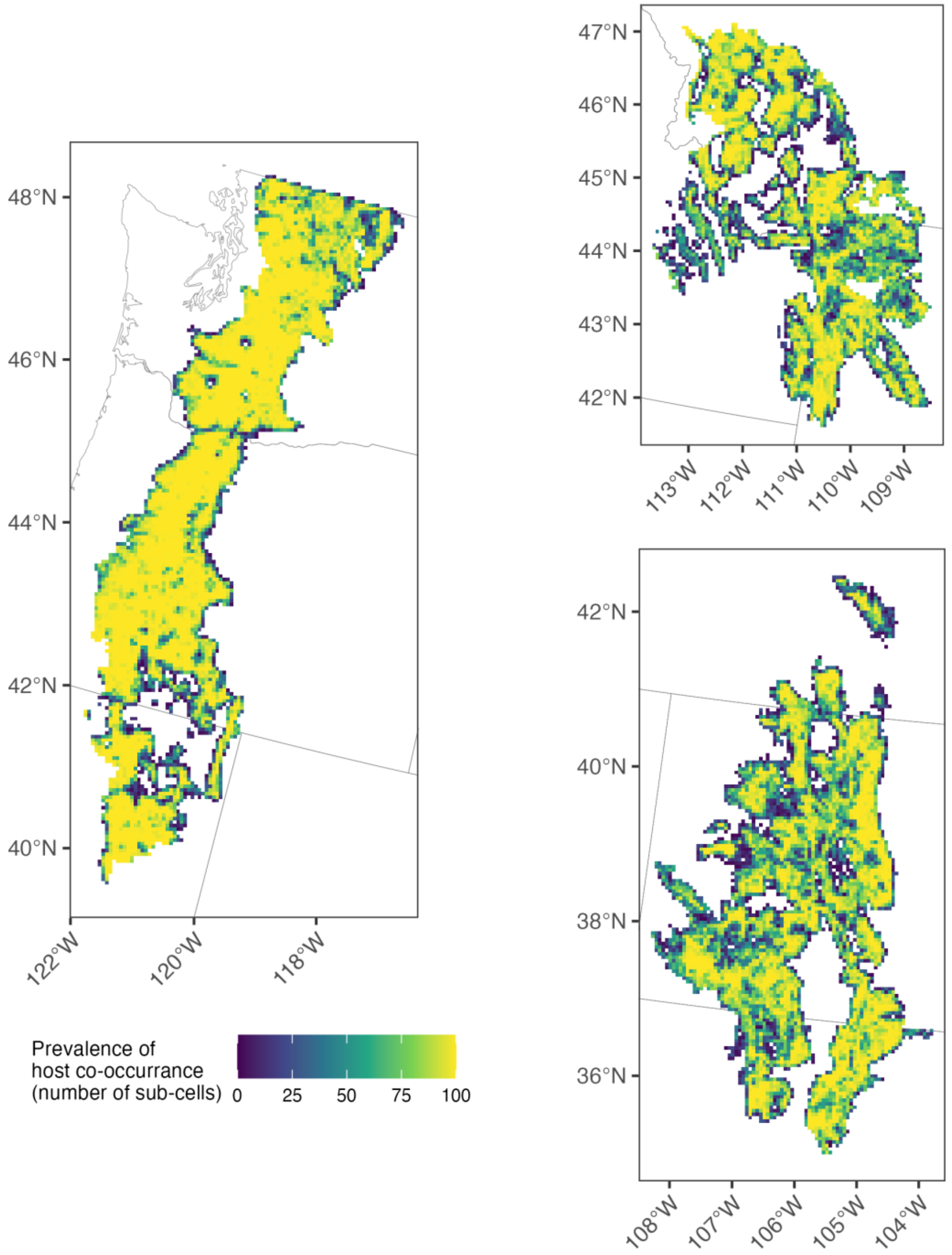

Figure 2.8. Prevalence of host co-occurrence within each study region. Prevalence of host co-occurrence is plotted at the 5.1-km scale and calculated as the number of 510-m subcells containing ≥2 potential host tree species.

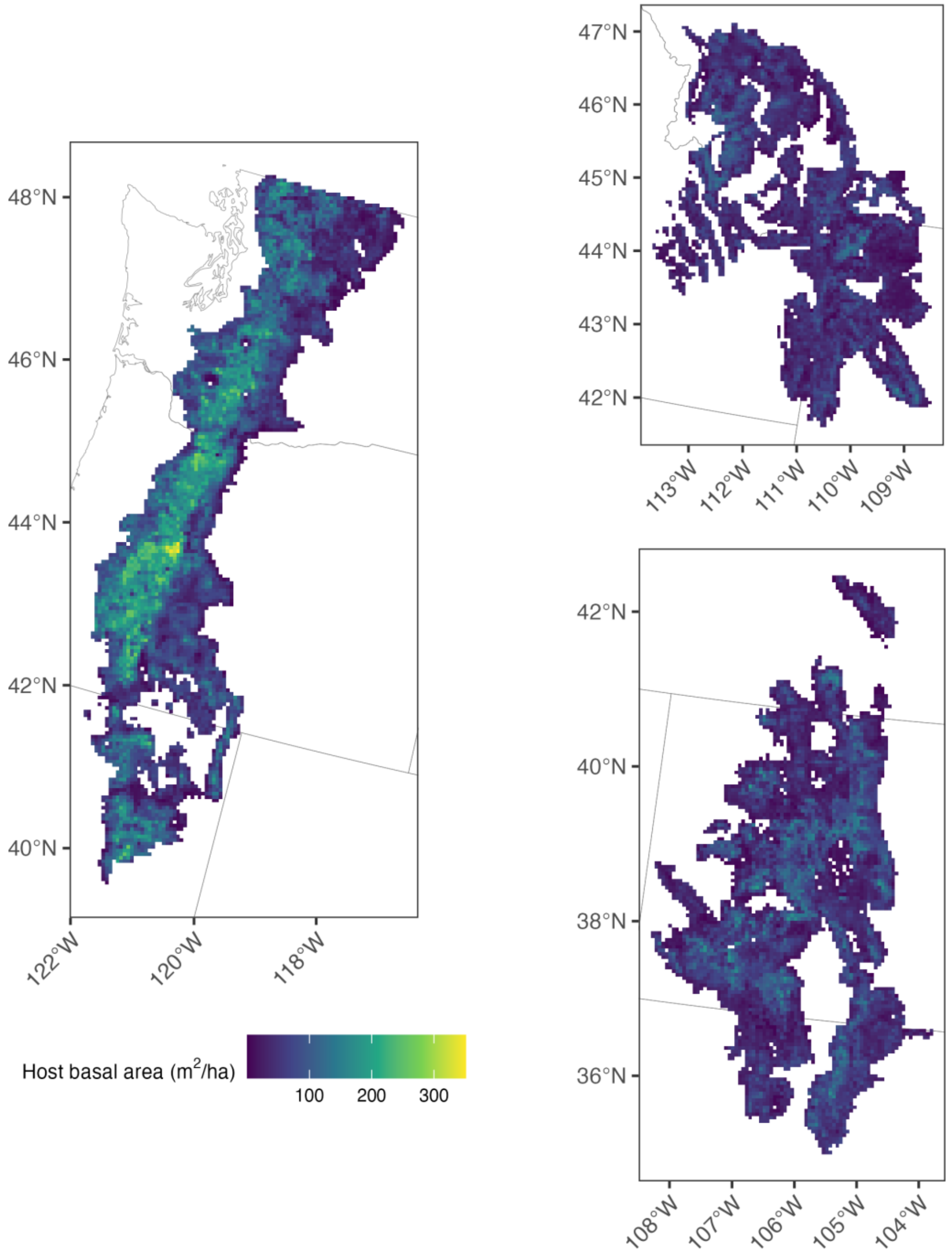

Figure 2.9. Host tree basal area within each study region. Host basal area is plotted at the 5.1-km scale and calculated as the average total host species basal area within 510-m subcells containing ≥2 potential host tree species.

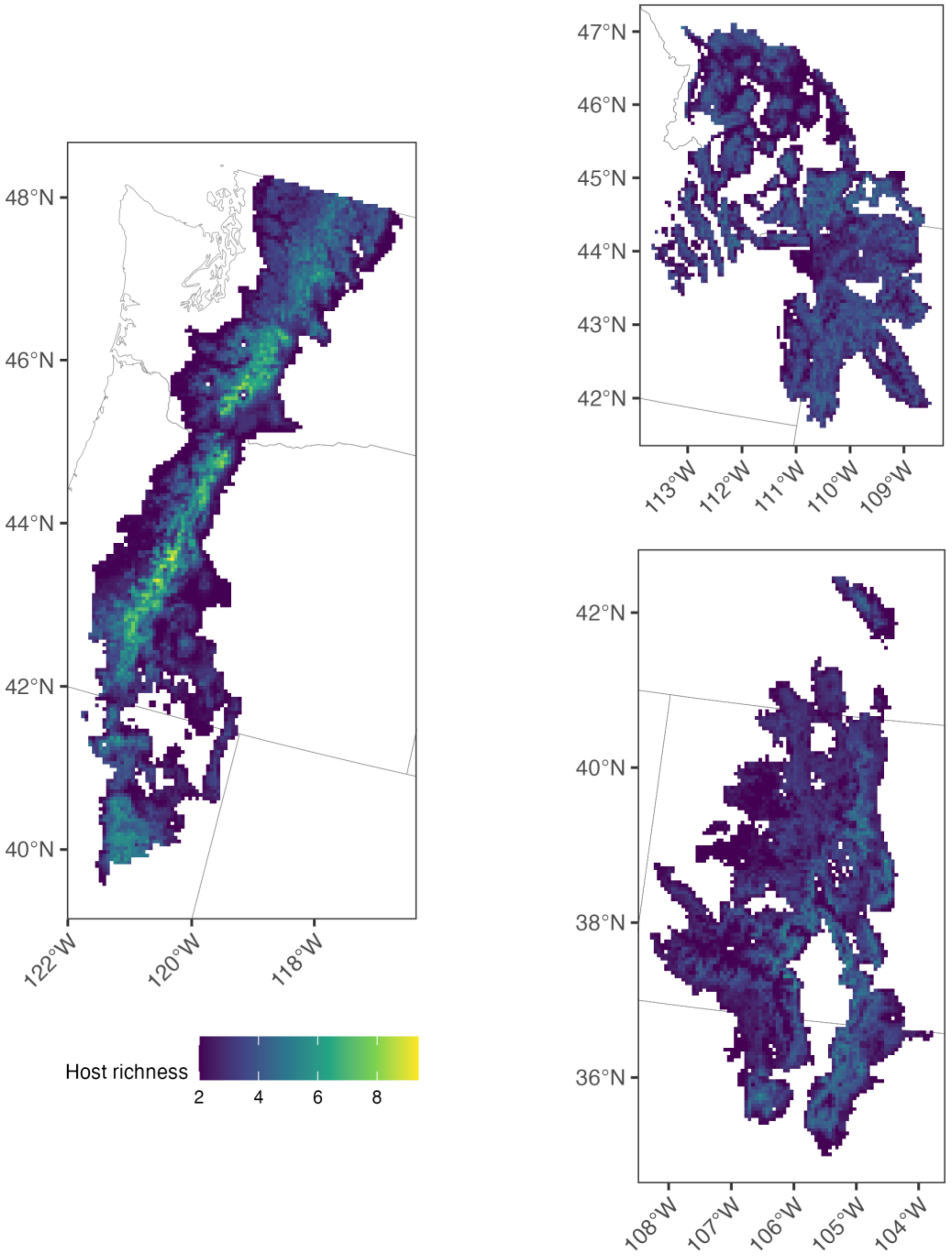

Figure 2.10. Host tree species richness within each study region. Host richness is plotted at the 5.1-km scale and calculated as the average host species richness within 510-m subcells containing ≥2 potential host tree species.

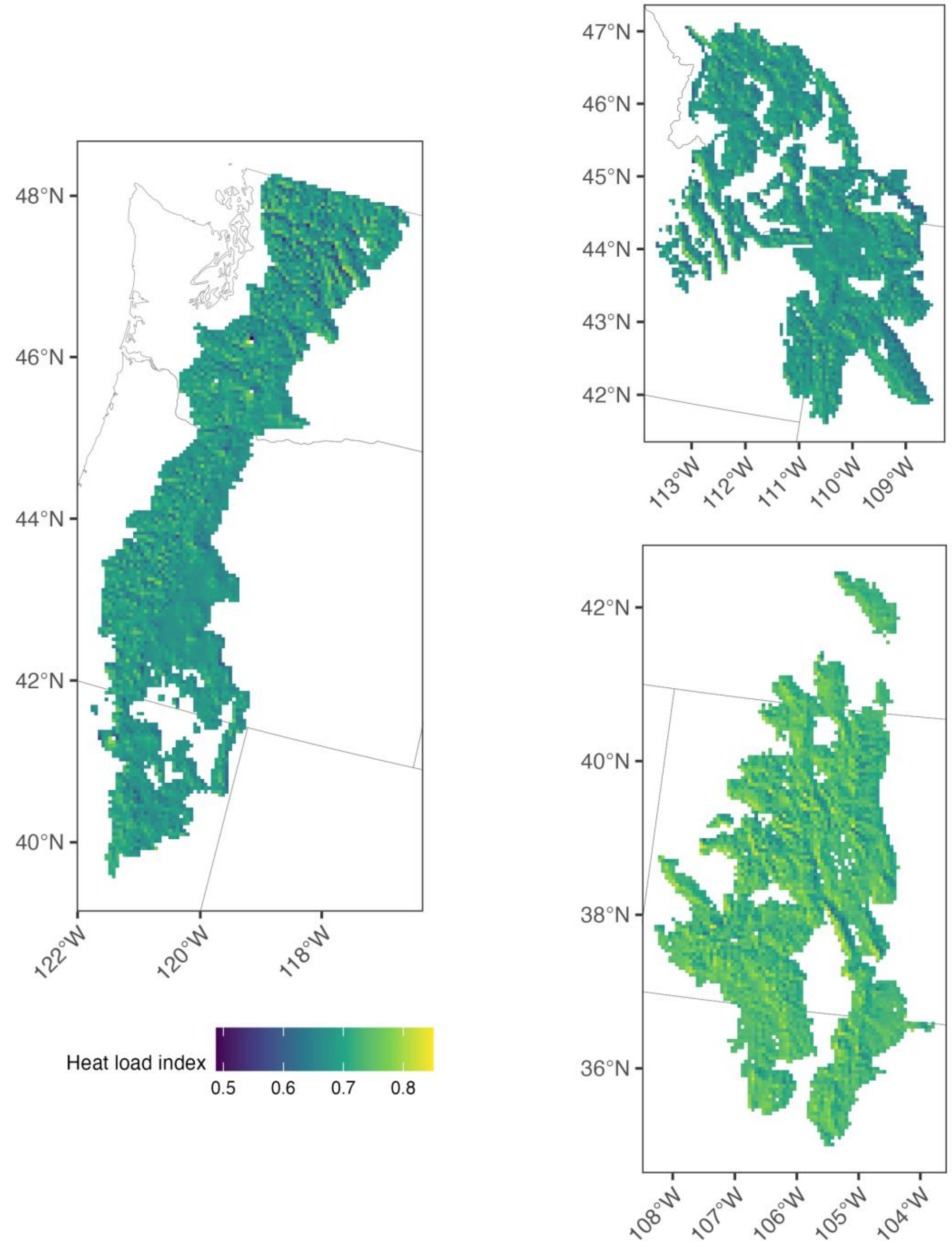

Figure 2.11. Topographic heat load index within each study region.

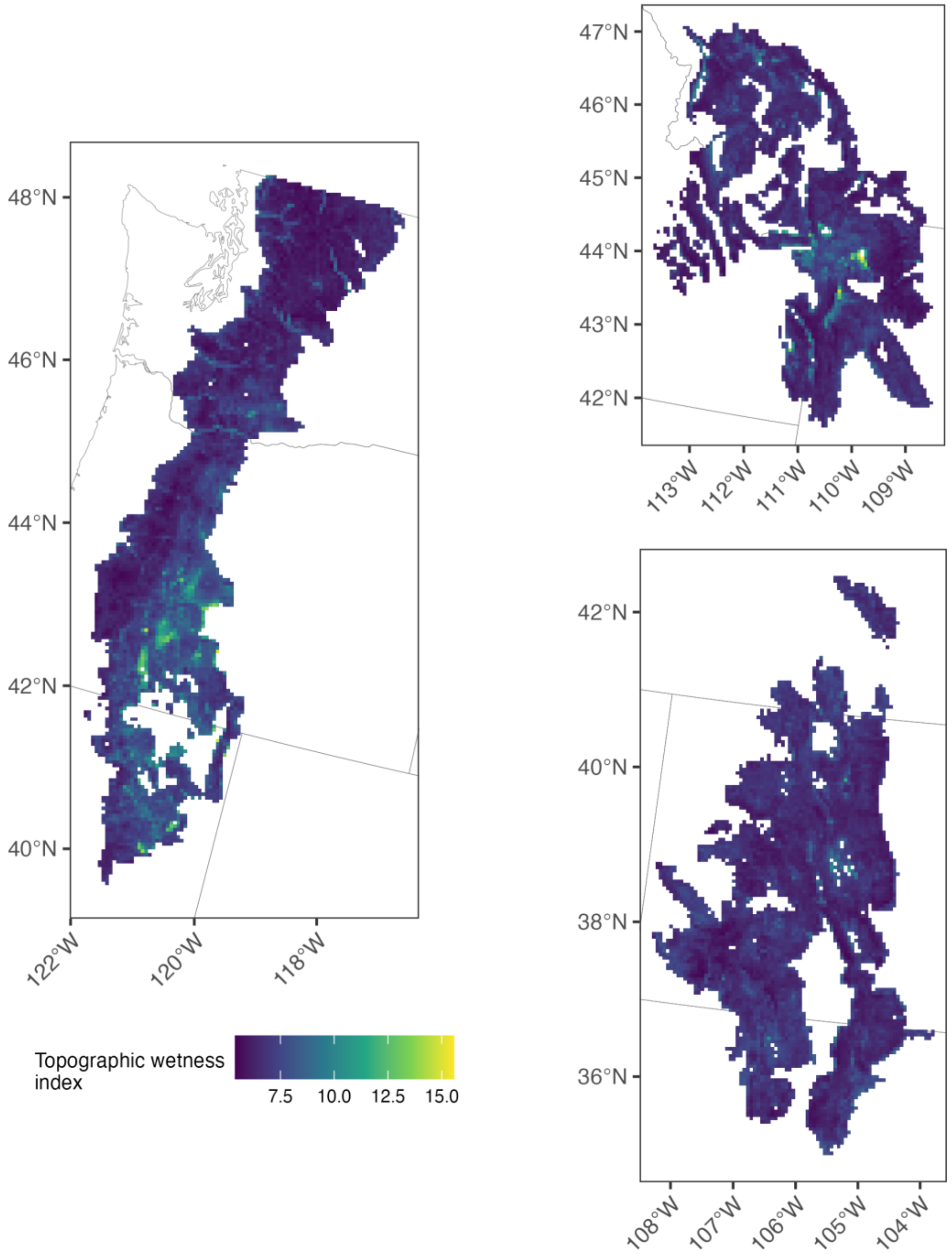

Figure 2.12. Topographic wetness index within each study region.

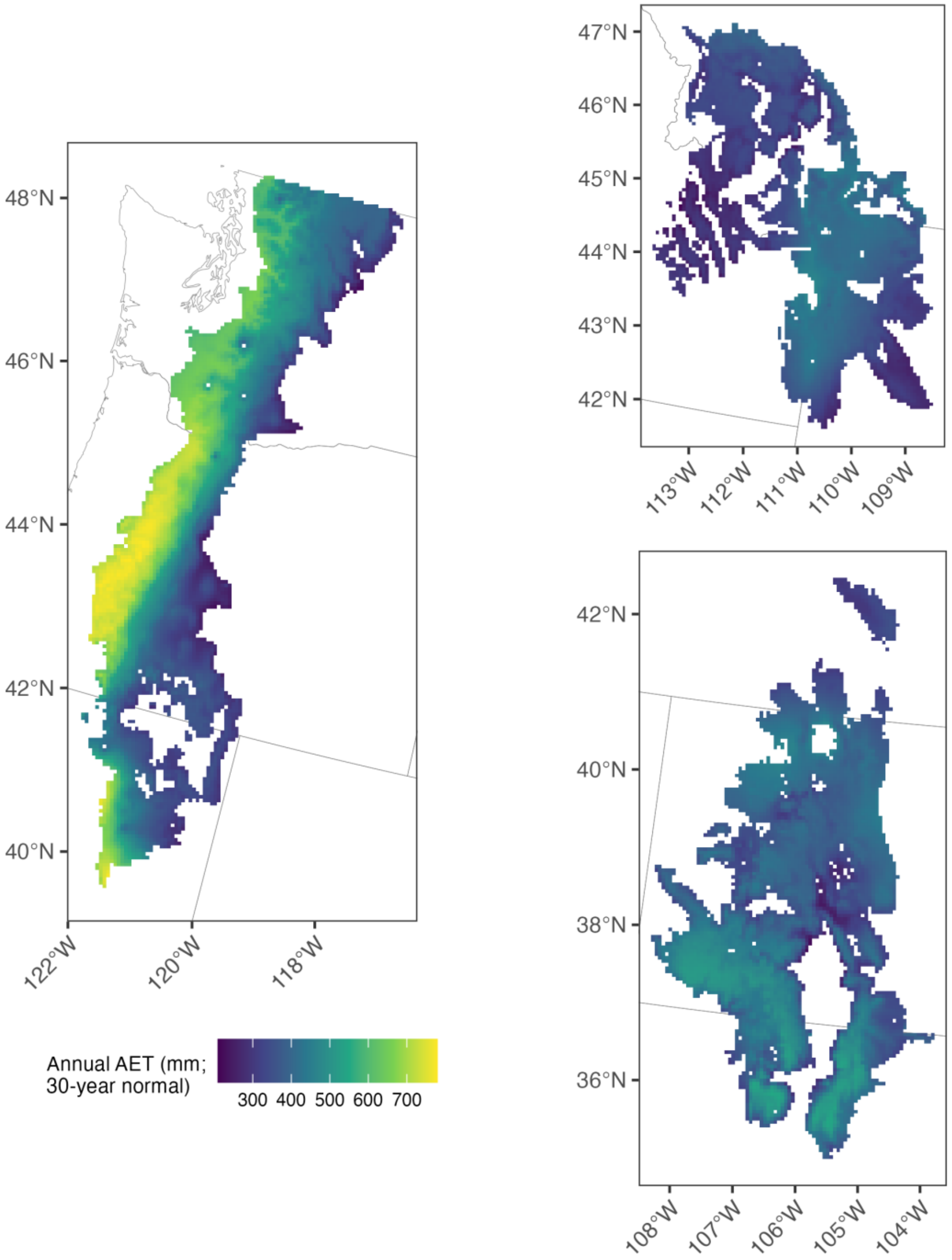

Figure 2.13. Annual actual evapotranspiration (AET) climate normals within each study region.

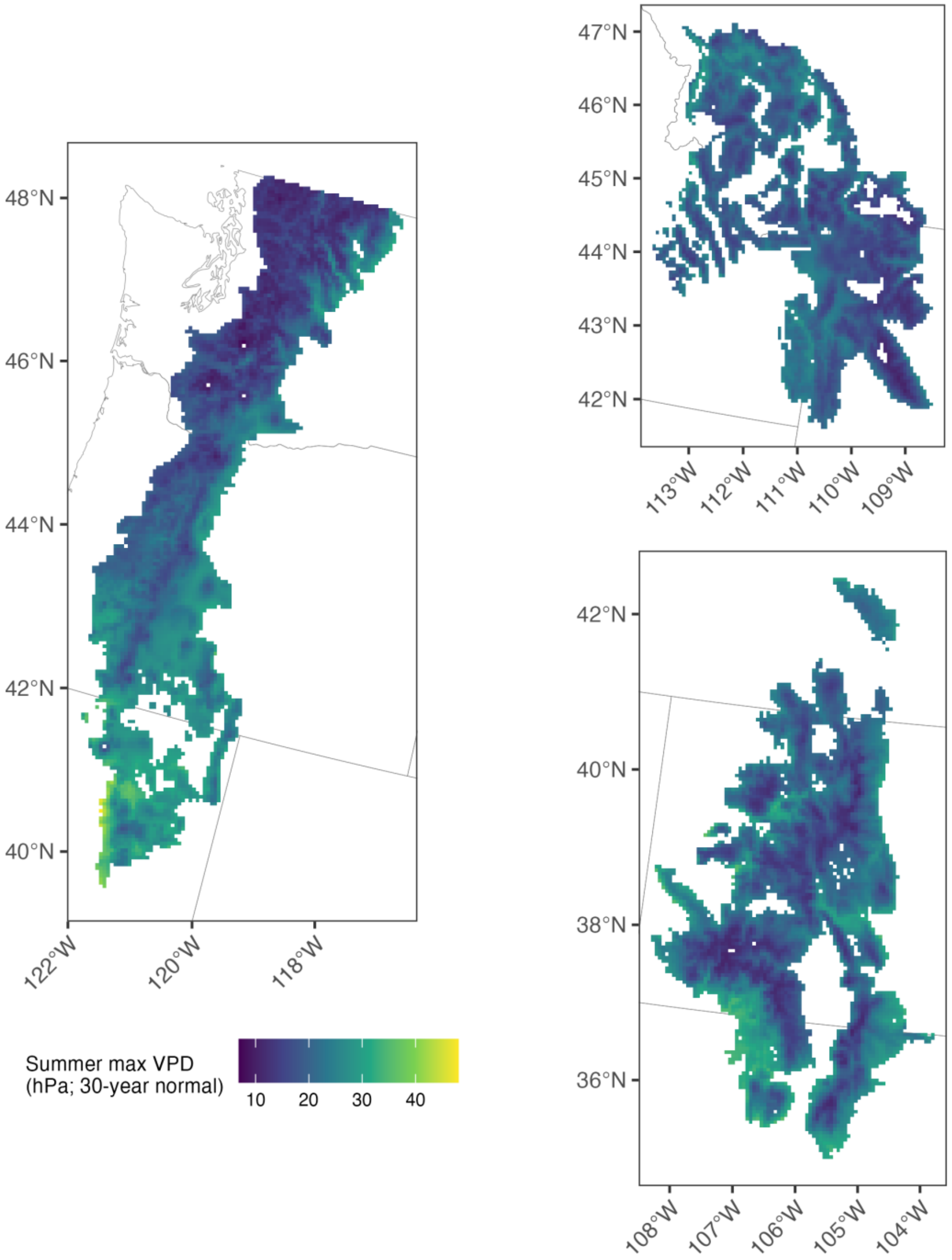

Figure 2.14. Summer maximum vapor pressure deficit (VPD) climate normals within each study region.

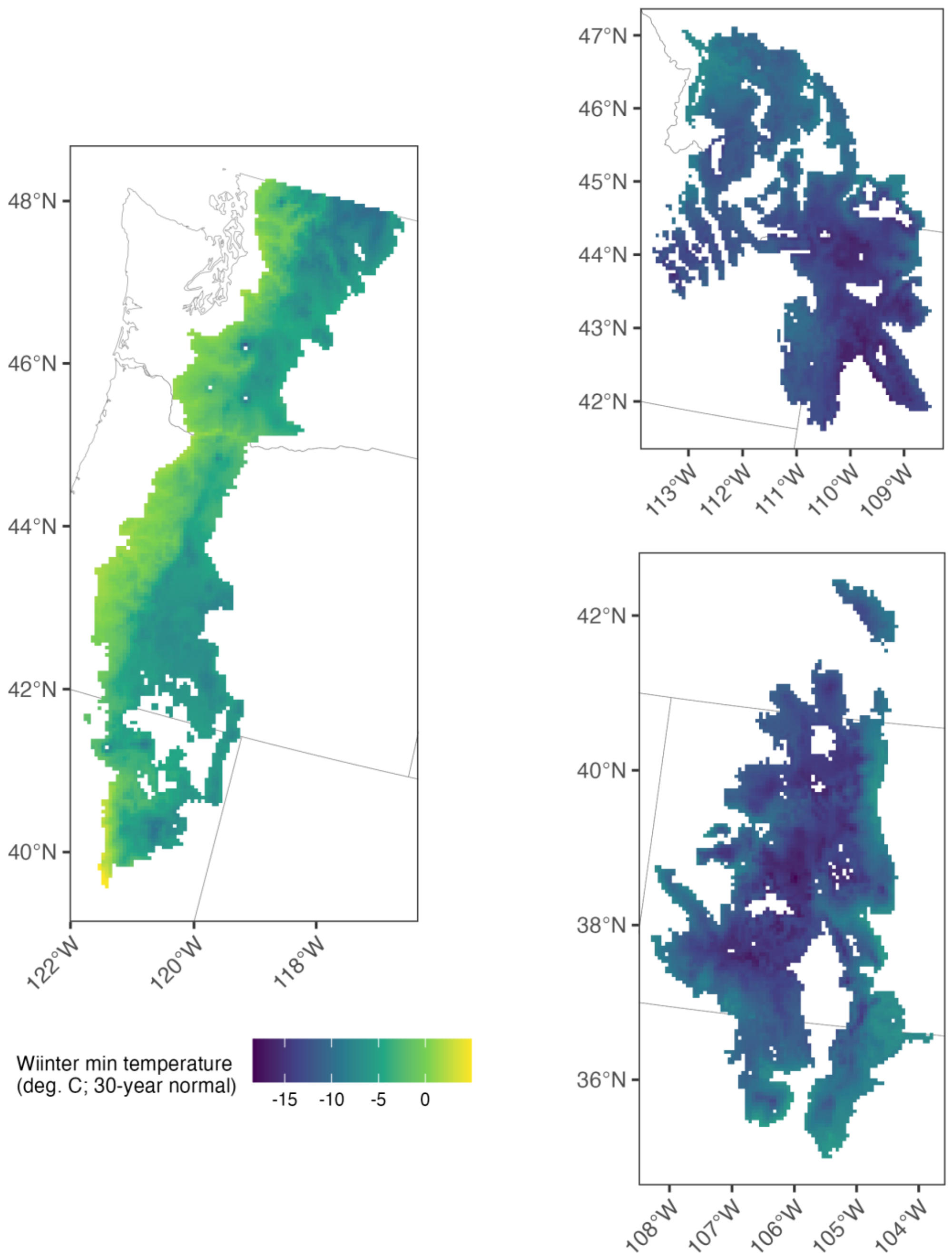

Figure 2.15. Winter minimum temperature climate normals within each study region.

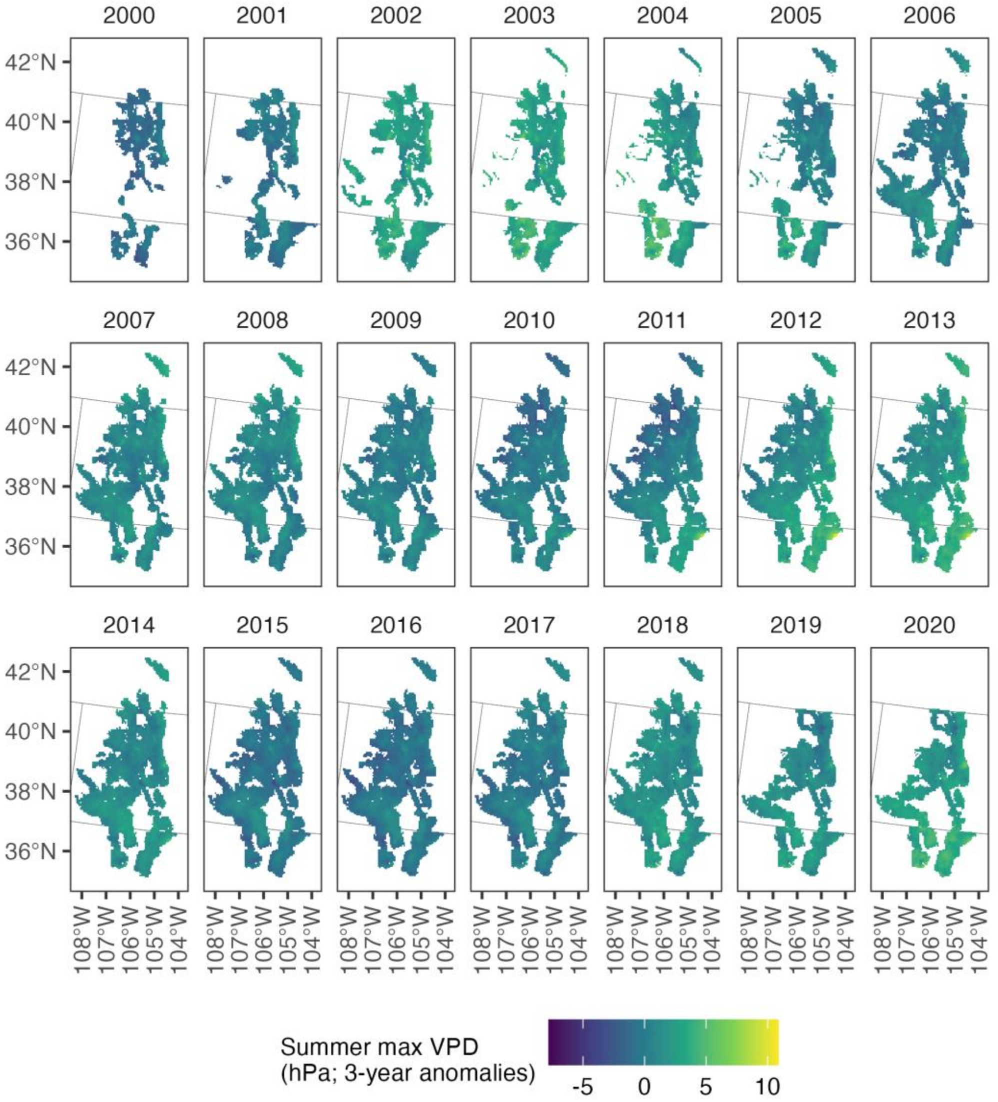

Figure 2.16. Summer maximum vapor pressure deficit (VPD) anomalies for the Southern Rockies study region.

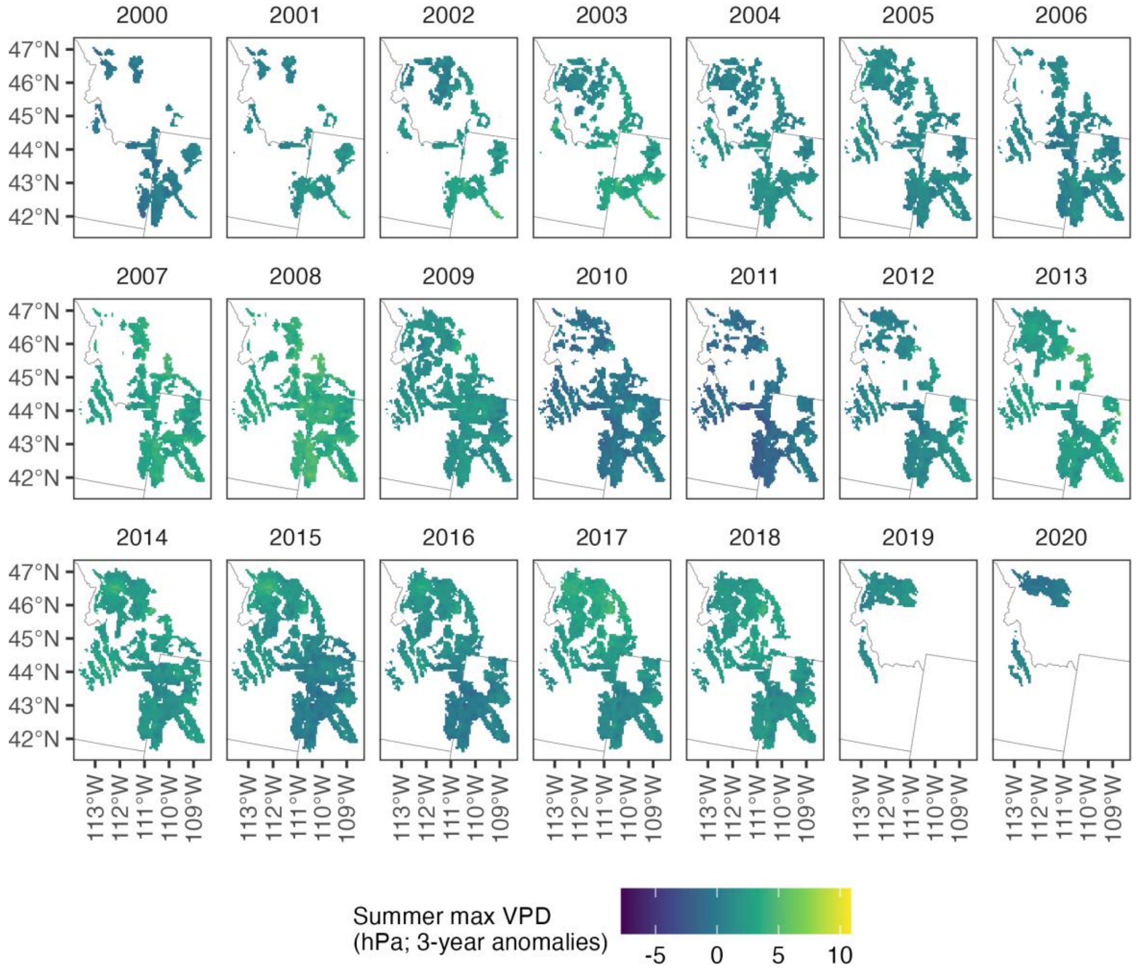

Figure 2.17. Summer maximum vapor pressure deficit (VPD) anomalies for the Middle Rockies study region.

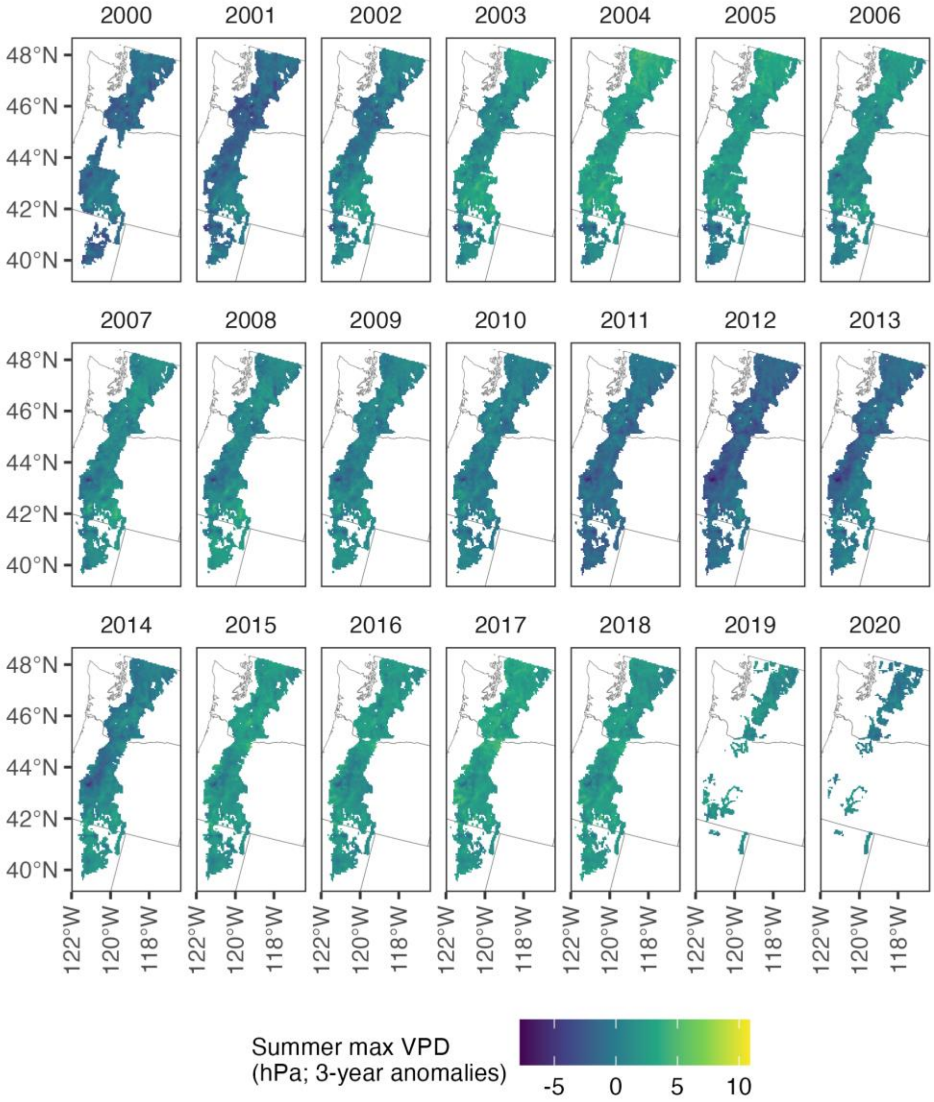

Figure 2.18. Summer maximum vapor pressure deficit (VPD) anomalies for the Cascades study region.

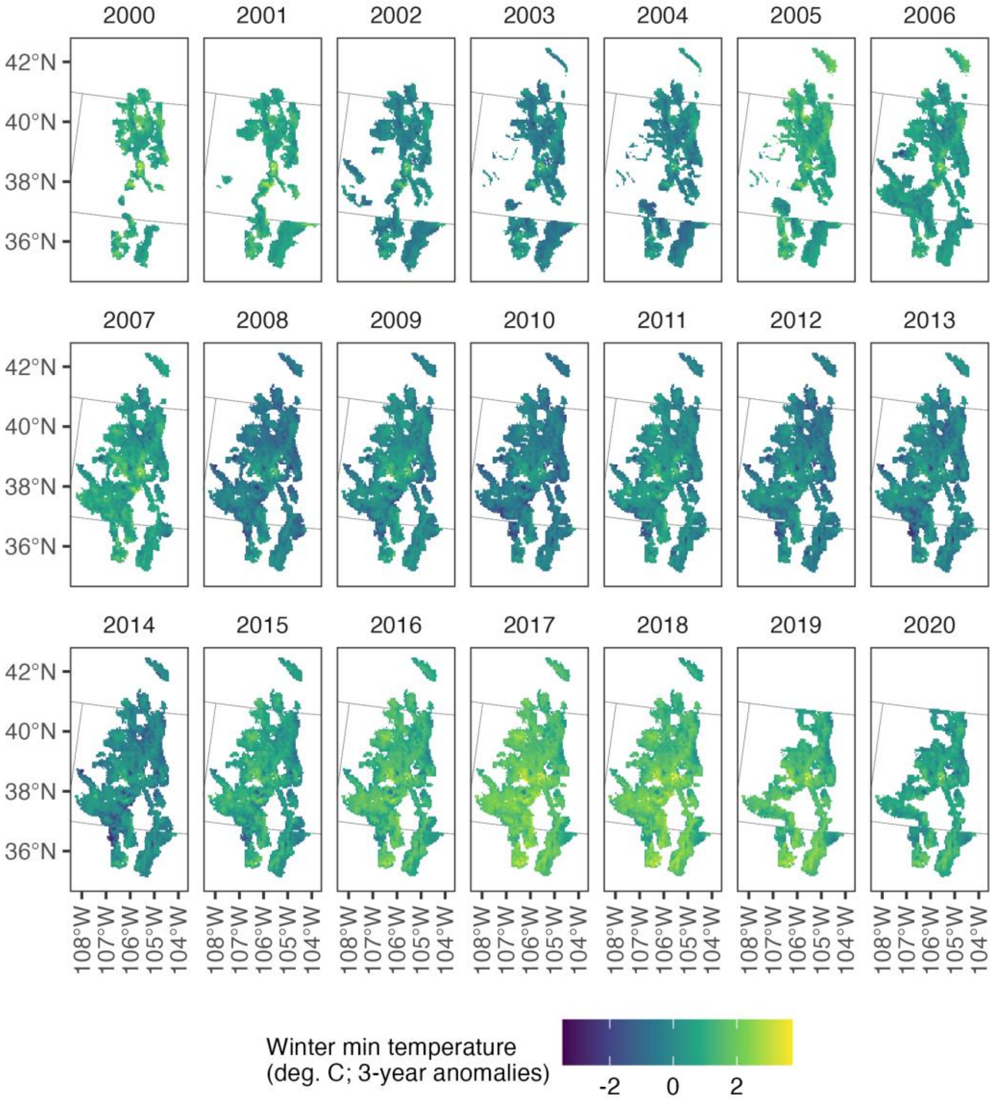

Figure 2.19. Winter minimum temperature anomalies for the Southern Rockies study region.

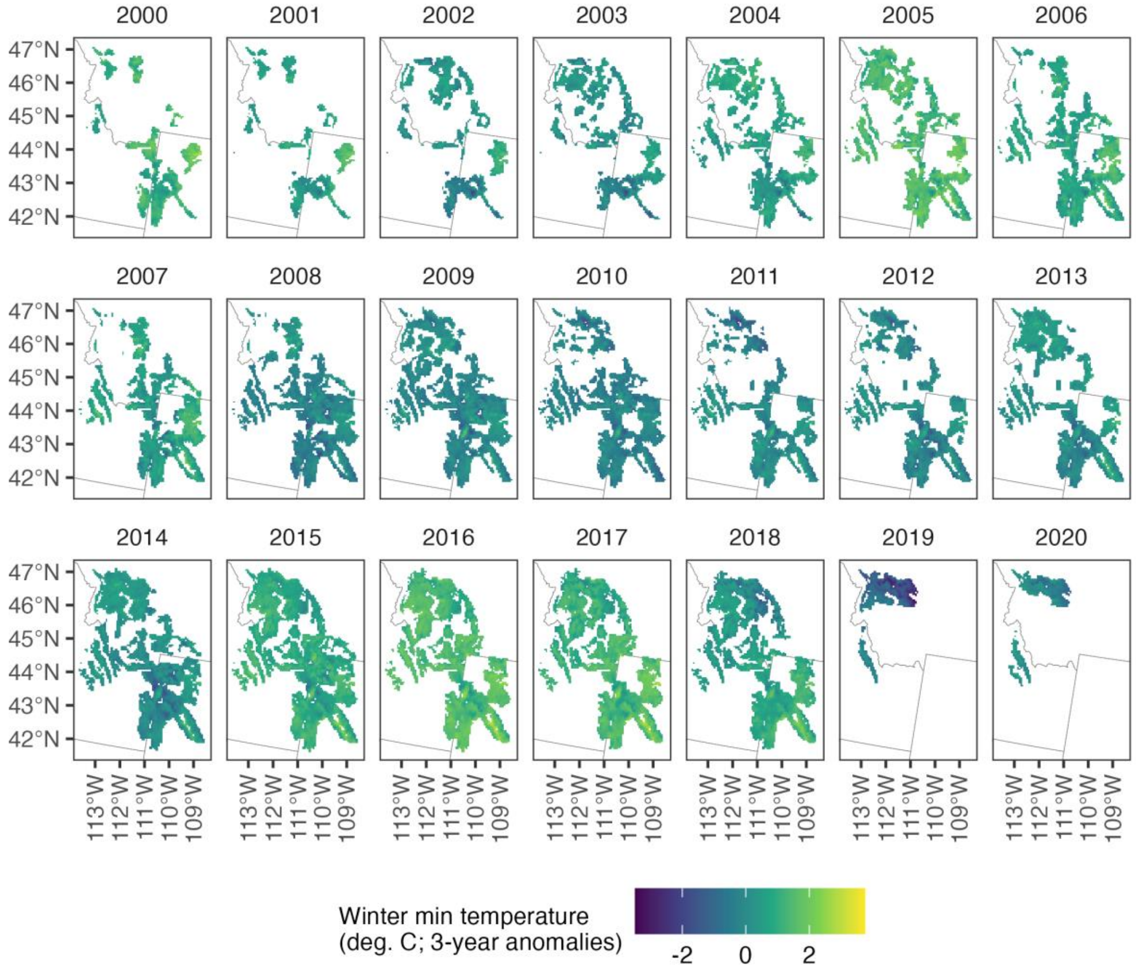

Figure 2.20. Winter minimum temperature anomalies for the Middle Rockies study region.

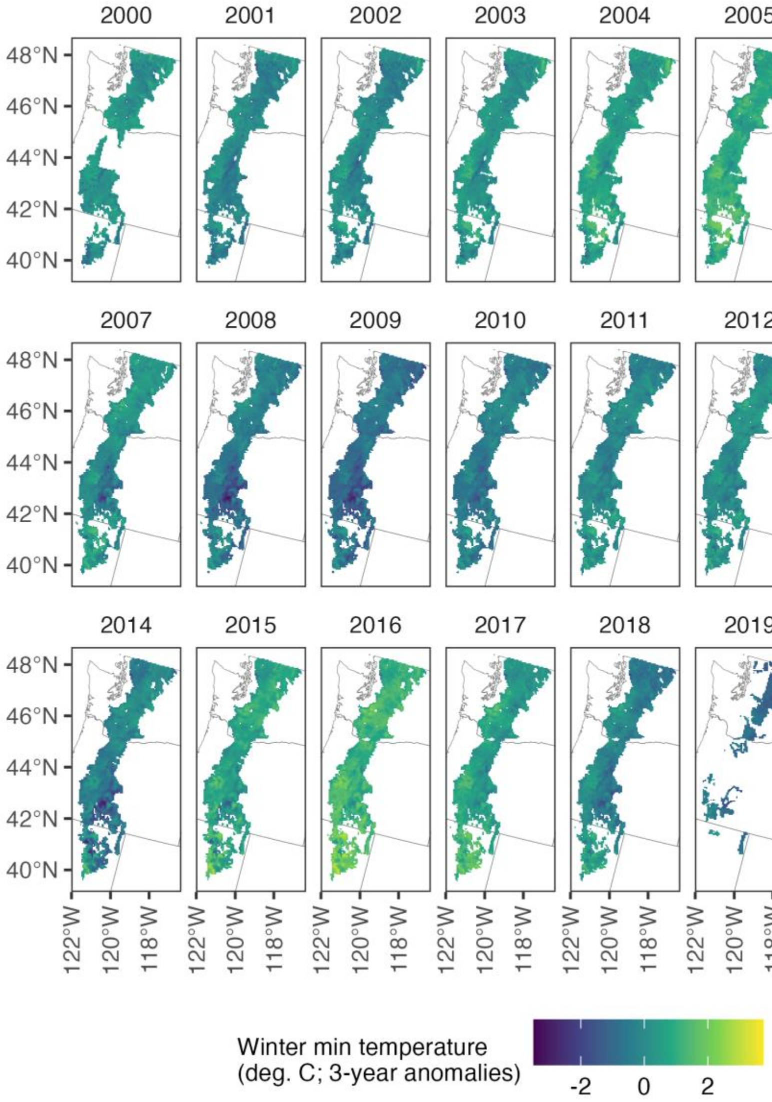

Figure 2.21. Winter minimum temperature anomalies for the Cascades study region.

2.7 APPENDIX D: STATISTICAL MODELING METHODS AND RESULTS

Table 2.4. Summary of fixed effects and hyperparameters for Southern Rockies model.

Response	Parameter	Mean	StDev	0.025quant	0.5quant	0.975quant
Fixed effects						
Occurrence	Prevalence of host co-occurrence	0.274	0.021	0.233	0.274	0.314
	Host basal area	0.295	0.021	0.254	0.295	0.336
	Host richness	0.152	0.024	0.106	0.152	0.198
	Topographic heat load index	-0.084	0.014	-0.111	-0.084	-0.057
	Topographic wetness index	-0.249	0.021	-0.291	-0.249	-0.207
	Annual AET (30-year normal)	0.161	0.063	0.038	0.161	0.285
	Winter minimum temp (30-year normal)	-0.128	0.062	-0.250	-0.128	-0.005
	Summer maximum VPD (30-year normal)	-0.172	0.051	-0.272	-0.172	-0.072
	Winter minimum temp (3-year anomaly)	0.193	0.040	0.115	0.193	0.271
	Winter minimum temp (normal:anomaly)	-0.172	0.030	-0.231	-0.172	-0.112
	Summer maximum VPD (3-year anomaly)	0.078	0.049	-0.018	0.078	0.174
	Summer maximum VPD (normal:anomaly)	0.136	0.022	0.092	0.136	0.179
Prevalence	Host basal area	0.196	0.006	0.183	0.196	0.208
	Host richness	0.065	0.008	0.049	0.065	0.080
	Topographic heat load index	-0.059	0.004	-0.067	-0.059	-0.051
	Topographic wetness index	-0.001	0.007	-0.014	-0.001	0.013
	Annual AET (30-year normal)	-0.062	0.021	-0.104	-0.062	-0.020
	Winter minimum temp (30-year normal)	-0.307	0.022	-0.351	-0.307	-0.264
	Summer maximum VPD (30-year normal)	-0.183	0.015	-0.213	-0.183	-0.152
	Winter minimum temp (3-year anomaly)	0.065	0.016	0.033	0.065	0.096
	Winter minimum temp (normal:anomaly)	-0.080	0.014	-0.107	-0.080	-0.053
	Summer maximum VPD (3-year anomaly)	0.179	0.017	0.147	0.179	0.212
	Summer maximum VPD (normal:anomaly)	0.070	0.010	0.051	0.070	0.089
Hyperparameters for random effects						
Occurrence	Year random walk σ	0.541	0.035	0.475	0.541	0.612
	Spatio-temporal random field r	55.562	2.237	51.327	55.498	60.150
	Spatio-temporal random field σ	2.677	0.085	2.515	2.675	2.850
	Spatio-temporal random field ϕ	0.911	0.007	0.896	0.911	0.925
Prevalence	Year random walk σ	0.159	0.009	0.143	0.159	0.176
	Spatio-temporal random field r	40.603	2.122	36.712	40.499	45.069
	Spatio-temporal random field σ	2.294	0.067	2.162	2.294	2.426
	Spatio-temporal random field ϕ	0.925	0.006	0.912	0.925	0.935

Table 2.5. Summary of fixed effects and hyperparameters for Middle Rockies model.

Response	Parameter	Mean	StDev	0.025quant	0.5quant	0.975quant
Fixed effects						
Occurrence	Prevalence of host co-occurrence	0.502	0.029	0.446	0.502	0.558
	Host basal area	0.154	0.028	0.098	0.154	0.209
	Host richness	0.091	0.034	0.024	0.091	0.157
	Topographic heat load index	-0.090	0.018	-0.127	-0.090	-0.054
	Topographic wetness index	-0.048	0.029	-0.105	-0.048	0.009
	Annual AET (30-year normal)	-0.243	0.100	-0.438	-0.243	-0.047
	Winter minimum temp (30-year normal)	-0.108	0.078	-0.261	-0.108	0.046
	Summer maximum VPD (30-year normal)	-0.271	0.041	-0.351	-0.271	-0.191
	Winter minimum temp (3-year anomaly)	-0.035	0.051	-0.135	-0.035	0.066
	Summer maximum VPD (3-year anomaly)	0.051	0.064	-0.074	0.051	0.177
Prevalence	Host basal area	0.171	0.008	0.156	0.171	0.185
	Host richness	0.081	0.009	0.063	0.081	0.099
	Topographic heat load index	-0.025	0.005	-0.036	-0.025	-0.015
	Topographic wetness index	0.157	0.010	0.139	0.157	0.176
	Annual AET (30-year normal)	-0.566	0.038	-0.640	-0.566	-0.492
	Winter minimum temp (30-year normal)	0.018	0.024	-0.029	0.018	0.064
	Summer maximum VPD (30-year normal)	-0.388	0.013	-0.413	-0.388	-0.364
	Winter minimum temp (3-year anomaly)	-0.098	0.016	-0.130	-0.098	-0.065
	Summer maximum VPD (3-year anomaly)	0.067	0.022	0.024	0.067	0.111
Hyperparameters for random effects						
Occurrence	Year random walk σ	1.058	0.185	0.790	1.023	1.506
	Spatio-temporal random field r	63.785	3.373	57.601	63.617	70.885
	Spatio-temporal random field σ	2.485	0.086	2.324	2.482	2.663
	Spatio-temporal random field ϕ	0.886	0.009	0.868	0.886	0.903
Prevalence	Year random walk σ	0.353	0.051	0.259	0.351	0.459
	Spatio-temporal random field r	38.289	1.742	34.953	38.258	41.812
	Spatio-temporal random field σ	2.402	0.069	2.270	2.401	2.540
	Spatio-temporal random field ϕ	0.902	0.007	0.887	0.902	0.916

Table 2.6. Summary of fixed effects and hyperparameters for Cascades model.

Response	Parameter	Mean	StDev	0.025quant	0.5quant	0.975quant
Fixed effects						
Occurrence	Prevalence of host co-occurrence	0.303	0.017	0.269	0.303	0.337
	Host basal area	0.337	0.027	0.284	0.337	0.390
	Host richness	0.351	0.028	0.297	0.351	0.405
	Topographic heat load index	-0.043	0.012	-0.066	-0.043	-0.020
	Topographic wetness index	-0.118	0.024	-0.165	-0.117	-0.071
	Annual AET (30-year normal)	0.903	0.124	0.660	0.903	1.145
	Summer maximum VPD (30-year normal)	-0.171	0.041	-0.251	-0.171	-0.091
	Winter minimum temp (3-year anomaly)	0.041	0.031	-0.019	0.041	0.101
	Summer maximum VPD (3-year anomaly)	0.044	0.039	-0.031	0.044	0.120
Prevalence	Host basal area	0.210	0.008	0.195	0.210	0.226
	Host richness	0.041	0.009	0.022	0.041	0.060
	Topographic heat load index	-0.015	0.004	-0.022	-0.015	-0.008
	Topographic wetness index	0.004	0.008	-0.013	0.004	0.021
	Annual AET (30-year normal)	0.489	0.051	0.389	0.489	0.589
	Summer maximum VPD (30-year normal)	-0.251	0.012	-0.275	-0.251	-0.227
	Winter minimum temp (3-year anomaly)	0.018	0.009	0.001	0.018	0.036
	Summer maximum VPD (3-year anomaly)	0.061	0.014	0.033	0.061	0.088
Hyperparameters for random effects						
Occurrence	Year random walk σ	0.420	0.055	0.340	0.410	0.552
	Spatio-temporal random field r	84.825	3.618	78.126	84.669	92.390
	Spatio-temporal random field σ	2.566	0.084	2.409	2.563	2.740
	Spatio-temporal random field ϕ	0.933	0.006	0.922	0.934	0.944
Prevalence	Year random walk σ	0.134	0.013	0.110	0.134	0.161
	Spatio-temporal random field r	35.626	1.644	32.458	35.601	38.943
	Spatio-temporal random field σ	2.345	0.065	2.222	2.343	2.479
	Spatio-temporal random field ϕ	0.923	0.005	0.914	0.924	0.933

Table 2.7. Standardized effect sizes for fixed versus random effects. Fixed effects include estimated effects for all covariates combined, and random effects include estimated temporal and spatio-temporal random effects combined. Logit-scale effects are expressed as one standard deviation of effects estimated across each modeled dataset. Odds ratios for fixed and random effects (x) are calculated as e^x.

Region	Response	SD of combined logit-scale effects (x)		Odds ratio (e^x)	
		Fixed	Random	Fixed	Random
Southern Rockies	Occurrence	0.92	2.43	2.50	11.32
	Prevalence	0.58	0.98	1.79	2.65
Middle Rockies	Occurrence	0.83	3.40	2.30	30.11
	Prevalence	0.76	1.20	2.15	3.30
Cascades	Occurrence	1.51	2.97	4.52	19.46
	Prevalence	0.75	1.35	2.13	3.84

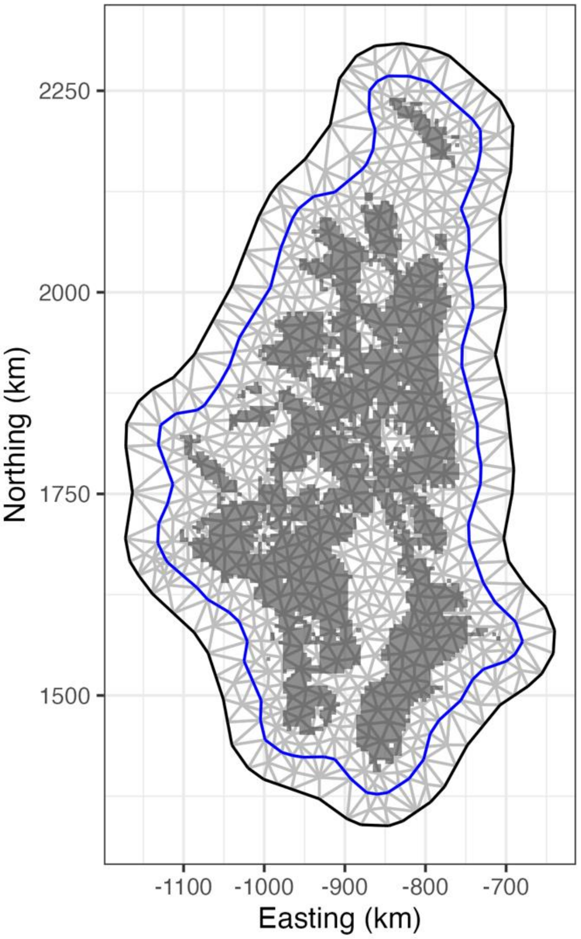

Figure 2.22. Triangulation of the Southern Rockies study region, which is used in the Stochastic Partial Differential Equation (SPDE) approach. Gray shaded areas indicate surveyed cells included in the analysis. Maximum distance between mesh nodes within the inner (blue) boundary is 30 km.

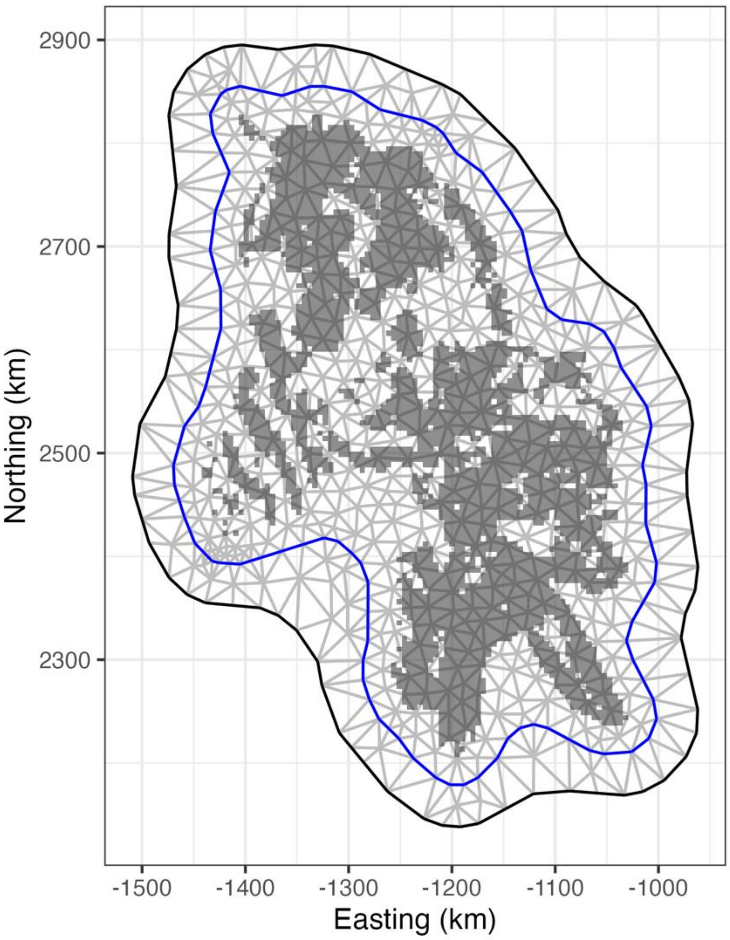

Figure 2.23. Triangulation of the Middle Rockies study region, which is used in the Stochastic Partial Differential Equation (SPDE) approach. Gray shaded areas indicate surveyed cells included in the analysis. Maximum distance between mesh nodes within the inner (blue) boundary is 30 km.

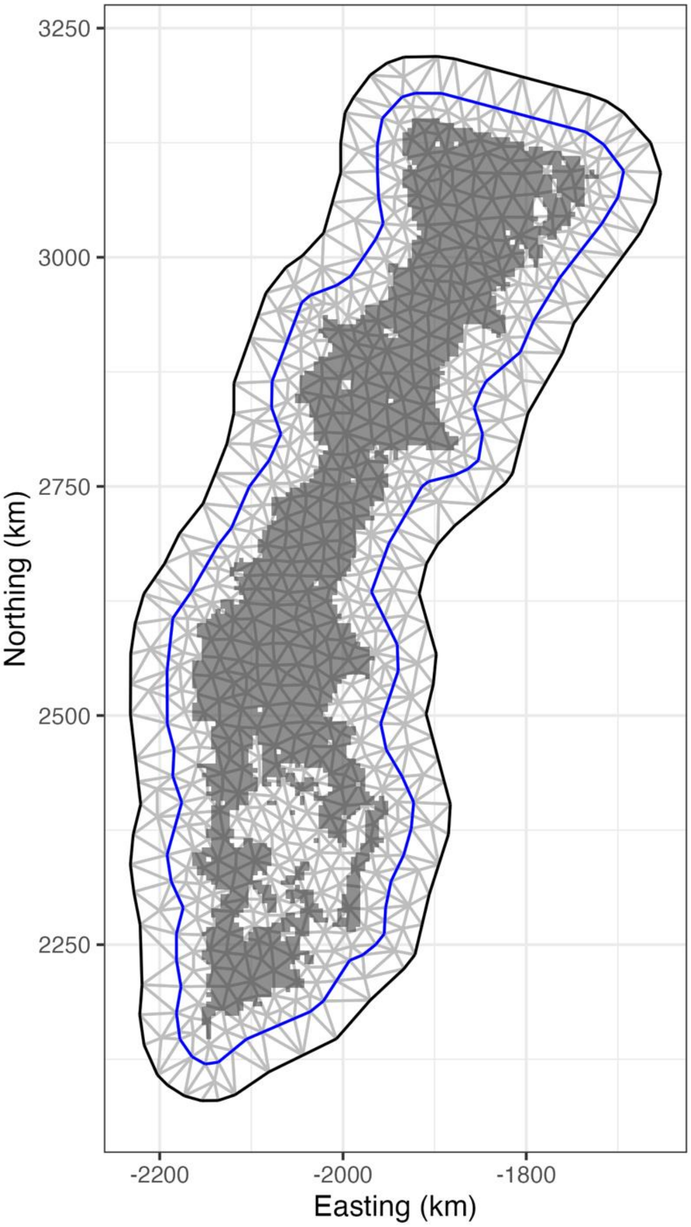

Figure 2.24. Triangulation of the Cascades study region, which is used in the Stochastic Partial Differential Equation (SPDE) approach. Gray shaded areas indicate surveyed cells included in the analysis. Maximum distance between mesh nodes within the inner (blue) boundary is 30 km.

(a) Occurrence

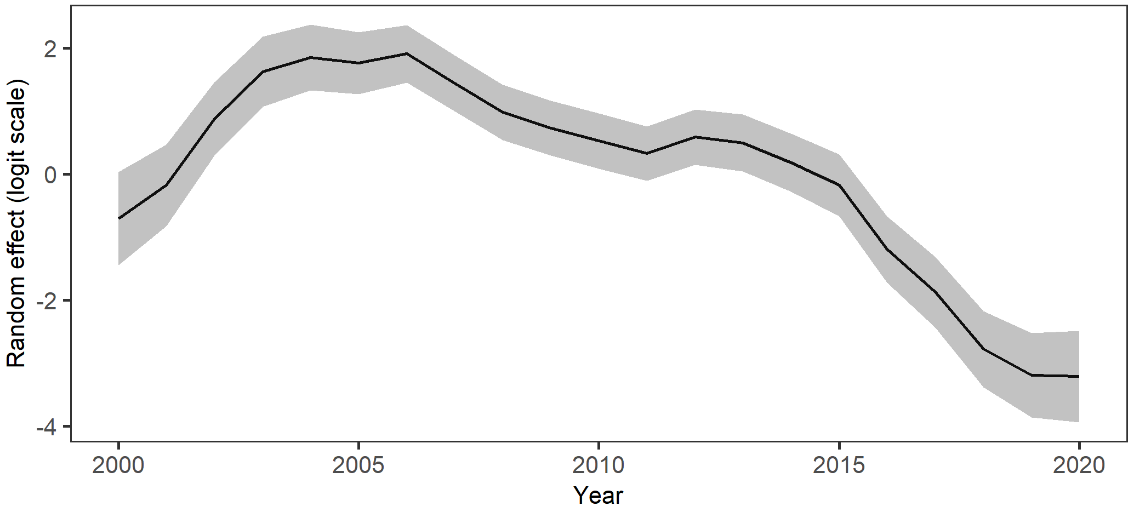

(b) Prevalence

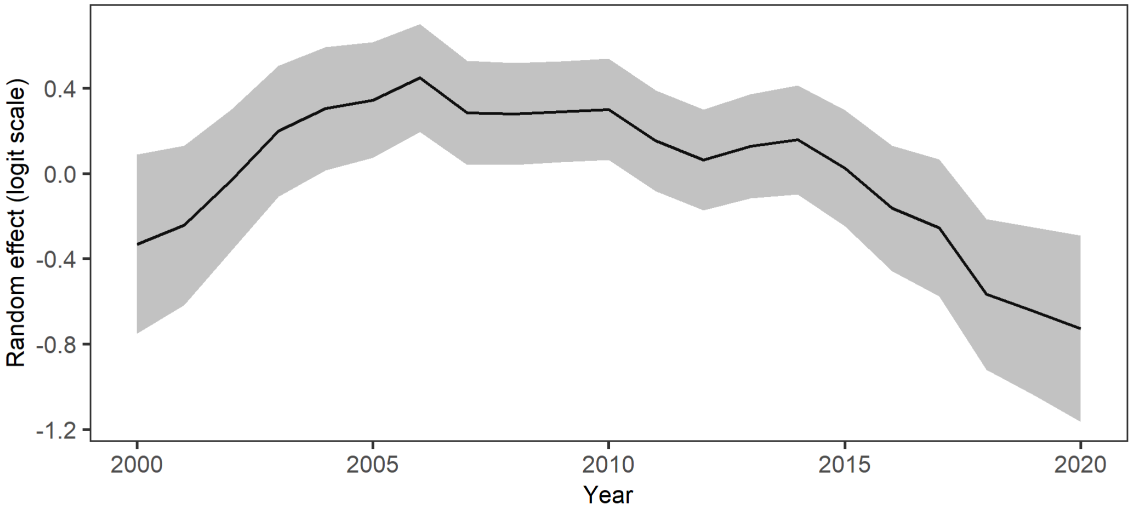

Figure 2.25. Time-varying random intercepts estimated for the Southern Rockies. Random effects were estimated separately for (a) hotspot occurrence and (b) hotspot prevalence. Solid lines are posterior means and shaded areas are 95% credible intervals in logit space.

(a) Occurrence

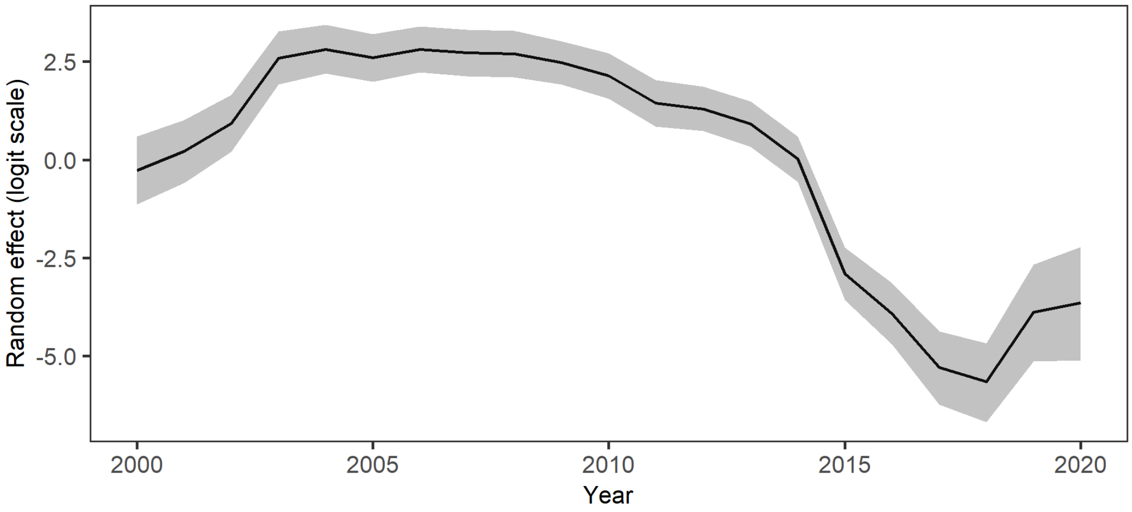

(b) Prevalence

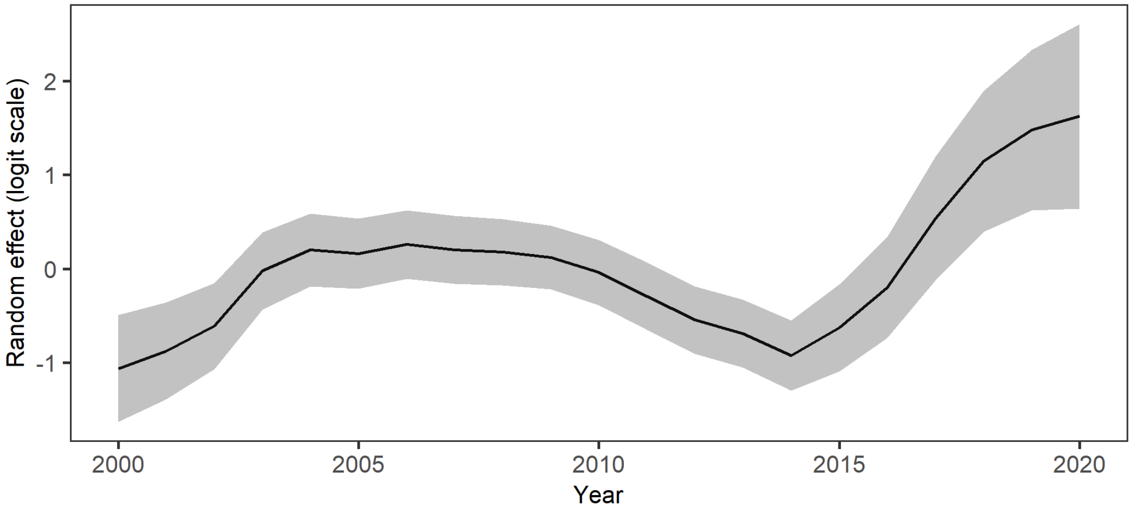

Figure 2.26. Time-varying random intercepts estimated for the Middle Rockies. Random effects were estimated separately for (a) hotspot occurrence and (b) hotspot prevalence. Solid lines are posterior means and shaded areas are 95% credible intervals in logit space.

(a) Occurrence

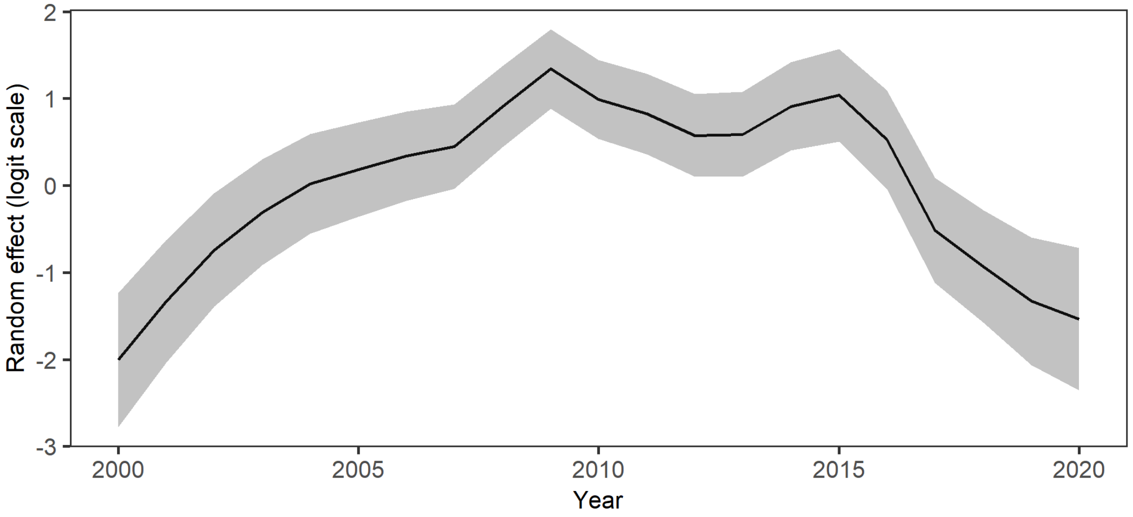

(b) Prevalence

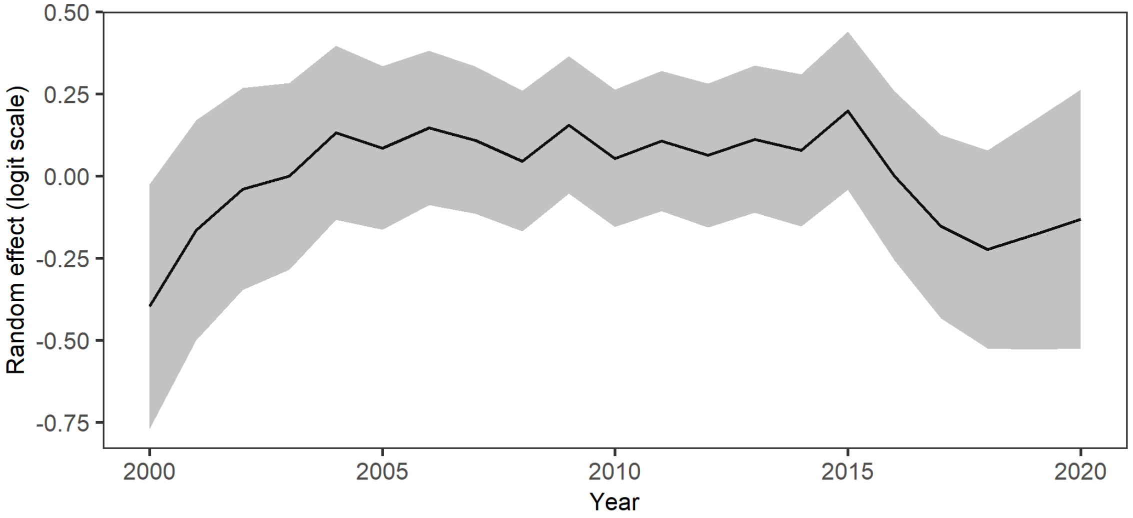

Figure 2.27. Time-varying random intercepts estimated for the Cascades. Random effects were estimated separately for (a) hotspot occurrence and (b) hotspot prevalence. Solid lines are posterior means and shaded areas are 95% credible intervals in logit space.

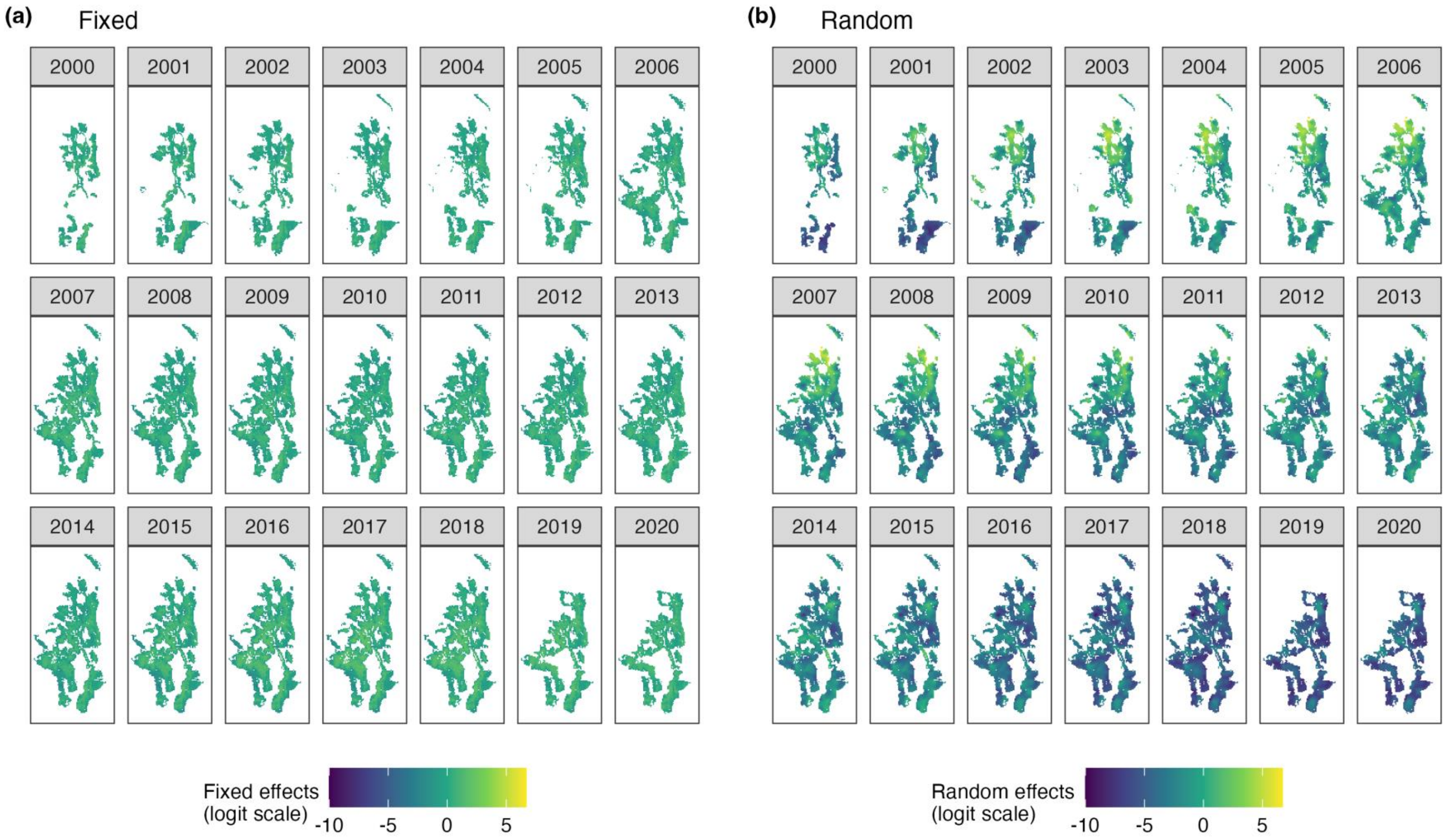

Figure 2.28. Fixed and random effects estimated for hotspot occurrence in the Southern Rockies. (a) Fixed effects include all covariates and (b) random effects include temporal plus spatio-temporal random effects. All effects are shown as posterior means in logit space.

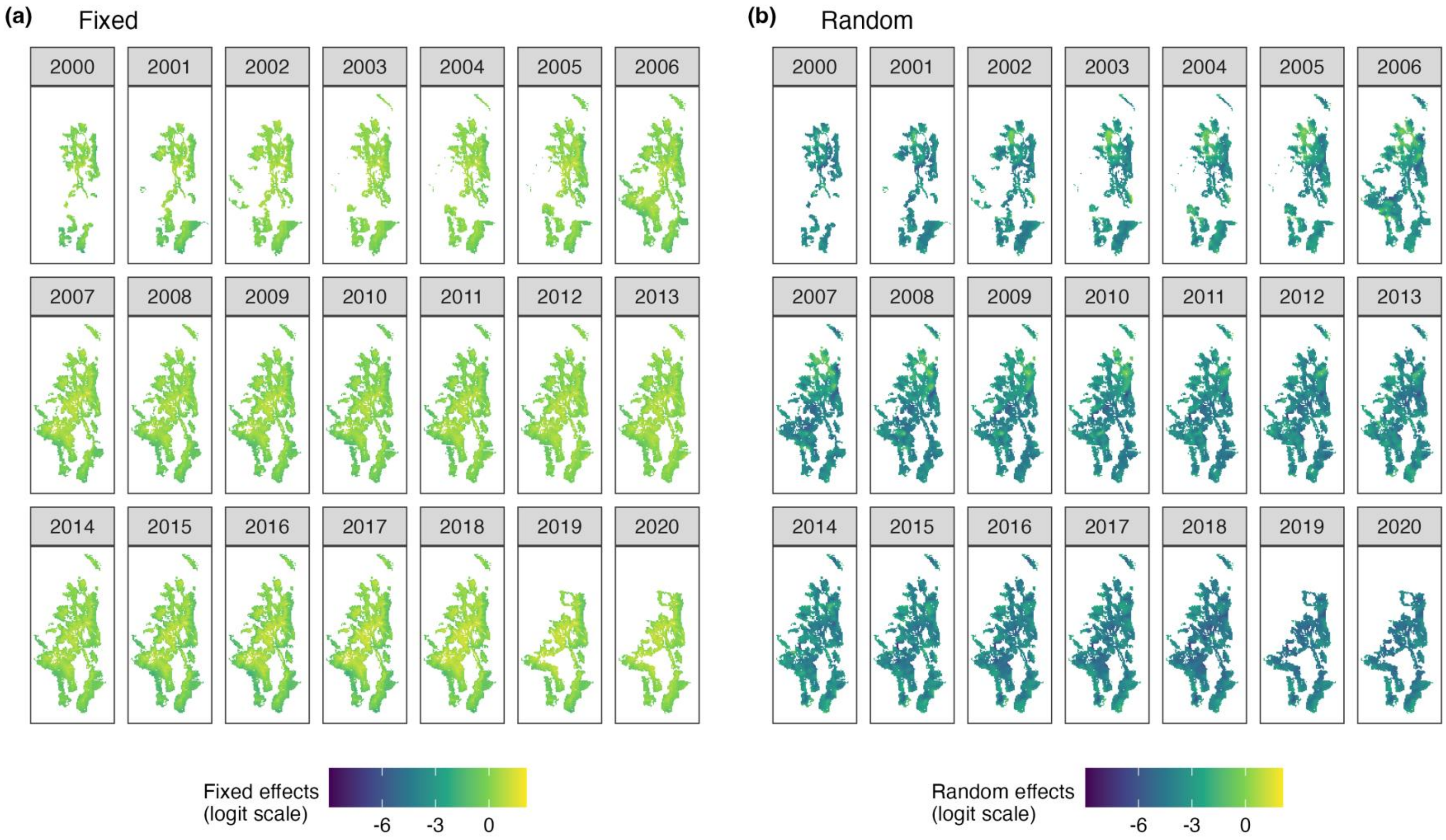

Figure 2.29. Fixed and random effects estimated for hotspot prevalence in the Southern Rockies. (a) Fixed effects include all covariates and (b) random effects include temporal plus spatio-temporal random effects. All effects are shown as posterior means in logit space.

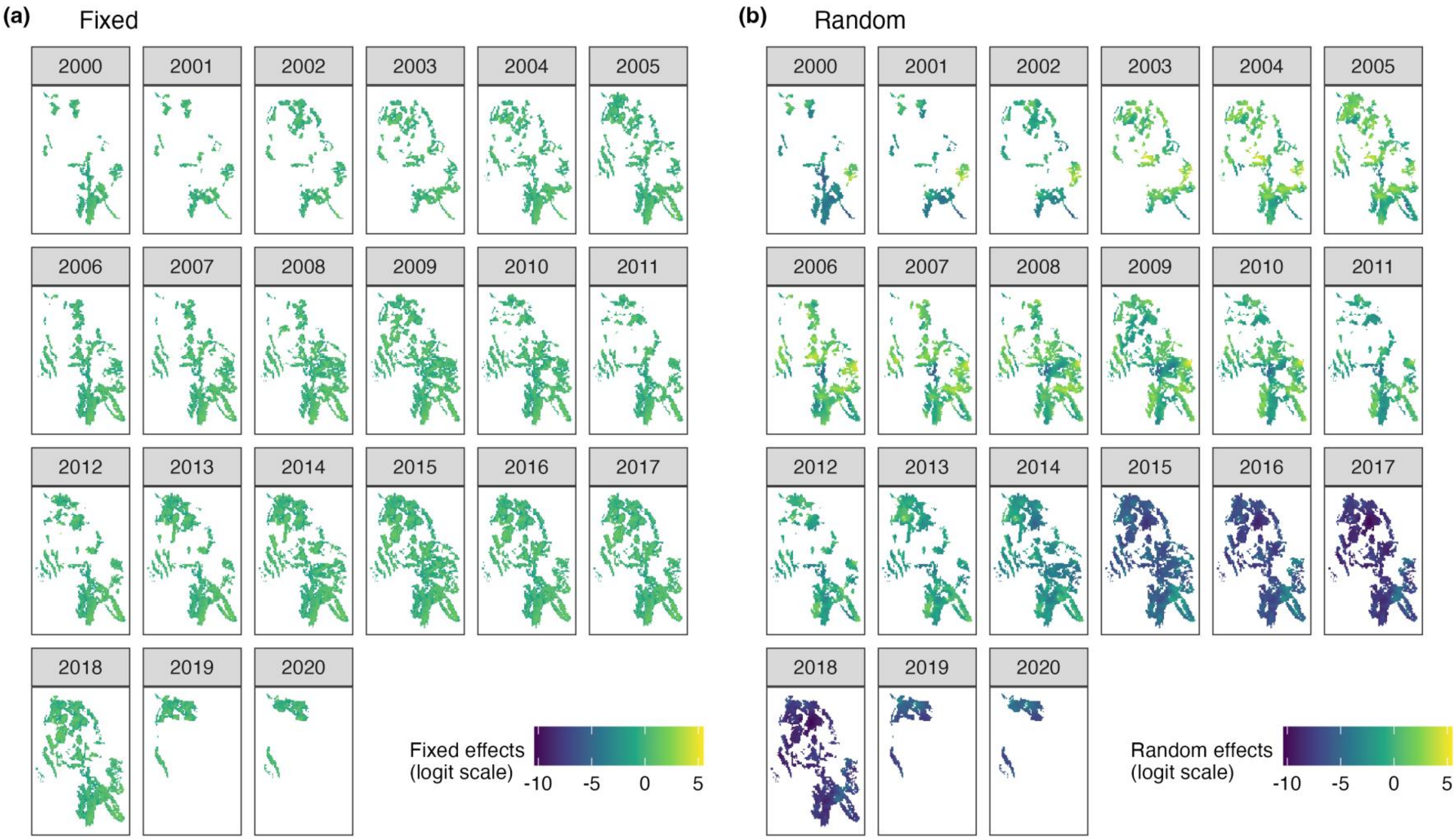

Figure 2.30. Fixed and random effects estimated for hotspot occurrence in the Middle Rockies. (a) Fixed effects include all covariates and (b) random effects include temporal plus spatio-temporal random effects. All effects are shown as posterior means in logit space.

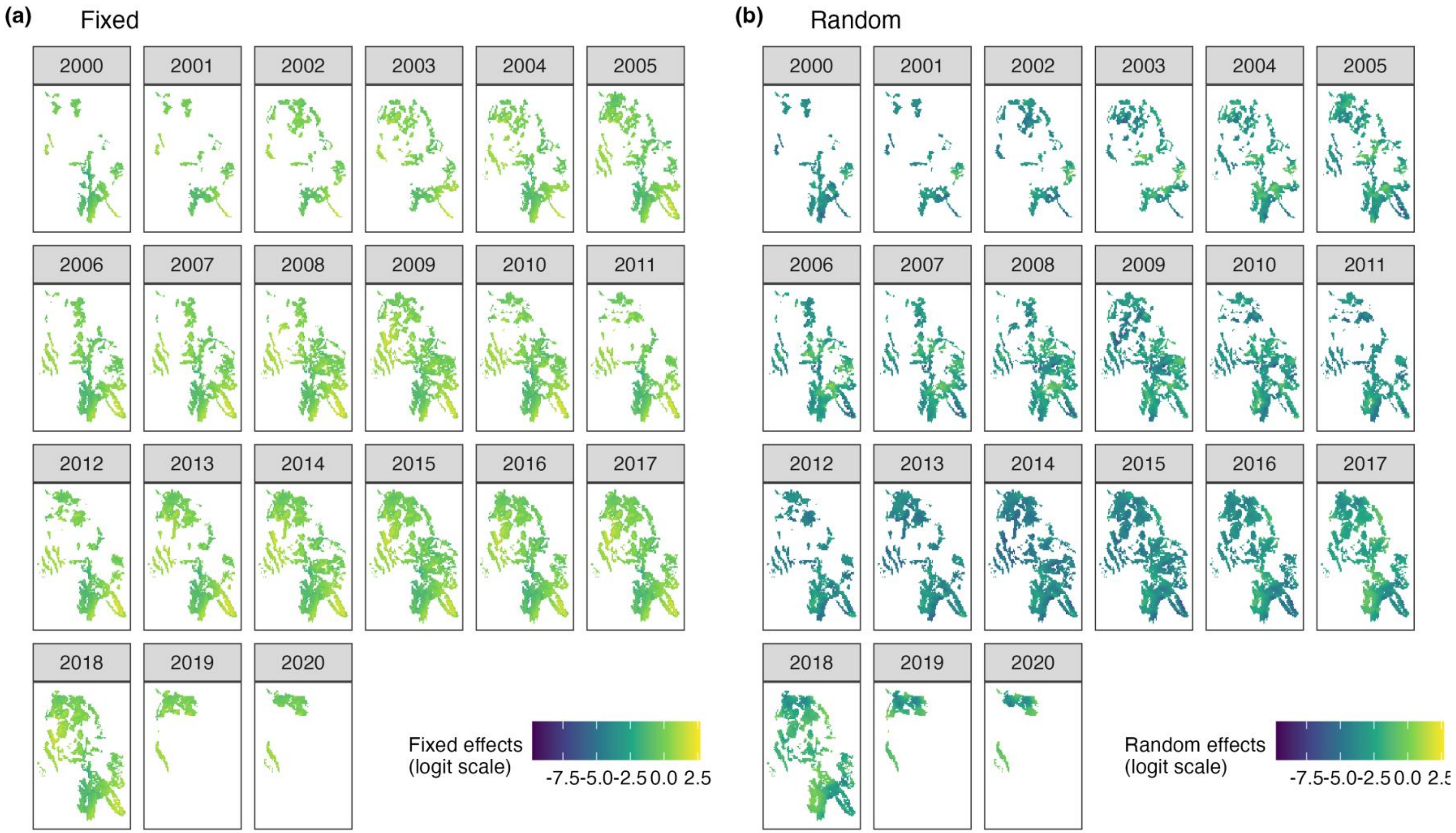

Figure 2.31. Fixed and random effects estimated for hotspot prevalence in the Middle Rockies. (a) Fixed effects include all covariates and (b) random effects include temporal plus spatio-temporal random effects. All effects are shown as posterior means in logit space.

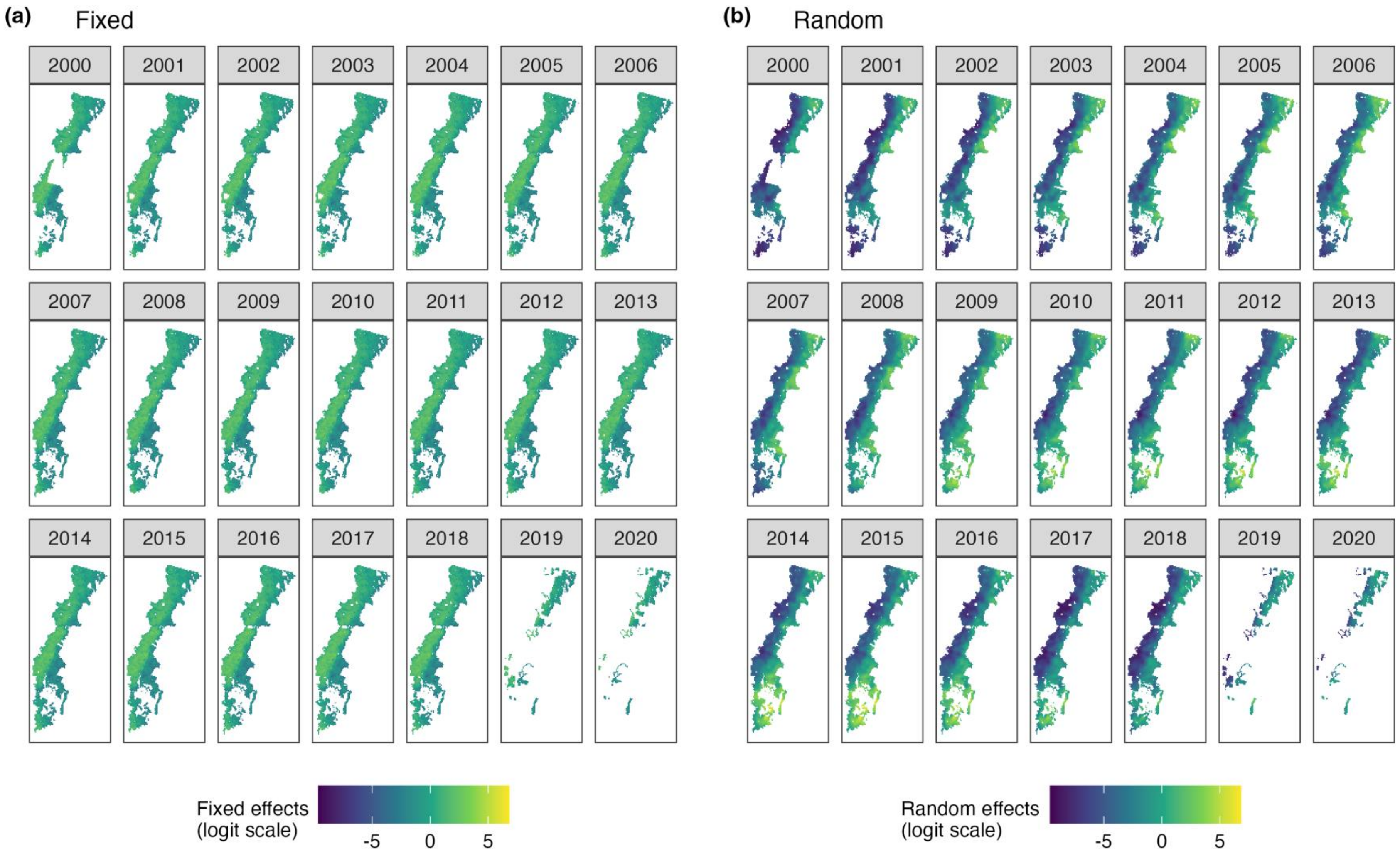

Figure 2.32. Fixed and random effects estimated for hotspot occurrence in the Cascades. (a) Fixed effects include all covariates and (b) random effects include temporal plus spatio-temporal random effects. All effects are shown as posterior means in logit space.

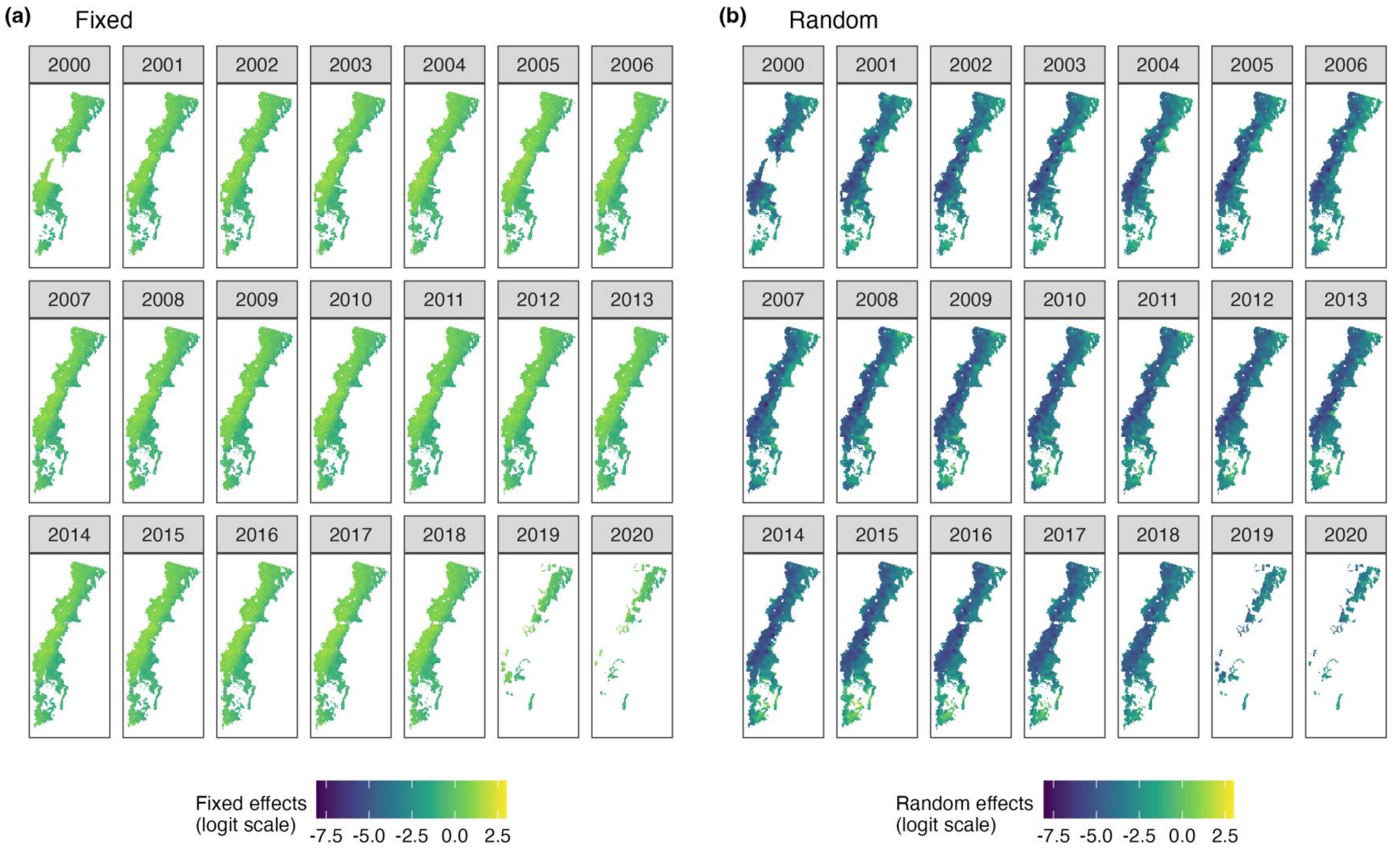

Figure 2.33. Fixed and random effects estimated for hotspot prevalence in the Cascades. (a) Fixed effects include all covariates and (b) random effects include temporal plus spatio-temporal random effects. All effects are shown as posterior means in logit space.

(a) Occurrence

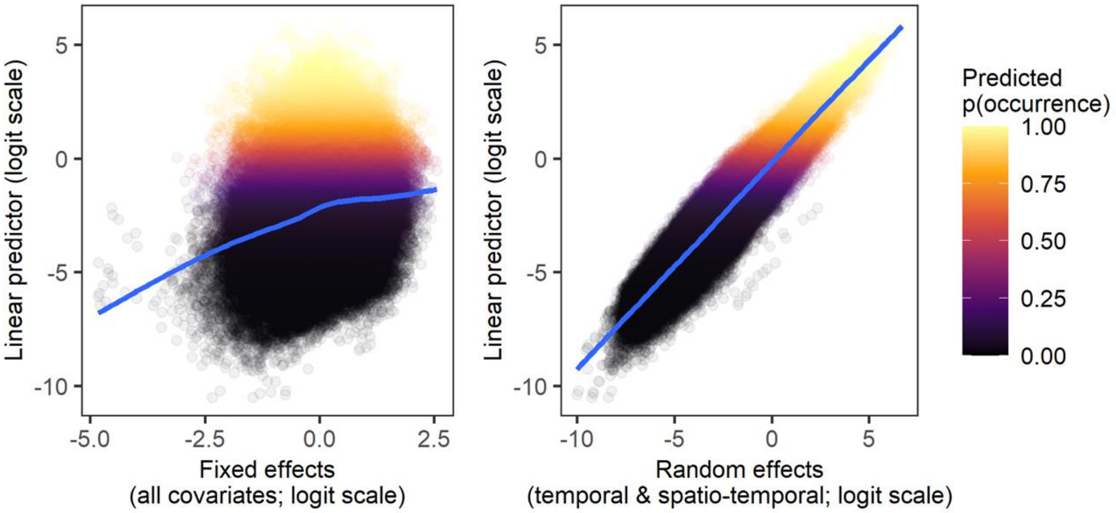

(b) Prevalence

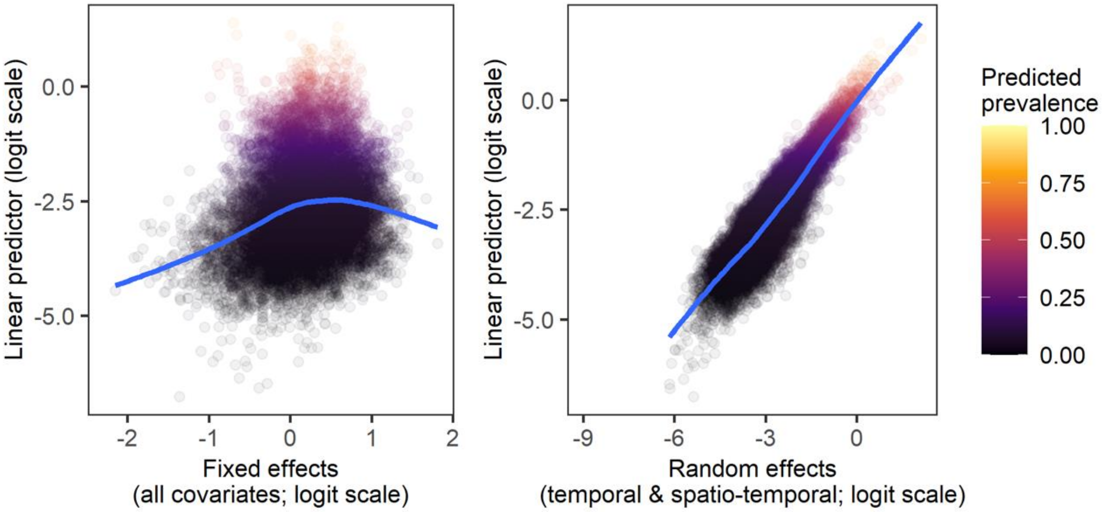

Figure 2.34. Linear predictor plotted against fixed and random effects estimated for the Southern Rockies. Hotspot occurrence shown in (a) and hotspot prevalence in (b). Color scale shows the linear predictor converted to a corresponding probability (i.e., inverse-logit transformed). Simple smoothed trend lines are shown in blue for reference.

(a) Occurrence

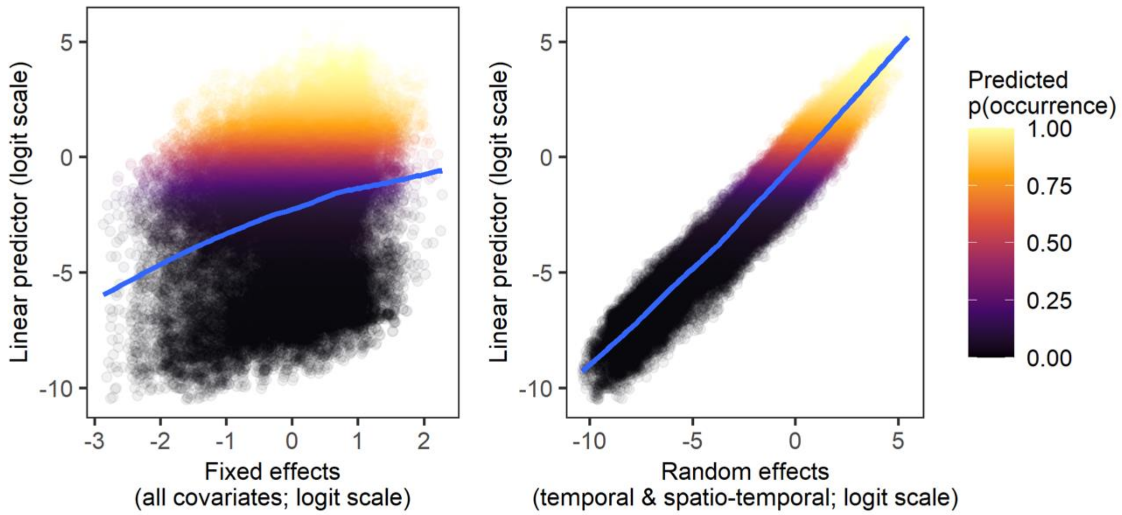

(b) Prevalence

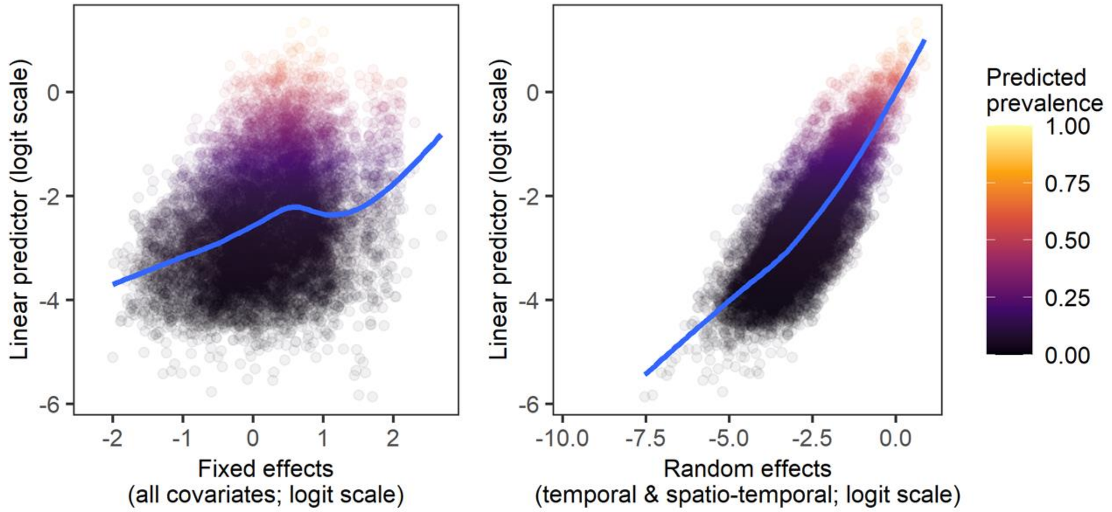

Figure 2.35. Linear predictor plotted against fixed and random effects estimated for the Middle Rockies. Hotspot occurrence shown in (a) and hotspot prevalence in (b). Color scale shows the linear predictor converted to a corresponding probability (i.e., inverse-logit transformed). Simple smoothed trend lines are shown in blue for reference.

(a) Occurrence

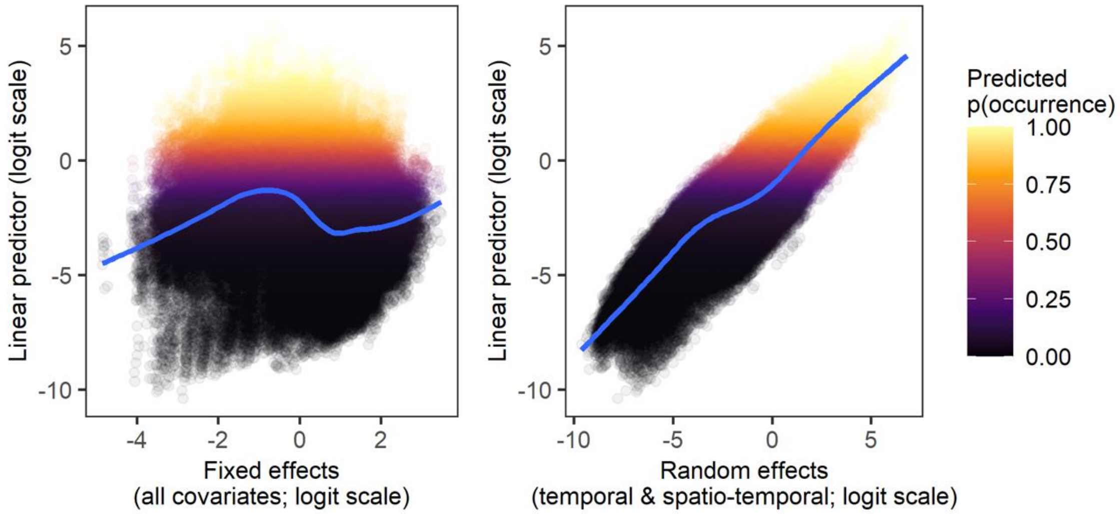

(b) Prevalence

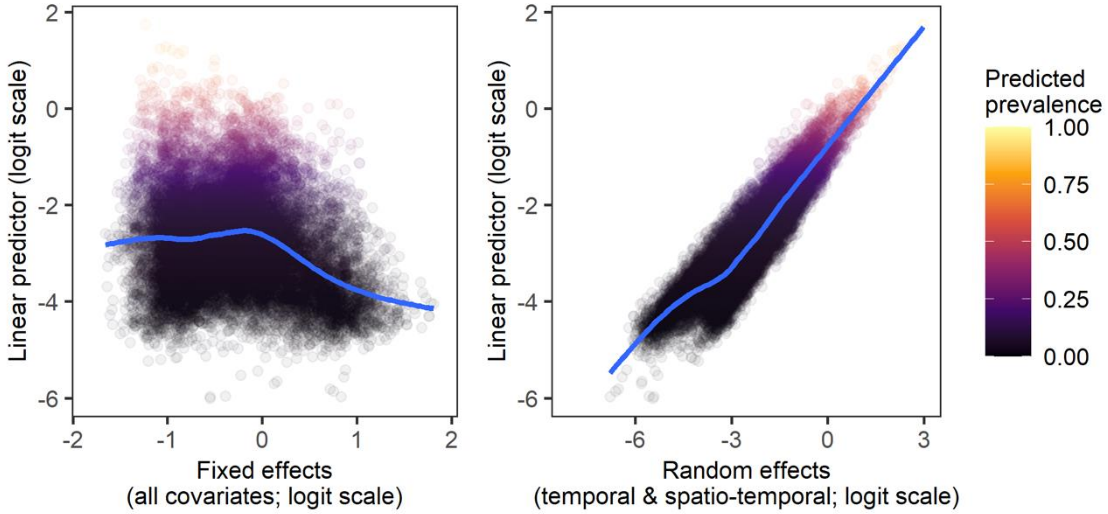

Figure 2.36. Linear predictor plotted against fixed and random effects estimated for the Cascades. Hotspot occurrence shown in (a) and hotspot prevalence in (b). Color scale shows the linear predictor converted to a corresponding probability (i.e., inverse-logit transformed). Simple smoothed trend lines are shown in blue for reference.

Chapter 3. CONSISTENT SPATIAL SCALING OF HIGH-SEVERITY WILDFIRE CAN INFORM EXPECTED FUTURE PATTERNS OF BURN SEVERITY

3.1 ABSTRACT

Increasing wildfire activity in forests worldwide has led to urgency in understanding current and future fire regimes. Spatial patterns of area burned at high severity (i.e., where most or all trees are killed by fire) are a key dimension of fire regimes and are strongly linked to post-fire forest resilience and myriad societal impacts. While the ability to forecast total area burned and large-fire probability has increased in recent years, anticipating spatial patterns of burn severity has remained difficult, as burn severity patterns are shaped by complex interactions between climate, fuels, and fire. To address this challenge, we quantify fundamental burn severity scaling relationships, which relate fire size to spatial patterns of burn severity, to characterize the range of burn severity patterns expected within contemporary fire regimes. Using 1,615 fire events occurring across the Northwest US between 1985 and 2020, we evaluate spatial scaling relationships within fire regimes and test whether these relationships vary across space and time. We show that spatial patterns of high-severity fire demonstrate clear and consistent scaling behavior across a range of fire regimes and forest ecosystems. Within fire regimes, as fire size increases, the size and spatial homogeneity of high-severity patches consistently increase, and within-fire patch-size distributions consistently converge toward a power law function. Scaling relationships did not differ substantially across space or time, suggesting that as climate warms and fire size distributions potentially shift toward larger fires, stationarity in patch-size scaling can be used to infer expected future patterns of burn severity.

3.2 INTRODUCTION

Total area burned and the frequency of large fires have increased over recent decades in many forested ecosystems across the globe (Parks & Abatzoglou 2020; Collins *et al.* 2021; Whitman *et al.* 2022). Fire activity is strongly driven by climate (Abatzoglou *et al.* 2018b), and continued increases are expected as fire seasons lengthen, ignitions increase, and extreme fire weather occurs more frequently (Bowman *et al.* 2020). Changing fire activity is expected to further increase area burned and change fire size distributions (Boulanger *et al.* 2018; Littell *et al.* 2018; Wang *et al.* 2022), with important implications for the spatial patterns and ecological effects of fire (Parks & Abatzoglou 2020; Collins *et al.* 2021), as well as forest resilience (Johnstone *et al.* 2016) and associated ecosystem services (Lecina- Diaz *et al.* 2021).

A key characteristic of forest fires is the amount and spatial configuration of area burned at high severity (i.e., areas where most or all trees are killed by fire). The size and spatial structure of high-severity patches directly shape post-fire seed availability and dispersal (Gill *et al.* 2022), formation and persistence of complex early-seral habitat (Steel *et al.* 2022), rates of forest regeneration (Harvey *et al.* 2016b) and carbon uptake (Turner *et al.* 2004), and likelihood of conversion to non-forest ecosystems (Coop *et al.* 2020). Within and among individual fire events, spatial patterns of burn severity are shaped by a complex mixture of broad-scale drivers (e.g., climate, fire weather) and local-scale constraints (e.g., topography, fuels) (Harvey *et al.* 2016a; Parks *et al.* 2018b). Within fire regimes (i.e., areas characterized by a prevailing frequency and severity of fire activity) (Moritz *et al.* 2011), the relative influence of broad-scale drivers and local-scale constraints shapes the typical or expected spatial dimensions of burn severity.

As fire activity increases worldwide, a critical gap remains in our ability to anticipate burn severity patch size and structure, and therefore potential ecological effects. Non-stationarity is expected in many direct relationships between climatic drivers and fire activity due to interacting effects of fuel structure and abundance, and this non-stationarity is often seen as a barrier to predicting future fire effects (Newman *et al.* 2019). In recent decades, total high-severity burned area has increased in many regions, driven by increases in total area burned and the occurrence of large fires (Parks & Abatzoglou 2020; Collins *et al.* 2021). However, whether fires are becoming proportionally more severe or homogenous over time, and what should be expected in the future for such trends, remains unclear. High-severity proportion has increased in some regions (Miller *et al.* 2009; Harvey *et al.* 2016a; Singleton *et al.* 2019; Parks & Abatzoglou 2020) but not others (Miller *et al.* 2012; Rivera-Huerta *et al.* 2016; Reilly *et al.* 2017; Collins *et al.* 2021; Whitman *et al.* 2022). In some cases, high-severity burned areas are becoming characterized by larger and/or simpler shaped patches (Rivera-Huerta *et al.* 2016; Reilly *et al.* 2017; Stevens *et al.* 2017), though whether such trends are directly a result of fire size (Harvey *et al.* 2016a) and are therefore likely to continue in the future is not well tested. Understanding these relationships is key to forecasting burn severity patterns as fire activity increases.

Scaling relationships can provide fundamental insights into how complex system behavior emerges as a function of event size and have been used to understand various dimensions of fire activity (McKenzie & Kennedy 2011). Quantifying scaling relationships describing how high-severity patch size and structure change with fire size could offer a means of forecasting the potential range of future fire effects, given projections for increasing area burned and shifting fire-size distributions. High-severity patch size and structure are strongly related to fire size and high-severity proportion (Cansler & McKenzie 2014; Harvey *et al.* 2016a; Collins *et al.* 2017), exhibiting characteristic scaling relationships both within fire events and within fire regimes. Across fire size distributions, scaling behavior arises in theory because the potential for large high-severity patches scales upward with the size of fire events (Gardner & Urban 2007). In reality, the relative influence of broad-scale drivers versus local-scale constraints will dictate, to varying degrees, the occurrence of increasingly large and contiguous high-severity patches with increasing fire size (Cansler & McKenzie 2014; Harvey *et al.* 2016a). Therefore, the forms of these scaling relationships are expected to vary by fire regime, and as with other facets of fire activity, to operate within some characteristic range of variation (Moritz *et al.* 2011). By integrating system-level interactions between climate and fuels, scaling relationships have the potential to exhibit stationarity and thus offer a credible approach to projecting future fire effects. Despite the potential for scaling relationships to yield insight into the ranges of burn severity patterns that emerge within fire regimes, these relationships have not yet been widely explored.

Here, we address the above knowledge gap by asking what spatial patterns of burn severity, and therefore ecological effects, are expected from fires of different sizes. Using contemporary (1985 – 2020) satellite burn severity data, we quantify spatial scaling relationships using 1,615 fires occurring across a gradient of fire regimes (frequent and low severity, moderately frequent and mixed severity, and infrequent and high severity) within a >600,000 km^2 forested region (the Northwest US; Figure 3.1), asking: *(Q1) What is the contemporary range of variation in high-severity patch size and structure expected from fires of different sizes? (Q2) Do spatial scaling relationships vary by geographic region and/or time period (i.e., do they appear stationary in space and/or time)?* As fire size distributions shift in the future, stationarity in the relationships between fire size and patterns of burn severity would enable future broad-scale patterns of burn severity to be inferred.

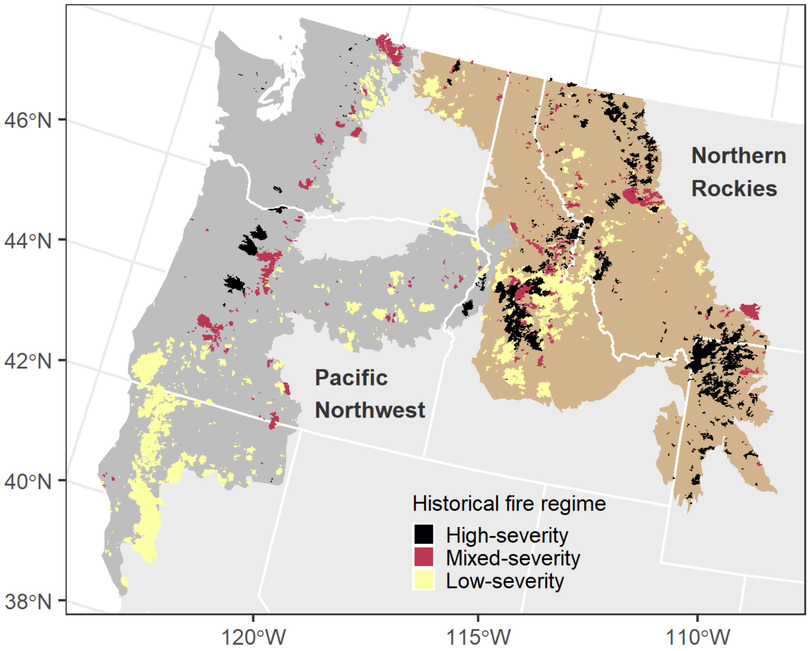

Figure 3.1. Study region with all wildfires categorized by primary historical fire regime. Fire regime classifications (frequent and low-severity, moderately frequent and mixed-severity, infrequent and high-severity) are from the LANDFIRE database (Rollins 2009).

To address these questions, we use nonparametric quantile regression to quantify the range of variation in scaling relationships for high-severity patch metrics, fitting smooth curves to multiple conditional quantiles of each metric across the range of observed fire sizes (400 – >400,000 ha). We thereby evaluate how the upper and lower bounds of high-severity patch size and structure (in addition to central tendency estimates) scale with fire size. To evaluate spatial and temporal stationarity, we test whether the scaling relationships that characterize fire regimes vary by geographic region (Pacific Northwest versus Northern Rockies; Figure 3.1), year, or time period [1985 – 2000 versus 2001 – 2020, the latter period being associated with increasing aridity and accelerating annual area burned in the western US (Juang *et al.* 2022)].

We evaluate spatial metrics describing both the size and structure of high-severity patches, including standard metrics often used in the landscape ecology of fire (area-weighted mean patch size and total interior core area). To complement these standard metrics, which describe central tendency or aggregate aspects of burn severity patterns, we evaluate additional metrics that quantify the full distributions of high-severity patch sizes (Figure 3.2a) and within-patch distances to unburned seed sources (Figure 3.2b) within each fire event. We introduce a novel approach for characterizing the high-severity patch size distribution within each fire event using a truncated lognormal distribution (Hantson *et al.* 2016), an approach previously applied to fire size distributions at broader scales. The shape of the distribution is determined by two parameters (curvature parameter ψ and slope parameter β) that describe the relative prevalence of small versus large patches within each fire event (Figure 3.2a). In this approach, $\psi < 0$ when fires are dominated by large patches and $\psi > 0$ when fires are dominated by small patches, with patch size distributions converging to a power law function when $\psi = 0$. We characterize distance-to-seed distributions using a shape parameter (the stand-replacing decay coefficient, SDC) that describes the rate at which the interior area of high-severity patches shrinks with distance to patch edge (Collins *et al.* 2017) (Figure 3.2b). In this approach, smaller values of SDC indicate larger and more homogenously shaped patches with interior areas far from surviving seed sources. See *Methods* for more information about satellite burn severity data, spatial metrics, and statistical analyses.

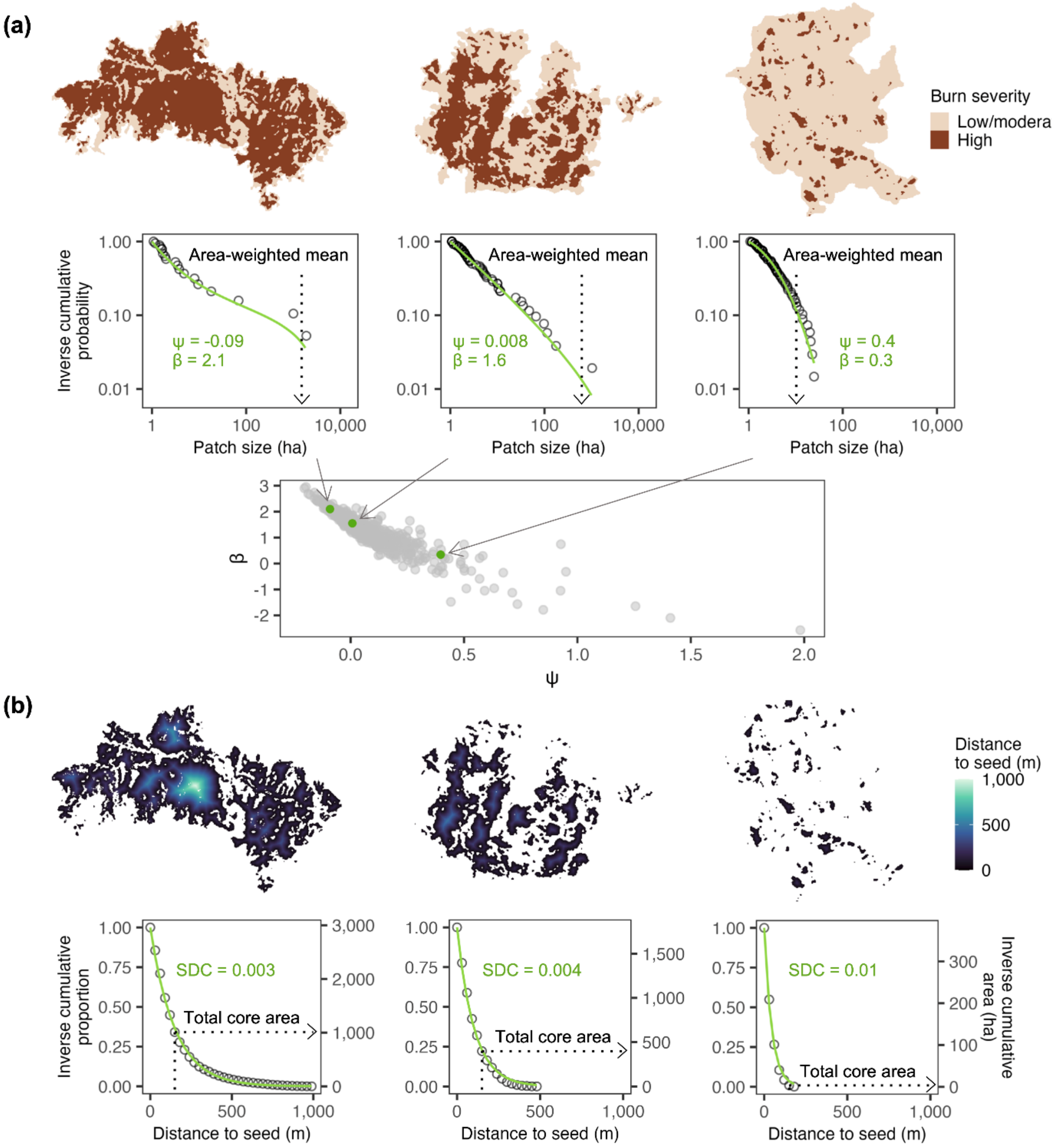

Figure 3.2. Schematic illustrating high-severity patch size and structure metrics. Metrics are shown for three wildfires that were similar in size (each 4,000 – 4,500 ha). Open circles represent observed data within each fire event, black dotted lines with arrows point to standard (aggregate or central tendency) metrics, and solid green lines represent metrics describing within-fire distributions. (a) Patch size metrics include area-weighted mean patch size and two parameters (ψ and β) describing the shape of the patch size distribution. When ψ is close to zero, patch size distributions resemble a power law function. When ψ is negative, patch size distributions curve upward and are typically characterized by one or more very large patches. When ψ is positive, patch size distributions curve downward and

are typically characterized by many small patches. Scatter plot of ψ and β shows parameter values for all fires in the dataset. (b) Patch structure metrics account for patch shape and forest cover and include total high-severity core area (previously forested pixels > 150 m from potential unburned seed source following fire) and one parameter (SDC) describing the shape of the distance-to-seed distribution for forested areas burned at high severity. Smaller values of SDC represent larger and more homogenously shaped patches with interior areas far from unburned seed sources. From left to right, example fires are the Fishhawk (Wyoming), Boze (Oregon), and Big Bend (Oregon) fires.

3.3 METHODS

3.3.1 *Study region*

Our study region is the forested ecoregions of the Northwest US (Wyoming, Montana, Idaho, Washington, Oregon, and northern California), delineated using EPA Level III Ecoregions (Commission for Environmental Cooperation 1997) (Figure 3.1). Climate, topography, and forest types vary widely across the study region, as do fire activity and fire-adapted traits of dominant tree species (Stevens *et al.* 2020; Hood *et al.* 2021; Reilly *et al.* 2021). Historical fire regimes range from frequent, low-severity fire in warmer and drier parts of the region to infrequent, high-severity fire in cooler and wetter parts of the region (Hood *et al.* 2021; Reilly *et al.* 2021). We used LANDFIRE land cover data to classify forested areas and fire regime groups (FRGs) throughout the study region (Rollins 2009). We identified potentially forested areas using LANDFIRE Environmental Site Potential (ESP) and classified the study region into three historical fire regimes: frequent and low severity (FRG I), moderately frequent and mixed severity (FRG III), and infrequent and high severity (FRG IV and FRG V).

3.3.2 *Fire severity data*

We obtained perimeters for all fire events $\geq$ 400 ha in size occurring within the study region between 1985 and 2020 from the Monitoring Trends in Burn Severity database (https://mtbs.gov/). We included only those fire events occurring in primarily forested areas ($\geq$ 50% forested based on LANDFIRE ESP) that were designated wildfires (i.e., we excluded prescribed fires). Each fire event was assigned its dominant historical fire regime (low-, mixed-, or high-severity) based on the most prevalent fire regime group within that fire's perimeter (Figure 3.1). In total, our dataset consisted of

1,615 individual fire events, with 751, 373, and 491 fire events assigned to the low-, mixed-, and high-severity fire regime groups, respectively.

Burn severity maps were generated for each fire event using Landsat satellite data and following previously established methods (Parks *et al.* 2018a). We quantified burn severity at a 30-m pixel scale using the relativized differenced normalized burn ratio (RdNBR), a satellite-based fire severity metric that estimates the amount of fire-induced vegetation change by comparing pre- and post-fire vegetation greenness indices (Miller & Thode 2007). We included an offset term in our calculation of RdNBR to account for phenological differences between pre- and post-fire imagery (Parks *et al.* 2018a). Following Harvey *et al.* (2023), we used statistical models calibrated to Northwest US field plots (Saberi & Harvey 2023) to identify a threshold of RdNBR (RdNBR $\geq$ 542) corresponding to $\geq$75% tree basal area mortality. We then used this threshold to categorize each burn severity map into high (RdNBR $\geq$ 542) and low-to-moderate (RdNBR < 542) burn severity classes. High-severity classifications based on satellite index thresholds regularly have the highest accuracy relative to other burn severity classes (Miller & Thode 2007; Cansler & McKenzie 2012; Lydersen *et al.* 2016), and similar thresholds for high-severity fire have been applied across a range of scales, from regional extents (Reilly *et al.* 2017; Stevens *et al.* 2017; Singleton *et al.* 2019) to the entirety of the western US (Parks *et al.* 2018b; Davis *et al.* 2023).

3.3.3 *Landscape metrics*

Our analysis focused on areas within each fire event that burned at high severity, quantifying landscape metrics describing both the size and spatial configuration of high-severity patches. High-severity patches were delineated using an eight-neighbor rule after a majority smoothing filter was applied to each categorized burn severity map to reduce the impact of single-pixel patches (Figure 3.2a). Within each high-severity patch, distance to seed source was quantified for each pixel that was potentially forested prior to burning. Distance to seed source was quantified by calculating the distance to the nearest potentially forested pixel that did not burn at high severity (Figure 3.2b).

We quantified the size of high-severity patches using two complementary approaches (Figure 3.2a). First, we calculated the area-weighted mean size of all high-severity patches within each fire event. By weighting larger patches more heavily, an area-weighted mean is larger than an arithmetic mean and represents the expected patch size that would be encountered in an average location within a landscape (Harvey *et al.* 2016a). Second, we characterized the shape of each patch size distribution using an approach that has, to the best of our knowledge, not previously been used to describe high-severity patch size distributions within fire events. Following the methods developed for fire size distributions by Hantson *et al.* (2016), we fit truncated lognormal distributions to the patch sizes within each fire event. The probability density function, p(x), for each patch size distribution takes the following form:

$$\ln p(x) = \ln C - \beta \ln(x) - \psi[\ln(x)]^2 \tag{3.1}$$

where C is a normalization constant, ensuring the area under p(x) sums to 1, and takes the following form:

$$C = \left(\int_{x_{min}}^{x_{max}} e^{-\beta \ln(x) - \psi[\ln(x)]^2} dx\right)^{-1} \tag{3.2}$$

The parameters x_{min} and x_{max} define the lower and upper truncation limits, respectively. We set x_{min} equal to 1 ha and x_{max} equal to the size of each individual fire event. Essentially, p(x) is a modified truncated power law function with an added term, ψ, that adds curvature to the distribution in log-log space (Pueyo 2006). Within the truncation limits, the parameters β and ψ determine the shape of each distribution (Figure 3.2a). When ψ is equal to 0, the distribution reduces to a power law function, and the shape of the distribution is a straight line in log-log space, with β determining the slope, or relative prevalence of small versus large patch sizes. When ψ is negative, the distribution curves upward in log-log space (i.e., there is a greater likelihood of large patches, relative to a power law function with the same value of β). When ψ is positive, the distribution curves downward in log-log space (i.e., there is a lower likelihood of large patches, relative to a power law function with the same value of β). In practice, the parameters β and ψ are highly correlated, with β decreasing as ψ increases (Figure 3.2a) (Hantson *et al.* 2016).

As with the size of high-severity patches, we quantified the spatial structure of high-severity patches using two complementary approaches (Figure 3.2b). First, we calculated total core area within the interior of high-severity patches, where core area is defined as previously forested pixels > 150 m from potential seed source following fire. This threshold of 150 m exceeds the likely seed dispersal distance for many conifers in the Northwest US (Donato *et al.* 2009; Harvey *et al.* 2016b). Second, using the approach proposed by (Collins *et al.* 2017), we characterized the rate at which the forested area within the interior of high-severity patches shrinks with increasing distance to potential seed source. In this approach, the proportion of total high-severity or “stand-replacing” forested area, P, exceeding a given distance to potential seed, dts, is modeled using a modified logistic function as follows:

$$P \sim \frac{1}{10^{\mathrm{SDC} \times \mathrm{dts}}} \tag{3.3}$$

Here, the stand-replacing decay coefficient (SDC) is a parameter determining the rate at which the proportional stand-replacing area decreases with increasing distance to potential seed. Larger values of SDC indicate a rapidly decaying interior area (i.e., most forested areas burned at high severity are relatively close to potential seed sources), whereas smaller values of SDC indicate a more slowly decaying interior area (i.e., more forested areas burned at high severity are far from potential seed sources) (Collins *et al.* 2017).

Area-weighted mean patch size and total core area were calculated using the *sf* and *raster* packages in R (Pebesma 2018; Hijmans *et al.* 2022). Patch size distribution shape parameters (β and ψ) were fit to the patch size distributions for each fire event using the maximum likelihood algorithm proposed by (Pueyo 2014). We only fit patch size distribution parameters for fire events with at least 10 patches that were $\geq$ 1 ha in size (Appendix E, Table 3.1). Distance-to-seed distribution parameters (SDC) were fit to the inverse cumulative distance-to-seed distributions for each fire event using nonlinear least squares, following Collins *et al.* (2017). Inverse cumulative distance-to-seed distributions were summarized using 30-m bins of pixel-level distance to potential seed source prior to parameter fitting, and parameters were fit only to those fire events with high-severity area falling within at least two 30-m bins (Appendix E, Table 3.2).

3.3.4 *Analysis*

We used nonparametric quantile regression to quantify the range of variation in high-severity patch size and structure metrics expected from fires of different sizes (Q1). Compared to standard regression approaches, which estimate the conditional mean of a response variable, quantile regression estimates the conditional quantiles of a response variable, thereby providing a fuller picture of the relationships between variables (Koenker & Bassett 1978; Cade & Noon 2003). This approach is particularly useful in ecological applications where complex interactions between multiple variables, many of which cannot be accounted for, lead to unequal variances in response distributions (Cade & Noon 2003). Rather than assuming linearity in scaling relationships, we used a nonparametric approach to fit smooth curves (via additive basis splines) to the conditional quantiles of each scaling relationship (Muggeo *et al.* 2021).

We fit smooth curves to five conditional quantiles (0.05, 0.25, 0.5, 0.75, and 0.95) of each patch size and structure metric across the range of observed fire sizes within each fire regime. Quantile curves were constrained to be monotonically increasing for area-weighted mean patch size and total core area, both of which are expected to continually increase with fire size (Cansler & McKenzie 2014; Harvey *et al.* 2016a; Reilly *et al.* 2017), and monotonically decreasing for the distance-to-seed parameter (SDC), which is expected to continually decrease with fire size (Collins *et al.* 2017). No monotonicity constraints were imposed for the patch size distribution parameters (β and ψ). Area-weighted mean patch size, total core area, and SDC were $\log_{10}$-transformed prior to model fitting; in cases where total core area was zero, we added 0.01 ha to enable $\log_{10}$-transformation. To evaluate potential differences between fire regimes, we also fit combined models for each metric with smooth terms for fire size that were allowed to vary by fire regime. We then evaluated whether there were significant differences between fire regime-specific scaling relationships by calculating pointwise differences, along with approximate 95% confidence intervals, between pairs of regime-specific quantile curves across the range of observed fire sizes following Rose *et al.* (2012). All quantile curves were fit using the *quantregGrowth* package in R (Muggeo 2021).

We used multiple lines of evidence to evaluate the spatial and temporal stationarity of scaling relationships (Q2). To evaluate spatial stationarity, we considered two broad geographic regions within our study area: the Pacific Northwest and the Northern Rockies (Figure 3.1). Unfortunately, within the high-severity fire regime, there were too few fire events in the Pacific Northwest (n = 42) for a robust comparison with the Northern Rockies (n = 449) (Appendix E, Table 3.1 and Table 3.2). Within the low- and mixed-severity fire regimes, however, we fit quantile regression models with smooth terms for fire size that were allowed to vary by geographic region. We then evaluated whether there were significant differences between region-specific scaling relationships by calculating pointwise differences between region-specific quantile curves, along with approximate 95% confidence intervals, following the approach used for fire regimes.

To evaluate temporal stationarity, we considered annual trends as well as two distinct time periods: an early period (1985 – 2000) and a late period (2001 – 2020), the latter of which is associated with increasing aridity and accelerating annual area burned in the western US (Juang *et al.* 2022). Within each fire regime, we fit three sets of quantile regression models. First, to assess interannual variation, we fit models with smooth terms for fire size and additional smooth terms for year. Second, to test for overall increasing or decreasing trends, we fit models with smooth terms for fire size and additional linear terms for year. Annual trends were considered statistically significant if $p < 0.05$ for the linear year term. Third, to evaluate whether there were significant differences between time period-specific scaling relationships, we fit quantile regression models with smooth terms for fire size that were allowed to vary by time period, following the approach used for fire regimes and geographic regions.

As an additional line of evidence, we used a 10-fold cross-validation procedure to evaluate whether adding a smooth term for year or allowing scaling relationships to vary either by time period or geographic region improved model predictive power over a null model (i.e., a model including fire size as the only predictor). Prediction error was calculated for quantiles 0.05, 0.5, and 0.95 using the quantile loss function (Koenker & Bassett 1978), which asymmetrically weights the absolute residuals and is analogous to the root mean square error used in standard regression models. Prediction error was averaged across quantiles and cross-validation folds for each model, with a reduction in overall average prediction error considered an improvement in model predictive power.

3.4 RESULTS

3.4.1 *Scaling relationships*

Across fire regimes, we observed qualitatively similar scaling relationships for high-severity patch size and structure (Figure 3.3a–j). Area-weighted mean patch size and total core area consistently increased with fire size (Figure 3.3a,b,g,h), reflecting the occurrence of increasingly large and spatially homogenous high-severity patches with increasing fire size. The distance-to-seed distribution parameter (SDC) consistently decreased with fire size (Figure 3.3i,j), indicating greater distances to unburned seed sources within patch interiors. Patch size distribution parameters were highly variable at small fire sizes, but as fire sizes increased, ψ approached a value of 0 and β a value of 1.5 (Figure 3.2a, Figure 3.3c–f). This suggests a convergence of patch size distributions toward a power law with increasing fire size.

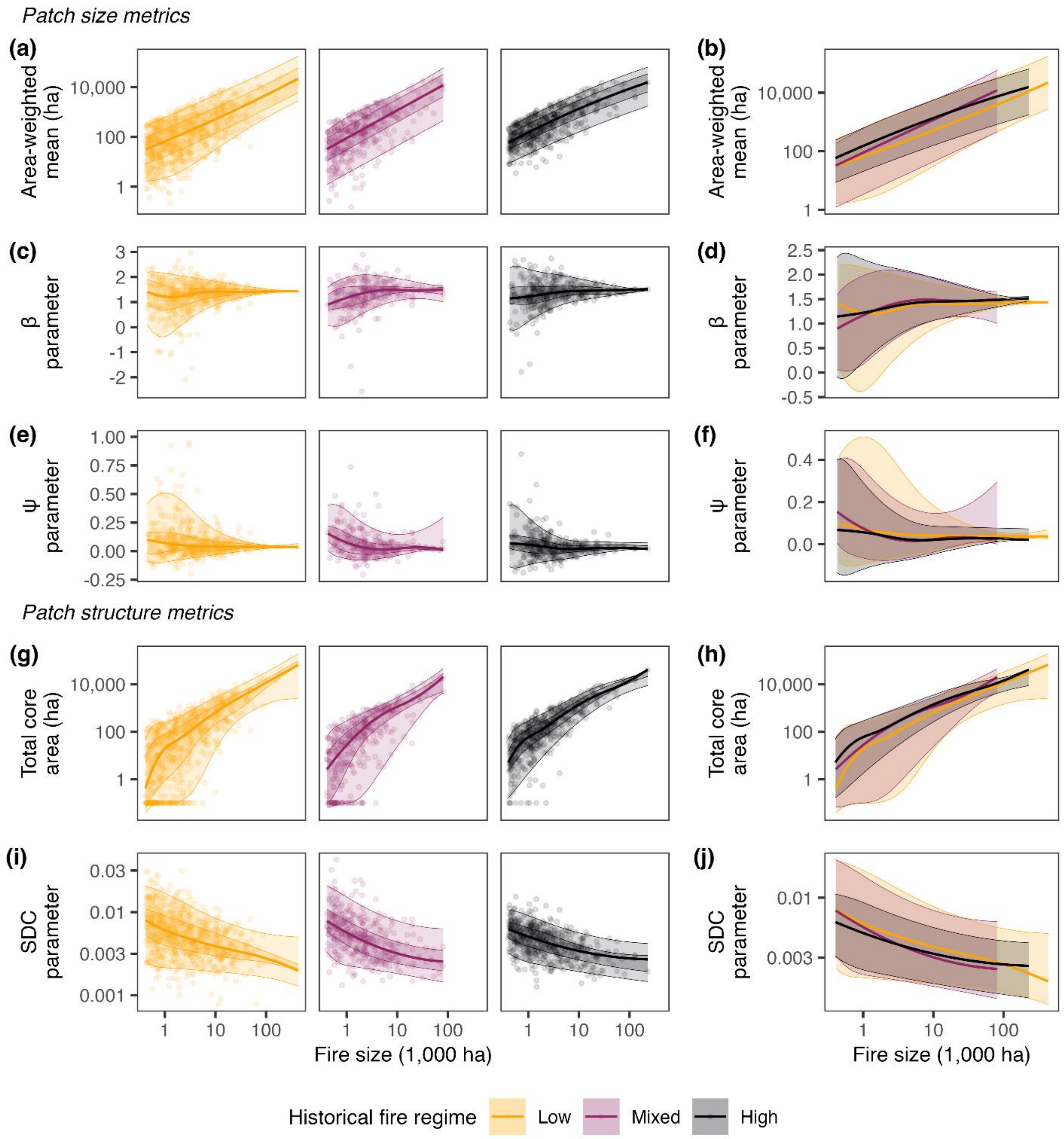

Figure 3.3. Quantile regression estimates for all high-severity patch size and structure metrics. Quantile regression estimates are plotted separately for each fire regime with observed data (left column) and overlaid for comparison across regimes (right column). Dots represent observed data, thick solid line is quantile 0.5, dark shaded region is interval between quantiles 0.25 and 0.75 (shown only in plots with observed data), and light shaded region is interval between quantiles 0.05 and 0.95. Three data points (for which $\psi > 1$) were excluded from (e) to improve visualization of quantile estimates.

Spatial scaling relationships were characterized by large ranges of variation, with the low- and mixed-severity fire regimes exhibiting wider ranges of variation for most metrics compared to the high-severity fire regime (Figure 3.3a–j). Across the range of fire sizes, the upper bounds for potential patch size and homogeneity (i.e., upper quantile estimates for area-weighted mean patch size and total core area, and lower quantile estimates for SDC) did not differ across fire regimes (Figure 3.3b,h,j, Appendix E, Figure 3.5). However, the lower bounds for potential patch size and homogeneity (i.e., lower quantile estimates for area-weighted mean patch size and total core area, and upper quantile estimates for SDC) varied across fire regimes (Figure 3.3b,h,j, Appendix E, Figure 3.5), with smaller and more heterogeneous patches tending to occur in the low- and mixed-severity regimes across the range of fire sizes.

3.4.2 *Spatial and temporal stationarity*

Within fire regimes, we observed both spatial and temporal stationarity in scaling relationships, as suggested by a lack of strong evidence that scaling relationships differ by region, time period, or year. After accounting for fire regime, region-specific scaling relationships (Pacific Northwest versus Northern Rockies; Figure 3.1) largely did not differ (in the low- and mixed-severity regimes, for which data were sufficient for robust regional comparisons; Appendix E, Figure 3.6), suggesting that fire regimes are characterized by consistent scaling relationships across space. We observed modest interannual variation in some scaling relationships (Figure 3.4); however, in most cases we detected no linear trend in scaling relationships over time (Figure 3.4) or difference in scaling relationships between time periods [early (1985 – 2000) versus late (2001 – 2020)] (Appendix E, Figure 3.7), suggesting the relationships between fire size and spatial patterns of burn severity are not yet changing over time and with warming climate. Cross-validation indicated that null models (i.e., models including fire size as the only predictor) offered the highest predictive power in most cases (Appendix E, Table 3.3 and Table 3.4); in cases where region, year, or time period did improve model performance, the improvement was slight (prediction error reduced by $\leq$1% compared to null models).

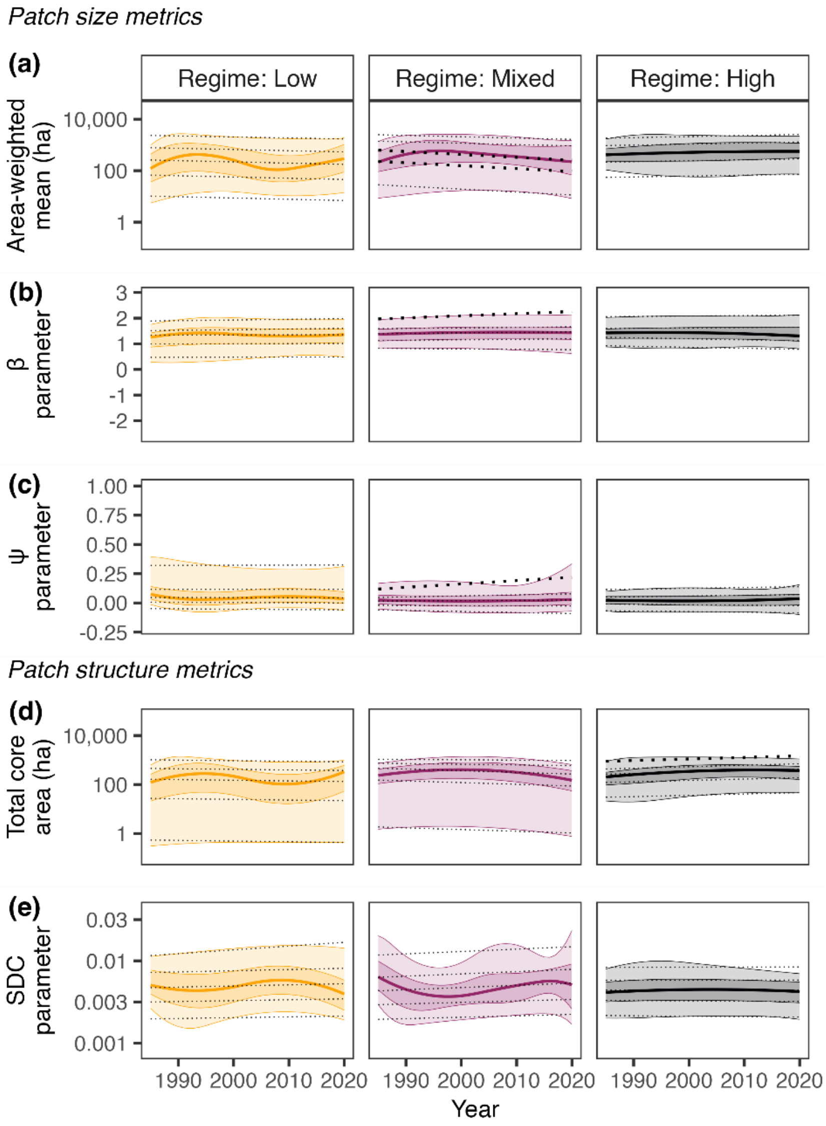

Figure 3.4. Estimated marginal effect of year for all metrics. Fire size is held constant at 3,000 ha. Solid lines and shaded intervals are quantile estimates from models with smooth term for year; solid line is quantile 0.5, dark shaded region is interval between quantiles 0.25 and 0.75, and light shaded region is interval between quantiles 0.05 and 0.95. Dotted lines are quantile estimates from models with linear term for year; heavy dotted lines indicate linear terms for which $p < 0.05$ and light dotted lines indicate linear terms for which $p \geq 0.05$. Linear terms were generally not statistically significant, suggesting temporal stationarity in the relationship between fire size and spatial patterns of burn severity.

3.5 DISCUSSION

Our findings demonstrate that spatial patterns of high-severity wildfire scale consistently with fire size, a phenomenon with important implications for how forests are shaped by increasing fire activity now and in the future. The robust scaling relationships that emerged within and among a range of forest ecosystems and fire regimes reveal characteristic signatures of contemporary forest fire activity. These scaling relationships, which appear stationary in both space and time, offer a powerful means to anticipate near-future patterns of burn severity as climate warming continues and fire sizes increase across ecosystems.

3.5.1 *Scaling relationships emerge within and among fire regimes*

High-severity patch size and structure followed clear scaling relationships that were qualitatively similar across fire regimes, demonstrating that across contemporary forest systems, larger wildfires consistently result in larger and more homogenous patches of severe fire effects. With greater fire size, high-severity patches tended to be larger and more spatially homogenous (greater area-weighted mean patch size and total core area), containing areas that were increasingly far from potential seed sources (lower SDC). In forested ecosystems that rely on seed dispersal for post-fire recovery, larger and simpler shaped high-severity patches can alter forest resilience, as these areas are more likely to regenerate slowly and to transition to non-forest vegetation states following fire (Coop *et al.* 2020).

Quantifying multiple conditional quantiles of patch size and structure revealed key similarities and differences in the ranges of burn severity patterns across fire regimes. The fire regimes in our study span a gradient of climate- to fuel-limitation, with fire activity in the infrequent, high-severity fire regime being primarily climate-limited and fire activity in the frequent, low-severity fire regime being primarily fuel-limited (Hood *et al.* 2021; Reilly *et al.* 2021). In the absence of other limiting factors, fire size itself imposes some natural upper limit to the size and homogeneity of high-severity burn patches. As limitations on fire severity increase in number and/or relative influence (e.g., in landscapes with complex topography, discontinuous fuel structure, and/or moderate fire weather conditions), patches are expected to become smaller in size or more complex in shape (Cansler & McKenzie 2014; Harvey *et al.* 2016a), therefore falling below the fire-size-imposed upper limits. Among fire regimes, the comparable upper bounds for patch size and homogeneity across the range of fire sizes suggests that when the influence of local-scale constraints is relatively weak (e.g., under extreme fire weather conditions), fire size itself imposes a comparable upper limit to patch size and structure across systems. In the low- and mixed-severity regimes, patches tended to fall below these fire-size-imposed upper limits more frequently than in the high-severity regime, with differing lower bounds emerging for patch size and homogeneity among fire regimes. This divergence in scaling relationships across fire regimes reflects the greater influence of local-scale constraints on fire severity in the low- and mixed-severity systems.

Contemporary ranges of variation in scaling relationships likely differ from historical ranges, particularly in the low- and mixed-severity regimes, due in large part to contemporary land management practices. Forests across the Northwest US have been subject to more than a century of fire exclusion and suppression (Hagmann *et al.* 2021), which can influence scaling relationships in multiple ways. First, since fire suppression efforts are less successful under extreme weather conditions (Arienti *et al.* 2006), the largest fires in our dataset are more likely to have burned under extreme conditions. In the absence of suppression efforts, a wider range of burn severity patterns for larger fires allowed to burn under mild or moderate weather conditions might be expected. Second, in low- and mixed-severity regimes, fire exclusion has led to an uncharacteristic buildup of fuels and a misalignment of forest structure and fire activity with historical conditions (Hagmann *et al.* 2021). Prior to European colonization, the low-severity regime was characterized predominantly by frequent but low-severity surface fires (Hood *et al.* 2021; Reilly *et al.* 2021). Although we found that burn severity patterns tended to be more heterogeneous in the low-severity regime, we also found that high-severity patches could be as large and homogenous as those observed in the high-severity regime, potentially reflecting this departure from historical conditions. This departure is a major concern for forest resilience in historically low-severity regimes, which are generally not as well adapted to recover from large patches of high-severity fire as are forests within high-severity regimes (Pausas *et al.* 2017; Stevens *et al.* 2020).

3.5.2 *Patch size distributions within large fires exhibit power law behavior*

The convergence of within-fire patch size distributions toward a power law function with increasing fire size carries implications for the scale of drivers operating within large fires. In the context of regional or global fire size distributions, power law behavior has been posited to emerge within facets of fire activity when there is a balance between broad-scale drivers and local-scale constraints (Moritz *et al.* 2011; McKenzie & Kennedy 2012; Povak *et al.* 2018). Here, the emergence of power law behavior for within-fire patch size distributions suggests that a similar balance may occur within fire events. For small- to moderate-sized fires (e.g., 400 – 10,000 ha), patch size distributions varied widely, with some fires characterized primarily by large patches and others primarily by small patches; this suggests that in smaller fires, either broad- or local-scale factors alone may primarily drive spatial patterns of burn severity. Conversely, the convergence of patch size distributions toward a power law function with increasing fire size suggests that both broad- and local-scale factors influence spatial patterns of burn severity within large fires (e.g., >10,000 ha). Large fires often coincide with (Clarke *et al.* 2020; Abatzoglou *et al.* 2021b) or can create their own (Fromm *et al.* 2010) extreme weather conditions, driving extreme fire behavior. The largest burn days and largest high-severity patches therefore occur when broad-scale drivers dominate (Peters *et al.* 2004). However, large fires can also burn over the course of many days to weeks (Scaduto *et al.* 2020), spanning a range of weather conditions and, by nature of covering large areas, encounter a range of topographic and vegetation structures. This wide range of conditions, alternating between places and times when broad- versus local-scale factors dominate, allows for the formation of a wide range of patch sizes, including many that are small but also some that are very large.

Despite occurring at the lowest frequency, the largest high-severity patches have the greatest ecological effect, both in terms of total high-severity burned area as well as distances to seed sources within patch interiors (Cansler & McKenzie 2014; Harvey *et al.* 2016a; Collins *et al.* 2017). Although patch size distributions within large fires consistently converged toward a probability distribution taking the form of a power law, the size of the largest high-severity patches still varied among fires. The lack of convergence in the distance-to-seed parameter (SDC) with increasing fire size suggests that even in the largest fires, ecological effects can vary widely, due to both the size and spatial configuration (i.e., shape and surrounding forest cover) of the largest patches.

3.5.3 *Stationary scaling relationships offer a means of projecting future fire effects*

Across a wide range of fire regimes and forest ecosystems, we found that the relationships between fire size and high-severity patch size and structure appear stationary in both space and time, even over a time period (1985 – 2020) where climate and fire size distributions themselves were temporally variable (Juang *et al.* 2022). Put plainly, even as fire size distributions have shifted toward larger fires, the ranges of burn severity patterns expected for fires of a given size have remained the same. As climate and fire activity continue to shift, and as fuel limitations potentially increase in areas subject to increasing fire activity (Kennedy *et al.* 2021; Turner *et al.* 2022), it is possible that the envelopes of potential burn severity patterns may shift in the future. Continued implementation of the methods presented here would permit such changes to be detected (e.g., downward shifts in scaling relationships might suggest an increasing prevalence of local-scale fuel constraints, thereby signaling potentially important changes in fire regimes). Within the contemporary fire record, however, our findings suggest that systematic shifts in scaling relationships have not yet occurred.

Managing for future fire requires not only projecting possible changes in regional metrics such as annual area burned, but also anticipating the potential ecological outcomes of those changes. Near-term shifts in fire size distributions alone (i.e., increasing frequency of large fires) will lead to predictable shifts in ecological effects (i.e., larger high-severity patches with interior burned areas far from potential seed sources). At broad scales, stationarity in scaling relationships offers a means of projecting the potential range of ecological effects expected with fire activity in the near future. Predicting burn severity patterns for a given landscape is difficult, since fire behavior is highly stochastic and weather conditions at the time of burning can strongly influence the burn severity patterns that result (Parks *et al.* 2018b; Prichard *et al.* 2020). However, by combining the range of variation in scaling relationships with projections for area burned and fire size distributions, it is possible to quantify the range of potential ecological effects of fire activity at a broader scale. Accounting for expected patterns of high-severity patch size and structure with increasing fire size enables bounds to be placed around potential outcomes, improving the ability to prepare for future fire activity.

3.6 CONCLUSION

Larger and simpler shaped high-severity burn patches can consistently be expected with larger fires, carrying important implications for forest resilience, ecosystem services, and societies living sustainably with fire. Wildfire-driven transitions of forests to alternative vegetation states are increasingly likely within large and homogenous high-severity burn patches, where post-fire tree regeneration is often limited by the availability of live seed sources. Spatial patterns of burn severity are therefore important to anticipate, as they can substantially alter habitat, hydrologic cycling, carbon storage, and the societal benefits provided by forests (Coop *et al.* 2020). Within contemporary fire regimes, the stationarity we observed in burn severity scaling relationships offers a means to anticipate the range of burn severity patterns expected with near-future fire activity. As fire activity continues to increase in many forested regions, and as the relative strength of climate drivers and fuel constraints potentially shift, these scaling relationships also offer a contemporary baseline that can be used to detect important changes that may occur within fire regimes in the future.

3.7 APPENDIX E

Table 3.1. Descriptive statistics for high-severity patch size metrics.

Fire regime	Region[a]	Time period[b]	n	Area-weighted mean (ha)					β parameter					ψ parameter				
				n[c]	Min	Max	Median	Mean	n[d]	Min	Max	Median	Mean	n[d]	Min	Max	Median	Mean
High	Combined	Combined	491	490	3.5	16,738	286	995	356	-1.78	2.74	1.36	1.35	356	-0.19	0.85	0.03	0.04
	N. Rockies	Combined	449	449	6.1	16,738	313	972	328	-1.78	2.74	1.38	1.36	328	-0.19	0.85	0.03	0.04
	P. Northwest	Combined	42	41	3.5	14,454	104	1,255	28	0.14	2.13	1.26	1.23	28	-0.12	0.25	0.06	0.07
	Combined	Early	144	143	3.5	16,738	228	897	100	-1.78	2.44	1.38	1.32	100	-0.15	0.85	0.03	0.05
	Combined	Late	347	347	7.9	15,227	300	1,036	256	-0.27	2.74	1.35	1.36	256	-0.19	0.42	0.03	0.04
Mixed	Combined	Combined	373	372	0.2	20,418	176	855	266	-2.57	2.90	1.40	1.32	266	-0.20	1.98	0.03	0.06
	N. Rockies	Combined	211	210	0.3	18,509	170	639	147	-0.37	2.47	1.40	1.38	147	-0.14	0.41	0.03	0.05
	P. Northwest	Combined	162	162	0.2	20,418	194	1,136	119	-2.57	2.90	1.39	1.25	119	-0.20	1.98	0.04	0.09
	Combined	Early	99	98	0.8	18,509	239	748	65	-1.57	2.47	1.39	1.27	65	-0.14	0.74	0.03	0.06
	Combined	Late	274	274	0.2	20,418	165	893	201	-2.57	2.90	1.40	1.33	201	-0.20	1.98	0.04	0.07
Low	Combined	Combined	751	747	0.2	28,602	153	772	531	-2.10	2.95	1.35	1.27	531	-0.20	1.41	0.05	0.08
	N. Rockies	Combined	261	259	0.4	17,374	114	690	187	-2.10	2.64	1.38	1.29	187	-0.15	1.41	0.04	0.08
	P. Northwest	Combined	490	488	0.2	28,602	182	816	344	-1.64	2.95	1.31	1.25	344	-0.20	1.26	0.05	0.09
	Combined	Early	252	250	0.4	14,345	158	695	174	-2.10	2.95	1.34	1.22	174	-0.20	1.41	0.05	0.09
	Combined	Late	499	497	0.2	28,602	152	811	357	-1.13	2.64	1.35	1.29	357	-0.15	0.95	0.05	0.08

[a] Statistics were calculated for two geographic regions (Northern Rockies and Pacific Northwest) as well as both regions combined.

[b] Statistics were calculated for two time periods [Early (1985 – 2000) and Late (2001 – 2020)] as well as both time periods combined.

[c] Area-weighted mean was calculated only for those fire events with one or more high-severity patches.

[d] β and ψ parameters were calculated only for those fire events with ≥ 10 high-severity patches that were ≥ 1 ha in size.

Table 3.2. Descriptive statistics for high-severity patch structure metrics.

Fire regime	Region[a]	Time period[b]	n	Total core area (ha)					SDC parameter				
				n	Min	Max	Median	Mean	n[c]	Min	Max	Median	Mean
High	Combined	Combined	491	491	0	41,569	127	894	490	0.0013	0.0153	0.0044	0.0047
	N. Rockies	Combined	449	449	0	41,569	138	863	449	0.0013	0.0143	0.0043	0.0046
	P. Northwest	Combined	42	42	0	16,212	63	1,228	41	0.0018	0.0153	0.0053	0.0059
	Combined	Early	144	144	0	41,569	86	980	143	0.0017	0.0153	0.0045	0.0049
	Combined	Late	347	347	0	18,137	138	858	347	0.0013	0.0124	0.0043	0.0047
Mixed	Combined	Combined	373	373	0	21,052	88	665	370	0.0013	0.0427	0.0049	0.0060
	N. Rockies	Combined	211	211	0	21,052	85	510	209	0.0015	0.0427	0.0049	0.0062
	P. Northwest	Combined	162	162	0	17,143	94	869	161	0.0013	0.0238	0.0048	0.0056
	Combined	Early	99	99	0	21,052	99	523	98	0.0015	0.0321	0.0044	0.0058
	Combined	Late	274	274	0	17,143	84	717	272	0.0013	0.0427	0.0051	0.0060
Low	Combined	Combined	751	751	0	66,319	85	825	742	0.0008	0.0312	0.0051	0.0062
	N. Rockies	Combined	261	261	0	16,427	57	691	256	0.0009	0.0279	0.0053	0.0064
	P. Northwest	Combined	490	490	0	66,319	103	897	486	0.0008	0.0312	0.0049	0.0061
	Combined	Early	252	252	0	16,427	81	541	248	0.0008	0.0305	0.0047	0.0057
	Combined	Late	499	499	0	66,319	86	969	494	0.0008	0.0312	0.0052	0.0064

[a] Statistics were calculated for two geographic regions (Northern Rockies and Pacific Northwest) as well as both regions combined.

[b] Statistics were calculated for two time periods [Early (1985 – 2000) and Late (2001 – 2020)] as well as both time periods combined.

[c] SDC parameter was calculated only for those fire events with high-severity area falling within at least two 30 m bins of pixel-level distance to potential seed source.

Table 3.3. Cross-validation results for evaluation of geographic region. Null models included fire size as the only predictor and do not account for region (i.e., Northern Rockies versus Pacific Northwest). Two region-specific model formulations were evaluated: one in which a combined model was fit to the data, within which quantile curves were allowed to vary by region ("1 model"), and another in which separate models were fit to each region ("2 models"). The highest ranked model for each combination of metric and fire regime is emphasized with bold font. Within the high-severity fire regime, there were too few fire events in the Pacific Northwest (n = 42) for a robust comparison with the Northern Rockies (n = 449).

Metric	Fire regime	Model rank	Model	Average quantile loss
Area-weighted mean	Low	**1**	**null**	**0.1432**
		2	region (2 models)	0.1434
		3	region (1 model)	0.1438
	Mixed	**1**	**null**	**0.1374**
		2	region (2 models)	0.1410
		3	region (1 model)	0.1418
β parameter	Low	**1**	**region (2 models)**	**0.0992**
		2	region (1 model)	0.1000
		3	null	0.1000
	Mixed	**1**	**null**	**0.1015**
		2	region (2 models)	0.1036
		3	region (1 model)	0.1050
ψ parameter	Low	**1**	**null**	**0.0246**
		2	region (1 model)	0.0251
		3	region (2 models)	0.0251
	Mixed	**1**	**null**	**0.0237**
		2	region (2 models)	0.0240
		3	region (1 model)	0.0249
Total core area	Low	**1**	**region (2 models)**	**0.1948**
		2	region (1 model)	0.1950
		3	null	0.1952
	Mixed	**1**	**null**	**0.1779**
		2	region (2 models)	0.1786
		3	region (1 model)	0.1794
SDC parameter	Low	**1**	**null**	**0.0483**
		2	region (2 models)	0.0483
		3	region (1 model)	0.0486
	Mixed	**1**	**null**	**0.0455**
		2	region (1 model)	0.0460
		3	region (2 models)	0.0463

Table 3.4. Cross-validation results for evaluation of year and time period. Null models included fire size as the only predictor and do not account for year or time period [i.e., Early (1985 – 2000) versus Late (2001 – 2020)]. Two time period-specific model formulations were evaluated: one in which a combined model was fit to the data, within which quantile curves were allowed to vary by time period ("1 model"), and another in which separate models were fit to each time period ("2 models"). The highest ranked model for each combination of metric and fire regime is emphasized with bold font.

Metric	Fire regime	Model rank	Model	Average quantile loss
Area-weighted mean	Low	**1**	**time period (2 models)**	**0.1423**
		2	year	0.1424
		3	time period (1 model)	0.1426
		4	null	0.1429
	Mixed	**1**	**null**	**0.1369**
		2	year	0.1385
		3	time period (2 models)	0.1389
		4	time period (1 model)	0.1393
	High	**1**	**null**	**0.0930**
		2	time period (2 models)	0.0931
		3	time period (1 model)	0.0943
		4	year	0.0944
β parameter	Low	**1**	**null**	**0.1006**
		2	time period (2 models)	0.1015
		3	year	0.1028
		4	time period (1 model)	0.1033
	Mixed	**1**	**null**	**0.1045**
		2	time period (1 model)	0.1047
		3	time period (2 models)	0.1053
		4	year	0.1078
	High	**1**	**year**	**0.0887**
		2	null	0.0892
		3	time period (2 models)	0.0950
		4	time period (1 model)	0.0974
ψ parameter	Low	**1**	**time period (2 models)**	**0.0246**
		2	null	0.0247
		3	year	0.0253
		4	time period (1 model)	0.0255
	Mixed	**1**	**null**	**0.0241**
		2	time period (2 models)	0.0246
		3	year	0.0248
		4	time period (1 model)	0.0251
	High	**1**	**null**	**0.0174**
		2	year	0.0176
		3	time period (2 models)	0.0186
		4	time period (1 model)	0.0190

Metric	Fire regime	Model rank	Model	Average quantile loss
Total core area	Low	**1**	**time period (1 model)**	**0.1944**
		2	year	0.1946
		3	time period (2 models)	0.1952
		4	null	0.1953
	Mixed	**1**	**null**	**0.1778**
		2	year	0.1802
		3	time period (1 model)	0.1810
		4	time period (2 models)	0.1811
	High	**1**	**null**	**0.1154**
		2	time period (2 models)	0.1171
		3	time period (1 model)	0.1176
		4	year	0.1190
SDC parameter	Low	**1**	**year**	**0.0479**
		2	time period (1 model)	0.0482
		3	time period (2 models)	0.0483
		4	null	0.0484
	Mixed	**1**	**year**	**0.0457**
		2	null	0.0458
		3	time period (1 model)	0.0460
		4	time period (2 models)	0.0461
	High	**1**	**null**	**0.0326**
		2	year	0.0330
		3	time period (2 models)	0.0331
		4	time period (1 model)	0.0332

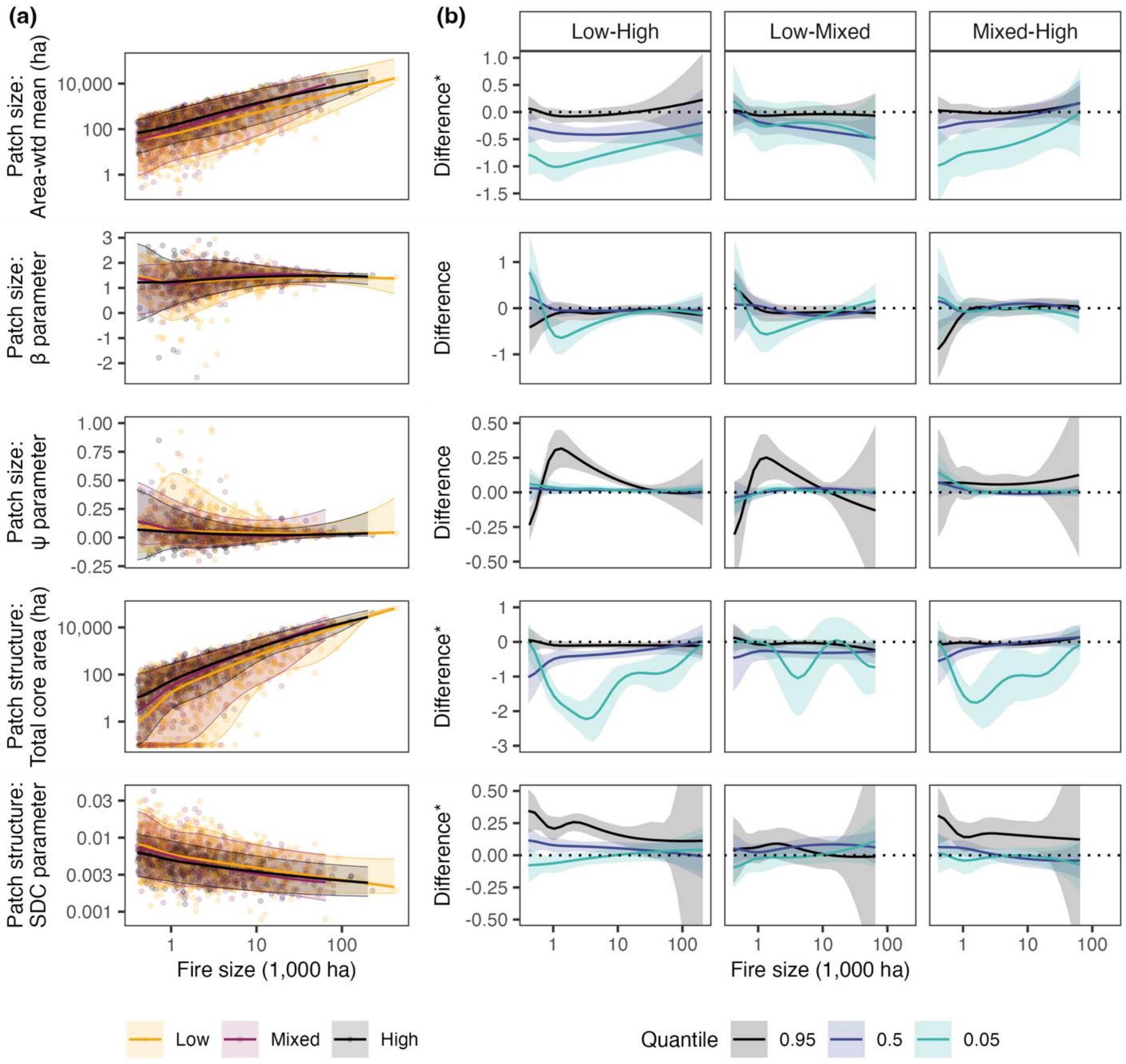

Figure 3.5. Quantile regression estimates where each quantile curve is allowed to vary by fire regime. (a) Solid line is quantile 0.5 and shaded region is interval between quantiles 0.05 and 0.95. (b) Estimated differences between quantile curves (solid lines) with 95% confidence intervals (shaded regions). Asterisks (*) indicate differences are on a $\log_{10}$-transformed scale.

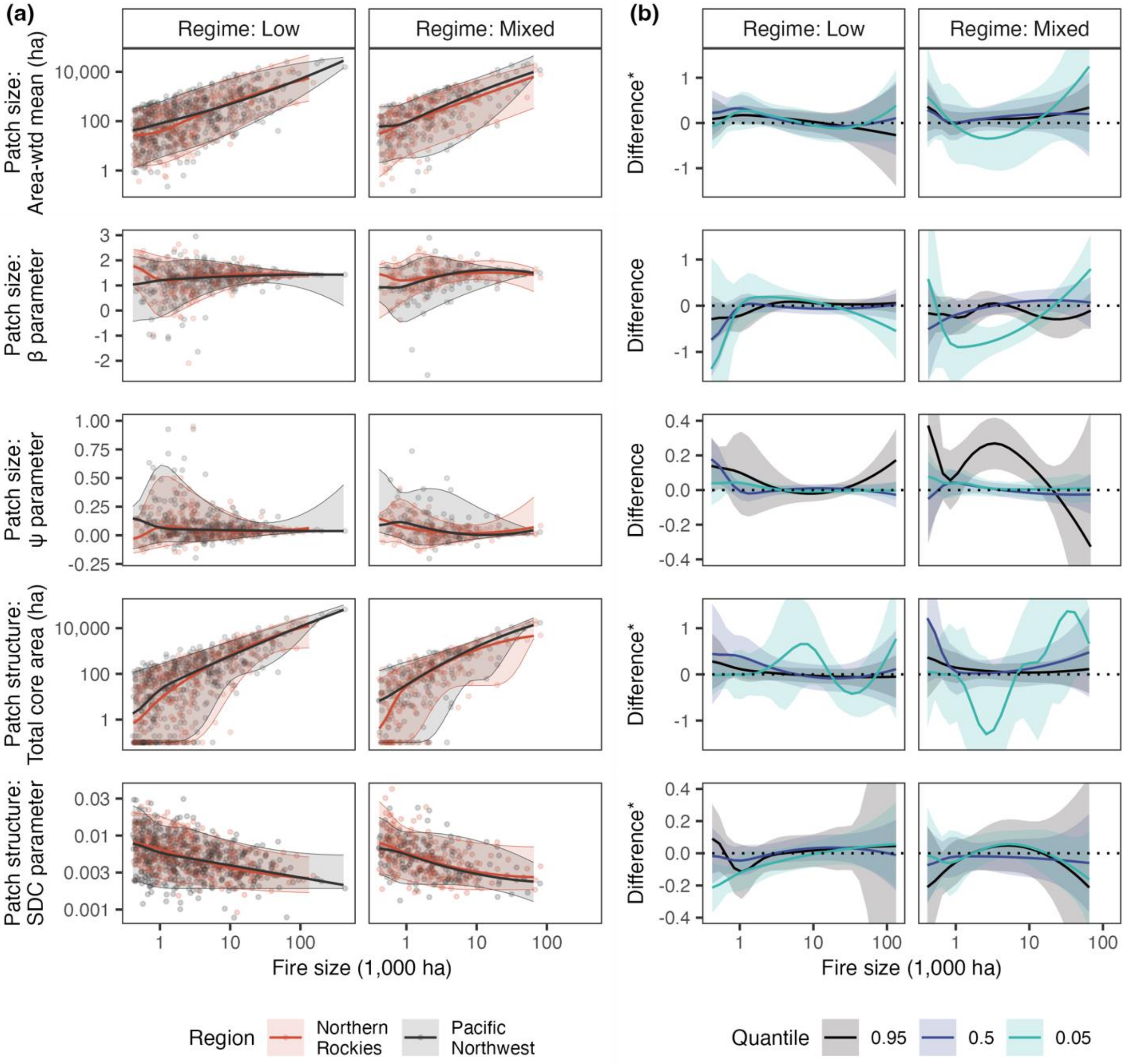

Figure 3.6. Quantile regression estimates where each quantile curve is allowed to vary by geographic region. (a) Solid line is quantile 0.5 and shaded region is interval between quantiles 0.05 and 0.95. (b) Estimated differences between quantile curves (Pacific Northwest minus Northern Rockies; solid lines) with 95% confidence intervals (shaded regions). Asterisks (*) indicate differences are on a log10-transformed scale. Within the high severity fire regime, there were too few fire events in the Pacific Northwest (n = 42) for a robust comparison with the Northern Rockies (n = 449).

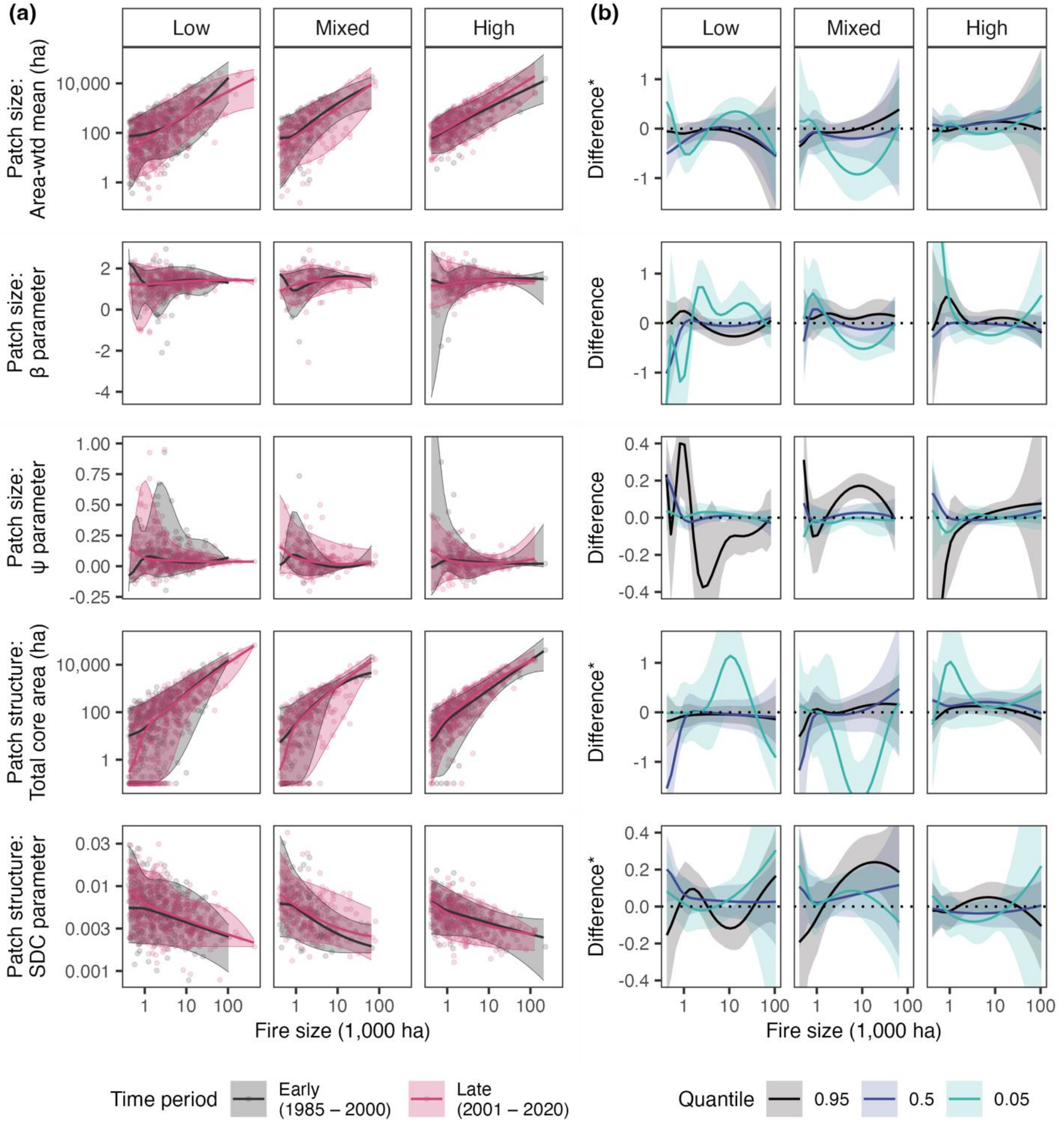

Figure 3.7. Quantile regression estimates where each quantile curve is allowed to vary by time period. Early period is defined as 1989 – 2000 and Late period is defined as 2001 – 2020. (a) Solid line is quantile 0.5 and shaded region is interval between quantiles 0.05 and 0.95. (b) Estimated differences between quantile curves (Late minus Early; solid lines) with 95% confidence intervals (shaded regions). Asterisks (*) indicate differences are on a $\log_{10}$-transformed scale.

Chapter 4. SCALING OF SEVERE FIRE PATTERNS ACROSS A RANGE OF FIRE SIZES AND FOREST ECOSYSTEMS YIELDS INSIGHTS FOR DATA-SPARSE AND INFREQUENT-FIRE REGIMES

4.1 ABSTRACT

As wildfire activity increases in many forested regions worldwide, anticipating the spatial patterns of burn severity expected with future fire activity is critical for informing management and policy actions regarding fire. In infrequent-fire forests where fire activity has historically been strongly limited by climate and ignitions, large increases in area burned are expected with warming and drying conditions. Characterizing expected burn severity patterns in these regions is challenging, however, because empirical data are inherently lacking. Here, leveraging a satellite burn severity dataset for 1,615 fire events occurring across the Northwest United States (US) between 1985 and 2020, we present an approach for characterizing expected patch-level burn severity patterns in data-sparse and infrequent-fire regimes. We use a specific focus region within the Pacific Northwest, US, where relatively infrequent but large and severe fires shape biomass-rich forests that underpin ecosystem services region-wide. We demonstrate how spatial scaling relationships relating overall fire size to high-severity patch size and shape, when combined with assumptions regarding regional area burned and fire size distributions, can be harnessed to anticipate future fire effects. Using a simulation approach, we quantify how for a given total burned area, the range of expected burn severity patterns varies widely but predictably, depending on the sizes of future fire events. Our results illustrate how shifts in fire size distributions towards larger fire events will lead to increasingly large high-severity burn patches with interior areas that are increasingly far from unburned seed sources following fire. In contrast, the same total area burned in more numerous but smaller fire events will result in qualitatively different patterns of burn severity, characterized by smaller high-severity patches and closer proximity to post-fire seed sources. These results have important management implications in forested regions characterized by infrequent but severe fire events, informing management actions ranging from pre-fire planning stages (e.g., fire response preparedness) to real-time decision-making (e.g., fire suppression versus managed wildfire use) and post-fire responses

(e.g., replanting to restore tree cover and/or promoting early-seral habitat). The approach we present can be applied across a range of fire regimes to forecast potential future fire effects.

4.2 INTRODUCTION

As climate changes worldwide, fire activity (i.e., area burned, fire frequency, and the occurrence of large fire events) is increasing in many forested ecosystems across the globe (Parks & Abatzoglou 2020; Collins *et al.* 2021; Duane *et al.* 2021). Climate-induced changes in fire activity are driven both by direct mechanisms (i.e., atmospheric effects on fuel moisture, winds) and indirect mechanisms (i.e., plant productivity effects on fuel accumulation and structure) (Abatzoglou *et al.* 2021a; Kennedy *et al.* 2021; McColl-Gausden *et al.* 2022). Because the relative influence of these mechanisms varies widely across forest ecosystems, climate-driven changes in fire activity are expected to vary across fire regimes (Littell *et al.* 2018; Halofsky *et al.* 2020; Whitman *et al.* 2022). Continued increases in fire activity are projected for many forested regions (Littell *et al.* 2018), underscoring the importance of understanding both the nature and ecological consequences of changing fire regimes.

While total area burned and fire size projections are important indicators of future fire activity and potential fire regime change, anticipating the ecological effects of fire requires also understanding the potential range of resulting burn severity patterns. Management actions, both before and after the occurrence of fire (e.g., vegetation management and replanting), can promote climate-adapted landscapes and reduce negative post-fire impacts on ecosystem services and forest function (Halofsky *et al.* 2018b; Prichard *et al.* 2021; Davis *et al.* 2023). However, preemptively developing post-fire response plans requires an understanding of the high-severity patch structure of individual fire events, as patches burned at high severity (i.e., areas in which most or all vegetation is killed by fire) are where post-fire management intervention is often of greatest priority. Because spatial patterns of burn severity are influenced by a complex mixture of drivers, they can be difficult to predict for any one landscape (Parks *et al.* 2018b; Newman *et al.* 2019; Prichard *et al.* 2020). More broadly, however, high-severity patch structure is strongly related to fire size and exhibits characteristic spatial scaling relationships (i.e., as fire size increases, so does the potential for large high-severity patches within which burned areas are very far from potential seed sources) (Cansler & McKenzie 2014; Harvey *et al.* 2016a; Collins *et al.* 2017). When combined with projections for total area burned and fire size distributions, as discussed in Chapter 3, these spatial scaling relationships can be harnessed to help anticipate future fire effects at regional scales.

As climate and fire activity continue to change, some of the largest future increases in area burned are expected to occur in historically cool, wet systems where fire activity has been limited by climate and ignitions rather than fuel (Littell *et al.* 2018; McColl- Gausden *et al.* 2022). Climate-limited fire regimes are typically characterized by infrequent fire activity, with fire return intervals on the order of centuries. While individual fire events can vary in both size and severity, the occurrence of large and severe fires is a common and expected feature of these regimes. Climate-limited regimes occur in many temperate and boreal forest zones across the globe, with one archetypical region being Northwestern Cascadia, a region in the Northwest United States (US) lying west of the Cascade Crest in Washington and northern Oregon (Figure 4.1). Forests in Northwestern Cascadia are highly biomass-rich and thus rarely fuel-limited, historically characterized by long fire-free intervals (i.e., >150 years) (Hemstrom & Franklin 1982; Agee 1993; Reilly *et al.* 2021). Though infrequent, fire events in Northwestern Cascadia have historically burned very large areas (i.e., 10^5 – 10^6 ha), with the largest fire events typically occurring when prolonged summer drought, an ignition, and a strong, synoptic east wind event coincide (Donato *et al.* 2020; Reilly *et al.* 2021). This was the case for the 2020 “Labor Day” fires in western Washington and Oregon, which collectively burned >300,000 ha over the course of just two weeks in September (Reilly *et al.* 2022). Climate projections for Northwestern Cascadia suggest summer fire seasons will become warmer and drier (Dalton *et al.* 2013; Mauger *et al.* 2015), and therefore the potential for fire activity, including very-large fire events, is expected to increase (Halofsky *et al.* 2018a, 2020).

Of particular interest as fire potential increases in many fire-prone regions is understanding how, for a given total burned area, burn severity patterns may differ if that area is burned in a few large fires versus many smaller fires. In climate-limited regimes such as Northwestern Cascadia, most fire events are relatively small, yet most burned area comes from a few very-large fire events (Agee 1998). Beyond their substantial contributions to total burned area, the largest fire events may also have the greatest cumulative ecological effects in terms of coarsening forest structure (Cova *et al.* 2023). As fire activity increases and fire size distributions potentially shift, a key question that arises is whether the occurrence of very-large fires is necessary to catalyze the greatest potential changes to forest structure (i.e., large patches of severe fire with long distances to surviving trees), or alternatively, whether the same total burned area distributed solely in small-to-moderate fire events might have comparable ecological effects. Understanding the cumulative impacts of varying fire size distributions will be critical for fire management planning that seeks to maintain forest resilience.

While there is historical precedent for fire activity in Northwestern Cascadia (Reilly *et al.* 2022), as with other landscapes characterized by infrequent yet severe disturbances, fires occurring in this region have been characteristically rare (n = 31) since the beginning of the satellite record (1985 – 2020). The sparseness of empirical data for Northwestern Cascadia limits understanding of fire and fire effects in this region and presents a challenge for quantifying statistically robust scaling relationships (i.e., relationships between fire size and burn severity patch metrics) using data solely from this region. During the same time period (1985 – 2020), however, fire activity throughout the broader Northwest US has been extensive. Many hundreds of fire events that have occurred in this broader region exhibit spatial scaling relationships that, while varying by fire regime, appear otherwise stationary in both space and time (see Chapter 3). Given the nature of fire activity in Northwestern Cascadia, we expect that burn severity patch structure in Northwestern Cascadia will exhibit spatial scaling relationships comparable to other high-severity fire regimes across the Northwest US. Due to the sparseness of empirical data in Northwestern Cascadia, however, a quantitative evaluation of how the Northwestern Cascadia region compares to the broader Northwest US has not yet been conducted.

Using a satellite fire severity dataset of 1,615 fire events occurring across the Northwest US between 1985 – 2020, we present an approach for characterizing burn severity patterns expected in the data-sparse and infrequent-fire region of Northwestern Cascadia. We ask: *(Q1) How do burn severity spatial scaling relationships in Northwestern Cascadia compare to other fire regimes across the Northwest US?* We evaluate the consistency of the sparse Northwestern Cascadia data with other fire regimes across the Northwest US, with the expectation that Northwestern Cascadia will be most consistent with infrequent, high-severity fire regimes (e.g., subalpine forests in the US Rocky Mountains). Then, harnessing a burn severity dataset that combines Northwestern Cascadia with its closest analogue fire regime in the broader Northwest US, we ask: *(Q2) How might the range of future burn severity patch structure in Northwestern Cascadia vary, depending on the size of future fire events?* Using simple fire size scenarios and a simulation-based approach, we assess how the cumulative effects of a given total burned area might vary, depending on whether the area burns in a small number of very-large fires versus more numerous but smaller fire events.

4.3 METHODS

4.3.1 *Study region*

Our primary study region is Northwestern Cascadia, the 6.1 million ha forested region west of the Cascade Crest in Washington and northern Oregon (Figure 4.1). This region has a Mediterranean climate, with most precipitation falling during the winter (i.e., between October and April) and summers that are typically warm and dry (Donato *et al.* 2020; Reilly *et al.* 2022). Northwestern Cascadia is dominated by the high-elevation, topographically complex Olympic Mountains, Western Cascades, and Coast Range. The Puget Lowlands and Willamette Valley, which transect this region and are characterized by lower elevations and simpler topography, are not considered part of our study scope (Figure 4.1). Forests in Northwestern Cascadia are some of the most productive, biomass-rich ecosystems in the world (Waring & Franklin 1979; Spies *et al.* 2018; Donato *et al.* 2020; Reilly *et al.* 2021). The primary vegetation zone in Northwestern Cascadia is the moist Douglas-fir/western hemlock zone, dominated by Douglas-fir (*Pseudotsuga menziesii*) successional to western hemlock (*Tsuga heterophylla*), with Pacific silver fir (*Abies amabilis*) and mountain hemlock (*Tsuga mertensiana*) vegetation zones occurring at the highest elevations (Reilly *et al.* 2021). Large, infrequent, and typically high-severity fires feature prominently in historical fire regimes throughout most of Northwestern Cascadia. More frequent mixed- or low-severity fires characterize lower elevation areas in the Puget Lowlands and Willamette Valley, where Indigenous burning practices were historically particularly important (Reilly *et al.* 2021, 2022). The southern boundary for Northwestern Cascadia is drawn at 44°44'N (approximately 20 km south of Salem, OR), as mixed- and low-severity fire regimes become more common at lower latitudes in western Oregon.

More broadly, for the purpose of comparison with Northwestern Cascadia, our study region also includes the forested ecoregions of the Northwest US (Wyoming, Montana, Idaho, Washington, Oregon, and northern California), delineated using EPA Level III Ecoregions (Commission for Environmental Cooperation 1997) (Figure 4.1). Climate, topography, and forest types vary widely across the Northwest US (Hood *et al.* 2021; Reilly *et al.* 2021). Historical fire regimes range from frequent, low-severity fire in warmer and drier parts of the region to infrequent, high-severity fire in cooler and wetter parts of the region (Agee 1993; Baker 2009; Hood *et al.* 2021; Reilly *et al.* 2021).

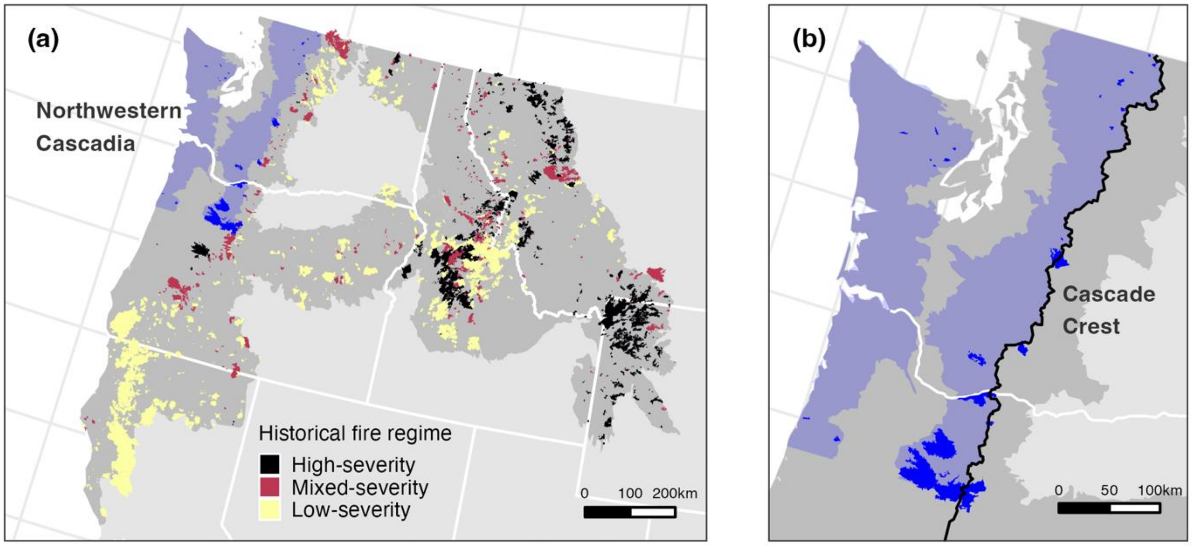

Figure 4.1. Study region map. (a) Northwest US study area (dark gray) with fire events categorized by primary historical fire regime group. (b) Inset showing Northwestern Cascadia region (light blue) and fire events (dark blue). Patch metrics for all Northwestern Cascadia fire events were calculated only for the portion of each fire that burned west of Cascade Crest.

4.3.2 *Fire severity data*

We used a satellite-derived fire severity dataset first described in Chapter 3, consisting of all fire events $\geq$ 400 ha in size occurring within the Northwest US between 1985 and 2020. Fire perimeters were obtained from the Monitoring Trends in Burn Severity database (https://mtbs.gov/), with prescribed fires and fire events occurring in primarily non-forest areas (< 50% forested based on LANDFIRE Environmental Site Potential [ESP]) excluded (Rollins 2009). Fire events were designated Northwestern Cascadia fires if they intersected the Northwestern Cascadia region and burned $\geq$ 400 ha west of the Cascade Crest. Each fire event falling outside of Northwestern Cascadia was assigned its dominant historical fire regime (low-, mixed-, or high-severity) based on the most prevalent LANDFIRE fire regime group within that fire's perimeter (Figure 4.1). In total, our dataset consisted of 1,615 individual fire events, with 31 Northwestern Cascadia fires and 751, 361, and 472 Northwest US fires assigned to the low-, mixed-, and high-severity fire regime groups, respectively.

Burn severity maps were generated for each fire event using 30-m resolution Landsat satellite data, following methods outlined by Parks *et al.* (2018a). To quantify burn severity, we used the relativized differenced normalized burn ratio (RdNBR), a metric that compares pre- and post-fire vegetation greenness indices (Miller & Thode 2007). Our calculation of RdNBR included an offset term to account for phenological differences between pre- and post-fire imagery and to facilitate comparison of RdNBR between fire events (Parks *et al.* 2018a). Following Harvey *et al.* (2023), we used statistical models calibrated to Northwest US field plots (Saberi & Harvey 2023) to identify a threshold of RdNBR (RdNBR $\geq$ 542) corresponding to $\geq$75% tree basal area mortality. We then used this threshold to categorize each burn severity map into high (RdNBR $\geq$ 542) and low-to-moderate (RdNBR < 542) burn severity classes. Satellite index thresholds have been shown to provide reliable approximations of high-severity burned areas (Lydersen *et al.* 2016) and have been used in many regional-scale burn-severity studies (Reilly *et al.* 2017; Stevens *et al.* 2017; Parks *et al.* 2018b; Singleton *et al.* 2019).

4.3.3 *Landscape metrics*

We quantified high-severity patch size and structure using the landscape metrics described in Chapter 3. First, we delineated high-severity patches using an eight-neighbor rule after applying a majority smoothing filter to each categorized burn severity map. Second, for pixels within each high-severity patch that were potentially forested (based on LANDFIRE ESP) prior to burning, we quantified distance to seed source by calculating the distance to the nearest potentially forested pixel that did not burn at high severity. Finally, we calculated five landscape metrics for each fire event (Table 4.1), with landscape metrics for Northwestern Cascadia fires calculated using only the portion of each fire that burned west of the Cascade Crest.

We quantified the size of high-severity patches within each fire event using two approaches (Table 4.1). First, we calculated the area-weighted mean patch size. Second, following the approach proposed in Chapter 3, we fit a truncated lognormal probability density function (Hantson *et al.* 2016) characterized by two shape parameters (β and ψ) to each patch size distribution. The probability density function, p(x), takes the following form:

$$\ln p(x) = \ln C - \beta \ln(x) - \psi[\ln(x)]^2 \tag{4.1}$$

where C is a normalization constant, ensuring the area under p(x) sums to 1. Within the lower and upper truncation limits (set equal to 1 ha and the size of each fire event, respectively), the parameters β and ψ determine the shape of each probability distribution. Fitted values of β and ψ are highly correlated, with β strongly decreasing as ψ increases (Hantson *et al.* 2016). When ψ is equal to 0, the distribution reduces to a power law function, and the shape of the distribution is a straight line in log-log space, with β determining the slope. When ψ is negative, patch size distributions curve upward in log-log space and are typically characterized by one or more very large patches. When ψ is positive, patch size distributions curve downward in log-log space and are typically characterized by many small patches.

We also quantified the structure of high-severity patches within each fire event using two approaches (Table 4.1). First, we calculated total core area, which includes all previously forested pixels within the interior of high-severity patches that are > 150 m from potential seed source following fire. The 150 m distance-to-seed threshold exceeds the likely seed dispersal distance for many wind-dispersed conifers in the Northwest US (Greene & Johnson 1989; Harvey *et al.* 2016b; Kemp *et al.* 2016). Second, we fit a parameter (the stand-replacing decay coefficient [SDC]) characterizing the rate at which the forested area within the interior of high-severity patches shrinks with increasing distance to potential seed source. Following the approach proposed by Collins *et al.* (2017), we used a modified logistic function to model the proportion of total high-severity or "stand-replacing" forested area, P_{dts}, exceeding a given distance to potential seed, dts, as follows:

$$P_{dts} \sim \frac{1}{10^{SDC \text{ x } dts}} \tag{4.2}$$

Larger values of the SDC parameter indicate a rapidly decaying interior area, whereas smaller values of SDC indicate a more slowly decaying interior area (Collins *et al.* 2017).

We calculated area-weighted mean patch size and total core area using the *sf* and *raster* packages in R (Pebesma 2018; Hijmans *et al.* 2022). For each fire event with $\geq$ 10 patches exceeding 1 ha in size, we fit patch size distribution shape parameters (β and ψ) using the maximum likelihood algorithm proposed by (Pueyo 2014). Finally, we summarized inverse cumulative distance-to-seed distributions for each fire event using 30 m bins of pixel-level distance-to-seed and fit SDC parameters using nonlinear least squares, following (Collins *et al.* 2017).

Table 4.1. Description of landscape metrics for high-severity patches used in analysis.

Metric	Units	Description
Patch size metrics		
Area-weighted mean patch size	ha	The expected patch size that would be encountered at an average location within the burned landscape (Harvey *et al.* 2016a).
β and ψ	unitless	Parameters characterizing the shape of each patch size frequency distribution. Fitted values of β (slope parameter) and ψ (curvature parameter) are highly correlated, with β strongly decreasing as ψ increases. When ψ is equal to 0, the distribution resembles a power law function, and the shape of the distribution is a straight line in log-log space. When ψ is negative, patch size distributions curve upward in log-log space and are typically dominated by one or more very large patches. When ψ is positive, patch size distributions curve downward in log-log space and are typically characterized by many small patches (Hantson *et al.* 2016).
Patch structure metrics		
Total core area	ha	Sum of all forested areas within the interior of high-severity patches that are > 150 m from potential seed source following fire. This distance-to-seed threshold exceeds the likely seed dispersal distance for many conifer species in the Northwest US (Greene & Johnson 1989; Harvey *et al.* 2016b; Kemp *et al.* 2016).
Stand-replacing decay coefficient (SDC)	unitless	Parameter characterizing the rate at which the interior forested area of high-severity patches shrinks with an increasing distance-to-seed threshold. Larger values indicate a rapidly decaying interior area (i.e., most forested areas that burned at high severity are relatively close to potential seed sources), whereas smaller values indicate a more slowly decaying interior area (i.e., more forested areas that burned at high severity are far from potential seed sources) (Collins *et al.* 2017).

4.3.4 *Spatial scaling relationships*

Following the approach used in Chapter 3, we used nonparametric quantile regression to quantify spatial scaling relationships across the Northwest US. Rather than estimating the conditional mean of a response variable distribution, quantile regression estimates the conditional quantiles, providing a fuller picture of the response distribution (Koenker & Bassett 1978; Cade & Noon 2003). Within each Northwest US fire regime group, we fit smooth curves to five conditional quantiles (0.05, 0.25, 0.5, 0.75, and 0.95) of each patch size and structure metric across the range of observed fire sizes. We constrained quantile curves to be monotonically increasing for area-weighted mean patch size and total core area and monotonically decreasing for the distance-to-seed parameter (SDC). No monotonicity constraints were imposed for the patch size distribution parameters (β and ψ). Area-weighted mean patch size, total core area, and SDC were $\log_{10}$-transformed prior to model fitting, and in cases where total core area was zero, we added 0.01 ha to enable $\log_{10}$-transformation. All quantile curves were fit via additive basis splines using the *quantregGrowth* package in R (Muggeo 2021).

To evaluate the consistency of Northwestern Cascadia with other fire regimes in the Northwest US (Q1), we compared the observed data for Northwestern Cascadia fire events to the predicted quantiles from each fire regime model. We calculated prediction error for each conditional quantile of each model using the quantile loss function (also called the quantile check function) (Koenker & Bassett 1978):

$$\rho_\tau(u) = \begin{cases} \tau u, & u \geq 0 \\ (\tau - 1)u, & u < 0 \end{cases} \tag{4.3}$$

Here, τ is the conditional quantile, with $0 < \tau < 1$, and u is the residual error (i.e., the observed Northwestern Cascadia value minus the model-predicted value). This function asymmetrically weights the absolute residuals and is analogous to the root mean square error used in standard regression models. Prediction error was averaged across quantiles for each model, and the model with the lowest overall average prediction error was considered most consistent with the Northwestern Cascadia data.

4.3.5 *Simulation study*

To illustrate how the range of future burn severity patch structure in Northwestern Cascadia might vary depending on the size of future fire events (Q2), we implemented a simulation study (Figure 4.2) that harnessed the range of variation in spatial scaling relationships expected for this region. We asked: *Assuming a total area of 1,000,000 ha were to burn in Northwestern Cascadia, what would the potential range of ecological effects be if this area were to burn as (a) 10 very large fires (each 100,000 ha), (b) 100 moderately large fires (each 10,000 ha), or (c) 1,000 smaller fires (each 1,000 ha)?* A total burned area of 1,000,000 ha would constitute 16% of the Northwestern Cascadia region and corresponds with the upper end of size estimates for historical fire episodes in this region (Donato *et al.* 2020). As a simple case study, we considered hypothetical fire sizes spanning three orders of magnitude (1,000 – 100,000 ha) (Figure 4.2a). For context, recent notable fire events in Northwestern Cascadia have spanned these same three orders of magnitude (e.g., the 2015 Paradise fire in Washington [1,140 ha], the 2020 Big Hollow fire in Washington [9,811 ha], and the 2020 Beachie Creek fire in Oregon [78,761 ha]).

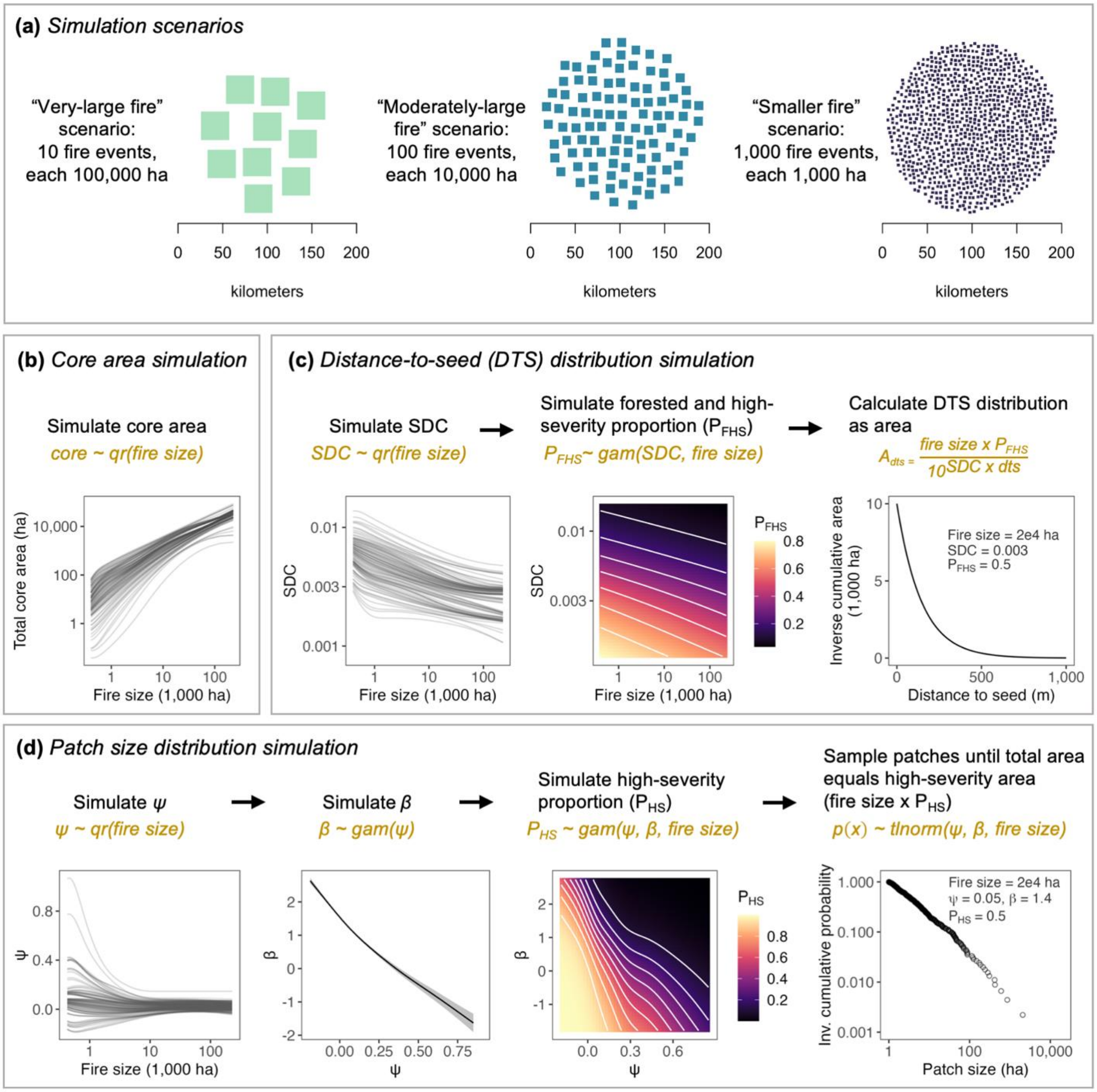

Figure 4.2. Simulation scenarios and workflows. (a) Conceptual illustration of simulation scenarios. Simulation study workflows are shown for (b) core areas, (c) distance-to-seed (DTS) distributions, and (d) patch size distributions. For more detailed information regarding simulation study methods, see Appendix F.

To conduct this simulation study, we first pooled the sparse data for Northwestern Cascadia together with the data from the most comparable fire regime in the Northwest US (from Q1). We then fit quantile regression models for each spatial metric to the pooled data, and using these combined models, we simulated a core area, distance-to-seed distribution, and patch size distribution for each hypothetical fire event based on its size (Figure 4.2b-d). We aggregated the simulated metrics across fire events in each scenario (e.g., for total core area in scenario [a], we summed together the individual core areas simulated for each of the 10 hypothetical fires) to quantify cumulative effects across the hypothetical 1,000,000 ha burned. Each scenario was simulated 100 times. Following (Kennedy 2019), who used principles of experimental design to determine the number replicates necessary to detect a given effect size for a stochastic model, we determined 100 replicates would be sufficient to detect aggregate core area effect sizes up to 9,000 ha.

The number of steps required to simulate each spatial metric varied, with total core area being the most straightforward, as it is an aggregate metric for each fire in units (ha) that can simply be further aggregated (i.e., summed) across fire events. To simulate total core area (Figure 4.2b), we fit smooth curves to 99 conditional quantiles (0.01 through 0.99) of the total core area distribution across the range of observed fire sizes. Then, to simulate total core area for a fire of any given size, we extracted the 99 conditional quantile predictions at that fire size and randomly drew one value. This sampling approach is a coarse and empirical adaptation of inverse transform sampling, a method that is frequently used to generate random samples from known probability distributions (Devroye 1986).

For the distance-to-seed and patch size distributions, additional assumptions and simulation steps were required. From the SDC parameter, we can calculate (using Equation 4.2) a proportional distance-to-seed distribution. Aggregating distance-to-seed distributions across fire events, however, requires calculating each distance-to-seed distribution in terms of areas (i.e., in ha); doing so requires knowing the total area within each fire that was both forested and burned at high severity. Similarly, from the β and ψ parameters, we can randomly draw (using Equation 4.1) some number of patch sizes from a truncated lognormal distribution. Aggregating patch size distributions across fire events, however, requires constraining the random sample of high-severity patches drawn for each fire, such that the total area of all high-severity patches is equal to the total high-severity burned area for that fire. Thus, for the distance-to-seed distributions, we needed to simulate the forested and high-severity proportion (P_{FHS}) of each fire (in addition to simulating SDC), and for the patch size distributions, we needed to simulate the high-severity proportion (P_{HS}) of each fire (in addition to simulating β and ψ).

Across fire events, landscape metrics describing spatial patterns of burn severity naturally tend to be correlated with one another (Neel *et al.* 2004). In our dataset, we observed that fire size, SDC, and

P_{FHS} were correlated with one another, as were fire size, β, ψ, and P_{HS}. This correlation enabled us to sequentially simulate sets of parameters jointly falling within the range of variation observed in our dataset. For example, once fire size is fixed, the conditional range of variation in SDC is reduced and we can sample from its conditional distribution given fire size; then, once fire size and SDC are fixed, the conditional range of variation in P_{FHS} is reduced and we can sample from its conditional distribution given fire size and SDC. We followed this logic for the simulation of both distance-to-seed and patch size distributions, as described below.

To simulate distance-to-seed distributions (Figure 4.2c), we first fixed fire size and simulated a value for SDC using the quantile regression approach described above for total core area. After simulating the SDC parameter, we simulated P_{FHS} for each fire using a generalized additive model (GAM) fit to P_{FHS} as a function of SDC and fire size. Finally, we used the simulated SDC parameter to calculate an area-based distance-to-seed distribution, where the cumulative area (in ha) exceeding each distance-to-seed threshold (A_{dts}) is calculated as a function of fire size, P_{FHS}, and SDC as follows:

$$A_{dts} = \frac{\text{fire size x } P_{FHS}}{10^{\text{SDC x dts}}} \tag{4.4}$$

Equation 4.4 is a modified version of Equation 4.2, where fire size and P_{FHS} are included as additional parameters to calculate an area-based rather than a proportional distance-to-seed distribution.

To simulate patch size distributions (Figure 4.2d), we first fixed fire size and simulated a value for ψ using the quantile regression approach described above for total core area and SDC. We then simulated a value for β, which is highly correlated with ψ, using a GAM fit to β as a function of ψ. After simulating the ψ and β parameters, we simulated P_{HS} for each fire using a GAM fit to P_{HS} as a function of ψ, β, and fire size. Finally, we used the simulated ψ and β to parameterize a truncated lognormal distribution, from which we sampled patches until the total area of patches equaled the simulated high-severity area (A_{HS}; calculated as fire size multiplied by P_{HS}). GAMs were fit using the *mgcv* package in R (Wood 2022). For a more detailed description and additional information regarding simulation study methods, see Appendix F.

4.4 RESULTS

4.4.1 *Comparison of Northwestern Cascadia to broader Northwest US fire regimes*

High-severity patch size and structure metrics for Northwestern Cascadia fall within the range of variation in scaling relationships for fire regimes across the broader Northwest US (Figure 4.3), with the high-severity fire regime being the closest analogue for Northwestern Cascadia overall. Scaling relationships were qualitatively similar across Northwest US fire regimes, with differences between fire regimes emerging only in those conditional quantiles corresponding to the lower bounds for potential patch size and homogeneity (i.e., lower quantile estimates for area-weighted mean patch size and total core area, and upper quantile estimates for the distance-to-seed parameter [SDC]; Figure 4.3; also see Chapter 3). For most patch metrics (area-weighted mean patch size, the ψ parameter for patch size, and total core area), scaling relationships for the high-severity regime were most consistent with the Northwestern Cascadia data, both visually (Figure 4.3) and in terms of overall average prediction error (Appendix G, Table 4.4). For the β parameter, the low-severity fire regime offered the lowest overall average prediction error (Appendix G, Table 4.4); however, scaling relationships for β did not differ strongly across fire regime groups (Figure 4.3). For the SDC parameter, although the mixed-severity fire regime offered the lowest overall average prediction error for the Northwestern Cascadia data (Appendix G, Table 4.4), the high-severity fire regime offered a comparable overall fit (Figure 4.3) and lower prediction error at the upper conditional quantile (0.95) where scaling relationships diverged across fire regimes (Appendix G, Figure 4.22). Thus, across metrics, the weight of evidence suggested that scaling relationships from the high-severity regime provide the closest available analogue for fires occurring in Northwest Cascadia.

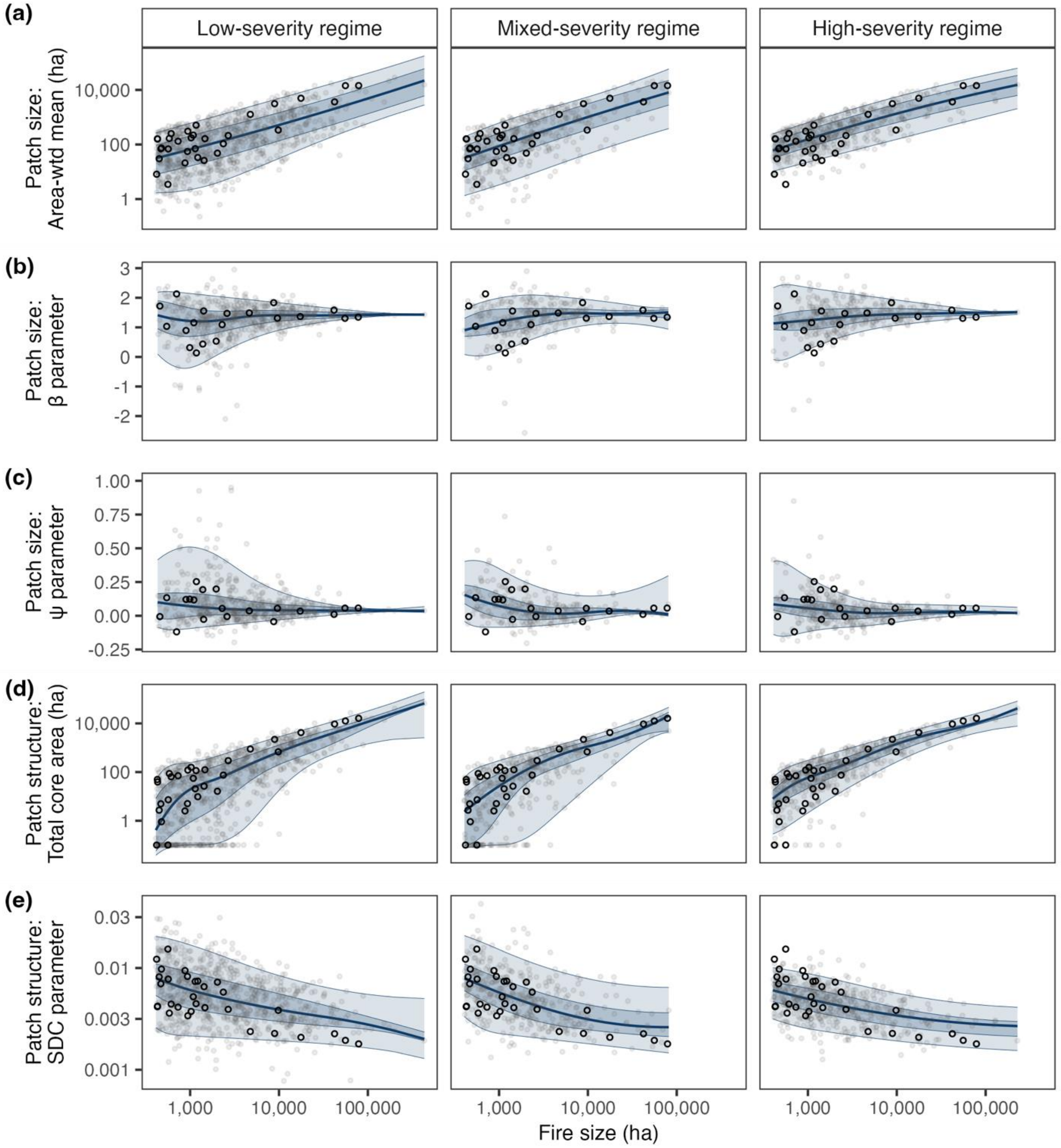

Figure 4.3. Northwestern Cascadia data overlaid on scaling relationships for Northwest US fire regime groups. Black open circles represent Northwestern Cascadia data and gray dots represent observed data for each fire regime group within the larger Northwest US study area. Solid line is quantile 0.5, dark shaded region is interval between quantiles 0.25 and 0.75, and light shaded region is interval between quantiles 0.05 and 0.95. Three Northwest US data points (for which $\psi > 1$) were excluded from (c) to improve visualization of quantile estimates.

4.4.2 *Simulation study*

Across simulation scenarios, as the size of fire events composing the hypothetical total 1,000,000 ha burned area increased (i.e., as burned area came from fewer but larger fire events), aggregate core areas increased and aggregate distance-to-seed distributions shifted to the right (i.e., greater amounts of high-severity burned forest area were farther from potential live seed sources) (Table 4.2, Figure 4.4). Aggregate core area increased substantially between the smallest (i.e., 1,000 ha) fire size scenario (mean = 88,775 ha, or 8.9% of the total burned area) and each of the larger fire size scenarios, though did not differ between the moderately-large (i.e., 10,000 ha) fire size scenario (mean = 154,720 ha, or 15.5% of the total burned area) and the very-large (i.e., 100,000 ha) fire size scenario (mean = 154,557 ha, or 15.5% of the total burned area; $p > 0.05$ using ANOVA and Tukey's HSD) (Table 4.2, Figure 4.4a). To evaluate whether this potential asymptote in aggregate core area (observed between the moderately- and very-larger fire size scenarios) was sensitive to the distance-to-seed threshold used to define core area, we replicated our simulation study for core areas calculated using a 300 m distance threshold. When we increased the distance threshold from 150 m to 300 m, aggregate core area consistently increased across fire size scenarios, with mean simulated core areas of 18,808 ha, 57,547 ha, and 72,842 ha (1.9%, 5.8%, and 7.3% of the total burned area) for the small, moderately-large, and very-large fire size scenarios, respectively (Appendix F).

Table 4.2. Descriptive statistics for simulated aggregate core areas and distance-to-seed distributions, summarized over 100 iterations of each simulation scenario.

Distance-to-seed threshold	Number and size of fire events	Area exceeding distance-to-seed threshold (ha)			
		Mean	SD	Min	Max
Core area approach					
150 m	10 x 100,000 ha	154,557	18,489	113,390	198,879
	100 x 10,000 ha	154,720	10,848	126,371	181,922
	1,000 x 1,000 ha	88,775	2,991	83,359	97,209
Distance-to-seed distribution approach					
150 m	10 x 100,000 ha	187,575	31,002	116,662	255,201
	100 x 10,000 ha	148,436	7,965	131,418	167,847
	1,000 x 1,000 ha	90,899	2,525	84,308	97,320
450 m	10 x 100,000 ha	41,786	12,529	17,075	74,860
	100 x 10,000 ha	22,734	2,323	17,867	28,281
	1,000 x 1,000 ha	8,967	522	7,735	10,053
750 m	10 x 100,000 ha	10,770	4,524	2,409	24,702
	100 x 10,000 ha	4,311	622	3,124	6,065
	1,000 x 1,000 ha	1,325	123	1,048	1,580

As fire size increased, the tails of the aggregate distance-to-seed distributions became heavier (i.e., more high-severity burned area exceeded greater distance-to-seed thresholds). For example, aggregate areas exceeding a distance of 750 m to the nearest unburned seed source were 1,325 ha, 4,311 ha, and 10,770 ha (0.1%, 0.4%, and 1.1% of the total burned area) on average in the small, moderately-large, and very-large fire size scenarios, respectively (Table 4.2, Figure 4.4b). Area estimates in the tails of the simulated distance-to-seed distributions are likely to be overestimates, since actual patch interior areas will reach zero with increasing distance-to-seed, whereas the modified logistic function we used to model distance-to-seed distributions (Equations 4.2, 4.4) only approaches zero (Collins *et al.* 2017). Nevertheless, the simulated distributions (Figure 4.4b) provide good approximations of the effect of increasing fire size.

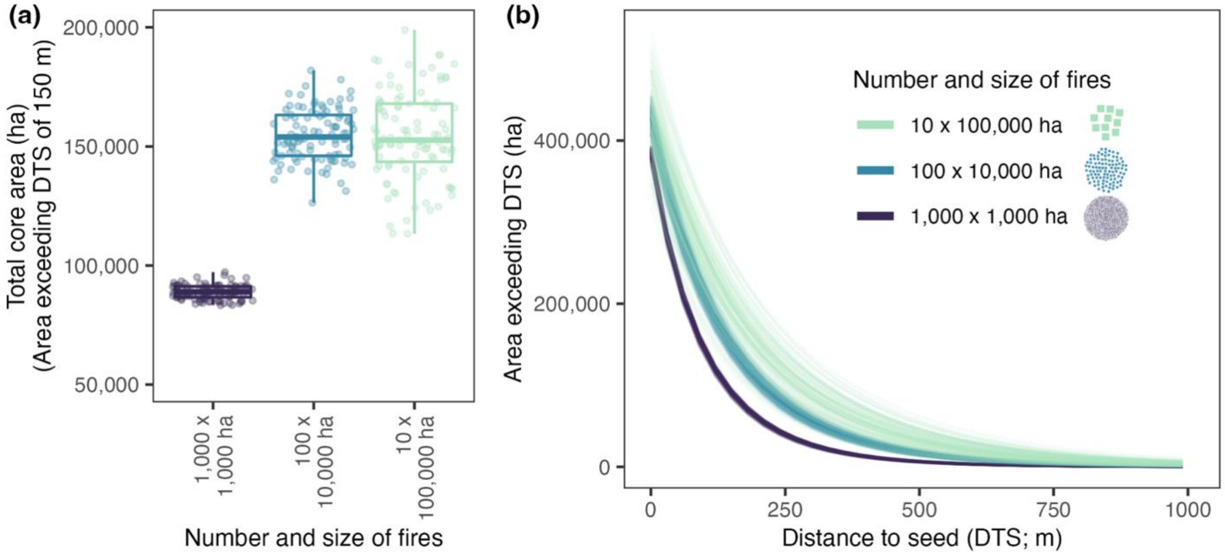

Figure 4.4. Simulated aggregate (a) core areas and (b) distance-to-seed distributions. Each scenario represents the same hypothetical total area burned (1,000,000 ha) and was simulated 100 times, with each iteration displayed as a single dot in (a) and single line in (b).

By definition, aggregate core area estimates in our study represent the total forested area burned at high severity and exceeding a threshold of 150 m to seed, and thus can be directly compared to aggregate distance-to-seed distribution estimates at that same threshold. The two approaches yielded qualitatively similar results, though estimates from the distance-to-seed distribution approach were biased slightly high relative to estimates from the core area approach in the very-large fire size scenario (Table 4.2, Appendix F).

Simulated aggregate patch size distributions were characterized by increasingly large patches as the size of fire events increased (Table 4.3, Figure 4.5). Area-weighted mean patch sizes consistently increased with the size of fire events, as did maximum patch sizes, the latter of which ranged from 602 – 811 ha across iterations in the smallest fire size scenario, from 5,406 – 8,166 ha across iterations in the moderately-large fire size scenario, and from 19,419 – 68,172 ha across iterations in the very-large fire size scenario (Table 4.3, Figure 4.5). Most patches across fire size scenarios were relatively small, with median patch sizes of ~3 ha on average across iterations and scenarios (Table 4.3). In the moderately- and very-large fire size scenarios, however, the contribution of large patches to the total high-severity burned area was substantial; on average, patches ≥ 1,000 ha accounted for 48% of the total high-severity burned area in the moderately-large fire size scenario (ranging from 39 – 56%) and 66% of the total high-severity burned area in the very-large fire size scenario (ranging from 45 – 84%) (Figure 4.5b).

Finally, we observed that the variation in simulated aggregate metrics consistently increased across fire size scenarios (Table 4.2, Table 4.3, Figure 4.4, Figure 4.5). For example, the standard deviation of simulated aggregate core area increased by a factor of four between the small and moderately-large fire size scenario, and by a factor of two between the moderately- and very-large fire size scenarios (Table 4.2). This finding was even more pronounced for the simulated patch size distributions; for example, the standard deviation of maximum simulated patch sizes increased by a factor of 14 between the small and moderately-large fire size scenarios, and by a factor of 19 between the moderately- and very-large fire size scenarios (Table 4.3).

Table 4.3. Descriptive statistics for simulated aggregate patch size distributions, summarized over 100 iterations of each simulation scenario.

Number and size of fire events	Median patch size (ha)				Area-weighted mean patch size (ha)				Maximum patch size (ha)			
	Mean	SD	Min	Max	Mean	SD	Min	Max	Mean	SD	Min	Max
10 x 100,000 ha	3.4	0.5	2.4	5.1	11,487	4,208	4,587	21,754	42,457	11,043	19,419	68,172
100 x 10,000 ha	3.3	0.1	3.0	3.6	1,594	162	1,194	2,008	6,658	569	5,406	8,166
1,000 x 1,000 ha	3.4	0.1	3.3	3.6	146	5	132	158	708	41	602	811

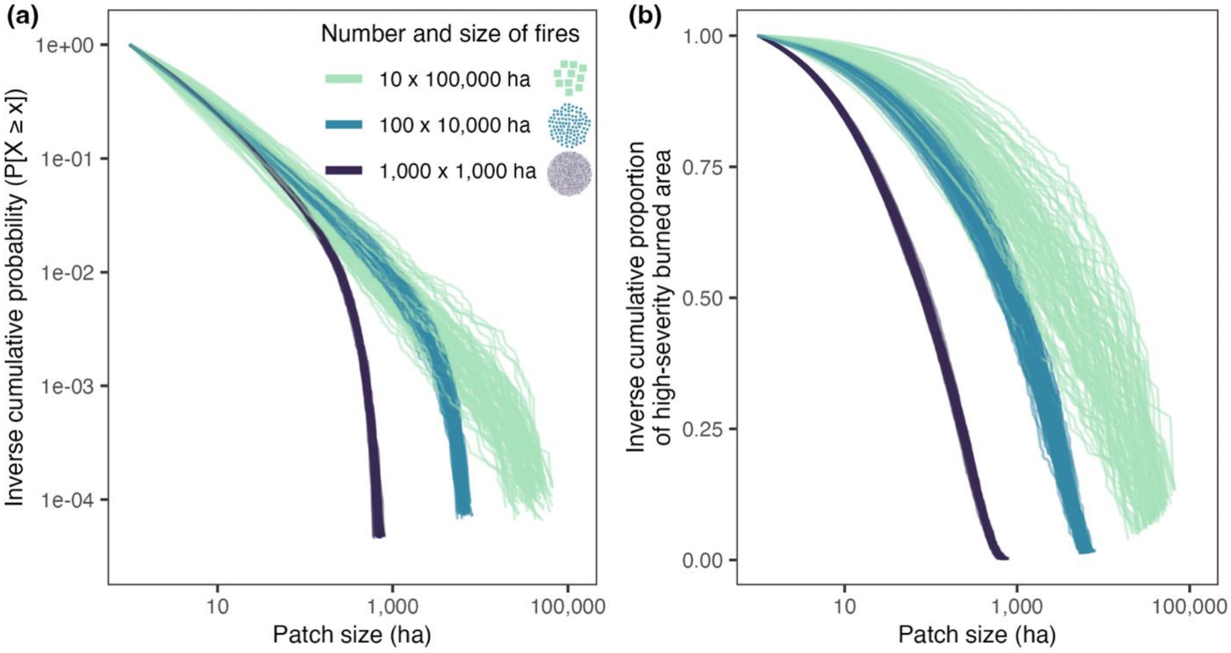

Figure 4.5. Simulated aggregate patch size distributions. Distributions are displayed as (a) inverse cumulative probability distributions and (b) inverse cumulative proportions of total high-severity burned area. Each scenario represents the same hypothetical total area burned (1,000,000 ha) and was simulated 100 times, with each iteration displayed as a single line. Note that the y-axis in (a) is log-transformed, but the y-axis in (b) is not.

4.5 DISCUSSION

Our approach demonstrates how burn severity spatial scaling relationships can be used to simulate potential future ranges of burn severity patterns in fire regimes for which empirical data are lacking. The fire size scenarios evaluated in our case study illustrate how for a given total burned area, shifts in fire size distributions towards larger fire events will lead to increasingly large high-severity burn patches with interior areas that are increasingly far from unburned seed sources following fire. Conversely, the same total burned area occurring in more numerous but smaller fire events will result in more heterogeneous burn severity patterns, characterized by smaller patches and greater proximity to unburned seed sources following fire. These results have important forest and fire management implications for Northwestern Cascadia and other historically climate-limited regions expected to see large increases in area burned with warming and drying climate.

4.5.1 *Gaining insights for a data-sparse and infrequent-fire regime*

Although fire activity in Northwestern Cascadia, an archetypical climate-limited fire regime, has historically been characterized by extremes (i.e., long fire-free intervals punctuated by rare but severe fire events reaching up to one million ha in size) (Donato *et al.* 2020), our findings demonstrate that contemporary burn severity patterns in Northwestern Cascadia fall within the range of patterns observed in other fire regimes across the Northwest US. Thus, while Northwestern Cascadia may stand apart from the broader Northwest US in terms of the productivity of its forests and the infrequency with which fire has historically occurred, the spatial patterns of wildfire in Northwestern Cascadia are comparable to other regions where fire has occurred more frequently within the contemporary record. This consistency in burn severity scaling relationships across the Northwest US enabled us to supplement the sparse empirical record for Northwestern Cascadia and thereby make inference about future potential burn severity patterns in this region.

By quantifying the range of burn severity metrics expected across a range of potential fire sizes in Northwestern Cascadia, we were able to simulate how the effects of a given burned area might vary, depending on the number and size of individual fire events. The simple scenarios used here bookend a range of potential future fire size distributions in Northwestern Cascadia, with the many-small fire scenario (1,000 fire events, each 1,000 ha in size) on one end and the few-large fire scenario (10 fire events, each 100,000 ha in size) on the other. Climate projections for Northwestern Cascadia suggest conditions conducive to fire will increase, with summer fire seasons projected to become warmer and drier (Dalton *et al.* 2013; Mauger *et al.* 2015). However, the largest fire events in Northwestern Cascadia are typically driven by synoptic east wind events (Donato *et al.* 2020; Reilly *et al.* 2022), and it is still unclear whether and how the frequency of these events might shift moving forward. Therefore, reliable fire size distribution projections (i.e., estimates of the relative frequency of small-to-moderate versus very-large fires) are not currently available for Northwestern Cascadia. As more refined projections for annual burned area and fire size distributions become available for this region, the approach and scaling relationships presented here can be applied to such projections to provide more realistic estimates of future burn severity patterns.

4.5.2 *Shifts in fire-size distributions toward larger fire events will lead to larger and more homogenous areas burned at high severity*

As fire size distributions shift to the right (i.e., increase in size), our findings illustrate how the size and spatial homogeneity of high-severity patches will also consistently increase, carrying implications for forest resilience in a period of increasing fire activity. In the western US, increasing aridity in recent decades has been linked to both increasing annual area burned as well as increasing fire event sizes (Juang *et al.* 2022), and these trends are expected to continue (Parks & Abatzoglou 2020). Even if total area burned were to remain the same, as assumed in our simulation study, a given area burned in fewer but larger fire events will result in larger high-severity patches with interior areas farther from live seed sources following fire. In forest ecosystems, the increasing size and homogeneity of high-severity patches will directly affect seed dispersal (Gill *et al.* 2022), rates of tree regeneration (Harvey *et al.* 2016b), formation and persistence of early-seral habitat, and the potential for conversion to non-forest systems (Coop *et al.* 2020) following fire.

Our finding that aggregate core area did not differ between the two largest fire size scenarios suggests that once fire size distributions become sufficiently large (e.g., composed of individual fire events ≥ 10,000 ha), an asymptote in forested area that is burned at high severity and located 150 m or farther from the nearest unburned seed source may begin to occur. It is possible this asymptotic behavior arises because high-severity patches become increasingly complex in their spatial configurations as they themselves increase in size (e.g., complex perimeters, heterogeneous forest cover, and within-patch "islands" of unburned live seed sources). However, this asymptotic behavior did not emerge when we increased the distance threshold used to define core area from 150 m to 300 m, suggesting that aggregate areas exceeding greater distance-to-seed thresholds do consistently increase with increasing fire size distributions. This conclusion is also supported by our continuous distance-to-seed distribution findings, which suggest that the tails of these distributions grow consistently heavier with increasing fire size. Thus, while area exceeding a 150 m distance-to-seed threshold may asymptote as fire size distributions shift to the right, areas that exceed longer distance-to-seed thresholds will likely continue to increase. Increases in the tails of distance-to-seed distributions are expected to amplify post-fire ecological effects, including slowing forest recovery trajectories (Harvey *et al.* 2016b; Gill *et al.* 2022) and increasing persistence of early-seral habitats.

4.5.3 *Implications for forest and fire management in Northwestern Cascadia*

Within the Northwest US, spatial patterns of burn severity in Northwestern Cascadia appear consistent with those in other climate-limited fire regimes, particularly those in the Northern Rockies, which comprised the bulk of the high-severity regime data in our study (449 of 472 fire events). As demonstrated here, insights about future patterns of burn severity in Northwestern Cascadia can therefore be drawn from this neighboring region that, while biophysically distinct, is comparably climate-limited in its fire regime. While these insights are critical, as spatial patterns of burn severity in many ways set the template for post-fire forest recovery (Gill *et al.* 2022), their implications must be considered in the context of the unique biophysical characteristics of the Northwestern Cascadia region.

Comparable burn severity patterns can lead to varying forest regeneration trajectories, depending on the fire-adapted traits of dominant tree species (Harvey *et al.* 2016b; Littlefield 2019). For example, serotinous (i.e., seed banking) and resprouting species can facilitate rapid and dense tree regeneration following fire, even in the interior portions of high-severity burn patches (Turner *et al.* 2003; Harvey *et al.* 2016b; Hood *et al.* 2021). While some serotinous and resprouting species do occur in Northwestern Cascadia (e.g., lodgepole pine [*Pinus contorta* var *latifolia*] and bigleaf maple [*Acer macrophyllum*], respectively), their populations are scattered and constitute relatively minor components of Northwestern Cascadia forest communities (Franklin & Dyrness 1973). For most dominant tree species in Northwestern Cascadia (e.g., Douglas-fir, western hemlock, western redcedar [*Thuja plicata*], noble fir [*Abies procera*], and Pacific silver fir), dispersal of seeds from unburned live trees is instead the primary mechanism of tree regeneration following fire (Reilly *et al.* 2021). In general, post-fire regeneration rates of conifer species that rely on wind-dispersed seeding will decrease with increasing distance to the nearest unburned seed source (Harvey *et al.* 2016b; Kemp *et al.* 2016; Littlefield 2019). However, the distance at which tree regeneration becomes severely limited can vary widely, and in Northwestern Cascadia, robust post-fire tree regeneration has been observed as far as 400 m from the nearest unburned seed source (Donato *et al.* 2009; Laughlin *et al.* In prep). Tree regeneration also varies with numerous additional factors, including pre-fire forest structure, topography, and post-fire climate conditions (Littlefield 2019; Davis *et al.* 2023; Laughlin *et al.* In prep). Therefore, planning for post-fire replanting in Northwestern Cascadia will be important in areas where maintaining forest cover is the management goal.

Large high-severity patches, while a concern for post-fire forest recovery and resilience, also play an important role in Northwestern Cascadia by creating early-seral habitat (Halofsky *et al.* 2018b; Steel *et al.* 2022). Naturally occurring early-seral forest ecosystems, including those that form following high-severity fire, are structurally complex and high in biodiversity, providing critical habitat for numerous plant and animal species (Swanson *et al.* 2011). Culturally important plant species, such as huckleberry (*Vaccinium myrtilloides* Michx.), thrive in these early-seral environments, and Indigenous tribes in Northwestern Cascadia and adjacent regions have historically managed these species using fire (LeCompte-Mastenbrook 2015; Wynecoop *et al.* 2019). Currently, structurally complex early-seral forest conditions are largely absent from Northwestern Cascadia, despite historically comprising up to 30% of the landscape (Donato *et al.* 2020). While increasingly large high-severity patches will on the one hand lead to decreasing forest regeneration rates, they will also in turn lead to increasing persistence of early-seral habitat. As fire activity increases in Northwestern Cascadia, therefore, the occurrence of large high-severity patches may help restore and maintain these important early-seral conditions across the region (Halofsky *et al.* 2018a).

Our findings have important implications for pre- and post-fire management in Northwestern Cascadia. First, when considering post-fire replanting needs, we found that the amount of forest area burned at high-severity and located more than 150 m from an unburned seed source may asymptote around ~15% of the total burned area once fire size distributions become sufficiently large (i.e., composed of individual fire events exceeding 10,000 ha). In other words, even in the largest fire size scenarios, ~85% of total burned area is unlikely to require post-fire replanting, being either burned at low-to-moderate severity and/or within the likely dispersal distance of unburned live seed sources. These proportions can provide a useful rule-of-thumb for managers planning for future fire events. Furthermore, given suitable post-fire climate, it is possible for robust tree regeneration to naturally occur in Northwestern Cascadia beyond a distance of 150 m from unburned seed sources (Donato *et al.* 2009; Laughlin *et al.* In prep); therefore, these proportions provide conservative estimates of the amount of area likely to require post-fire replanting. In areas where the goal is to restore tree densities required by existing policies and management objectives, but resources available for replanting are limited, efforts should focus on the largest high-severity patches where interior areas exceed the likely dispersal distances of unburned seed sources. For example, our analysis suggests that <5% of total burned area is likely to be both burned at high-severity and located more than 450 m from an unburned seed source following fire (ranging from

0.9% to 4.2% on average across fire size scenarios). These are areas that may be in greatest need of post-fire replanting, or alternatively, areas that may naturally be restored to early-seral habitat and likely to persist in this state following fire. While these proportions are modest, it is important to recognize that the areas may not be trivial, depending on the total area affected by fire.

Our findings also have important real-time fire management implications, particularly in the decision-making realm regarding fire suppression versus managed wildfire use. In climate-limited fire regimes such as Northwestern Cascadia, suppressing fires can in general be both an ecologically and socially defensible strategy (Halofsky *et al.* 2018b), as fire suppression is necessary in many cases to protect human values and is unlikely to lead to the type of uncharacteristic fuel buildup that has occurred in historically fuel-limited regimes across the western US (Hagmann *et al.* 2021). However, reintroducing fire in high-severity regimes can restore landscape patterns falling within the historic range of variability (Agee 1998), and given the current deficit in early-seral habitat conditions across Northwestern Cascadia (Donato *et al.* 2020), allowing some fires to burn may also be a useful strategy in certain cases. Furthermore, managing forests for resilience to both fire and changing climate will likely require increasing forest species and structural diversity at a regional scale (Halofsky *et al.* 2018b). Forest management strategies may therefore need to consider harnessing wildfire activity to accomplish broad-scale "treatment" goals (North *et al.* 2021; Churchill *et al.* 2022). Our results suggest that if all burned area in Northwestern Cascadia came solely from smaller fire events, fire activity would cumulatively have lesser ecological effects in terms of coarsening and restoring forest structure. Conversely, the same total area burned in moderately-large fire events (e.g., 10,000 ha) would have a substantially greater ecological effect, comparable in some ways to the cumulative effects of very-large fire events (e.g., 100,000 ha). Therefore, allowing some fires to reach moderately-large sizes (i.e., a practice of modified fire suppression) may be beneficial in some cases to promote the resilience of Northwestern Cascadia forest landscapes.

4.5.4 *Model assumptions and limitations*

Our modeling approach assumes that within each fire regime, the relationships between fire size and patterns of burn severity (i.e., high-severity patch size and shape) are stationary in both space and time. In other words, after accounting for fire regime, we assume that the range of burn severity patterns expected at any given fire size does not vary by region or time period. As shown in Chapter 3, this assumption is well supported in the Northwest US within the contemporary fire record (1985

– 2020), despite this period being marked by increasing aridity, annual area burned, and fire event sizes (Juang et al. 2022). As fire activity continues to increase, however, fuel limitations may begin to strengthen in some regions, potentially altering fire size and severity as a result (Abatzoglou *et al.* 2021a; Kennedy *et al.* 2021). It is possible that strengthening fuel limitations in such regions could also erode the stationarity in scaling relationships that has been observed over the contemporary record, with the range of high-severity patches shifting toward smaller sizes and more heterogeneous shapes at any given fire size. In Northwestern Cascadia, however, where forests are highly productive and biomass-rich (Spies *et al.* 2018), fuel limitations are not likely to increase in the coming decades (Halofsky *et al.* 2020; Abatzoglou *et al.* 2021a). Therefore, stationarity in scaling relationships is a reasonable assumption in Northwestern Cascadia for the foreseeable future.

The only driver of burn severity patterns that is explicitly accounted for in our modeling approach is fire size. By drawing from the full empirical distributions of patch size and shape across the range of observed fire sizes, we effectively integrate over a wide range of potential drivers, including vegetation types, fuel loads, and weather at the time of burning. We feel that this approach is reasonable and appropriate, given the goal of modeling potential burn severity patches over a large regional extent. In smaller landscapes or more specific contexts with a narrower range of potential drivers, however, our approach has the potential to over- or under-estimate potential ecological effects. For example, there is historical precedence in Northwestern Cascadia for areas burned in very-large fires to partially reburn numerous times in the decades following the initial fire event (Reilly *et al.* 2022). When short-interval reburns such as these do occur, fuel limitations introduced by earlier fires can limit patch size and homogeneity in subsequent fires. These types of negative feedbacks have mainly been observed in short-interval (e.g., <15 year) reburns in low-severity fire regimes of the Northwest US, and less so in other fire regimes (Harvey *et al.* 2023). However, it is possible that our approach, which does not explicitly account for fuel loads, may not be appropriate for anticipating high-severity patch structure in landscapes burned multiple times within a few decades. Furthermore, ecological effects can be compounded in areas affected by short-interval reburns (Braziunas *et al.* 2023), particularly in areas that burn twice or more at high-severity (Turner *et al.* 2019; Harvey *et al.* 2023). Modeling high-severity patch size and shape alone is not sufficient for anticipating potentially compound ecological effects that may occur in these contexts.

Our analysis is limited by the observed fire size and severity data available within the contemporary satellite record. Given that fire size distributions tend to be strongly right-skewed (McKenzie &

Kennedy 2011), the frequency of fire events and therefore availability of empirical data naturally decreases as fire size increases. Since our approach relies on simulating from models fit to empirical distributions, the uncertainty in our model predictions and simulations therefore increases with fire size as the empirical data become increasingly sparse. This greater uncertainty, along with the wider range of variation in patch size and structure metrics that is observed for larger fire events, may partially explain the increasing variation in simulated patch metrics that we observed across fire size scenarios. However, the increasing variation also arises in part from the simulation study design itself and the properties of the central limit theorem; because the number of simulated fires decreases across scenarios (i.e., 1,000 fires are simulated in each iteration of the smallest fire size scenario, compared to 100 fires in the moderately-large fire size scenario and 10 fires in the very-large fire size scenario), the variance in the sampling distribution naturally increases across scenarios. The increasing variation in simulated metrics across fire size scenarios likely stems from both of these causes, though it is difficult in our approach to disentangle the two.

4.6 CONCLUSION

Anticipating the ecological effects of future fire activity is challenging in historically climate-limited, infrequent-fire regimes for which empirical fire data are lacking. Our analysis and approach address this challenge, demonstrating that spatial scaling relationships (i.e., relationships between fire size and expected patterns of burn severity) offer a means to anticipate future fire effects at a regional scale. The approach we present here can be used to evaluate potential outcomes of different area burned and fire size distribution scenarios, with our case study illustrating how the ecological effects of a given total burned area might vary depending on the number and size of individual fire events (i.e., a small number of very-large fires versus many smaller fires). Our results suggest a given total area that is burned in a few large fires will result in larger high-severity patches with interior areas farther from unburned seed sources, as compared to the same total area being burned in more numerous but smaller fire events. These findings have important implications for forest resilience and management in a period of increasing fire activity and shifting fire-size distributions.

Studies such as these can prove useful in scenario planning and developing regional pre- and post-fire management plans in the face of uncertainty. Furthermore, as projections for total area burned and fire size distributions continue to be refined, our approach can also be used to put quantitative bounds on more realistic potential outcomes of future fire activity, and therefore management considerations such as post-fire planting needs. While this approach is especially useful in data-poor regions, it can also be applied to more frequent-fire regions where empirical data are more readily available but the potential effects of future fire activity and changing fire regimes remain uncertain.

4.7 APPENDIX F: SIMULATION STUDY METHODS

F.1 *Drawing random samples from empirical distributions using quantile regression*

Our goal in this simulation study was to harness quantile regression models to simulate high-severity patch size and structure metrics at any given fire size. The approach that we use is a coarse and empirical adaptation of inverse transform sampling, a method that is frequently used to generate random samples from known probability distributions (Devroye 1986). In inverse transform sampling, random samples are drawn from a known probability distribution by (1) generating a uniform [0,1] random variate u, and then (2) returning $F^{-1}(u)$, where F^{-1} is the inverse cumulative distribution function.

In our application, the probability distribution of each patch metric varies with fire size. While the patch metric probability distributions (conditional on fire size) are not known exactly, they can be empirically estimated using quantile regression. To estimate these conditional distributions, we fit smooth curves to 99 conditional quantiles (0.01 through 0.99) of the empirical data across the range of observed fire sizes. An empirical estimate of the probability distribution for a given patch metric at a given fire size can then obtained by extracting the 99 conditional quantile predictions at that fire size. Following the notation introduced in the previous paragraph, these 99 conditional quantile predictions correspond to $F^{-1}(\mathbf{D})$, where $\mathbf{D} = \{0.01, 0.02, 0.03, \ldots, 0.99\}$. Therefore, to generate a random sample from this empirical distribution, we randomly draw one of the 99 conditional quantile values. This is equivalent to the inverse transform sampling approach, where instead of generating a continuous uniform [0,1] random variate u, we generate a discrete uniform [0.01,0.99] random variate d and return $F^{-1}(d)$.

F.2 *Core area simulation*

To simulate total core area for any given fire size, we used the following procedure.

First, we quantified the relationship between fire size and core area using non-parametric quantile regression. We fit smooth curves to 99 conditional quantiles (0.01 through 0.99) of the total core area distribution across the range of observed fire sizes, constraining the curves to be monotonically increasing (Figure 4.6). Then, to simulate total core area at any given fire size, we extracted the 99 conditional quantile predictions at that fire size and randomly drew one value.

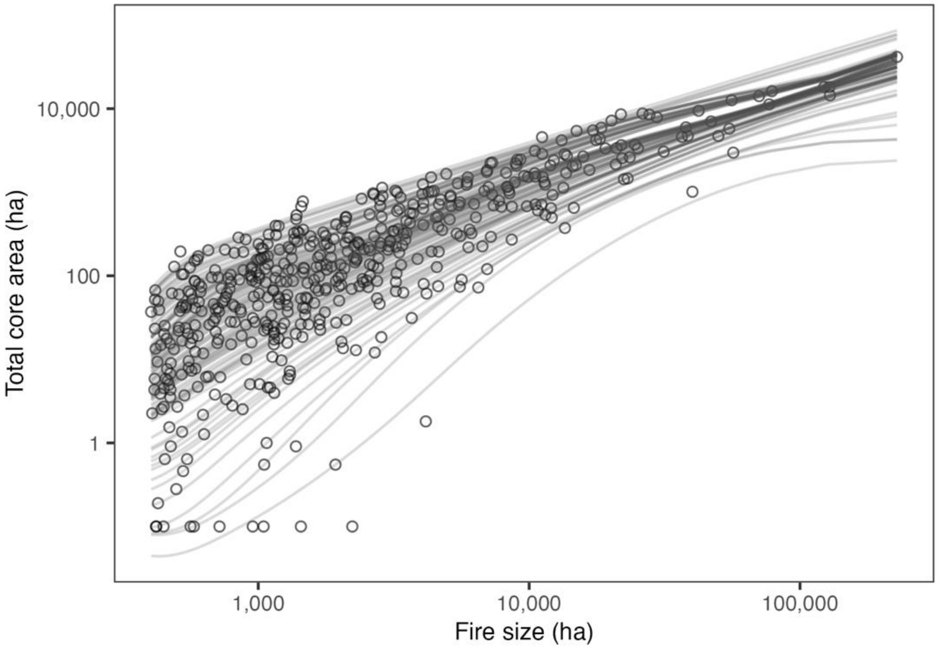

Figure 4.6. Conditional quantiles used to simulate core area at any given fire size. Observed data are shown with open circles, conditional quantiles (0.01 through 0.99) are shown with gray lines.

F.3 *Effect of increasing the distance-to-seed threshold used to define core area*

We conducted a sensitivity analysis to evaluate how simulated aggregate core area might differ depending on the distance-to-seed threshold used to define core area. In our primary analysis, core area is defined as the total forested area burned at high severity and exceeding a threshold of 150 m to seed. We increased this distance threshold to 300 m and re-calculated core area using this threshold, then repeated our simulation study to evaluate whether our results and conclusions might qualitatively differ.

As above, we quantified the relationship between fire size and core area (defined using a 300 m distance threshold) using non-parametric quantile regression. We fit smooth curves to 99 conditional quantiles (0.01 through 0.99) of the total core area distribution across the range of observed fire sizes, constraining the curves to be monotonically increasing (Figure 4.7). Then, to simulate total core area at any given fire size, we extracted the 99 conditional quantile predictions at that fire size and randomly drew one value.

Simulated aggregate core area increased between the smallest (i.e., 1,000 ha) fire size scenario (mean = 18,808 ha, or 1.9% of the total burned area) and each of the larger fire size scenarios, as well as between the moderately-large (i.e., 10,000 ha) fire size scenario (mean = 57,547 ha, or 5.8% of the total burned area) and the very-large (i.e., 100,000 ha) fire size scenario (mean = 72,842 ha, or 7.3% of the total burned area; $p < 0.05$ using ANOVA and Tukey's HSD) (Figure 4.8).

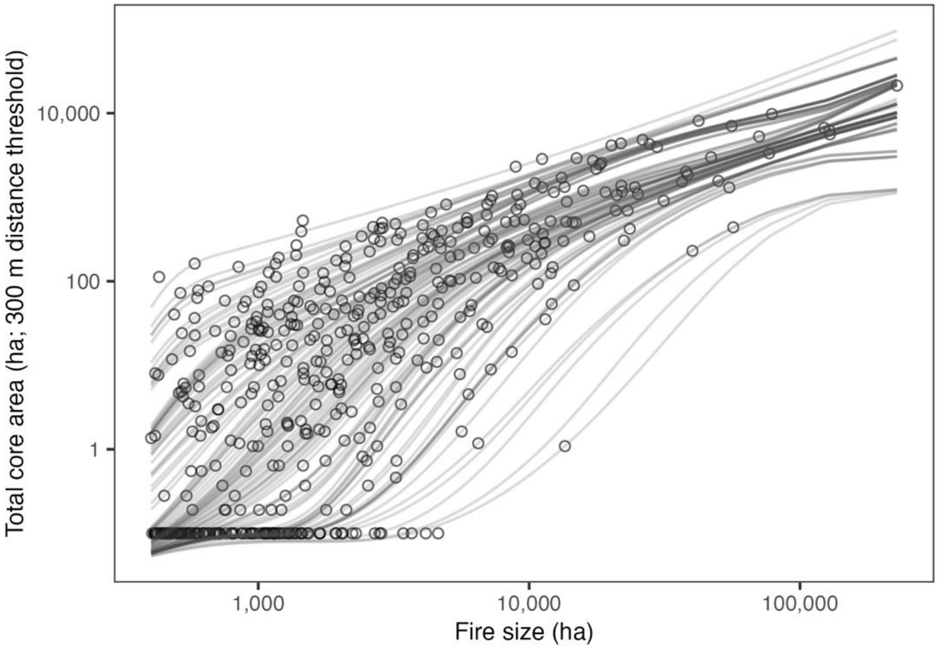

Figure 4.7. Conditional quantiles used to simulate core area, where core area is defined using a 300 m distance-to-seed threshold. Observed data are shown with open circles, conditional quantiles (0.01 through 0.99) are shown with gray lines.

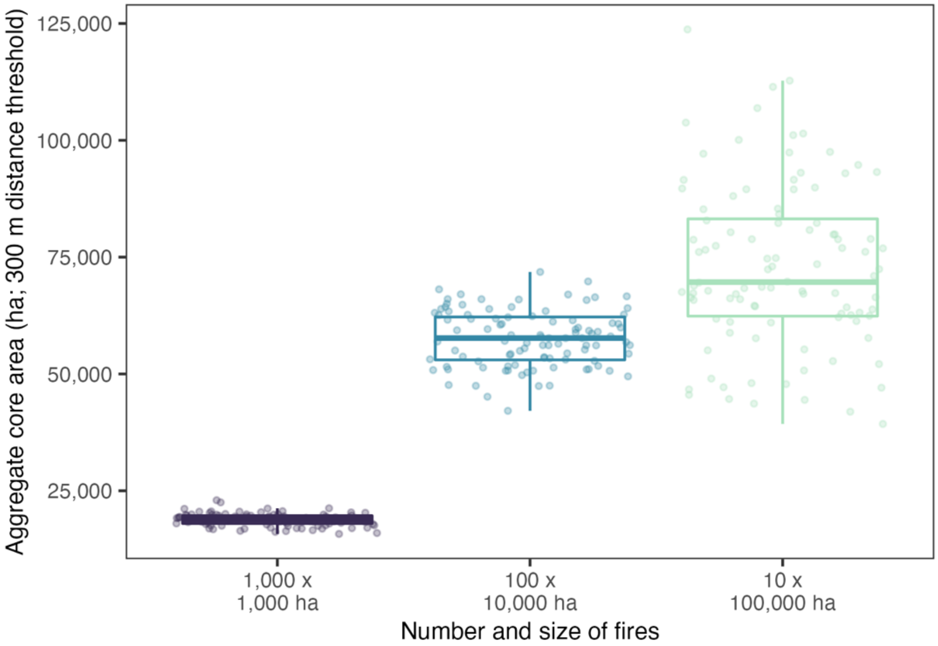

Figure 4.8. Simulated aggregate core area, where core area is defined using a 300 m distance threshold. Each scenario represents the same hypothetical total area burned (1,000,000 ha) and was simulated 100 times, with each iteration displayed as a single dot.

F.4 *Distance-to-seed distribution simulation*

The continuous distance-to-seed distribution within each fire event is quantified using the SDC parameter. The SDC parameter describes the *proportional* decay of total high-severity or "stand-replacing" forested area with increasing distance to seed, given the following equation (Collins *et al.* 2017):

$$P_{dts} = \frac{1}{10^{SDC \times dts}} \qquad (I)$$

Here, P_{dts} is the proportion of forested high-severity area exceeding each distance-to-seed threshold, dts. Building on Equation I, we wanted to simulate distance-to-seed distributions in terms of areas (ha) rather than proportions. This would facilitate aggregating (summing) simulated distance-to-seed distributions across fire events. By introducing additional terms into Equation I, we can express the decay in total high-severity forested *area* (in ha) with increasing dts as follows:

$$A_{dts} = \frac{A \times P_{FHS}}{10^{SDC \times dts}} \qquad (II)$$

Here, A_{dts} is the total forested high-severity area (in ha) exceeding each distance-to-seed threshold, A is the size of the fire event (in ha), and P_{FHS} is the proportion of the fire event (the proportion of A) that was forested and burned at high severity.

Simulating distance-to-seed distributions therefore required three parameters: fire size (A), SDC, and P_{FHS}. In our dataset, we found that P_{FHS} is correlated with both fire size (A) and SDC. This correlation enabled us to sequentially simulate sets of parameters jointly falling within the range of variation observed in our dataset. In other words, once fire size is fixed, the conditional range of variation in SDC is reduced and we can sample from its conditional distribution given fire size; then, once fire size and SDC are fixed, the conditional range of variation in P_{FHS} is reduced and we can sample from its conditional distribution given fire size and SDC. Following this logic, we used the following procedure to simulate a distance-to-seed distribution for any given fire size.

First, we quantified the relationship between fire size and the SDC parameter using non-parametric quantile regression. We fit smooth curves to 99 conditional quantiles (0.01 through 0.99) of the SDC parameter distribution across the range of observed fire sizes, constraining the curves to be monotonically decreasing (Figure 4.9). Then, to simulate SDC at any given fire size, we extracted the 99 conditional quantile predictions at that fire size and randomly drew one value.

Second, after simulating the SDC parameter, we simulated P_{FHS} for each fire using a generalized additive model (GAM) fit to P_{FHS} as a function of $\log_{10}$(SDC) and fire size (Figure 4.10). We fit the P_{FHS} GAM using a beta response distribution with a logit link.

Finally, we used the fire size, simulated SDC parameter, and simulated P_{FHS} to calculate the area-based distance-to-seed distribution (A_{dts}) using Equation II (Figure 4.11).

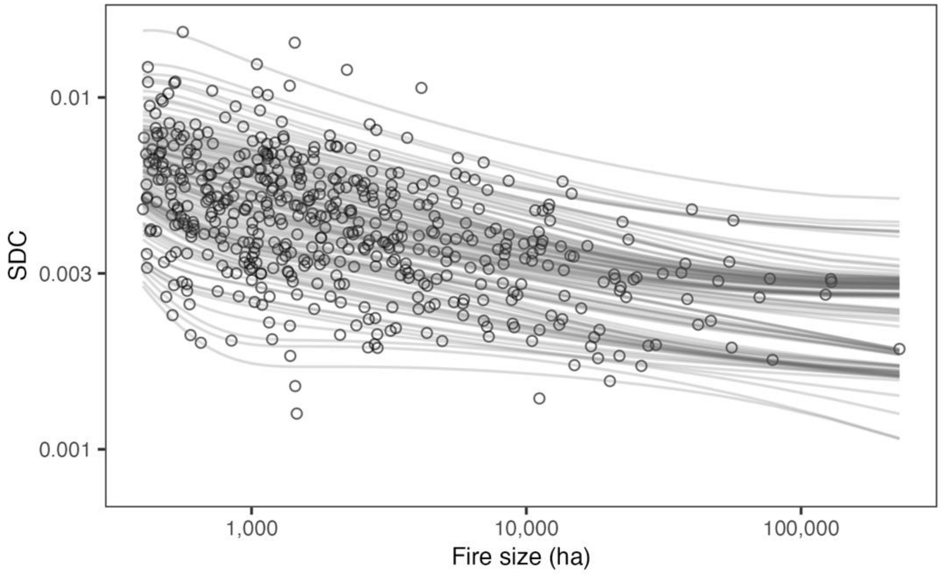

Figure 4.9. Conditional quantiles used to simulate the SDC parameter at any given fire size. Observed data are shown with open circles, conditional quantiles (0.01 through 0.99) are shown with gray lines.

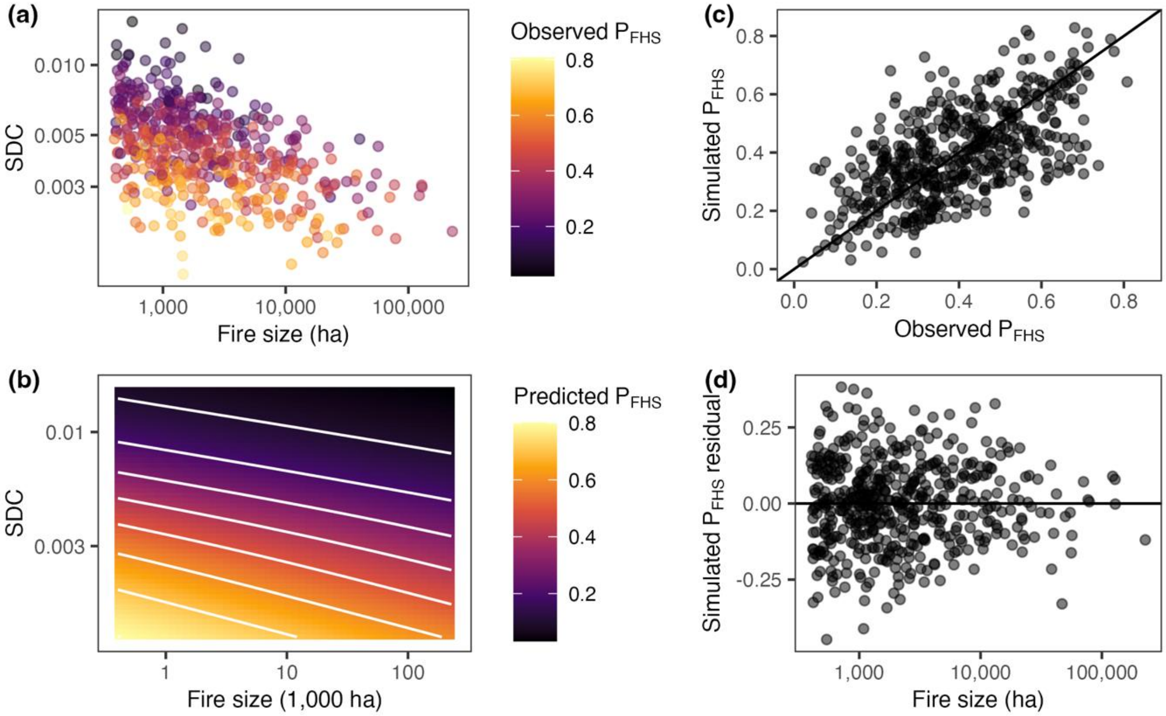

Figure 4.10. Visualization of GAM used to simulate P_{FHS} at any given fire size and value of SDC. (a) Observed and (b) predicted values of P_{FHS} as a function of fire size and SDC. (c) Simulated versus observed values of P_{FHS}. (d) Simulated P_{FHS} residuals (observed minus simulated values) plotted against fire size.

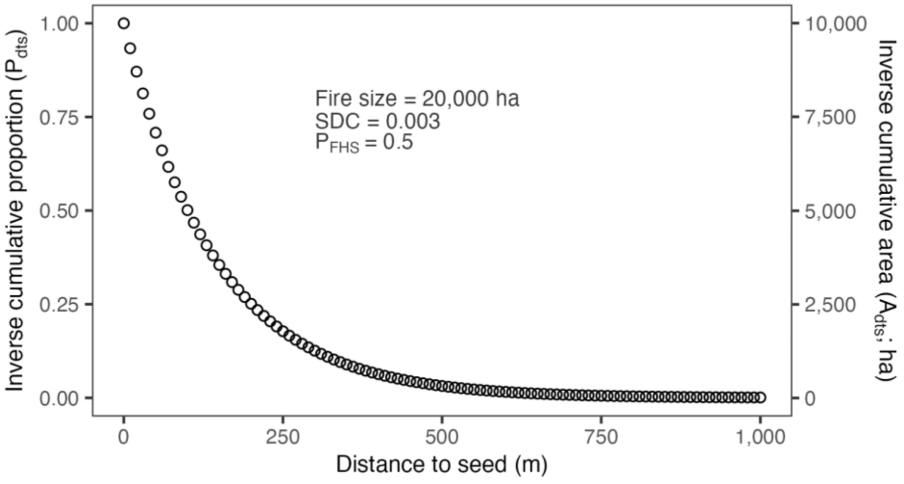

Figure 4.11. Example of calculated distance-to-seed distribution. Distribution is expressed both in terms of proportions (P_{dts}, calculated using Equation I; left y-axis) and areas (A_{dts}, calculated using Equation II; right y-axis). Distribution was calculated for a fire size (A) of 20,000 ha, simulated SDC of 0.003, and simulated P_{FHS} of 0.5.

F.5 *Comparison of core area and distance-to-seed distribution approaches*

To evaluate the consistency of the core area and SDC-based distance-to-seed approaches, we compared aggregate core areas (based on 150 and 300 m thresholds of distance-to-seed) derived using the direct core area approach (Figure 4.6, Figure 4.7) and the SDC approach (Figure 4.9 – Figure 4.11). Over 100 iterations of the three simulation scenarios, we found that both approaches produced qualitatively similar results; in the very-large fire size scenario, however, aggregate areas derived using the SDC approach were biased high relative to analogous areas derived using the direct core area approach (Figure 4.12).

We believe that aggregate areas derived using the SDC approach may be biased high for very-large fire events due to a limitation of the model we used to simulate the forested and high-severity proportion (P_{FHS}) of each fire event. In our dataset, we observe a narrowing in the range of P_{FHS} toward intermediate values with increasing fire size (Figure 4.13). Although the GAM we used to simulate P_{FHS} at any given fire size and value of SDC does a reasonable job at capturing the changes in mean P_{FHS} with these two predictor variables (Figure 4.10), it does not adequately capture the reduced variation in P_{FHS} with increasing fire size (Figure 4.13). At very-large fire sizes, therefore, the tendency to simulate values of P_{FHS} that appear to be outside of the range of variation observed in our dataset (Figure 4.13) results in aggregate distance-to-seed distributions that are biased high.

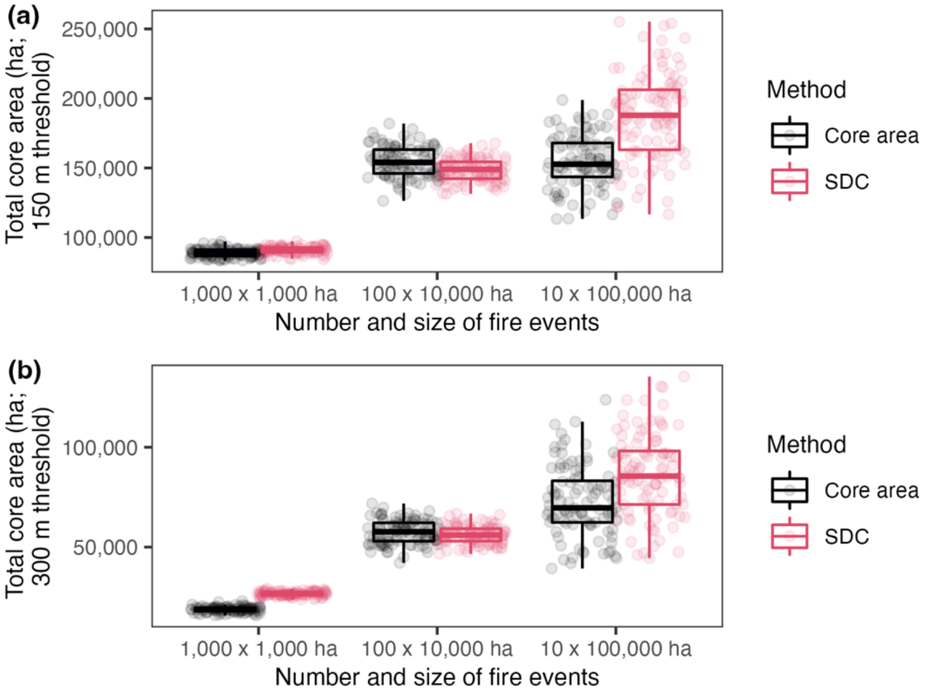

Figure 4.12. Comparison of aggregate total core area derived using core area and SDC approaches. Core areas are based on distance-to-seed thresholds of (a) 150 m and (b) 300 m.

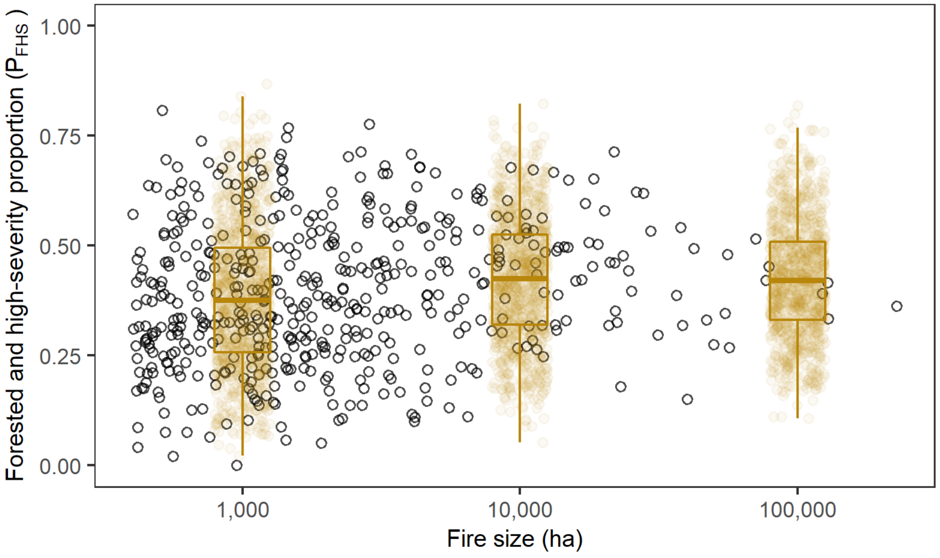

Figure 4.13. Comparison of observed and simulated values of P_{FHS}. Open circles represent observed values and brown circles represent simulated values. One thousand values of P_{FHS} were simulated at each of three fire sizes: 1,000 ha, 10,000 ha, and 100,000 ha. The x-axis positions of simulated P_{FHS} values are jittered for improved visibility.

F.6 *Patch size distribution simulation*

The patch size distribution within each fire event is quantified using a truncated lognormal probability distribution parameterized by ψ and β, which takes the following form (Hantson *et al.* 2016):

$$\ln p(x) = \ln C - \beta \ln(x) - \psi[\ln(x)]^2 \qquad (\text{ III })$$

Here, C is a normalization constant ensuring the area under p(x) sums to 1, taking the following form:

$$C = \left(\int_{x_{min}}^{x_{max}} e^{-\beta \ln(x) - \psi[\ln(x)]^2} dx\right)^{-1} \qquad (\text{ IV })$$

The parameters x_{min} and x_{max} define the lower and upper truncation limits, respectively.

Patch size distributions can be simulated by generating random samples from this known distribution. However, because the total size of all high-severity patches within a fire cannot exceed the total high-severity burned area, we also needed to simulate a value for the proportion of each fire that burned at high severity (P_{HS}), which can be multiplied by fire size (A) to yield the total area within each fire burned at high severity (A_{HS}) in ha. The simulated A_{HS} can then be used as an upper constraint to limit the total size of randomly generated high-severity patches.

Simulating patch size distributions therefore required four parameters: fire size (A), ψ, β, and P_{HS}. In our dataset, we found that ψ and β are strongly correlated, and that P_{HS} is correlated with fire size (A), ψ, and β. This correlation enabled us to sequentially simulate sets of parameters jointly falling within the range of variation observed in our dataset. In other words, once fire size is fixed, the conditional range of variation in ψ is reduced and we can sample from its conditional distribution given fire size; then, once fire size and ψ are fixed, the conditional range of variation in β is reduced and we can sample from its conditional distribution given fire size and ψ. Finally, once fire size, ψ, and β are fixed, we can sample from the conditional distribution of P_{HS} following similar logic. Therefore, we used the following procedure to simulate a patch size distribution for any given fire size.

First, we quantified the relationship between fire size and ψ using non-parametric quantile regression. We fit smooth curves to 99 conditional quantiles (0.01 through 0.99) of the ψ parameter distribution across the range of observed fire sizes (Figure 4.14). Then, to simulate ψ at any given fire size, we extracted the 99 conditional quantile predictions at that fire size and randomly drew one value.

Second, given the clear dependency we observed between ψ and β, we simulated a value for β using a GAM fit to β as a function of ψ (Figure 4.15). We fit the β GAM using a gaussian response distribution with an identity link.

Third, after simulating the ψ and β parameters, we simulated the high-severity proportion (P_{HS}) of each fire using a GAM fit to P_{HS} as a function of ψ, β, and fire size (Figure 4.16). We fit the P_{HS} GAM using a beta response distribution with a logit link.

Finally, we used the simulated ψ and β to parameterize a truncated lognormal probability distribution, using Equations III and IV. We set x_{min} equal to 1 ha and x_{max} equal to the size of each fire event (A). Using the parameterized probability distribution, we randomly sampled patch sizes until the total area of patches equaled the simulated high-severity area (A_{HS}; calculated as P_{HS} x A) (Figure 4.17). The patch size sampling algorithm proceeded as follows:

```
While (sum(patch distribution) < A_HS):
    • Randomly draw a patch size ("new patch") from parameterized
      distribution
    • If (new patch + sum(patch distribution) < A_HS):
        o Add new patch to the patch distribution
    • Else:
        o Add "last patch" to the patch distribution, calculated as
          follows:
        o last patch = A_HS - sum(patch distribution)
```

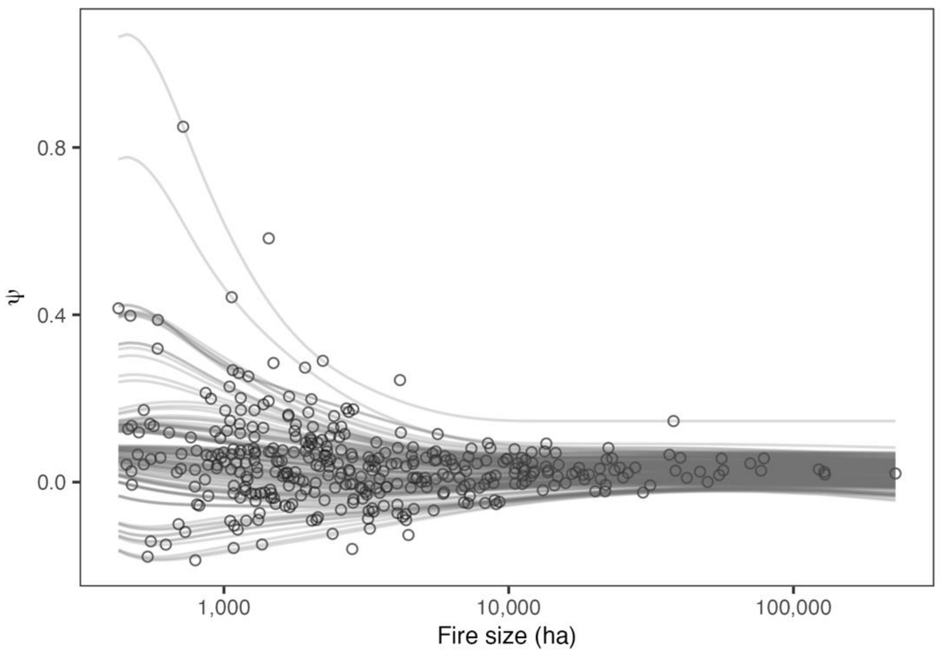

Figure 4.14. Conditional quantiles used to simulate the ψ parameter at any given fire size. Observed data are shown with open circles, conditional quantiles (0.01 through 0.99) are shown with gray lines.

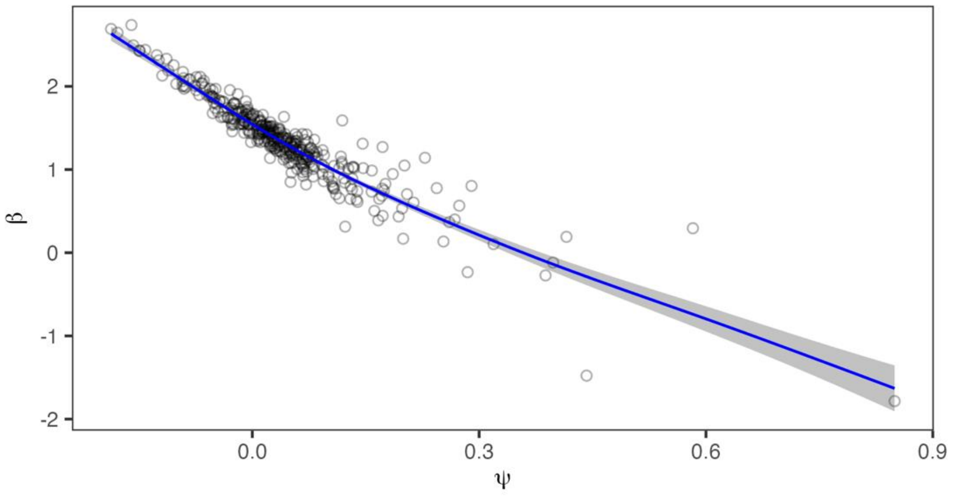

Figure 4.15. Visualization of GAM used to simulate β at any given value of ψ. Observed data are shown with open circles, fitted mean is shown with solid line, and 95% confidence interval is shown with shading.

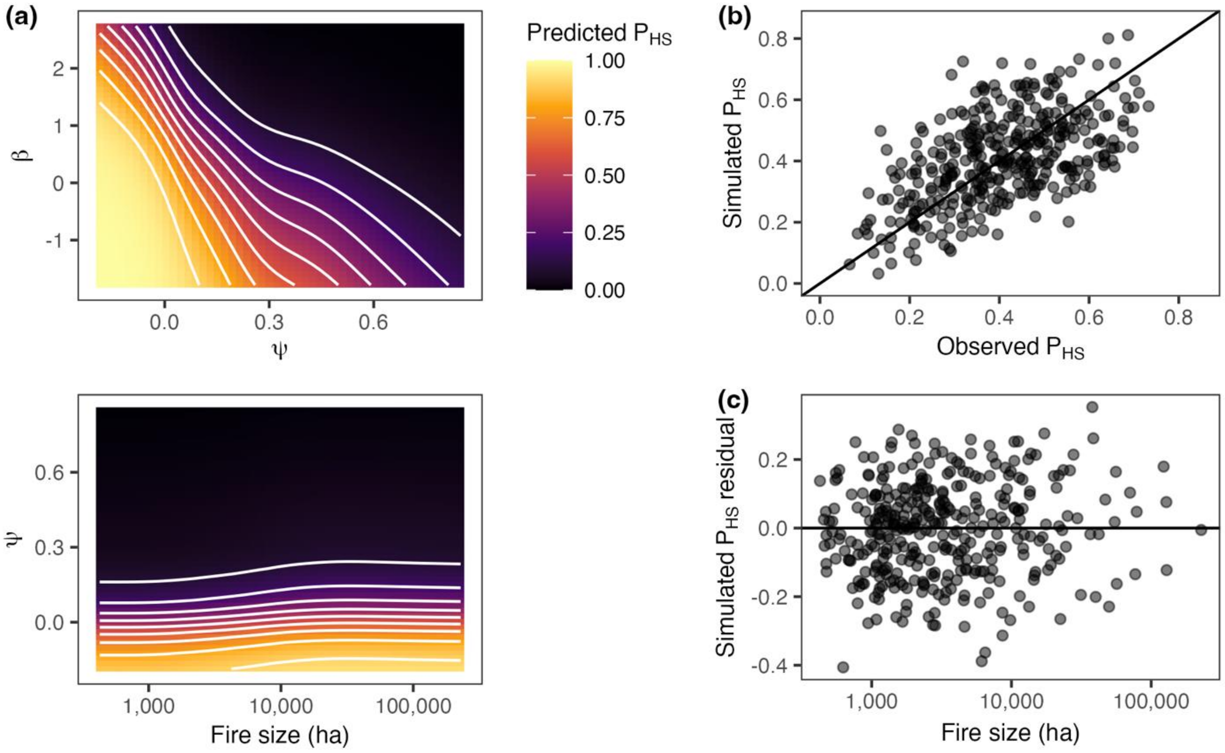

Figure 4.16. Visualization of GAM used to simulate P_{HS} at any given fire size and values of ψ and β. (a) Predicted values of P_{HS}. In top panel, fire size is held constant at 3,000 ha; in bottom panel, β is held constant at 1.4. (b) Simulated versus observed values of P_{HS}. (c) Simulated P_{HS} residuals (observed minus simulated values) plotted against fire size.

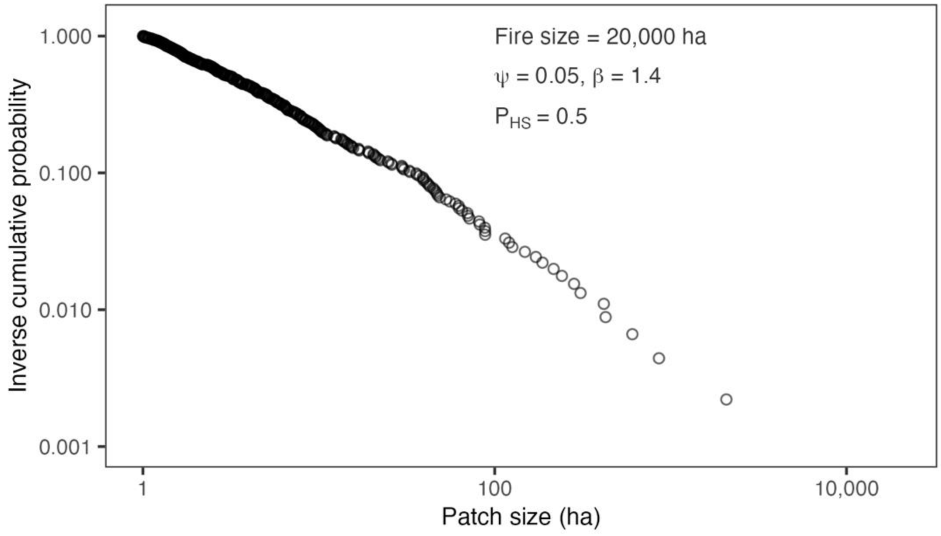

Figure 4.17. Example of a randomly generated patch size distribution. Distribution was randomly generated for a fire size of 20,000 ha, simulated ψ of 0.05, simulated β of 1.4, and simulated P_{HS} of 0.5.

F.7 *Evaluation of patch size distribution simulation approach*

To evaluate whether our patch size simulation approach generates realistic patch size distributions, we conducted additional analyses to compare observed and simulated values.

First, we compared observed and simulated area-weighted mean patch sizes for individual fire events. For all Northwestern Cascadia and Northwest US high-severity regime fire events, we re-calculated area-weighted mean patch sizes using only those patches $\geq$ 1 ha in size, for comparison with simulated patch size distributions. We fit a quantile regression model to the re-calculated area-weighted mean patch sizes. Then, using each fire size in the observed dataset, we followed the simulation procedure described above to simulate ψ, β, and P_{HS}, and randomly generate a patch size distribution. We calculated the area-weighted mean for each simulated patch size distribution and compared these simulated values to the observed values (Figure 4.18). Compared to the observed data, we found that the simulated area-weighted mean patch sizes followed a scaling relationship with a qualitatively similar range of variation, suggesting that our simulation procedure can generate realistic patch size distributions across the range of observed fire sizes.

Second, we compared observed and simulated patch size distributions for individual fire events. Using the sizes of one very large Northwestern Cascadia fire event (Beachie Creek; 78,761 ha) and one relatively small Northwestern Cascadia fire event (Goodell; 2,681 ha), we followed the simulation procedure described above to simulate ψ, β, and P_{HS}, and randomly generate a patch size distribution. We iterated through this procedure 100 times for each fire event and compared the simulated patch size distributions to each observed patch size distribution (Figure 4.19). In both cases, we found that the observed patch size distribution fell within the range of simulated patch size distributions.

Third, we compared observed and simulated patch size distributions aggregated across fire events. Using the sizes of ten very large fire events (30,000 – 100,000 ha in size) and ten relatively small fire events (1,000 – 3,000 ha in size) from the combined Northwestern Cascadia and Northwest US high-severity regime dataset, we followed the simulation procedure described above to simulate ψ, β, and P_{HS}, and randomly generate a patch size distribution for each fire event. We separately aggregated the patch size distributions for the ten very large and ten relatively small fire events. We iterated through this procedure 100 times for each group of fire event sizes and compared the simulated patch size distributions to each observed patch size distribution (Figure 4.20). In both cases, we found that the observed patch size distribution fell within the range of simulated patch size distributions.

Finally, we evaluated whether simulating the patch size distribution parameters in a different order would affect the simulation results. Specifically, we switched the order in which we simulated ψ and β, with β simulated first using the quantile regression approach and ψ simulated second using GAM fit to ψ as a function of β. The remainder of the simulation procedure was left unchanged. We found that switching the order in which ψ and β did not qualitatively change results (Figure 4.21).

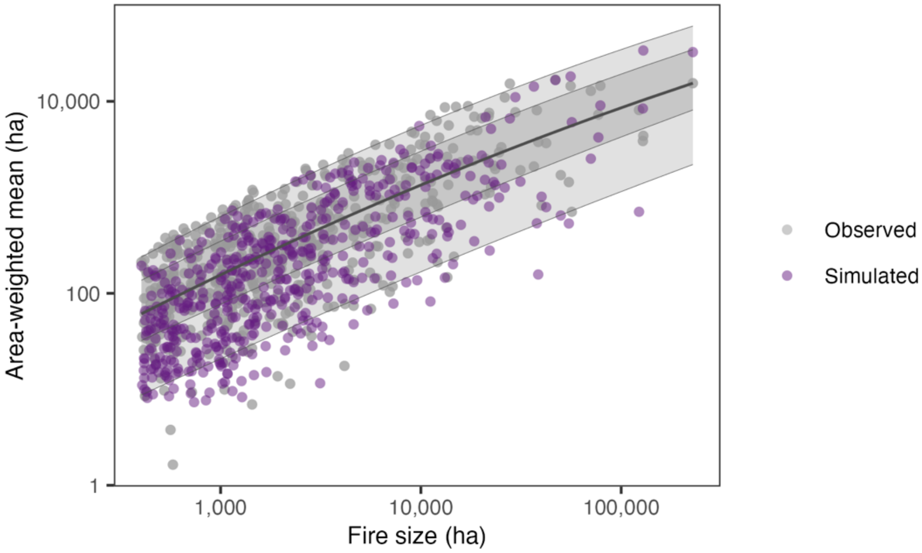

Figure 4.18. Observed and simulated area-weighted mean patch sizes. Area-weighted means were calculated using only those patches ≥ 1 ha in size. Quantile regression model fit to the observed values is represented by the solid line (quantile 0.5), dark shaded region (interval between quantiles 0.25 and 0.75), and light shaded region (interval between quantiles 0.05 and 0.95).

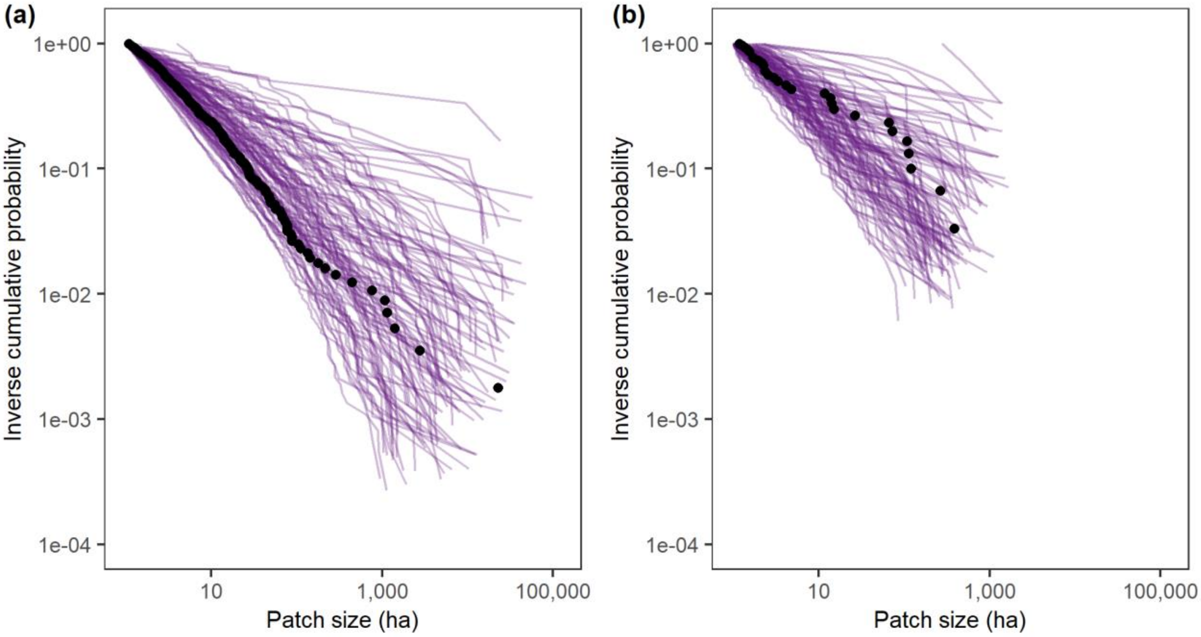

Figure 4.19. Observed and simulated patch size distributions for individual fire events. Fires are (a) the Beachie Creek fire (78,761 ha) and (b) the Goodell fire (2,681 ha). Observed patch size distributions are shown with black circles. Simulated patch size distributions (100 iterations) are shown with purple lines.

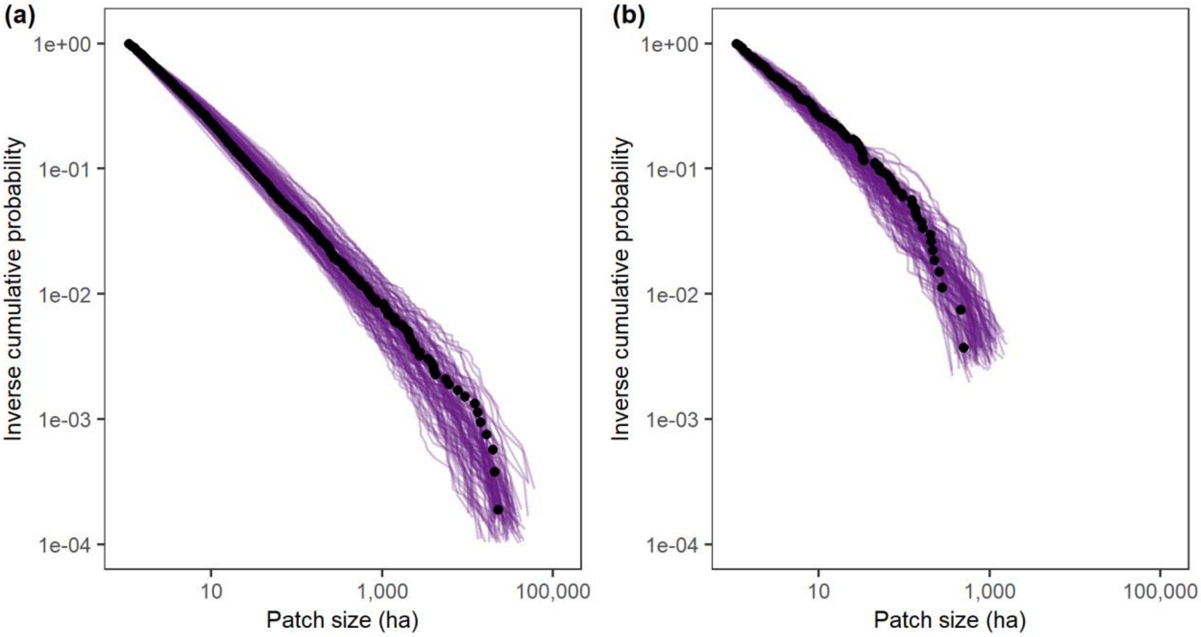

Figure 4.20. Observed and simulated patch size distributions for aggregated fire events. Distributions are for (a) ten very large fire events (30,000 – 100,000 ha in size) and (b) ten relatively small fire events (1,000 – 3,000 ha in size). Observed distributions are shown with black circles. Simulated distributions (100 iterations) are shown with purple lines.

(a) Scenario: 10 fires, each 100,000 ha

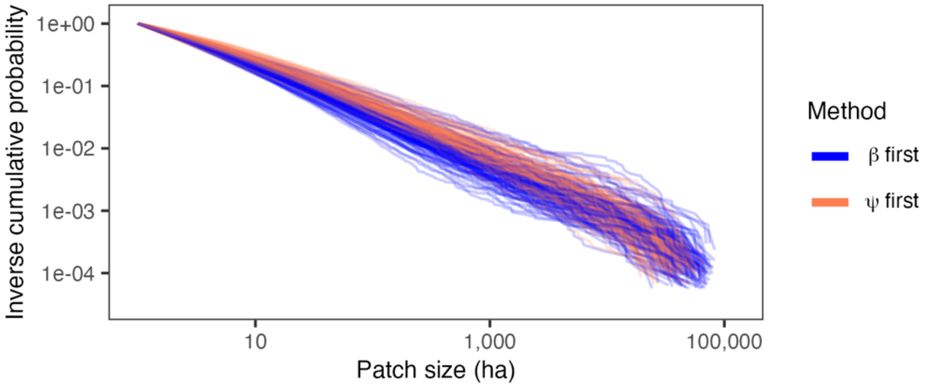

(b) Scenario: 100 fires, each 10,000 ha

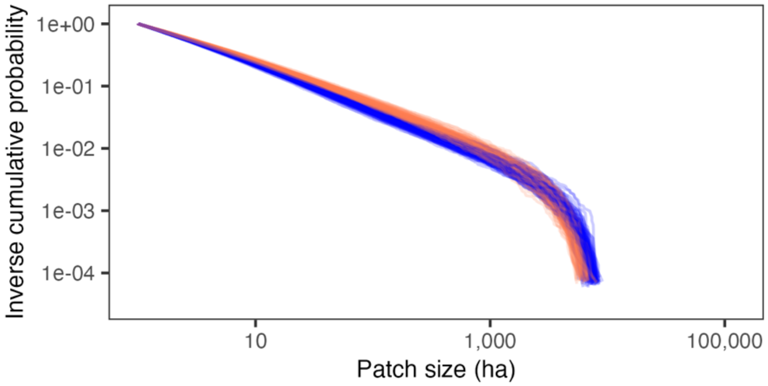

(c) Scenario: 1,000 fires, each 1,000 ha

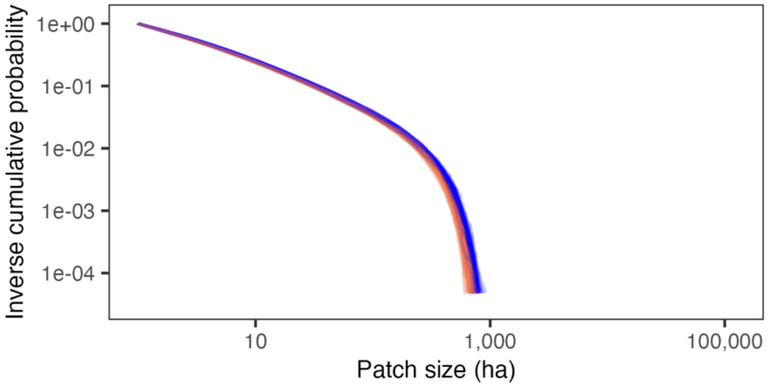

Figure 4.21. Comparison of simulated patch size distributions where the order for simulation of ψ and β is switched. Aggregate simulated patch size distributions are compared for (a) very large fire scenario, (b) moderately large fire scenario, and (c) smaller fire scenario.

4.8 APPENDIX G: NORTHWESTERN CASCADIA QUANTILE LOSS CALCULATIONS

Table 4.4. Average quantile loss (i.e., prediction error) calculated for the observed Northwestern Cascadia data using each fire regime model. Model with the lowest overall average quantile loss was considered most consistent with the Northwestern Cascadia data.

Metric	Fire regime model	Model rank	Average quantile loss	Reduction in average loss (%, relative to lowest ranked model)
Area-weighted mean patch size	**High**	**1**	0.126	13%
	Mixed	2	0.127	12%
	Low	3	0.144	0%
β parameter	**Low**	**1**	0.111	8%
	High	2	0.121	0%
	Mixed	3	0.121	0%
ψ parameter	**High**	**1**	0.021	8%
	Low	2	0.021	7%
	Mixed	3	0.023	0%
Total core area	**High**	**1**	0.175	16%
	Mixed	2	0.181	13%
	Low	3	0.208	0%
SDC parameter	**Mixed**	**1**	0.044	9%
	High	2	0.047	5%
	Low	3	0.049	0%

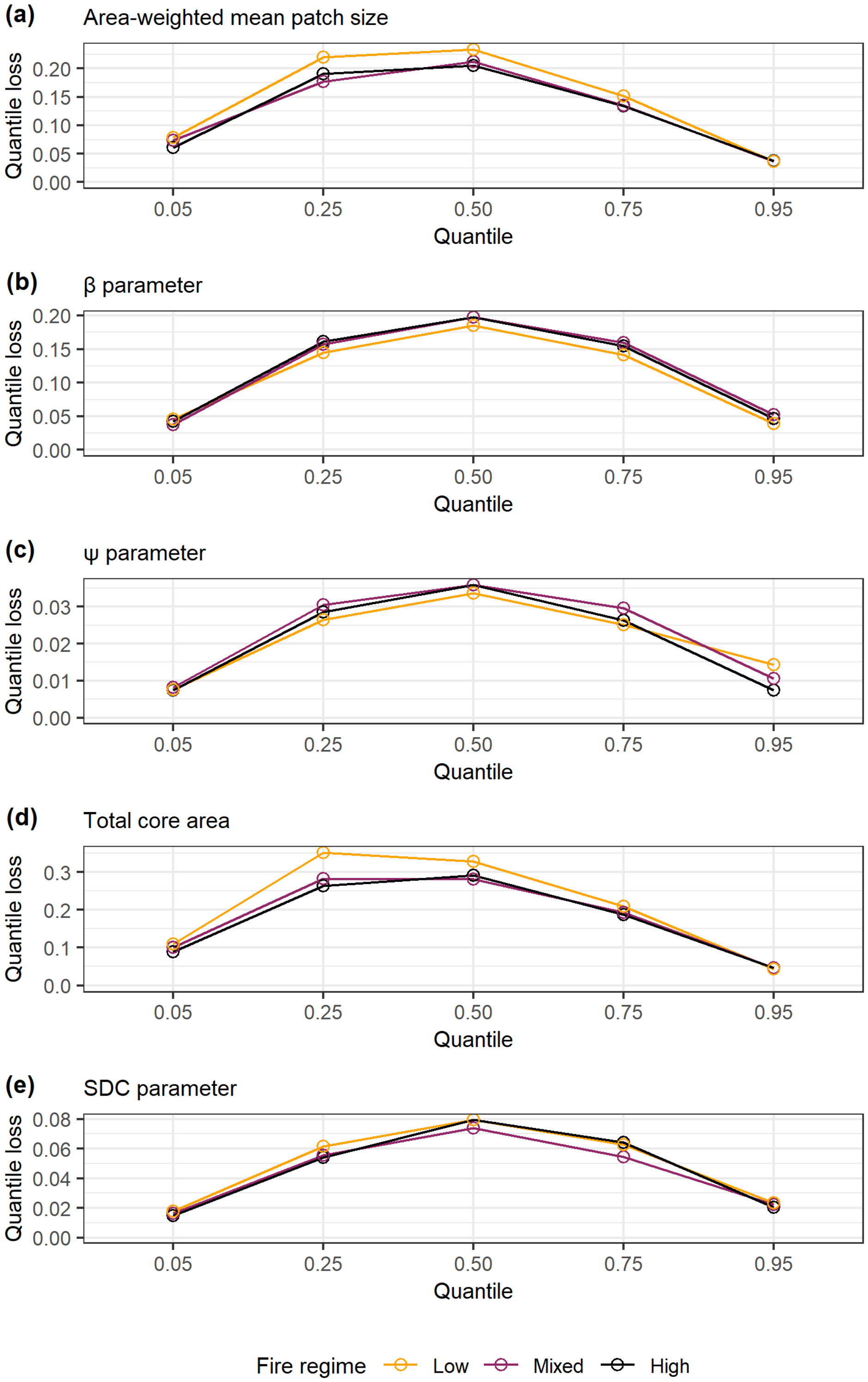

Figure 4.22. Quantile-specific quantile loss (i.e., prediction error) calculated for Northwestern Cascadia using each fire regime model.

CONCLUSION

Forest ecosystems are complex and dynamic systems that provide innumerable services to society, wildlife, and the global environment. As climate continues to change and natural disturbance regimes change in response, understanding the implications of these changes for forest resilience remains a critical research frontier. In this dissertation, I quantified various facets of forest resilience to biotic disturbance (i.e., insects, plant pathogens) and wildfire in temperate forest ecosystems of western North America. The key findings from each chapter, major themes unifying this body of work, and directions for future research are summarized below. Overall, this dissertation provides insights that deepen our understanding of natural disturbance activity in forest ecosystems during a period of rapid climate change.

KEY FINDINGS

Forests are well-adapted to respond to natural disturbances, particularly those with which they have evolved for millennia or more. Following outbreaks of native bark beetles, for example, forests demonstrate robust compensatory responses facilitated by increased growth rates of surviving trees. These growth responses are strongly shaped by both the characteristics and spatial arrangement of surviving trees (Chapter 1). Even when disturbances result in severe tree mortality, compensatory responses can act as key mechanisms of forest resilience and provide post-disturbance continuity in forest function.

As disturbance activity increases, interactions among multiple disturbances are also increasing, which have the potential to alter compensatory responses and thereby erode mechanisms of forest resilience. 'Hotspots' of biotic disturbance activity, or areas where two or more distinct biotic disturbance agents co-occur in space and time, are an emerging and widespread disturbance interaction occurring across the western United States (US) in recent decades. Spatio-temporal patterns of biotic disturbance hotspots are driven primarily by forest composition and regionally important bioclimatic factors (Chapter 2). However, as with individual biotic disturbances, hotspots are stochastic and dynamic processes and therefore cannot be predicted solely from deterministic landscape characteristics or other known drivers (Chapter 2). Understanding and anticipating these types of disturbance interactions is critical, given their potential to alter mechanisms of post-disturbance forest recovery.

The natural ranges of variation in forest disturbance regimes (e.g., the typical ranges of disturbed area, vegetation composition, or patch size distributions) define the bounds within which disturbances typically shape forest ecosystems. In fire-prone systems, spatial patterns of burn severity, and in particular high-severity patches where most trees are killed, are a key driver of post-fire forest regeneration potential. Anticipating the ecological effects of future fire therefore requires understanding the potential range of resulting burn severity patterns. In response to warming and drying conditions, annual burned area and the frequency of large fire events have increased in recent decades in many forest ecosystems worldwide. Despite these changes in climate and fire activity, the range of variation in high-severity burn patches, conditional on fire size, has remained remarkably stationary in Northwest US forest ecosystems (Chapter 3). This stationarity in the relationship between fire size and burn severity patterns offers a simple yet powerful means to quantify the range of ecological effects of future fire activity at regional scales (Chapters 3, 4). For example, as regional fire-size distributions potentially change, shifts towards larger fire events will lead to increasingly large high-severity burn patches with interior areas that are increasingly far from unburned seed sources following fire (Chapter 4). These findings have important implications for a range of forest ecosystems, informing management actions ranging from pre-fire planning stages to post-fire responses.

MAJOR THEMES

Spatial configuration is central to both disturbance ecology and forest resilience. Natural disturbances are by nature contagious processes; the movement of insects (in the case of biotic disturbance) or flames (in the case of wildfire) from one tree to the next strongly shapes how disturbances unfold, the legacies they leave behind, and the effects they have on forest ecosystems. Stochastic processes, including contagion, can overwhelm deterministic factors that might otherwise tend make certain locations resistant to disturbance. For this reason, the spatial patterns of forest disturbance are often difficult to precisely predict. Despite this challenge, understanding the spatial attributes of disturbance processes is key, as the mechanisms and rates of post-disturbance forest recovery strongly depend on the pre- and post-outbreak configuration of live and dead trees, along with forest landscape position at scales ranging from stands to ecoregions.

Throughout this dissertation, I harnessed the spatial configuration of disturbance-affected forest landscapes to better understand ecological processes and anticipate the potential effects of future disturbance activity. The analytical approaches that I used varied with the unique questions and goals of each chapter. In Chapters 1 and 2, I used statistical models accounting for the spatial and temporal structure of biotic disturbance data to estimate the effects of potentially important drivers. Importantly, while controlling for spatial and/or temporal autocorrelation is necessary from a statistical standpoint, doing so can also reveal important facets of disturbance activity. The statistical models used in Chapter 2, for example, simultaneously estimated the effects of forest composition and climate on disturbance patterns while also quantifying the relative contribution of contagion and other dynamic factors. In Chapters 3 and 4, spatial pattern was not controlled for, but rather was itself the primary focus of analysis. While landscape patterns can be quantified in countless ways, I focused on a small number of patch-based metrics that could be directly linked to the ecological effects of wildfire activity. Spatial metrics can be powerful tools for detecting and understanding landscape processes, but their usefulness hinges on specifically designing or selecting metrics that reflect said processes.

It is important to look beyond the mean in any scientific endeavor, and in this dissertation, the importance of variability was a consistent theme. First, landscape heterogeneity is often of particular interest in the fields of landscape ecology and disturbance ecology, largely due to the reciprocal relationship between landscape heterogeneity and disturbance activity (i.e., landscape heterogeneity shapes disturbance activity, which shapes landscape heterogeneity in turn; Turner & Gardner 2015). Fine-scale landscape heterogeneity was the focus of Chapter 1, for example, and plays a key role in shaping forest responses to disturbance. Second, ranges of variation are often more meaningful than central tendencies when characterizing disturbance activity in terms of regimes. For example, quantifying the full range of burn severity patch distributions reveals important similarities and differences between fire regimes that could not be captured by central tendencies alone (Chapter 3). Further, these ranges of variation can be harnessed to simulate the effects of future disturbance activity across a range of scenarios (Chapter 4). Finally, it is the infrequent occurrence of rare events (rather than the most commonly occurring or expected events) that often have the greatest impact. In Chapters 3 and 4, high-severity patch size distributions are shown to take the form of power laws, with a small number of very-large patches having the greatest cumulative ecological effects. Overall, variation played a key role in each chapter of this dissertation, reflecting its importance in many fundamental ecological processes.

FUTURE DIRECTIONS FOR RESEARCH

This dissertation advances several lines of research within the fields of forest disturbance ecology, landscape ecology, and ecosystem resilience. However, many key knowledge gaps remain. For example, building on Chapters 1 and 2, it remains unclear whether and to what extent compensatory responses may be altered in forests affected by multiple biotic agents within a short period of time. Further exploration of the mechanisms driving biotic disturbance interactions is also warranted to provide a deeper understanding of potential feedbacks and links between specific biotic agents. Building on Chapters 3 and 4, it will be important to continue monitoring burn severity patterns and evaluating where those patterns fall relative to contemporary (early 21st century) ranges of variation. Shifts in the ranges of variation characterizing fire regimes may signal potentially important shifts in the drivers of fire activity (e.g., increasing prevalence of fuel constraints in some regions) as fire activity continues to increase.

I relied on empirical statistical modeling approaches throughout this dissertation. While statistical models are powerful analytical tools, there are inherently limits to what we can infer and predict using statistical models. Notably, it is not appropriate to use statistical models to extrapolate beyond the limits of the observed data on which they are trained, as statistical relationships often do not remain stationary under novel conditions. As we look towards managing forest ecosystems under novel future climates, anticipating the potential implications of climate change for disturbance activity and forest resilience will be necessary to guide climate-adapted resource management. Process-based landscape modeling approaches (e.g., Scheller *et al.* 2007; Seidl *et al.* 2012; Hansen *et al.* 2022) are often better equipped to explore how complex systems might respond under novel conditions and over long time scales. Therefore, harnessing insights from both statistical and process-based models will be key to managing forests as climate continues to change.

Forest resilience is a primary focus of this dissertation, and an implicit assumption made throughout this body of work is that maintaining the essential characteristics of forests in their current form is a preferable and/or beneficial management goal. While maintaining forest resilience will be beneficial in many cases, forest reorganization or transition to non-forest ecosystems following disturbance will at times be inevitable (Seidl & Turner 2022), and facilitating transitions within forests will be important for maintaining and promoting climate-adapted landscapes. Therefore, forest management strategies may increasingly need to adopt a *resist*, *accept*, or *direct* framework (*sensu* Lynch *et al.* 2021) regarding ecosystem change in order to preserve essential ecosystem services and functions.

Finally, each chapter of this dissertation was developed with the goal of providing timely scientific information that can aid in natural resource management and decision-making. My hope is that the information contained in this dissertation will be useable in a variety of contexts. Often, however, a gap remains between what scientists consider useful and what decision-makers consider useable (Lemos et al. 2012). This is an area where, along with the broader scientific community, I intend to continue to focus and hone my efforts.

REFERENCES

Abatzoglou, J.T., Battisti, D.S., Williams, A.P., Hansen, W.D., Harvey, B.J. & Kolden, C.A. (2021a). Projected increases in western US forest fire despite growing fuel constraints. *Commun Earth Environ*, 2, 227.

Abatzoglou, J.T., Dobrowski, S.Z., Parks, S.A. & Hegewisch, K.C. (2018a). TerraClimate, a high-resolution global dataset of monthly climate and climatic water balance from 1958-2015. *Scientific Data*, 5, 1–12.

Abatzoglou, J.T., Rupp, D.E., O'Neill, L.W. & Sadegh, M. (2021b). Compound Extremes Drive the Western Oregon Wildfires of September 2020. *Geophysical Research Letters*, 48, e2021GL092520.

Abatzoglou, J.T., Williams, A.P., Boschetti, L., Zubkova, M. & Kolden, C.A. (2018b). Global patterns of interannual climate–fire relationships. *Global Change Biology*, 24, 5164–5175.

Agee, J.K. (1993). *Fire ecology of Pacific Northwest forests*. Island Press, Washington, DC.

Agee, J.K. (1998). The landscape ecology of western forest fire regimes. *Northwest Science*, 72, 24–34.

Albrich, K., Rammer, W., Turner, M.G., Ratajczak, Z., Braziunas, K.H., Hansen, W.D., *et al.* (2020). Simulating forest resilience: A review. *Global Ecol. Biogeogr.*, 29, 2082–2096.

Alfaro, R.I., Campbell, R., Vera, P., Hawkes, B. & Shore, T.L. (2003). *Dendroecological Reconstruction of Mountain Pine Beetle Outbreaks in the Chilcotin Plateau of British Columbia*. Mountain Pine Beetle Symposium: Challenges and Solutions.

Allen, C.R., Angeler, D.G., Cumming, G.S., Folke, C., Twidwell, D. & Uden, D.R. (2016). Quantifying spatial resilience. *J Appl Ecol*, 53, 625–635.

Amman, G.D. (1969). *Mountain pine beetle emergence in relation to depth of lodgepole pine bark* (No. INT-96). USDA Forest Service, Intermountain Forest and Range Experiment Station, Ogden, UT.

Andrus, R.A., Harvey, B.J., Chai, R.K. & Veblen, T.T. (2018). Different vital rates of Engelmann spruce and subalpine fir explain discordance in understory and overstory dominance. *Can. J. For. Res.*, 48, 1554–1562.

Arienti, M.C., Cumming, S.G. & Boutin, S. (2006). Empirical models of forest fire initial attack success probabilities: the effects of fuels, anthropogenic linear features, fire weather, and management. *Can. J. For. Res.*, 36, 3155–3166.

Astrup, R., Coates, K.D. & Hall, E. (2008). Recruitment limitation in forests: Lessons from an unprecedented mountain pine beetle epidemic. *For. Ecol. Manag.*, 256, 1743–1750.

Axelson, J.N., Alfaro, R.I. & Hawkes, B.C. (2009). Influence of fire and mountain pine beetle on the dynamics of lodgepole pine stands in British Columbia, Canada. *For. Ecol. Manag.*, 257, 1874–1882.

Bače, R., Svoboda, M., Janda, P., Morrissey, R.C., Wild, J., Clear, J.L., *et al.* (2015). Legacy of Pre-Disturbance Spatial Pattern Determines Early Structural Diversity following Severe Disturbance in Montane Spruce Forests. *PLoS ONE*, 10, e0139214.

Backsen, J.C. & Howell, B. (2013). Comparing Aerial Detection and Photo Interpretation for Conducting Forest Health Surveys. *Western Journal of Applied Forestry*, 28, 3–8.

Bai, W., Dong, M., Li, L., Feng, C. & Xu, W. (2021). Randomized quantile residuals for diagnosing zero-inflated generalized linear mixed models with applications to microbiome count data. *BMC Bioinformatics*, 22, 564.

Baker, W.L. (2009). *Fire ecology in Rocky Mountain landscapes*. Island Press, Washington, DC.

Beck, H.E., Zimmermann, N.E., McVicar, T.R., Vergopolan, N., Berg, A. & Wood, E.F. (2018). Present and future Köppen-Geiger climate classification maps at 1-km resolution. *Sci Data*, 5, 180214.

Bentz, B.J., Régnière, J., Fettig, C.J., Hansen, E.M., Hayes, J.L., Hicke, J.A., *et al.* (2010). Climate Change and Bark Beetles of the Western United States and Canada: Direct and Indirect Effects. *BioScience*, 60, 602–613.

Berner, L.T., Law, B.E., Meddens, A.J.H. & Hicke, J.A. (2017). Tree mortality from fires, bark beetles, and timber harvest during a hot and dry decade in the western United States (2003–2012). *Environ. Res. Lett.*, 12, 065005.

Beven, K.J. & Kirkby, M.J. (1979). A physically based, variable contributing area model of basin hydrology. *Hydrological Sciences Journal*, 24, 43–69.

Blangiardo, M. & Cameletti, M. (2015). *Spatial and spatio-temporal Bayesian models with R-INLA*. John Wiley & Sons.

Boulanger, Y., Parisien, M.-A. & Wang, X. (2018). Model-specification uncertainty in future area burned by wildfires in Canada. *Int. J. Wildland Fire*, 27, 164–175.

Bowman, D.M.J.S., Kolden, C.A., Abatzoglou, J.T., Johnston, F.H., van der Werf, G.R. & Flannigan, M. (2020). Vegetation fires in the Anthropocene. *Nat Rev Earth Environ*, 1, 500–515.

Bradford, J.B., Birdsey, R.A., Joyce, L.A. & Ryan, M.G. (2008). Tree age, disturbance history, and carbon stocks and fluxes in subalpine Rocky Mountain forests. *Global Change Biology*, 14, 2882–2897.

Braziunas, K.H., Kiel, N.G. & Turner, M.G. (2023). Less fuel for the next fire? Short-interval fire delays forest recovery and interacting drivers amplify effects. *Ecology*, e4042.

Brown, M.G., Black, T.A., Nesic, Z., Fredeen, A.L., Foord, V.N., Spittlehouse, D.L., *et al.* (2012). The carbon balance of two lodgepole pine stands recovering from mountain pine beetle attack in British Columbia. *Agricultural and Forest Meteorology*, 153, 82–93.

Buma, B. (2015). Disturbance interactions: characterization, prediction, and the potential for cascading effects. *Ecosphere*, 6, 1–15.

Buonanduci, M.S., Morris, J.E., Agne, M.C. & Harvey, B.J. (2020). Neighborhood context mediates probability of host tree mortality in a severe bark beetle outbreak. *Ecosphere*, 11, e03236.

Burton, P.J., Jentsch, A. & Walker, L.R. (2020). The Ecology of Disturbance Interactions. *BioScience*, 70, 854–870.

Cade, B.S. & Noon, B.R. (2003). A gentle introduction to quantile regression for ecologists. *Front Ecol Environ*, 1, 412–420.

Cansler, C.A. & McKenzie, D. (2012). How Robust Are Burn Severity Indices When Applied in a New Region? Evaluation of Alternate Field-Based and Remote-Sensing Methods. *Remote Sensing*, 4, 456–483.

Cansler, C.A. & McKenzie, D. (2014). Climate, fire size, and biophysical setting control fire severity and spatial pattern in the northern Cascade Range, USA. *Ecol Appl*, 24, 1037–1056.

Caspersen, J.P., Vanderwel, M.C., Cole, W.G. & Purves, D.W. (2011). How Stand Productivity Results from Size- and Competition-Dependent Growth and Mortality. *PLoS ONE*, 6, e28660.

Chai, R.K., Andrus, R.A., Rodman, K., Harvey, B.J. & Veblen, T.T. (2019). Stand dynamics and topographic setting influence changes in live tree biomass over a 34-year permanent plot record in a subalpine forest in the Colorado Front Range. *Can. J. For. Res.*, 49, 1256–1264.

Chambers, J.C., Allen, C.R. & Cushman, S.A. (2019). Operationalizing Ecological Resilience Concepts for Managing Species and Ecosystems at Risk. *Front. Ecol. Evol.*, 7, 241.

Chapman, T.B., Veblen, T.T. & Schoennagel, T. (2012). Spatiotemporal patterns of mountain pine beetle activity in the southern Rocky Mountains. *Ecology*, 93, 2175–2185.

Chesson, P. (2000). Mechanisms of Maintenance of Species Diversity. *Annu. Rev. Ecol. Syst.*, 31, 343–366.

Churchill, D.J., Jeronimo, S.M.A., Hessburg, P.F., Cansler, C.A., Povak, N.A., Kane, V.R., *et al.* (2022). Post-fire landscape evaluations in Eastern Washington, USA: Assessing the work of contemporary wildfires. *For. Ecol. Manag.*, 504, 119796.

Clarke, H., Penman, T., Boer, M., Cary, G.J., Fontaine, J.B., Price, O., *et al.* (2020). The Proximal Drivers of Large Fires: A Pyrogeographic Study. *Front. Earth Sci.*, 8, 90.

Cliff, A.D. & Ord, J.K. (1981). *Spatial processes: models & applications*. Taylor & Francis.

Cole, H.M., Andrus, R.A., Butkiewicz, C., Rodman, K.C., Santiago, O., Tutland, N.J., *et al.* (2022). Outbreaks of Douglas-Fir Beetle Follow Western Spruce Budworm Defoliation in the Southern Rocky Mountains, USA. *Forests*, 13, 371.

Cole, W.E. & Amman, G.D. (1980). *Mountain pine beetle dynamics in lodgepole pine forests, Part I: Course of an infestation* (No. INT-188). USDA Forest Service, Intermountain Forest and Range Experiment Station.

Coleman, T.W., Graves, A.D., Heath, Z., Flowers, R.W., Hanavan, R.P., Cluck, D.R., *et al.* (2018). Accuracy of aerial detection surveys for mapping insect and disease disturbances in the United States. *For. Ecol. Manag.*, 430, 321–336.

Collins, B.J., Rhoades, C.C., Battaglia, M.A. & Hubbard, R.M. (2012). The effects of bark beetle outbreaks on forest development, fuel loads and potential fire behavior in salvage logged and untreated lodgepole pine forests. *For. Ecol. Manag.*, 284, 260–268.

Collins, B.J., Rhoades, C.C., Hubbard, R.M. & Battaglia, M.A. (2011). Tree regeneration and future stand development after bark beetle infestation and harvesting in Colorado lodgepole pine stands. *For. Ecol. Manag.*, 261, 2168–2175.

Collins, B.M., Stevens, J.T., Miller, J.D., Stephens, S.L., Brown, P.M. & North, M.P. (2017). Alternative characterization of forest fire regimes: incorporating spatial patterns. *Landsc Ecol*, 32, 1543–1552.

Collins, L., Bradstock, R.A., Clarke, H., Clarke, M.F., Nolan, R.H. & Penman, T.D. (2021). The 2019/2020 mega-fires exposed Australian ecosystems to an unprecedented extent of high-severity fire. *Environ. Res. Lett.*, 16, 044029.

Commission for Environmental Cooperation. (1997). *Ecological regions of North America: toward a common perspective*.

Contreras, M.A., Affleck, D. & Chung, W. (2011). Evaluating tree competition indices as predictors of basal area increment in western Montana forests. *For. Ecol. Manag.*, 262, 1939–1949.

Coop, J.D., Parks, S.A., Stevens-Rumann, C.S., Crausbay, S.D., Higuera, P.E., Hurteau, M.D., *et al.* (2020). Wildfire-Driven Forest Conversion in Western North American Landscapes. *BioScience*, 70, 659–673.

Cooper, L.A., Reed, C.C. & Ballantyne, A.P. (2018). Mountain pine beetle attack faster growing lodgepole pine at low elevations in western Montana, USA. *For. Ecol. Manag.*, 427, 200–207.

Cova, G., Kane, V.R., Prichard, S., North, M. & Cansler, C.A. (2023). The outsized role of California's largest wildfires in changing forest burn patterns and coarsening ecosystem scale. *For. Ecol. Manag.*, 528, 120620.

Craine, J.M. & Dybzinski, R. (2013). Mechanisms of plant competition for nutrients, water and light. *Funct Ecol*, 27, 833–840.

Cumming, G.S. (2011). Spatial resilience: integrating landscape ecology, resilience, and sustainability. *Landsc Ecol*, 26, 899–909.

Dale, V.H., Joyce, L.A., Mcnulty, S., Neilson, R.P., Ayres, M.P., Flannigan, M.D., *et al.* (2001). Climate Change and Forest Disturbances. *BioScience*, 51, 723.

Dalton, M.M., Mote, P. & Snover, A.K. (2013). *Climate change in the Northwest: Implications for our landscapes, waters, and communities*. Island Press, Washington, DC.

Davis, K.T., Robles, M.D., Kemp, K.B., Higuera, P.E., Chapman, T., Metlen, K.L., *et al.* (2023). Reduced fire severity offers near-term buffer to climate-driven declines in conifer resilience across the western United States. *Proc. Natl. Acad. Sci. U.S.A.*, 120, e2208120120.

Davis, T.S., Meddens, A.J.H., Stevens-Rumann, C.S., Jansen, V.S., Sibold, J.S. & Battaglia, M.A. (2022). Monitoring resistance and resilience using carbon trajectories: Analysis of forest management–disturbance interactions. *Ecol Appl*, 32, e2704.

DeRose, R.J. & Long, J.N. (2010). Regeneration response and seedling bank dynamics on a Dendroctonus rufipennis-killed Picea engelmannii landscape. *Journal of Vegetation Science*, 21, 377–387.

Devroye, L. (1986). *Non-Uniform Random Variate Generation*. Springer.

Dhar, A. & Hawkins, C.D.B. (2011). Regeneration and growth following mountain pine beetle attack: a synthesis of knowledge. *BC Journal of Ecosystems and Management*, 12, 1–16.

Diskin, M., Rocca, M.E., Nelson, K.N., Aoki, C.F. & Romme, W.H. (2011). Forest developmental trajectories in mountain pine beetle disturbed forests of Rocky Mountain National Park, Colorado. *Can. J. For. Res.*, 41, 782–792.

Donato, D.C., Fontaine, J.B., Campbell, J.L., Robinson, W.D., Kauffman, J.B. & Law, B.E. (2009). Conifer regeneration in stand-replacement portions of a large mixed-severity wildfire in the Klamath–Siskiyou Mountains. *Can. J. For. Res.*, 39, 823–838.

Donato, D.C., Halofsky, J.S. & Reilly, M.J. (2020). Corralling a black swan: natural range of variation in a forest landscape driven by rare, extreme events. *Ecol Appl*, 30.

Donato, D.C., Harvey, B.J., Romme, W.H., Simard, M. & Turner, M.G. (2013). Bark beetle effects on fuel profiles across a range of stand structures in Douglas-fir forests of Greater Yellowstone. *Ecol Appl*, 23, 3–20.

Duane, A., Castellnou, M. & Brotons, L. (2021). Towards a comprehensive look at global drivers of novel extreme wildfire events. *Climatic Change*, 165, 43.

Evans, J.S. (2021). Package "spatialEco."

Fettig, C.J., Klepzig, K.D., Billings, R.F., Munson, A.S., Nebeker, T.E., Negrón, J.F., *et al.* (2007). The effectiveness of vegetation management practices for prevention and control of bark beetle infestations in coniferous forests of the western and southern United States. *For. Ecol. Manag.*, 238, 24–53.

Franklin, J.F. & Dyrness, C.T. (1973). *Natural vegetation of Oregon and Washington*. US Government Printing Office.

Franklin, J.F., Lindenmayer, D., MacMahon, J.A., McKee, A., Magnuson, J., Perry, D.A., *et al.* (2000). Threads of continuity: Ecosystem disturbances, biological legacies and ecosystem recovery. *Conservation in Practice*, 1, 8–17.

Franklin, J.F., Spies, T.A., Pelt, R.V., Carey, A.B., Thornburgh, D.A., Berg, D.R., *et al.* (2002). Disturbances and structural development of natural forest ecosystems with silvicultural implications, using Douglas-fir forests as an example. *For. Ecol. Manag.*, 155, 399–423.

Fromm, M., Lindsey, D.T., Servranckx, R., Yue, G., Trickl, T., Sica, R., *et al.* (2010). The Untold Story of Pyrocumulonimbus. *Bull. Amer. Meteor. Soc.*, 91, 1193–1210.

Fuglstad, G.-A., Simpson, D., Lindgren, F. & Rue, H. (2019). Constructing Priors that Penalize the Complexity of Gaussian Random Fields. *Journal of the American Statistical Association*, 114, 445–452.

Gardner, R.H. & Urban, D.L. (2007). Neutral models for testing landscape hypotheses. *Landsc Ecol*, 22, 15–29.

Gaylord, M.L., Kolb, T.E., Pockman, W.T., Plaut, J.A., Yepez, E.A., Macalady, A.K., *et al.* (2013). Drought predisposes piñon–juniper woodlands to insect attacks and mortality. *New Phytol*, 198, 567–578.

Getzin, S., Dean, C., He, F., A. Trofymow, J., Wiegand, K. & Wiegand, T. (2006). Spatial patterns and competition of tree species in a Douglas-fir chronosequence on Vancouver Island. *Ecography*, 29, 671–682.

Gill, N.S., Turner, M.G., Brown, C.D., Glassman, S.I., Haire, S.L., Hansen, W.D., *et al.* (2022). Limitations to Propagule Dispersal Will Constrain Postfire Recovery of Plants and Fungi in Western Coniferous Forests. *BioScience*, 72, 347–364.

Gonzalez, A. & Loreau, M. (2009). The Causes and Consequences of Compensatory Dynamics in Ecological Communities. *Annu. Rev. Ecol. Evol. Syst.*, 40, 393–414.

Greene, D.F. & Johnson, E.A. (1989). A Model of Wind Dispersal of Winged or Plumed Seeds. *Ecology*, 70, 339–347.

Griesbauer, H. & Green, S. (2006). Examining the utility of advance regeneration for reforestation and timber production in unsalvaged stands killed by the mountain pine beetle: Controlling factors and management implications. *BC Journal of Ecosystems and Management*, 7, 81–92.

Hadley, K.S. & Veblen, T.T. (1993). Stand response to western spruce budworm and Douglas-fir bark beetle outbreaks, Colorado Front Range. *Can. J. For. Res.*, 23, 479–491.

Hagmann, R.K., Hessburg, P.F., Prichard, S.J., Povak, N.A., Brown, P.M., Fulé, P.Z., *et al.* (2021). Evidence for widespread changes in the structure, composition, and fire regimes of western North American forests. *Ecol Appl*, 31.

Halofsky, J.E., Peterson, D.L. & Harvey, B.J. (2020). Changing wildfire, changing forests: the effects of climate change on fire regimes and vegetation in the Pacific Northwest, USA. *Fire Ecol.*, 16, 4.

Halofsky, J.S., Conklin, D.R., Donato, D.C., Halofsky, J.E. & Kim, J.B. (2018a). Climate change, wildfire, and vegetation shifts in a high-inertia forest landscape: Western Washington, U.S.A. *PLoS ONE*, 13, e0209490.

Halofsky, J.S., Donato, D.C., Franklin, J.F., Halofsky, J.E., Peterson, D.L. & Harvey, B.J. (2018b). The nature of the beast: examining climate adaptation options in forests with stand-replacing fire regimes. *Ecosphere*, 9, e02140.

Hansen, W.D., Krawchuk, M.A., Trugman, A.T. & Williams, A.P. (2022). The Dynamic Temperate and Boreal Fire and Forest-Ecosystem Simulator (DYNAFFOREST): Development and evaluation. *Environmental Modelling & Software*, 156, 105473.

Hantson, S., Pueyo, S. & Chuvieco, E. (2016). Global fire size distribution: from power law to log-normal. *Int. J. Wildland Fire*, 25, 403.

Hart, S.J., Veblen, T.T., Schneider, D. & Molotch, N.P. (2017). Summer and winter drought drive the initiation and spread of spruce beetle outbreak. *Ecology*, 98, 2698–2707.

Harvey, B.J., Andrus, R.A., Battaglia, M.A., Negrón, J.F., Orrego, A. & Veblen, T.T. (2021). Droughty times in mesic places: factors associated with forest mortality vary by scale in a temperate subalpine region. *Ecosphere*, 12, e03318.

Harvey, B.J., Buonanduci, M.S. & Turner, M.G. (2023). Spatial interactions among short-interval fires reshape forest landscapes. *Global Ecol Biogeogr*, 32, 586–602.

Harvey, B.J., Donato, D.C. & Turner, M.G. (2016a). Drivers and trends in landscape patterns of stand-replacing fire in forests of the US Northern Rocky Mountains (1984–2010). *Landsc Ecol*, 31, 2367–2383.

Harvey, B.J., Donato, D.C. & Turner, M.G. (2016b). High and dry: post-fire tree seedling establishment in subalpine forests decreases with post-fire drought and large stand-replacing burn patches: Drought and post-fire tree seedlings. *Global Ecol. Biogeogr.*, 25, 655–669.

Harvey, B.J., Hart, S.J., Tobin, P.C., Veblen, T.T., Donato, D.C., Buonanduci, M.S., *et al.* (In press). Emergent hotspots of biotic disturbances and their consequences for forest resilience. *Front Ecol Environ.*

Hawkes, B., Taylor, S.W., Stockdale, C., Shore, T.L., Alfaro, R.I., Campbell, R., *et al.* (2003). *Impact of Mountain Pine Beetle on Stand Dynamics in British Columbia*. Mountain Pine Beetle Symposium: Challenges and Solutions.

Hawkins, C.D.B., Dhar, A. & Balliet, N.A. (2013). Radial growth of residual overstory trees and understory saplings after mountain pine beetle attack in central British Columbia. *For. Ecol. Manag.*, 310, 348–356.

Heath, R. & Alfaro, R.I. (1990). Growth response in a Douglas-fir/lodgepole pine stand after thinning of lodgepole pine by the mountain pine beetle: A case study. *Journal of the Entomological Society of British Columbia*, 87, 16–21.

Hédl, R., Svátek, M., Dančák, M., Rodzay, A.W., Salleh A.B., M. & Kamariah, A.S. (2009). A new technique for inventory of permanent plots in tropical forests: a case study from lowland dipterocarp forest in Kuala Belalong, Brunei Darussalam. *Blumea - Biodiversity, Evolution and Biogeography of Plants*, 54, 124–130.

Hemstrom, M.A. & Franklin, J.F. (1982). Fire and Other Disturbances of the Forests in Mount Rainier National Park. *Quaternary Research*, 18, 32–51.

Hicke, J.A., Xu, B., Meddens, A.J.H. & Egan, J.M. (2020). Characterizing recent bark beetle-caused tree mortality in the western United States from aerial surveys. *For. Ecol. Manag.*, 475, 118402.

Hijmans, R.J., van Etten, J., Sumner, M., Cheng, J., Baston, D., Bevan, A., *et al.* (2022). Package "raster."

Holling, C.S. (1973). Resilience and Stability of Ecological Systems. *Annu. Rev. Ecol. Syst.*, 24.

Hood, S.M., Harvey, B.J., Fornwalt, P.J., Naficy, C.E., Hansen, W.D., Davis, K.T., *et al.* (2021). Fire Ecology of Rocky Mountain Forests. In: *Fire Ecology and Management: Past, Present, and Future of US Forested Ecosystems*, Managing Forest Ecosystems (eds. Greenberg, C.H. & Collins, B.). Springer International Publishing, Cham, pp. 287–336.

Howe, M., Carroll, A., Gratton, C. & Raffa, K.F. (2021). Climate-induced outbreaks in high-elevation pines are driven primarily by immigration of bark beetles from historical hosts. *Global Change Biology*, 27, 5786–5805.

Hubbard, R.M., Rhoades, C.C., Elder, K. & Negron, J. (2013). Changes in transpiration and foliage growth in lodgepole pine trees following mountain pine beetle attack and mechanical girdling. *For. Ecol. Manag.*, 289, 312–317.

Huckaby, L.S. & Moir, W.H. (1998). Forest communities at Fraser Experimental Forest, Colorado. *The Southwestern Naturalist*, 43, 204–218.

Jarvis, D.S. & Kulakowski, D. (2015). Long-term history and synchrony of mountain pine beetle outbreaks in lodgepole pine forests. *J. Biogeogr.*, 42, 1029–1039.

Johnson, E.W. & Ross, J. (2008). Quantifying error in aerial survey data. *Australian Forestry*, 71, 216–222.

Johnson, E.W. & Wittwer, D. (2008). Aerial detection surveys in the United States. *Australian Forestry*, 71, 212–215.

Johnstone, J.F., Allen, C.D., Franklin, J.F., Frelich, L.E., Harvey, B.J., Higuera, P.E., *et al.* (2016). Changing disturbance regimes, ecological memory, and forest resilience. *Front Ecol Environ*, 14, 369–378.

Juang, C.S., Williams, A.P., Abatzoglou, J.T., Balch, J.K., Hurteau, M.D. & Moritz, M.A. (2022). Rapid Growth of Large Forest Fires Drives the Exponential Response of Annual Forest-Fire Area to Aridity in the Western United States. *Geophysical Research Letters*, 49.

Kane, J.M. & Kolb, T.E. (2010). Importance of resin ducts in reducing ponderosa pine mortality from bark beetle attack. *Oecologia*, 164, 601–609.

Kautz, M., Meddens, A.J.H., Hall, R.J. & Arneth, A. (2017). Biotic disturbances in Northern Hemisphere forests - a synthesis of recent data, uncertainties and implications for forest monitoring and modelling. *Global Ecol. Biogeogr.*, 26, 533–552.

Kemp, K.B., Higuera, P.E. & Morgan, P. (2016). Fire legacies impact conifer regeneration across environmental gradients in the U.S. northern Rockies. *Landsc Ecol*, 31, 619–636.

Kennedy, M.C. (2019). Experimental design principles to choose the number of Monte Carlo replicates for stochastic ecological models. *Ecological Modelling*, 394, 11–17.

Kennedy, M.C., Bart, R.R., Tague, C.L. & Choate, J.S. (2021). Does hot and dry equal more wildfire? Contrasting short- and long-term climate effects on fire in the Sierra Nevada, CA. *Ecosphere*, 12.

Koenker, R. & Bassett, G. (1978). Regression quantiles. *Econometrica*.

Krainski, E.T., Gómez-Rubio, V., Bakka, H., Lenzi, A., Castro-Camilo, D., Simpson, D., *et al.* (2019). *Advanced Spatial Modeling with Stochastic Partial Differential Equations Using R and INLA*. Chapman & Hall/CRC Press.

Krist, F.J. (2014). *2013-2027 National insect and disease forest risk assessment*. United States Department of Agriculture, Forest Service, Forest Health Technology Enterprise Team.

Laughlin, M.M., Rangel-Parra, L.K., Morris, J.E., Donato, D.C., Halofsky, J.S. & Harvey, B.J. (In prep). Patterns and drivers of conifer regeneration following stand-replacing wildfire in western Cascadia.

Lecina-Diaz, J., Martínez-Vilalta, J., Alvarez, A., Banqué, M., Birkmann, J., Feldmeyer, D., *et al.* (2021). Characterizing forest vulnerability and risk to climate-change hazards. *Front Ecol Environ*, 19, 126–133.

LeCompte-Mastenbrook, J.K. (2015). Restoring Coast Salish foods and landscapes: a more-than-human politics of place, history and becoming. Dissertation. University of Washington.

Lemos, M.C., Kirchhoff, C.J. & Ramprasad, V. (2012). Narrowing the climate information usability gap. *Nature Clim Change*, 2, 789–794.

van Lierop, P., Lindquist, E., Sathyapala, S. & Franceschini, G. (2015). Global forest area disturbance from fire, insect pests, diseases and severe weather events. *For. Ecol. Manag.*, 352, 78–88.

Lindgren, F., Rue, H. & Lindström, J. (2011). An Explicit Link between Gaussian Fields and Gaussian Markov Random Fields: The Stochastic Partial Differential Equation Approach. *Journal of the Royal Statistical Society Series B: Statistical Methodology*, 73, 423–498.

Linnakoski, R., Kasanen, R., Dounavi, A. & Forbes, K.M. (2019). Editorial: Forest Health Under Climate Change: Effects on Tree Resilience, and Pest and Pathogen Dynamics. *Front. Plant Sci.*, 10, 1157.

Littell, J.S., McKenzie, D., Wan, H.Y. & Cushman, S.A. (2018). Climate Change and Future Wildfire in the Western United States: An Ecological Approach to Nonstationarity. *Earth's Future*, 6, 1097–1111.

Littlefield, C.E. (2019). Topography and post-fire climatic conditions shape spatio-temporal patterns of conifer establishment and growth. *Fire Ecol.*, 15, 34.

Long, J.N., Dean, T.J. & Roberts, S.D. (2004). Linkages between silviculture and ecology: examination of several important conceptual models. *For. Ecol. Manag.*, 200, 249–261.

Long, J.N. & Vacchiano, G. (2014). A comprehensive framework of forest stand property–density relationships: perspectives for plant population ecology and forest management. *Annals of Forest Science*, 71, 325–335.

Lutz, J.A., Larson, A.J., Furniss, T.J., Donato, D.C., Freund, J.A., Swanson, M.E., *et al.* (2014). Spatially nonrandom tree mortality and ingrowth maintain equilibrium pattern in an old-growth *Pseudotsuga–Tsuga* forest. *Ecology*, 95, 2047–2054.

Lydersen, J.M., Collins, B.M., Miller, J.D., Fry, D.L. & Stephens, S.L. (2016). Relating Fire-Caused Change in Forest Structure to Remotely Sensed Estimates of Fire Severity. *Fire Ecol.*, 12, 99–116.

Lynch, A.J., Thompson, L.M., Beever, E.A., Cole, D.N., Engman, A.C., Hawkins Hoffman, C., *et al.* (2021). Managing for RADical ecosystem change: applying the Resist-Accept-Direct (RAD) framework. *Front Ecol Environ*, 19, 461–469.

Manion, P.D. (1981). *Tree disease concepts*. Prentice-Hall, Inc., Englewood Cliffs, NJ.

Marston, R.A. & Anderson, J.E. (1991). Watersheds and Vegetation of the Greater Yellowstone Ecosystem. *Conservation Biology*, 5, 338–346.

Mauger, G., Casola, J.H., Morgan, H.A., Strauch, R.L., Jones, B., Curry, B., *et al.* (2015). *State of Knowledge: Climate Change in Puget Sound* (Report prepared for the Puget Sound Partnership and the National Oceanic and Atmospheric Administration). Climate Impacts Group, University of Washington, Seattle.

McColl-Gausden, S.C., Bennett, L.T., Clarke, H.G., Ababei, D.A. & Penman, T.D. (2022). The fuel–climate–fire conundrum: How will fire regimes change in temperate eucalypt forests under climate change? *Global Change Biology*, 28, 5211–5226.

McConnell, T.J., Johnson, E.W. & Burns, B. (2000). *A guide to conducting aerial sketchmapping surveys*. US Department of Agriculture, Forest Service, Forest Health Technology Enterprise Team.

McCune, B. (2007). Improved estimates of incident radiation and heat load using non-parametric regression against topographic variables. *Journal of Vegetation Science*, 18, 751–754.

McCune, B. & Keon, D. (2002). Equations for potential annual direct incident radiation and heat load. *Journal of Vegetation Science*, 13, 603–606.

McKenzie, D. & Kennedy, M.C. (2011). Scaling Laws and Complexity in Fire Regimes. In: *The Landscape Ecology of Fire*, Ecological Studies (eds. McKenzie, D., Miller, C. & Falk, D.A.). Springer Netherlands, Dordrecht, pp. 27–49.

McKenzie, D. & Kennedy, M.C. (2012). Power laws reveal phase transitions in landscape controls of fire regimes. *Nat Commun*, 3, 726.

McKenzie, D., Miller, C. & Falk, D.A. (2011). *The landscape ecology of fire*. Springer Science & Business Media.

Meddens, A.J.H., Hicke, J.A. & Ferguson, C.A. (2012). Spatiotemporal patterns of observed bark beetle-caused tree mortality in British Columbia and the western United States. *Ecol Appl*, 22, 1876–1891.

Millar, C.I. & Stephenson, N.L. (2015). Temperate forest health in an era of emerging megadisturbance. *Science*, 349, 823–826.

Miller, J.D., Safford, H.D., Crimmins, M. & Thode, A.E. (2009). Quantitative Evidence for Increasing Forest Fire Severity in the Sierra Nevada and Southern Cascade Mountains, California and Nevada, USA. *Ecosystems*, 12, 16–32.

Miller, J.D., Skinner, C.N., Safford, H.D., Knapp, E.E. & Ramirez, C.M. (2012). Trends and causes of severity, size, and number of fires in northwestern California, USA. *Ecol Appl*, 22, 184–203.

Miller, J.D. & Thode, A.E. (2007). Quantifying burn severity in a heterogeneous landscape with a relative version of the delta Normalized Burn Ratio (dNBR). *Remote Sensing of Environment*, 109, 66–80.

Moritz, M.A., Hessburg, P.F. & Povak, N.A. (2011). Native Fire Regimes and Landscape Resilience. In: *The Landscape Ecology of Fire*, Ecological Studies (eds. McKenzie, D., Miller, C. & Falk, D.A.). Springer Netherlands, Dordrecht, pp. 51–86.

Morris, J.E., Buonanduci, M.S., Agne, M.C., Battaglia, M.A. & Harvey, B.J. (2022). Does the legacy of historical thinning treatments foster resilience to bark beetle outbreaks in subalpine forests? *Ecol Appl*, 32.

Muggeo, V.M.R. (2021). Additive Quantile regression with automatic smoothness selection: the R package quantregGrowth.

Muggeo, V.M.R., Torretta, F., Eilers, P.H.C., Sciandra, M. & Attanasio, M. (2021). Multiple smoothing parameters selection in additive regression quantiles. *Statistical Modelling*, 21, 428–448.

Neel, M.C., McGarigal, K. & Cushman, S.A. (2004). Behavior of class-level landscape metrics across gradients of class aggregation and area. *Landsc Ecol*, 19, 435–455.

Negrón, J.F. & Huckaby, L. (2020). Reconstructing historical outbreaks of mountain pine beetle in lodgepole pine forests in the Colorado Front Range. *For. Ecol. Manag.*, 473, 118270.

Newman, E.A., Kennedy, M.C., Falk, D.A. & McKenzie, D. (2019). Scaling and Complexity in Landscape Ecology. *Front. Ecol. Evol.*, 7, 293.

Nigh, G.D., Antos, J.A. & Parish, R. (2008). Density and distribution of advance regeneration in mountain pine beetle killed lodgepole pine stands of the Montane Spruce zone of southern British Columbia. *Can. J. For. Res.*, 38, 2826–2836.

North, M.P., York, R.A., Collins, B.M., Hurteau, M.D., Jones, G.M., Knapp, E.E., *et al.* (2021). Pyrosilviculture Needed for Landscape Resilience of Dry Western United States Forests. *Journal of Forestry*, 119, 520–544.

Oliver, C.D. & Larson, B.A. (1996). *Forest stand dynamics*. John Wiley & Sons.

Paine, R.T., Tegner, M.J. & Johnson, E.A. (1998). Compounded Perturbations Yield Ecological Surprises. *Ecosystems*, 1, 535–545.

Parks, S., Holsinger, L., Voss, M., Loehman, R. & Robinson, N. (2018a). Mean Composite Fire Severity Metrics Computed with Google Earth Engine Offer Improved Accuracy and Expanded Mapping Potential. *Remote Sensing*, 10, 879.

Parks, S.A. & Abatzoglou, J.T. (2020). Warmer and Drier Fire Seasons Contribute to Increases in Area Burned at High Severity in Western US Forests From 1985 to 2017. *Geophysical Research Letters*, 47.

Parks, S.A., Holsinger, L.M., Panunto, M.H., Jolly, W.M., Dobrowski, S.Z. & Dillon, G.K. (2018b). High-severity fire: evaluating its key drivers and mapping its probability across western US forests. *Environ. Res. Lett.*, 13, 044037.

Pausas, J.G., Keeley, J.E. & Schwilk, D.W. (2017). Flammability as an ecological and evolutionary driver. *J Ecol*, 105, 289–297.

Pebesma, E. (2018). Simple Features for R: Standardized Support for Spatial Vector Data. *The R Journal*, 10, 439.

Pebesma, E.J. (2004). Multivariable geostatistics in S: the gstat package. *Computers & Geosciences*, 30, 683–691.

Peet, R.K. (1978). Forest vegetation of the Colorado Front Range: Patterns of species diversity. *Vegetatio*, 37, 65–78.

Peters, D.P.C., Pielke, R.A., Bestelmeyer, B.T., Allen, C.D., Munson-McGee, S. & Havstad, K.M. (2004). Cross-scale interactions, nonlinearities, and forecasting catastrophic events. *Proc. Natl. Acad. Sci. U.S.A.*, 101, 15130–15135.

Pettit, L.I. (1990). The Conditional Predictive Ordinate for the Normal Distribution. *Journal of the Royal Statistical Society: Series B (Methodological)*, 52, 175–184.

Pfeifer, E.M., Hicke, J.A. & Meddens, A.J.H. (2011). Observations and modeling of aboveground tree carbon stocks and fluxes following a bark beetle outbreak in the western United States. *Global Change Biology*, 17, 339–350.

Pickett, S.T. & White, P.S. (1985). *The ecology of natural disturbance and patch dynamics*. Academic Press.

Porté, A. & Bartelink, H.H. (2002). Modelling mixed forest growth: a review of models for forest management. *Ecological Modelling*, 150, 141–188.

Povak, N.A., Hessburg, P.F. & Salter, R.B. (2018). Evidence for scale-dependent topographic controls on wildfire spread. *Ecosphere*, 9.

Preisler, H.K., Hicke, J.A., Ager, A.A. & Hayes, J.L. (2012). Climate and weather influences on spatial temporal patterns of mountain pine beetle populations in Washington and Oregon. *Ecology*, 93, 2421–2434.

Prichard, S.J., Hessburg, P.F., Hagmann, R.K., Povak, N.A., Dobrowski, S.Z., Hurteau, M.D., *et al.* (2021). Adapting western North American forests to climate change and wildfires: 10 common questions. *Ecol Appl*, 31.

Prichard, S.J., Povak, N.A., Kennedy, M.C. & Peterson, D.W. (2020). Fuel treatment effectiveness in the context of landform, vegetation, and large, wind-driven wildfires. *Ecol Appl*, 30.

PRISM Climate Group. (2021). PRISM Gridded Climate Data.

Pueyo, S. (2006). Diversity: between neutrality and structure. *Oikos*, 112, 392–405.

Pueyo, S. (2014). Algorithm for the maximum likelihood estimation of the parameters of the truncated normal and lognormal distributions.

Pukkala, T., Lähde, E. & Laiho, O. (2009). Growth and yield models for uneven-sized forest stands in Finland. *For. Ecol. Manag.*, 258, 207–216.

R Core Team. (2022). R: A language and environment for statistical computing.

Raffa, K.F., Aukema, B.H., Bentz, B.J., Carroll, A.L., Hicke, J.A., Turner, M.G., *et al.* (2008). Cross-scale Drivers of Natural Disturbances Prone to Anthropogenic Amplification: The Dynamics of Bark Beetle Eruptions. *BioScience*, 58, 501–517.

Reilly, M.J., Dunn, C.J., Meigs, G.W., Spies, T.A., Kennedy, R.E., Bailey, J.D., *et al.* (2017). Contemporary patterns of fire extent and severity in forests of the Pacific Northwest, USA (1985-2010). *Ecosphere*, 8, e01695.

Reilly, M.J., Halofsky, J.E., Krawchuk, M.A., Donato, D.C., Hessburg, P.F., Johnston, J.D., *et al.* (2021). Fire Ecology and Management in Pacific Northwest Forests. In: *Fire Ecology and Management: Past, Present, and Future of US Forested Ecosystems*, Managing Forest Ecosystems (eds. Greenberg, C.H. & Collins, B.). Springer International Publishing, Cham, pp. 393–435.

Reilly, M.J., Zuspan, A., Halofsky, J.S., Raymond, C., McEvoy, A., Dye, A.W., *et al.* (2022). Cascadia Burning: The historic, but not historically unprecedented, 2020 wildfires in the Pacific Northwest, USA. *Ecosphere*, 13.

Rhoades, C.C., Hubbard, R.M. & Elder, K. (2017). A Decade of Streamwater Nitrogen and Forest Dynamics after a Mountain Pine Beetle Outbreak at the Fraser Experimental Forest, Colorado. *Ecosystems*, 20, 380–392.

Rivera-Huerta, H., Safford, H.D. & Miller, J.D. (2016). Patterns and Trends in Burned Area and Fire Severity from 1984 to 2010 in the Sierra de San Pedro Mártir, Baja California, Mexico. *Fire Ecol.*, 12, 52–72.

Rodman, K.C., Andrus, R.A., Butkiewicz, C.L., Chapman, T.B., Gill, N.S., Harvey, B.J., *et al.* (2021). Effects of Bark Beetle Outbreaks on Forest Landscape Pattern in the Southern Rocky Mountains, U.S.A. *Remote Sensing*, 13, 1089.

Rodman, K.C., Andrus, R.A., Carlson, A.R., Carter, T.A., Chapman, T.B., Coop, J.D., *et al.* (2022). Rocky Mountain forests are poised to recover following bark beetle outbreaks but with altered composition. *Journal of Ecology*, 1365-2745.13999.

Rollins, M.G. (2009). LANDFIRE: a nationally consistent vegetation, wildland fire, and fuel assessment. *Int. J. Wildland Fire*, 18, 235.

Romme, W.H., Floyd, M.L. & Hanna, D. (2009). *Historical Range of Variability and Current Landscape Condition Analysis: South Central Highlands Section, Southwestern Colorado & Northwestern New Mexico*. Colorado Forest Restoration Institute.

Romme, W.H., Knight, D.H. & Yavitt, J.B. (1986). Mountain Pine Beetle Outbreaks in the Rocky Mountains: Regulators of Primary Productivity? *The American Naturalist*, 127, 484–494.

Rose, N.L., Yang, H., Turner, S.D. & Simpson, G.L. (2012). An assessment of the mechanisms for the transfer of lead and mercury from atmospherically contaminated organic soils to lake sediments with particular reference to Scotland, UK. *Geochimica et Cosmochimica Acta*, 82, 113–135.

Rouvinen, S. & Kuuluvainen, T. (1997). Structure and asymmetry of tree crowns in relation to local competition in a natural mature Scots pine forest. *Can. J. For. Res.*, 27, 890–902.

Saberi, S.J. & Harvey, B.J. (2023). What is the color when black is burned? Quantifying (re)burn severity using field and satellite remote sensing indices. *Fire Ecol.*, 19.

Scaduto, E., Chen, B. & Jin, Y. (2020). Satellite-Based Fire Progression Mapping: A Comprehensive Assessment for Large Fires in Northern California. *IEEE J. Sel. Top. Appl. Earth Observations Remote Sensing*, 13, 5102–5114.

Scheller, R.M., Domingo, J.B., Sturtevant, B.R., Williams, J.S., Rudy, A., Gustafson, E.J., *et al.* (2007). Design, development, and application of LANDIS-II, a spatial landscape simulation model with flexible temporal and spatial resolution. *Ecological Modelling*, 201, 409–419.

Seidl, R., Rammer, W., Scheller, R.M. & Spies, T.A. (2012). An individual-based process model to simulate landscape-scale forest ecosystem dynamics. *Ecological Modelling*, 231, 87–100.

Seidl, R., Spies, T.A., Peterson, D.L., Stephens, S.L. & Hicke, J.A. (2016). Searching for resilience: addressing the impacts of changing disturbance regimes on forest ecosystem services. *J Appl Ecol*, 53, 120–129.

Seidl, R., Thom, D., Kautz, M., Martin-Benito, D., Peltoniemi, M., Vacchiano, G., *et al.* (2017). Forest disturbances under climate change. *Nature Clim Change*, 7, 395–402.

Seidl, R. & Turner, M.G. (2022). Post-disturbance reorganization of forest ecosystems in a changing world. *Proc. Natl. Acad. Sci. U.S.A.*, 119, e2202190119.

Shore, T.L., Safranyik, L. & Lemieux, J.P. (2000). Susceptibility of lodgepole pine stands to the mountain pine beetle: testing of a rating system, 30.

Simard, M., Powell, E.N., Raffa, K.F. & Turner, M.G. (2012). What explains landscape patterns of tree mortality caused by bark beetle outbreaks in Greater Yellowstone?: Landscape patterns of bark beetle outbreaks. *Global Ecology and Biogeography*, 21, 556–567.

Simpson, M. (2013). *Developer of the forest vegetation zone map*. Ecologist, Central Oregon Area Ecology and Forest Health Program, USDA Forest Service, Bend, OR.

Singleton, M.P., Thode, A.E., Sánchez Meador, A.J. & Iniguez, J.M. (2019). Increasing trends in high-severity fire in the southwestern USA from 1984 to 2015. *For. Ecol. Manag.*, 433, 709–719.

Spies, T.A., Stine, P.A., Gravenmier, R.A., Long, J.W. & Reilly, M.J. (2018). *Synthesis of science to inform land management within the Northwest Forest Plan area* (No. PNW-GTR-966). U.S. Department of Agriculture, Forest Service, Pacific Northwest Research Station, Portland, OR.

Steel, Z.L., Fogg, A.M., Burnett, R., Roberts, L.J. & Safford, H.D. (2022). When bigger isn't better—Implications of large high-severity wildfire patches for avian diversity and community composition. *Diversity and Distributions*, 28, 439–453.

Stevens, J.T., Collins, B.M., Miller, J.D., North, M.P. & Stephens, S.L. (2017). Changing spatial patterns of stand-replacing fire in California conifer forests. *For. Ecol. Manag.*, 406, 28–36.

Stevens, J.T., Kling, M.M., Schwilk, D.W., Varner, J.M. & Kane, J.M. (2020). Biogeography of fire regimes in western U.S. conifer forests: A trait-based approach. *Global Ecol Biogeogr*, 29, 944–955.

Swanson, M.E., Franklin, J.F., Beschta, R.L., Crisafulli, C.M., DellaSala, D.A., Hutto, R.L., *et al.* (2011). The forgotten stage of forest succession: early-successional ecosystems on forest sites. *Front Ecol Environ*, 9, 117–125.

Thom, D. & Seidl, R. (2016). Natural disturbance impacts on ecosystem services and biodiversity in temperate and boreal forests. *Biol Rev*, 91, 760–781.

Thompson, R.D., Daniels, L.D. & Lewis, K.J. (2007). A new dendroecological method to differentiate growth responses to fine-scale disturbance from regional-scale environmental variation. *Can. J. For. Res.*, 37, 1034–1043.

Thorpe, H.C., Astrup, R., Trowbridge, A. & Coates, K.D. (2010). Competition and tree crowns: A neighborhood analysis of three boreal tree species. *For. Ecol. Manag.*, 259, 1586–1596.

Tishmack, J., Mata, S.A. & Schmid, J.M. (2005). *Mountain pine beetle emergence from lodgepole pine at different elevations near Fraser, CO* (No. RMRS-RN-27). U.S. Department of Agriculture, Forest Service, Rocky Mountain Research Station, Ft. Collins, CO.

Trumbore, S., Brando, P. & Hartmann, H. (2015). Forest health and global change. *Science*, 349, 814–818.

Turner, M.G. (2010). Disturbance and landscape dynamics in a changing world. *Ecology*, 91, 2833–2849.

Turner, M.G., Braziunas, K.H., Hansen, W.D. & Harvey, B.J. (2019). Short-interval severe fire erodes the resilience of subalpine lodgepole pine forests. *Proc. Natl. Acad. Sci. U.S.A.*, 116, 11319–11328.

Turner, M.G., Braziunas, K.H., Hansen, W.D., Hoecker, T.J., Rammer, W., Ratajczak, Z., *et al.* (2022). The magnitude, direction, and tempo of forest change in Greater Yellowstone in a warmer world with more fire. *Ecological Monographs*, 92.

Turner, M.G., Donato, D.C. & Romme, W.H. (2013). Consequences of spatial heterogeneity for ecosystem services in changing forest landscapes: priorities for future research. *Landsc Ecol*, 28, 1081–1097.

Turner, M.G. & Gardner, R.H. (2015). *Landscape Ecology in Theory and Practice*. Springer New York, New York, NY.

Turner, M.G., Romme, W.H. & Tinker, D.B. (2003). Surprises and lessons from the 1988 Yellowstone fires. *Front Ecol Environ*, 1, 351–358.

Turner, M.G., Tinker, D.B., Romme, W.H., Kashian, D.M. & Litton, C.M. (2004). Landscape Patterns of Sapling Density, Leaf Area, and Aboveground Net Primary Production in Postfire Lodgepole Pine Forests, Yellowstone National Park (USA). *Ecosystems*, 7, 751–775.

Tutland, N.J., Rodman, K.C., Andrus, R.A. & Hart, S.J. (2023). Overlapping outbreaks of multiple bark beetle species are rarely more severe than single-species outbreaks. *Ecosphere*, 14, e4478.

Vašíčková, I., Šamonil, P., Král, K., Fuentes Ubilla, A.E., Daněk, P. & Adam, D. (2019). Driving factors of the growth response of *Fagus sylvatica* L. to disturbances: A comprehensive study from Central-European old-growth forests. *For. Ecol. Manag.*, 444, 96–106.

Vázquez-González, C., Sampedro, L., Rozas, V. & Zas, R. (2020). Climate drives intraspecific differentiation in the expression of growth-defence trade-offs in a long-lived pine species. *Sci Rep*, 10, 10584.

Veblen, T.T., Hadley, K.S., Reid, M.S. & Rebertus, A.J. (1991). The Response of Subalpine Forests to Spruce Beetle Outbreak in Colorado. *Ecology*, 72, 213–231.

Vorster, A.G., Evangelista, P.H., Stohlgren, T.J., Kumar, S., Rhoades, C.C., Hubbard, R.M., *et al.* (2017). Severity of a mountain pine beetle outbreak across a range of stand conditions in Fraser Experimental Forest, Colorado, United States. *For. Ecol. Manag.*, 389, 116–126.

Wang, X., Swystun, T. & Flannigan, M.D. (2022). Future wildfire extent and frequency determined by the longest fire-conducive weather spell. *Science of The Total Environment*, 830, 154752.

Waring, R.H. & Franklin, J.F. (1979). Evergreen coniferous forests of the Pacific Northwest. *Science*, 204, 1380–1386.

Weed, A.S., Ayres, M.P. & Hicke, J.A. (2013). Consequences of climate change for biotic disturbances in North American forests. *Ecological Monographs*, 83, 441–470.

Weiner, J. & Thomas, S.C. (2001). The nature of tree growth and the "age-related decline in forest productivity." *Oikos*, 94, 374–376.

Weiss, A. (2001). *Topographic position and landforms analysis*.

Whitman, E., Parks, S.A., Holsinger, L.M. & Parisien, M.-A. (2022). Climate-induced fire regime amplification in Alberta, Canada. *Environ. Res. Lett.*, 17, 055003.

Wild, J., Kopecký, M., Svoboda, M., Zenáhlíková, J., Edwards-Jonášová, M. & Herben, T. (2014). Spatial patterns with memory: tree regeneration after stand-replacing disturbance in *Picea abies* mountain forests. *J Veg Sci*, 25, 1327–1340.

Wilm, H.G. & Dunford, E.G. (1948). *Effect of timber cutting on water available for stream flow from a lodgepole pine forest*. USDA Technical Bulletin 9681–43.

Wood, S. (2022). Package "mgcv."

Woodall, C.W., Fiedler, C.E. & Milner, K.S. (2003). Intertree competition in uneven-aged ponderosa pine stands. *Can. J. For. Res.*, 33, 1719–1726.

Wright, E.F., Canham, C.D. & Coates, K.D. (2000). Effects of suppression and release on sapling growth for 11 tree species of northern, interior British Columbia, 30, 10.

Wynecoop, M.D., Morgan, P., Strand, E.K. & Sanchez Trigueros, F. (2019). Getting back to fire sumés: exploring a multi-disciplinary approach to incorporating traditional knowledge into fuels treatments. *Fire Ecol.*, 15, 17.